Study on low-threshold random lasing by means of finite element method

Garuda FUJII

Nagoya University

Study on low-threshold random lasing by means of finite element method

A dissertation submitted in partial satisfaction
of the requirements for the degree
Doctor of Philosophy in Department of Mechanical Science and Engineering,
Nagoya University

by

Garuda FUJII

2011

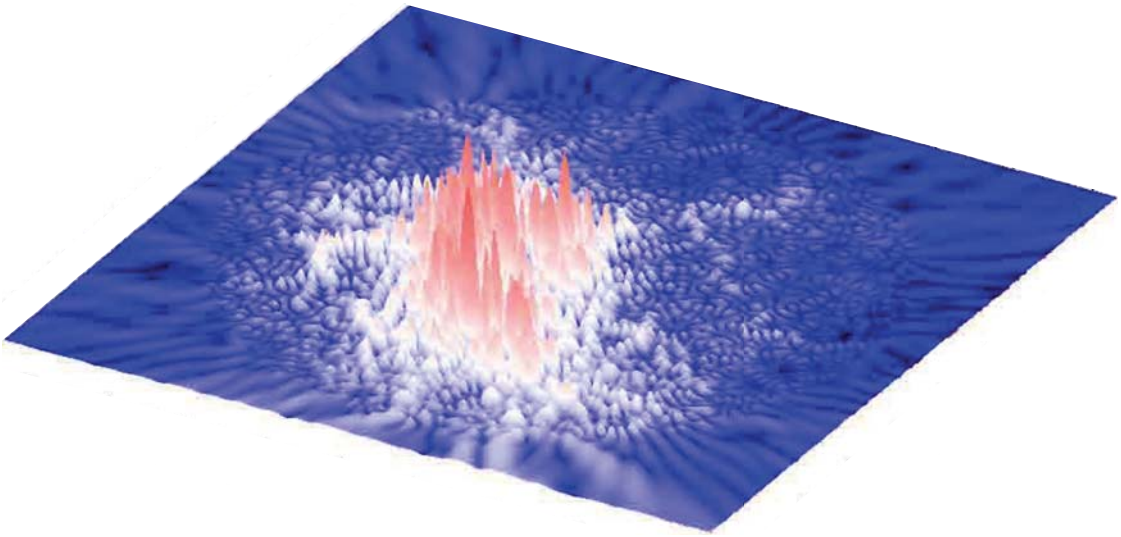

Study on low-threshold random lasing
by means of finite element method

Table of Contents

List of Figures

List of Tables

Acknowledgments

I would like first to acknowledge my advisor Prof. Tsuyoshi Ueta for all the helps he gave me during this work. He gave me the opportunity to study physics, helpful advice and discussion all my studies about photonics.

I offer thanks to my supervisor Prof. Toshiro Matsumoto for his advise and teaching, especially for writing papers and presenting in international conferences. I want to express my appreciation for his careful reading and checking of my papers.

I would like to express my gratitude to lecturer Toru Takahashi for his encouragements. Thanks to him, I could improve my skill and ability especially for high speed and parallel computing. He always give me good solutions and valuable advices when I ask him to help.

I am grateful for assistant prof. Takayuki Yamada. His talk, especially about optimization, is very interesting and new for me.

I am deeply grateful to Prof. Fukuzawa and Prof. Zhang for their careful reading and helpful comments for the improvement of my doctoral thesis.

I wish to thank all members of Matsumoto laboratory for their encouragements.

Vita

1984	Born, Gifu, Japan.
2003	Graduate, Gifu High School.
2007	B.S. (Mechanical Science and Engineering), Nagoya University.
2009	M.S. (Mechanical Science and Engineering), Nagoya University.
2008–2011	Teaching Assistant, Department of Mechanical Science and Engineering, Nagoya University. Taught sections of First Sofeware Engineerings for Computation (beginning computer programming course:Fortan 90) under direction of Professor Toshiro Matsumoto.
2009–2011	Reasearch Assistant, Department of Micro-Nano Systems Engineering, Nagoya University.

Publications and Presentations

Peer Reviewed Papers

Finite element analysis for laser action in honeycomb photonic crystals with random dangling bonds, Garuda FUJII, Hitoshi MATSUDA, Toshiro MATSUMOTO, Toru TAKAHASHI, Takayuki YAMADA and Tsuyoshi UETA, *Transactions of the Japanese Society for Computational Methods in Engineering*, Vol. 11, pp.89–94, 2011.

A study on the effect of filling factor for laser action in dielectric random media, G. Fujii, T. Matsumoto, T. Takahashi and T. Ueta, *Applied Physics A* , DOI: 10.1007/s00339-011-6734-0, 2011.

Study on transition from photonic-crystal laser to random laser, G. Fujii, T. Matsumoto, T. Takahashi and T. Ueta, *Optics Express* , 2011.(Submitted)

Finite Element Analysis of Laser Modes within Photonic Random Media, G. Fujii, T. Matsumoto, T. Takahashi and T. Ueta, *Journal of Physics B: Atomic, Molecular and Optical Physics* (Conditional Acceptance), 2011.

Study on Electric Intensity Dependency of Laser action in Randomly Distributed Dielectric Rod, G. Fujii, T. Matsumoto, T. Takahashi, T. Yamada and T. Ueta, *IEEJ Trans. EIS*, Vol. 132, No. 1, pp.89–95, 2012.

Finite Element Analysis for Laser Oscillation in Random System Consisting of Heterogeneous Dielectric Materials, Garuda FUJII, Toshiro MATSUMOTO, Toru TAKAHASHI, and Tsuyoshi UETA, *Transactions of the Japanese Society for Computational Methods in Engineering*, Vol. 10 pp. 117–122, 2011.

Proceedings of International Conferences

A Level Set-Based Topology Optimization Method for Three-Dimensional Acoustic Problems Using Fast Multipole Boundary Element Method, S. Harada, A. Suzuki, T. Takahashi, T. Yamada, G. Fujii and T. Matsumoto, *Proceedings of 9th WCSMO, (2011), WCSMO9*, 13-17 June 2011, Shizuoka, Japan.

A study on optical properties of photonic crystals consisting of hollow rods, G.

Fujii, T. Matsumoto, T. Takahashi and T. Ueta, *IOP Conference Series: Materials Science and Engineering*, 10, 012072, 2010.

Oral Presentations in International Conferences

A study on transition from photonic-crystal laser to random laser, G. Fujii, T. Matsumoto, T. Takahashi and T. Ueta, *Talk 23, Session 6, The 6th Nagoya University - UCLA International Symposium*, 26 June - 1 July 2011, UCLA , Los Angels, USA.

Detailed analysis for low-threshold laser oscillation in randomly distributed dielectric media, G. Fujii, T. Matsumoto, T. Takahashi and T. Ueta, *S6-5, Symposium S (Active Metamaterials II), ICMAT 2011*, 26 June - 1 July 2011, Suntec, Singapore.

A Level Set-based Topology Optimization Method for Three-dimensional Compliance Problem Using Boundary Element Method, S. Shichi, A. Suzuki, T. Yamada, T. Takahashi, G. Fujii and T. Matsumoto, *No.105 − 1, Shape and Topology Optimization (7), WCSMO-9*, 13-17 June 2011, Granship Shizuoka, Shizuoka, Japan.

A Level Set-Based Topology Optimization Method for Three-Dimensional Acoustic Problems Using Fast Multipole Boundary Element Method, S. Harada, A. Suzuki, T. Takahashi, T. Yamada, G. Fujii and T. Matsumoto, *No.059 − 1, Shape and Topology Optimization (3), WCSMO-9*, 13- 17 June 2011, Granship, Shizuoka, Japan.

Finite element analysis of laser modes within photonic random media, G. Fujii, T. Takahashi, T. Matsumoto and T. Ueta, *Contributed Session III-A, FEMTEC 2011*, 9-13 May 2011, Harvey ' s Casino and Resort, Reno, USA.

A study on optical properties of photonic crystals consisting of hollow rods, G. Fujii, T. Matsumoto, T. Takahashi and T. Ueta, *MS6041; Advanced Computations for Photonic/Phononic Crystals, WCCM/APCOM 2010*, 19 - 23 July 2010, Convention Center, Sydney, Australia.

Poster Presentations in International Conferences

Study on Transition from Photonic-Crystal Laser to Random Laser, Garuda Fujii, Toshiro Matsumoto, Toru Takahashi, and Tsuyoshi Ueta, *P1-8, Poster Session*

I, MHS 2011, 7 June - 9 November 2011, Nagoya University, Nagoya, Japan.

A study on effect of filling factor for laser actions in dielectric random media, G. Fujii, T. Takahashi, T. Matsumoto and T. Ueta, *S-PO2-4, Symposium S Poster Session, ICMAT 2011*, 26 June - 1 July 2011, Suntec, Singapore.

Finite element analysis for laser oscillations in random systems, G. Fujii, T. Takahashi, T. Matsumoto and T. Ueta, *P1-13, Poster Session I, MHS 2010*, 7 June - 10 November 2010, Nagoya University, Nagoya, Japan.

Finite element simulations of Anderson localization in random systems, G. Fujii, T. Takahashi and T. Matsumoto, *P1-51, Poster Session I, MHS 2009*, 8 - 11 June November 2000, Nagoya University, Nagoya, Japan.

Oral Presentations in Domestic Conferences

Finite element analysis for laser action in honeycomb photonic crystals with random dangling bonds, Garuda FUJII, Hitoshi MATSUDA, Toshiro MATSUMOTO, Toru TAKAHASHI, Takayuki YAMADA and Tsuyoshi UETA, *JASCOME symposium 2011*, 16 December 2011.

A Study on the Transition from Photonic-Crystal Laser to Random Laser, Garuda FUJII, Toshiro MATSUMOTO, Toru TAKAHASHI, Takayuki YAMADA and Tsuyoshi UETA, *1303, OS-13, Designs and Simulations of Photonic and Phononic Structures, JSME 24th Computational Mechanics Division Conference*, 8 - 10 December 2011, Okayama University, Okayama, Japan.

A Study on the Transition from Photonic-Crystal Laser to Random Laser, G. Fujii, T. Matsumoto, T. Takahashi, T. Yamada, T. Ueta, *24aTN-1, Photonic Crystal, JPS Annual Conference in Autumn 2011*, 21 - 24 September 2011, Toyama University, Toyama, Japan.

Topology Optimization of Elastic Body Using Boundary Element Method Based on the Level Set Boundary Expressions, Shinichiro SHICHI, Akihisa SUZUKI, Garuda FUJII, Takayuki YAMADA, Toru TAKAHASHI, and Toshiro Matsumoto, *A-11-2, OS25, Boundary Element Method/Fast Boundary Element Method*, 25 - 27 May 2011, The University of Tokyo, Tokyo, Japan.

Level-Set Based Topology Optimization for Acoustic Problems Using Fast Multi-

ple Boundary Element Method, Shinya HARADA, Zheng, C.J., Akihisa SUZUKI, Toru TAKAHASHI, Takayuki YAMADA, Garuda FUJII, and T. Matsumoto, *A-11-1, OS25, Boundary Element Method/Fast Boundary Element Method*, 25 - 27 May 2011, The University of Tokyo, Tokyo, Japan.

Finite Element Analysis for Laser Oscillation in Dielectric Random Media, G. Fujii, T. Matsumoto, T. Takahashi, T. Yamada, T. Ueta, *25aHB-6, Photonic Crystal, JPS Annual Conference in Spring 2011*, 25 - 28 March 2011, Niigata University, Niigata, Japan.

A study on dependence of laser oscillations on electric intensity in randomly distributed dielectric structure, Garuda FUJII, Toshiro MATSUMOTO, Toru TAKAHASHI, Tsuyoshi UETA, *OS05-15, OS5-4, Mathematical Physics and Application of Wave Phenomena,* , 8 - 10 March 2011, Tokyo Institute of Technology, Tokyo, Japan.

Finite Element Analysis for Laser Oscillation in Random System Consisting of Heterogeneous Dielectric Materials, Garuda FUJII, Toshiro MATSUMOTO, Toru TAKAHASHI, and Tsuyoshi UETA, *21-101210, Electromagnetics · Optics, JASCOME symposium 2010*, 10 December 2010, Niigata University, Niigata, Japan.

Finite Element Analysis of Anderson Localization of Electromagnetic Waves in Randomly Distributed Dielectric Media, Garuda FUJII, Toshiro MATSUMOTO, Toru TAKAHASHI, and Tsuyoshi UETA, *1904, OS-19, Designs and Simulations of Photonic and Phononic Structures, JSME 23th Computational Mechanics Division Conference*, 23 - 25 September 2010, Kitami Institute of Technology, Kitami, Japan.

A Study on Optical Properties of Photonic Crystals Consisting of Rods with center Cavities, Garuda FUJII, Toru TAKAHASHI, Tsuyoshi UETA, and Toshiro MATSUMOTO, *1705, OS-17, Designs and Simulations of Photonic and Phononic Structures, JSME 23th Computational Mechanics Division Conference*, 10 - 12 October 2009, Kanazawa University, Kanazawa, Japan.

A Study on Optical Properties of Photonic Crystals Consisting of Rods with center Cavities, Garuda FUJII, Toru TAKAHASHI, Tsuyoshi UETA, and Toshiro MATSUMOTO, *1705, OS-17, Designs and Simulations of Photonic and Phononic Structures, JSME 23th Computational Mechanics Division Conference*, 1 - 3

November 2008, Ryukyus University, Okinawa, Japan.

Others

Dependence of threshold of random laser on the amount of disorder, Garuda Fujii, *Proceedings of International Workshop for the Interaction of Young Researcher on Micro-nano Mechatronics*, p. 15, Satellite Session, MHS 2011, 6-10 November 2011, Nagoya University, Nagoya, Japan.

Finite element analysis for laser oscillations in random systems composed of dielectric materials, Garuda Fujii, *Proceedings of International Symposium on Frontier Research in Micro-Nano Systems and Mechatroncs*, p. 15, Satellite Session, MHS 2010, 7-11 November 2010, Nagoya University, Nagoya, Japan.

Finite element analysis of laser oscillations and Anderson localization of electromagnetic waves in a random configuration of dielectric materials, Garuda Fujii, *The Second Symposium of Young Researcers -System Integration and its Application to Medical Technology-*, p. 28, 26 March 2010, Nagoya University, Nagoya, Japan.

Abstract of the Dissertation

Study on low-threshold random lasing by means of finite element method

by

Garuda FUJII
Doctor of Philosophy in Department of Mechanical Science and Engineering,
Nagoya University
Nagoya University 2011
Professor Toshiro Matsumoto, Chair

This dissertation presents detailed analyses of lasing phenomena in two-dimensional disordered structures called "random lasers" by means of finite element method. The excitation pumping for optically active materials, that is, population inversion is modeled by negative value in imaginary part of relative permittivity. Perfectly matched layer boundary condition is used to simulate light scatterings in an open region. The amplifications of light waves emitted from disordered systems are computed by changing frequency and population inversion of active medium.

The dependence of properties of random lasing on the excitation pumping of optically active materials are revealed for the first time. The effects of location of active medium, lasing frequency, filling factor of dielectric cylinders, the amount of positional disorder of cylinders, and the materials of cylinders on lasing threshold are investigated precisely. Appropriate random systems for low-threshold random lasing are investigated based on the results of the dependence.

CHAPTER 1

Introduction

1.1 Background

Light control with micro-nano optical structures are receiving much attention because of their high potential for light confinements. "Laser device" is one of the most active research topics to which micro-nano optical structures are applied. Laser is usually composed of two basic elements: optically active medium that gives light amplifications through stimulated emission and optical cavities that confine light waves. Light waves are nonlinearly amplified by cavity confinements that work as feedback mechanisms repeating light amplifications. Hence, the cavities determine the properties of laser devices and are essential to laser action. When light amplifications overpower losses in systems, the systems reach lasing threshold and lase. The lasing threshold is strongly influenced by light trapping. Lower-threshold laser devices can lase by lower excitation energy for the pumping of optically active medium, that is, energy-saving laser devices.

Photonic crystals are nano periodic structures composed of dielectric or metallic materials. Photonic crystals can prohibit light propagations in certain frequency ranges called "photonic band gaps" [1, 2]. The band gaps occur from Bragg's reflections, that is, coherent multiple reflections by periodic structures. Photonic crystals are applied to optical filters, optical fibers, waveguides, mirrors, etc. Laser devices in which photonic crystals are used as cavities, called photonic crystal lasers, can lase even in a lower pumped state of optically active material because of the extremely low group velocities at band edge frequencies [3, 4, 5]. At such frequencies, light waves are localized in photonic crystals as standing waves that work as feedback mechanisms repeating light amplifications. Recently, photonic crystal cavities with extremely high quality factor are reported [6, 7, 8, 9]. The quality-factors are dynamically controlled [7].

The properties of non-periodic optical structures are studied actively in recent years. Such media with non-periodicities are called with the terms "random

system" or "disordered structure" in the previous articles. Lasing phenomena in disordered structures are called "random lasers." Random lasing phenomena were experimentally observed by Lawandy [10] in 1994. They experimented laser action in random systems composed of laser dye and colloidal suspension of titanium dioxide particles. After the first observation of random lasing, random lasers were discussed whether the light amplifying phenomena are lasing phenomena or amplified spontaneous emission because the light amplifications occur in disordered structures and there is no cavity-like structure [11]. Random lasers have several unique lasing properties which conventional laser devices cannot give. Actually, the modes of random laser are determined by random multiple scatterings in disordered structures. Random lasing occurs from random multiple scatterings and interference effects of scattered light waves. Hence, their laser modes and lasing mechanisms are quite varied and complicated.

In order to investigate such complex lasing phenomena intensively, numerical simulation using large scale computation models is inevitable and actually the most powerful method. Finite difference time domain method (FDTD method) are frequently used for the analyses of random lasers [12, 13, 14, 15]. In the above numerical analyses, lasing frequency, lasing mechanisms, laser modes, localized regimes of lasing states, and the effect of filling factor and system sizes for intensity of electric field are investigated. Fixed pumping excitations of optically active medium are assumed in the analyses of lasing states and light confinements of non-excited and lasing states in disordered structures are compared with each other.

In the first experimental report of random lasers by Lawandy, it is mentioned that the threshold of random laser is "surprisingly low" [10]. However, because of the above assumption of the fixed excitation, no numerical analysis investigated lasing threshold of random lasers. Burin et al. presented theoretically that lasing threshold becomes lower as random system size increases [16]. Chang et al. investigated lasing threshold of one-dimensional random lasers consisting of randomly positioned multi-layers [17]. But the lasing threshold of random lasers and the dependency of lasing properties of random lasers on pumping excitations of optical gain are not discussed sufficiently.

Hence, in the present dissertation, we present the dependence of lasing properties of random lasers on the excitation of active medium by means of finite element method. The excitation of optically active medium, namely, population inver-

sion density of active gain is modeled by giving a negative value to the imaginary part of relative permittivity. We assume lasing phenomena in two-dimensional disordered structures consisting of random arrangement of homogeneous dielectric cylinders. Some appropriate random systems for having low-threshold laser action are proposed.

1.2 Objective

The objective of this thesis is to give appropriate random systems having low-threshold laser action for developing energy-saving random lasers by investigating the dependencies of the arrangement of dielectric inclusions, their filling rate, and optically active materials on lasing properties.

Numerical computations of lasing phenomena are indispensable for extensive analyses of the lasing properties and finite element method is used for this purpose. The dependence of the properties of random lasers on the excitation energy of optically active medium is investigated by modeling population inversion density of active medium as a negative imaginary part of the relative permittivity. Such approach with modeling of population inversion has been used in the analyses of photonic crystal lasers. This approach is used, for the first time in this study, to the analyses of random lasing. This approach enables us to investigate the lasing threshold of random lasers directly. The analyses are focused on low-threshold laser action, i.e., lasing phenomena oscillating in lower excited state of optically active materials.

The following factors characterizing random systems are investigated in this thesis.

- Influence of the location of active medium
- Influence of lasing frequency on lasing properties and lasing threshold
- Relation between the amplification of emitted light waves and electric field intensity in random systems
- Effect of the filling factor of dielectric cylinders on lasing threshold of random lasing
- Effect of the amount of positional disorder of dielectric cylinders on lasing threshold

- Effect of rod materials

The influence of the location of active medium is first investigated. It is expected to occur low-threshold laser action when light waves are localized in optically active medium. Hence the investigation of the location of light localizations in disordered structures is important. Two types of random systems are considered: one with optically active medium in interspaces among nonactive dielectric cylinders and the other consisting of optically active cylinders within nonactive medium. The light waves are amplified in interspaces among dielectric cylinders in the former random systems, while in the latter random systems, light waves are amplified in active cylinders. Simulations of lasing phenomena in both random systems are given and the lasing thresholds of both types are compared.

Then, the influence of lasing frequency on lasing properties and lasing threshold is investigated. It is supposed that transfer mean free path (TMFP) needs to be shorter than the wavelength of light so that the random lasing is activated. In order to find a state in which light waves are localized in the interspaces among neighboring dielectric cylinders, the relation between wavelength and TMFP and the relation between lasing properties and lasing frequencies are studied. Also computed is the light amplifications for a wide frequency range with a fixed population inversion density of active medium.

The relation between the amplification of emitted light waves and electric field intensity in random systems are investigated next. Although only the intensity of electric field in random systems are computed and lasing phenomena are related only to their divergent peaks in the previous studies [18, 12, 13], amplification of light wave is essentially not an enhancement of electric field intensity but an amplification of light wave. Therefore in the thesis, both the amplification and the intensity are computed and compared with each other.

The effect of the filling factor of dielectric cylinders on lasing threshold of random lasing is investigated next. The filling factor of dielectric cylinders is one of the most important factor giving large influence on the intensity of multiple scattering of light waves in disordered structures. However, relation between lasing threshold of random laser and the filling factor of dielectric cylinders is not studied yet. Therefore, lasing phenomena in disordered structures with various filling factors of dielectric cylinders are simulated.

Then, the effect of the amount of positional disorder of dielectric cylinders

on lasing threshold is studied. Laser action in periodic structures, i.e., photonic crystal laser, can lase even in low excited state of optically active medium because of extremely low group velocity at band edge frequencies. As mentioned in a previous study by Lawandy [10], random laser can realize low-threshold laser action. Therefore, the influence of the amount of disorder on lasing threshold of random lasers are discussed.

Finally, the effect of rod materials is studied. Random lasings in disordered structures consisting of metallic cylinders, called metallic random lasers, is studied. Noble metals reflect light perfectly on their surfaces because of the existence of free electrons. Surface plasmon which is coherent electron oscillations work to keep out light waves. Hence, it is expected that multiple scatterings are enhanced in disordered structures consisting of noble metals. Moreover, in the case of random systems with optically active medium in interspaces among metallic cylinders, all light waves are kept in active medium, and thus, lasing threshold of metallic random lasers are expected to be extremely low. Lasing threshold of metallic random lasers is studied.

In addition to the above studies on the characteristics of random lasing, we also present simulations of random laser action in honeycomb structures including random link removals as a new type of random laser devices. The honeycomb structure proposed by Florescu et al. [19] is different from conventional random systems consisting of cylinders. They investigated the effect of random link removals on the band structures of honeycomb structures. A random lasing is also expected to occur in such a honeycomb structure including random link removals. Hence, random lasing properties and lasing threshold of this structure is investigated as a related topic.

1.3 Overview of the thesis

This dissertation is organized as follows.

Chapter 2

Photonic crystals, random lasers, and basic formulations of numerical methods are introduced.

In the introduction of photonic crystals, we describe the properties of electromagnetic waves in optical periodic structures as Bloch state, band structures

(band gaps), and transmission spectrum. Several analysis methods based on Maxwell's equations and the properties of light waves in optical periodic structures are introduced in order to explain the origin of the properties of photonic crystals. Several previous studies about advanced laser devices to which photonic crystals are applied are also introduced.

Random lasers are also introduced in this chaper. Lasing mechanism, lasing properties, previous studies, and applications are described. Detailed descriptions of our analysis objects are given. Disordered optical structures analyzed in this dissertation and the materials used to fabricate them are explaned. The mathematical modeling of the physical phenomena in random lasing is given using Maxwell's equations. Basic equations of electromagnetic scatterings in open regions are derived from Maxwell's equations. Optically active medium amplifying light waves and the parameter which is proportional to the population inversion density are introduced, and perfectly matched layer boundary condition for simulating electromagnetic scatterings in open regions is explained. Outline of the numerical methods frequently used for the analysis of optical phenomena are also shown.

Chapter 3

Random lasing in a disordered structure consisting of optically active cylinders within non-active medium are simulated. The amplification of light waves flowing out from the random systems, electric amplitude distributions of lasing states, radiation directions, and lasing threshold are computed. Five samples with different rod arrangements are analyzed in order to confirm common physics and average of lasing threshold.

Chapter 4

Simulated results of random lasing in random systems consisting of non-active cylinders within active medium are presented.

In section 4.2, random lasing phenomena in the random system with optically active medium in interspaces among dielectric cylinders are simulated. Five samples with different rod arrangements are analyzed in order to confirm common physics and average of lasing threshold. The simulated results of random lasing show that the random system is appropriate for lower threshold laser action because light waves are localized in interspaces filled with active medium. Lasing

threshold of random laser oscillating in the random systems are compared with that oscillating in random systems consisting of active cylinders. It is shown that the random systems with active medium in interspaces among nonactive cylinders can activate lower-threshold laser action than the random systems consisting of active cylinders do.

In section 4.3, the influence of lasing frequency on lasing threshold and types of laser modes are discussed. Based on the result obtained in section 4.2, we consider random systems with active medium in interspaces among nonactive cylinders as the target of study. Amplification of light waves flowing out from disordered systems for wide frequency range is computed, and the influence of lasing frequency on lasing properties is investigated.

In section 4.4, the relation between light amplification and electric intensity in random systems and the role of disordered structures are presented. Light amplification is compared with electric intensity in random systems. Random systems with active medium in interspaces among nonactive cylinders are assumed because of low lasing threshold shown in 4.2. Some laser modes which are different from "cavity modes" are newly found, and these modes are defined as "non-cavity modes". The similarity of electric amplitude distributions between excited and non-excited states of active medium are evaluated by using normalized mean square error. By this evaluation, lasing phenomena are distinguished between cavity modes and non-cavity modes, and thus, disordered structures are judged if they work as cavities or not. It is found that cavity modes tend to lase in lower pumped states than non-cavity ones.

In section 4.5, the effect of filling factor of dielectric materials on lasing threshold is investigated. Lasing phenomena in disordered structures with filling factors 10%, 20%, 30%, 40%, and 50% are simulated. Optically active medium are introduced in interspaces among dielectric cylinders. It is found that optical structures with higher filling factor are more appropriate for lower-threshold laser action because light confinements become strong as the filling factor of dielectric materials increases. The results indicate that strong light confinement is important for low-threshold laser action.

In section 4.6, transition from photonic crystal laser to random laser is simulated. The amount of positional disorder is parameterized as the distance between a grid point of fictitious triangular lattice and the center of a randomly distributed rod. Lasing phenomena is sensitive for the disorder of dielectric structures. The

laser action caused by random multiple scatterings occurs even if the amount of positional disorder is quite small. Such laser action start to occur from higher frequency range and spread for lower frequency range.

Chapter 5

Lasing phenomena and lasing threshold of random laser occurring in disordered structures composed of metallic cylinders are investigated. Metals are expressed by Drude-type relative permittivity derived from motion equation of electrons and realize high reflectance on their surface. Extremely intensive multiple scatterings and strong light confinements in active medium are expected. Thresholds of random lasers in metallic disordered structures are compared with those in dielectric ones of same rod arrangements.

Extremely low threshold lasing phenomena are observed in the results of random lasers in metallic disordered structures.

Chapter 6

Lasing phenomena in honeycomb structures including randomly positioned dangling bonds are investigated. Such structures are appropriate for including optically active medium and are fabricated actually in order to apply to optical devices. Optically active medium is introduced into hexagonal hollows, and 100 dielectric links are randomly removed from the hexagonal structures. It is found that random lasing occurs in the honeycomb structures including randomly positioned dangling bonds, but the threshold of laser action in the honeycomb structures becomes higher than that in random systems consisting of nonactive cylinder within active medium.

Chapter 7

Conclusions of the thesis are presented.

CHAPTER 2

Fundamentals

2.1 Photonic crystals

Photonic crystals are periodic structures composed of dielectric materials. The length of the periods are approximately equal to the wavelength of visible light waves. Photonic crystals can be classified into one-, two-, and three-dimensional crystals shown in Figs. 2.14(a), 2.14(b), and 2.14(c), respectively, based on their periodicities. Photonic crystals can prohibit the propagations of light waves in certain frequency ranges. The opaque frequency ranges and the property against light propagations are called "photonic bandgaps".

Photon energy-band structure of a periodic dielectric structure was theoretically proposed by Ohtaka [1] based on the similarity between a Helmholtz equation derived from Maxwell's equations and the Schrödinger equation without time dependent terms in 1979. In 1987, Yablonovitch proposed a possibility of realizing a three-dimensional photonic bandgap [2]. Periodic dielectric structures called photonic crystals prohibit the propagation of light waves in specific frequency ranges. Such property of photonic crystals is called "photonic bandgap". Photonic badgaps occur from Bragg reflection of light waves, caused by periodic dielectric structures. After the proposition by Yablonovitch, many researchers study photonic crystals intensively.

(a) One dimensional structure. (b) Two dimensional structure. (c) Three dimensional structure.

Figure 2.1: Photonic crystals.

2.1.1 Bloch state

The electric field $\mathbf{E}$ becomes Bloch state in optical periodic structures as follows

$$\mathbf{E}_{kn}(\mathbf{r}) = e^{\mathrm{i}kx} u_{kn}(\mathbf{r}), \tag{2.1}$$

where $\mathbf{r}$ express positions in optical periodic structures, k is wavenumber, n is a integer in order to make a distinction between eigenmodes having same wavenumber k, and $u_{kn}(\mathbf{r})$ is a periodic function satisfying a following periodicity:

$$u_{kn}(\mathbf{r} + \mathbf{a}) = u_{kn}(\mathbf{r}),$$

where $\mathbf{a}$ is the lattice vector of optical periodic structures. We derive above Bloch state.

The eigenfunction of the electric field is expressed by a Fourier integral form as

$$\mathbf{E}(\mathbf{r}) = \int \mathbf{A}(\mathbf{k}) e^{i\mathbf{k}\cdot\mathbf{r}} d\mathbf{k}, \tag{2.2}$$

where the integral domain is the whole wave-number space. In photonic crystals, relative permittivity $\epsilon(\mathbf{r})$ becomes a periodic function and can be written by a Fourier series expansion as follows:

$$\mathbf{E}(\mathbf{r}) = \sum_{\mathbf{G}} \xi(\mathbf{G}) e^{i\mathbf{G}\cdot\mathbf{r}}. \tag{2.3}$$

By substituting Eqs. (2.2) and (2.3) into the wave equation

$$\nabla \times [\nabla \times \mathbf{E}(\mathbf{r})] = \frac{\omega^2}{c^2} \epsilon(\mathbf{r}) \mathbf{E}(\mathbf{r}), \tag{2.4}$$

we have the following equation:

$$\int d\mathbf{k} \left\{ \mathbf{k} \times [\mathbf{k} \times \mathbf{A}(\mathbf{k})] + \frac{\omega^2}{c^2} \sum_{\mathbf{G}} \xi(\mathbf{G}) \mathbf{A}(\mathbf{k} - \mathbf{G}) \right\} e^{i\mathbf{k}\cdot\mathbf{r}} = 0. \tag{2.5}$$

Because Eq. (2.5) holds for all $\mathbf{r}$, we obtain

$$\mathbf{k} \times [\mathbf{k} \times \mathbf{A}(\mathbf{k})] + \frac{\omega^2}{c^2} \sum_{\mathbf{G}} \xi(\mathbf{G}) \mathbf{A}(\mathbf{k} - \mathbf{G}) = 0.$$

Above equation indicates that the coefficient function $A(\mathbf{k})$ is related to $A(\mathbf{k} - \mathbf{G})$.

The solution of Eq. (2.4) can be expressed by the summation of the Fourier coefficients as

$$\begin{aligned}\mathbf{E}_{\mathbf{k}} &= \sum_{\mathbf{G}} \mathbf{A}(\mathbf{k}-\mathbf{G}) e^{i(\mathbf{k}-\mathbf{G})\cdot\mathbf{r}} \\ &= \sum_{\mathbf{G}} \mathbf{u}_{\mathbf{k}}(\mathbf{r}) e^{i\mathbf{k}\cdot\mathbf{r}},\end{aligned}$$

where $\mathbf{u}_{\mathbf{k}}(\mathbf{r})$ is a periodic function defined as

$$\mathbf{u}_{\mathbf{k}}(\mathbf{r}) = \sum_{\mathbf{G}} \mathbf{A}(\mathbf{k}-\mathbf{G}) e^{-i\mathbf{G}\cdot\mathbf{r}}$$

satisfying

$$\begin{aligned}\mathbf{u}_{\mathbf{k}}(\mathbf{r}+a_i) &= \sum_{\mathbf{G}} \mathbf{A}(\mathbf{k}-\mathbf{G}) e^{-i\mathbf{G}\cdot(\mathbf{r}+\mathbf{a}_i)} \\ &= \mathbf{u}_{\mathbf{k}}(\mathbf{r}).\end{aligned}$$

2.1.2 Dispersion relation and band gaps

Dispersion relations are the relations between circular frequency ω and wave number k. In homogeneous dielectric medium whose relative permittivity ϵ_{h} is constant, the dispersion relation becomes linear as

$$k = \frac{\omega}{c}\sqrt{\epsilon_{\mathrm{h}}}.$$

However, in photonic crystals, relative permittivity becomes position dependent function as $\epsilon(\mathbf{r})$, and then, dispersion relation becomes nonlinear.

2.1.2.1 Band calculation for one-dimensional photonic crystal by using tight-binding approximation

In one-dimensional photonic crystals, namely, dielectric multilayer structures, the Helmholtz equation derived from Maxwell's equations for TM mode becomes

$$\frac{\partial^2 E(x)}{\partial x^2} + \frac{\omega^2}{c^2}\epsilon(x)E(x) = 0, \tag{2.6}$$

where $\epsilon(x)$ satisfies

$$\epsilon(x+a) = \epsilon(x),$$

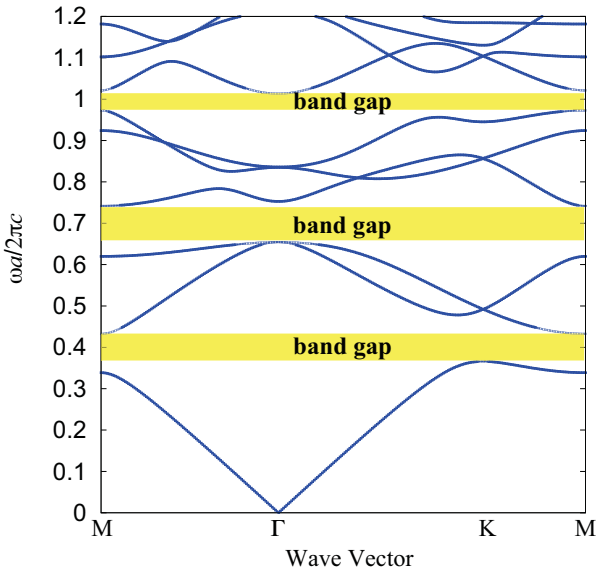

(a) Band structure.

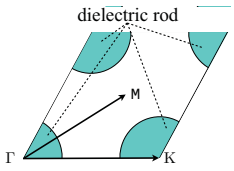

(b) Unit cell.

Figure 2.2: The band structure of a 2D photonic crystal consisting of dielectric cylinders whose radius is $R = 0.3a$. Dielectric cylinders, whose permittivities are 4.0, are arranged on triangular lattices. This dispersion relation is computed by plane wave expansion method.

where a is the periodic length of the multilayer structures. The partial spatial derivative in Eq. (2.6) is discretized by using the central difference as

$$\frac{\partial E(x)}{\partial x} = \frac{E(x + a/2) - E(x - a/2)}{a},$$

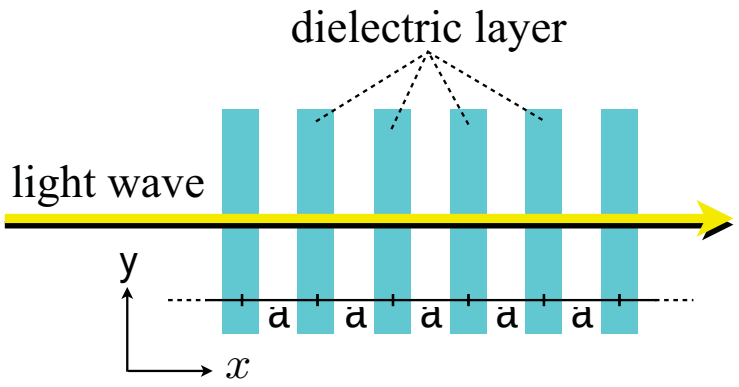

Figure 2.3: An image of a one-dimensional photonic crystal (multilayer structure).

which leads to

$$\frac{\partial^2 E(x)}{\partial x^2} = \frac{1}{a}\left[\frac{E(x+a)-E(x)}{a} - \frac{E(x)-E(x-a)}{a}\right]$$
$$= \frac{E(x+a)-2E(x)+E(x-a)}{a^2}. \tag{2.7}$$

By substituting Eq. (2.7) into the Helmholtz equation (2.6), and using Bloch's theorem (2.1), we obtain an eigenvalue equation as

$$\left[\frac{\exp(\mathrm{i}ka)+\exp(-\mathrm{i}ka)-2}{a^2} + \frac{\omega^2}{c^2}\right] E(x) = 0,$$

from which we have

$$\frac{\omega a}{2\pi c} = \pm\frac{a}{2\pi}\sqrt{\frac{2-\exp\left(\mathrm{i}\frac{\mathrm{ka}}{2\pi}2\pi\right)-\exp\left(-\mathrm{i}\frac{ka}{2\pi}2\pi\right)}{a^2}}$$
$$= \pm\frac{1}{2\pi}\sqrt{2-\exp\left[\mathrm{i}2\pi\left(\frac{ka}{2\pi}\right)\right]-\exp\left[-\mathrm{i}2\pi\left(\frac{ka}{2\pi}\right)\right]},$$

where k is the wave number in the range $-\frac{\pi}{a} \leq k \leq \frac{\pi}{a}$.

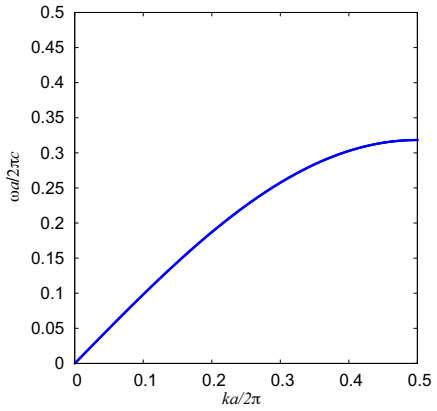

Figure 2.4: A dispersion relation of a one-dimensional photonic crystal computed by tight-binding approximation.

2.1.2.2 Band calculation for two-dimensional triangular lattice by using tight-binding approximation

The lattice vectors of triangular lattice are defined as follows:

$$\begin{aligned} \mathbf{a}_1 &= (a, 0)\,, \quad \mathbf{a}_2 = \left(\tfrac{1}{2}a, \tfrac{\sqrt{3}}{2}a\right), \quad \mathbf{a}_3 = \left(-\tfrac{1}{2}a, \tfrac{\sqrt{3}}{2}a\right), \\ \mathbf{a}_4 &= (-a, 0)\,, \quad \mathbf{a}_5 = \left(-\tfrac{1}{2}a, -\tfrac{\sqrt{3}}{2}a\right), \quad \mathbf{a}_6 = \left(\tfrac{1}{2}a, -\tfrac{\sqrt{3}}{2}a\right), \end{aligned} \tag{2.8}$$

where a is a lattice constant.

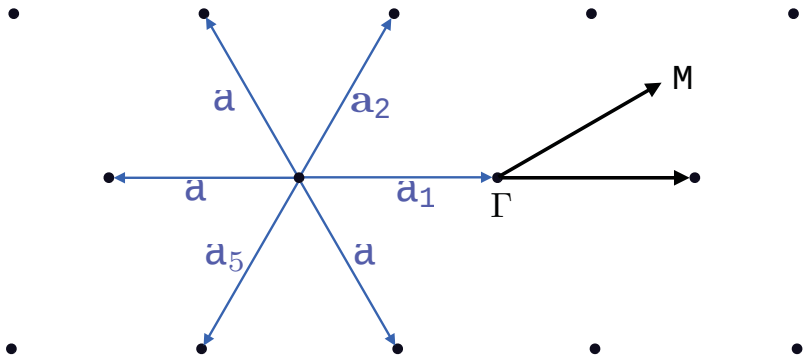

Figure 2.5: Triangular lattices.

The electric field at each lattice point, $E(\mathbf{r} + \mathbf{a}_i)$, is expressed by a Taylor expansion as

$$\begin{aligned} E(\mathbf{r} + \mathbf{a}_i) &= E(\mathbf{r}) + (\mathbf{a}_i \cdot \nabla) E(\mathbf{r}) + \frac{1}{2} (\mathbf{a}_i \cdot \nabla)^2 E(\mathbf{r}) \\ &= E(\mathbf{r}) + \left[a_x^i \frac{\partial}{\partial x} E(\mathbf{r}) + a_y^i \frac{\partial}{\partial y} E(\mathbf{r}) \right] \\ &\quad + \frac{1}{2} \left[(a_x^i)^2 \frac{\partial^2}{\partial x^2} E(\mathbf{r}) + (a_y^i)^2 \frac{\partial^2}{\partial y^2} E(\mathbf{r}) \right], \end{aligned} \tag{2.9}$$

where a_x^i and a_y^i are the x and y components of $\mathbf{a}_i$, respectively. In Eq. (2.9), the terms whose orders are larger than 3 are neglected because they are sufficiently small. We sum up all the electric field at $\mathbf{r} + \mathbf{a}_i$ $(i = 1 \cdots 6)$ as

$$\begin{aligned} \sum_{i=1}^{6} E(\mathbf{r} + \mathbf{a}_\mathrm{i}) &= 6E(\mathbf{r}) + 0 + \frac{1}{2} \left[3a^2 \frac{\partial^2}{\partial x^2} E(\mathbf{r}) + 3a^2 \frac{\partial^2}{\partial y^2} E(\mathbf{r}) \right] \\ &= 6E(\mathbf{r}) + \frac{3a^2}{2} \nabla^2 E(\mathbf{r}) \end{aligned}$$

resulting in

$$\nabla^2 E(\mathbf{r}) = \frac{2}{3a^2} \left[\sum_{i=1}^{6} \exp(\mathrm{i}\mathbf{k} \cdot \mathbf{a}_\mathrm{i}) - 6 \right] E(\mathbf{r}), \tag{2.10}$$

where the relation $E(\mathbf{r}+\mathbf{a}_\mathrm{i}) = E(\mathbf{r})\exp(\mathrm{i}\mathbf{k}\cdot\mathbf{a}_\mathrm{i})$ derived from Bloch's theorem is used. We substitute Eq. (2.10) into the Helmholtz equation to have

$$\begin{aligned}\nabla^2 E(\mathbf{r}) + \frac{\omega^2}{c^2}E(\mathbf{r}) &= \frac{2}{3a^2}\left[\sum_{i=1}^{6}\exp(\mathrm{i}\mathbf{k}\cdot\mathbf{a}_\mathrm{i}) - 6 + \frac{\omega^2}{c^2}\frac{3a^2}{2}\right]E(\mathbf{r}) \\ &= 0\end{aligned}$$

resulting in

$$\sum_{i=1}^{6}\exp(\mathrm{i}\mathbf{k}\cdot\mathbf{a}_\mathrm{i}) - 6 + \frac{\omega^2}{c^2}\frac{3a^2}{2} = 0.$$

The dispersion relation of a triangular lattice, derived from tight-binding approximation is finally becomes

$$\begin{aligned}\frac{\omega^2 a^2}{c^2} &= \frac{2}{3}\left[-\sum_{i=1}^{6}\exp(\mathrm{i}\mathbf{k}\cdot\mathbf{a}_\mathrm{i}) + 6\right] \\ &= \frac{2}{3}\times 6 - \frac{2}{3}\Bigg[2\cos(k_x a) + 2\cos\left(\frac{a}{2}k_x + \frac{\sqrt{3}a}{2}k_y\right) \\ &\qquad + 2\cos\left(-\frac{a}{2}k_x + \frac{\sqrt{3}a}{2}k_y\right)\Bigg] \\ &= 4 - \frac{4}{3}\left[\cos(k_x a) + \cos\left(\frac{a}{2}k_x + \frac{\sqrt{3}a}{2}k_y\right) + \cos\left(-\frac{a}{2}k_x + \frac{\sqrt{3}a}{2}k_y\right)\right] \\ &= 4 - \frac{4}{3}\left[\cos(k_x a) + 2\cos\left(\frac{\sqrt{3}a}{2}k_y\right)\cos\left(\frac{a}{2}k_x\right)\right] \\ &= 4 - \frac{4}{3}\cos(k_x a) - \frac{8}{3}\cos\left(\frac{\sqrt{3}a}{2}k_y\right)\cos\left(\frac{a}{2}k_x\right),\end{aligned}$$

and

$$\frac{\omega a}{2\pi c} = \frac{1}{2\pi}\sqrt{4 - \frac{4}{3}\cos(k_x a) - \frac{8}{3}\cos\left(\frac{\sqrt{3}a}{2}k_y\right)\cos\left(\frac{a}{2}k_x\right)}. \tag{2.11}$$

We also try to derive the velocity of energy propagation of light waves, that is, group velocity $\mathbf{v}_\mathrm{g}$ defined as

$$\mathbf{v}_\mathrm{g} = \left(\frac{\partial\omega}{\partial k_x}, \frac{\partial\omega}{\partial k_y}\right). \tag{2.12}$$

From Eq. (2.11), normalized frequency is derived as

$$\begin{aligned}\omega_n &= \frac{\omega a}{2\pi c} \\ &= \pm\frac{1}{2\pi}\sqrt{4-\frac{4}{3}\cos(k_x a)-\frac{8}{3}\cos\left(\frac{\sqrt{3}a}{2}k_y\right)\cos\left(\frac{a}{2}k_x\right)} \\ &= \pm\frac{1}{2\pi}\sqrt{4-\frac{4}{3}\cos(2\pi k_{x\mathrm{n}})-\frac{8}{3}\cos\left(\sqrt{3}\pi k_{y\mathrm{n}}\right)\cos\left(\pi k_{x\mathrm{n}}\right)}. \end{aligned} \tag{2.13}$$

The relation between k_x and k_y is derived from Eq. (2.13) as

$$\begin{aligned}\cos\left(\frac{\sqrt{3}a}{2}k_y\right) &= \frac{3}{8\cos\left(\frac{k_x a}{2}\right)}\left[4-\frac{4}{3}\cos(k_x a)-\frac{\omega^2 a^2}{c^2}\right] \\ &= \frac{3}{8\cos\left(\frac{k_x a}{2}\right)}\left[4-\frac{4}{3}\cos(k_x a)-4\pi^2\omega_n^2\right],\end{aligned}$$

and

$$\begin{aligned}\frac{\sqrt{3}a}{2}k_y &= \pm\cos^{-1}\left\{\frac{3}{8\cos\left(\frac{k_x a}{2}\right)}\left[4-\frac{4}{3}\cos(k_x a)-\frac{\omega^2 a^2}{c^2}\right]\right\} \\ &= \pm\cos^{-1}\left\{\frac{3}{8\cos\left(\frac{k_x a}{2}\right)}\left[4-\frac{4}{3}\cos(k_x a)-4\pi^2\omega_n^2\right]\right\},\end{aligned}$$

then,

$$\sqrt{3}\pi k_{y\mathrm{n}} = \pm\cos^{-1}\left\{\frac{3}{8\cos\left(\pi k_{x\mathrm{n}}\right)}\left[4-\frac{4}{3}\cos(2\pi k_{x\mathrm{n}})-4\pi^2\omega_n^2\right]\right\}$$

where $k_{x\mathrm{n}}$ and $k_{y\mathrm{n}}$ are the x and y components of normalized wave vector denoted as

$$\begin{aligned}\mathbf{k}_{\mathrm{n}} &= (k_{x\mathrm{n}},\ k_{y\mathrm{n}}) \\ &= \left(\frac{k_x a}{2\pi},\ \frac{k_y a}{2\pi}\right).\end{aligned}$$

The range of $k_{x\mathrm{n}}$ becomes $0 \le k_{x\mathrm{n}} \le \frac{2}{3}$ based on the first Brillouin zone.

The group velocity defined by Eq. (2.12) finally becomes as

$$\begin{aligned}
\frac{\partial \omega_{\mathrm{n}}}{\partial k_{x\mathrm{n}}} &= \pm \frac{1}{4\pi\sqrt{4 - \frac{4}{3}\cos(2\pi k_{x\mathrm{n}}) - \frac{8}{3}\cos\left(\sqrt{3}\pi k_{y\mathrm{n}}\right)\cos\left(\pi k_{x\mathrm{n}}\right)}} \\
&\quad \times \left[\frac{8\pi}{3}\sin(2\pi k_{x\mathrm{n}}) + \frac{8\pi}{3}\sin(\pi k_{x\mathrm{n}})\cos\left(\sqrt{3}\pi k_{y\mathrm{n}}\right)\right] \\
&= \pm \frac{1}{4\pi\sqrt{4 - \frac{4}{3}\cos(2\pi k_{x\mathrm{n}}) - \frac{8}{3}\cos\left(\sqrt{3}\pi k_{y\mathrm{n}}\right)\cos\left(\pi k_{x\mathrm{n}}\right)}} \\
&\quad \times \left[\frac{8\pi}{3}\sin(2\pi k_{x\mathrm{n}}) + \frac{8\pi}{3}\sin(\pi k_{x\mathrm{n}})\right. \\
&\quad \left. \times \cos\left(\cos^{-1}\left\{\frac{3}{8\cos\left(\pi k_{x\mathrm{n}}\right)}\left(4 - \frac{4}{3}\cos(2\pi k_{x\mathrm{n}}) - 4\pi^2\omega_n^2\right)\right\}\right)\right]
\end{aligned}$$

$$\begin{aligned}
\frac{\partial \omega_{\mathrm{n}}}{\partial k_{y\mathrm{n}}} &= \pm \frac{1}{4\pi\sqrt{4 - \frac{4}{3}\cos(2\pi k_{x\mathrm{n}}) - \frac{8}{3}\cos\left(\sqrt{3}\pi k_{y\mathrm{n}}\right)\cos\left(\pi k_{x\mathrm{n}}\right)}} \\
&\quad \times \left[\pm\frac{8\pi}{\sqrt{3}}\sin\left(\sqrt{3}\pi k_{y\mathrm{n}}\right)\cos(\pi k_{x\mathrm{n}})\right] \\
&= \pm \frac{1}{4\pi\sqrt{4 - \frac{4}{3}\cos(2\pi k_{x\mathrm{n}}) - \frac{8}{3}\cos\left(\sqrt{3}\pi k_{y\mathrm{n}}\right)\cos\left(\pi k_{x\mathrm{n}}\right)}} \\
&\quad \times \left[\pm\frac{8\pi}{\sqrt{3}}\sin\left\{\cos^{-1}\left[\frac{3}{8\cos\left(\pi k_{x\mathrm{n}}\right)}\left(4 - \frac{4}{3}\cos(2\pi k_{x\mathrm{n}}) - 4\pi^2\omega_n^2\right)\right]\right\}\right. \\
&\quad \left. \times \cos(\pi k_{x\mathrm{n}})\right]
\end{aligned}$$

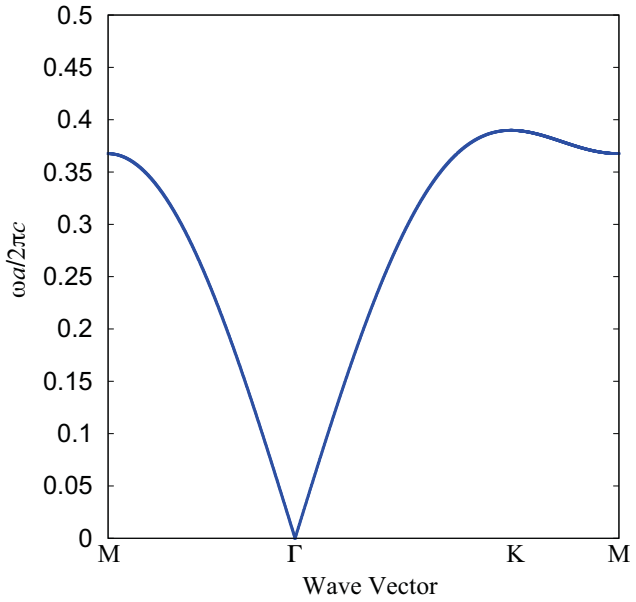

(a) Dispersion relation.

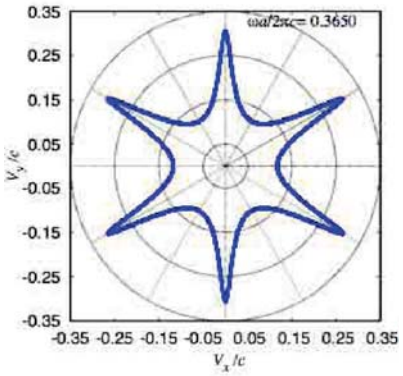

(i) $\omega a/2\pi c = 0.3650$.

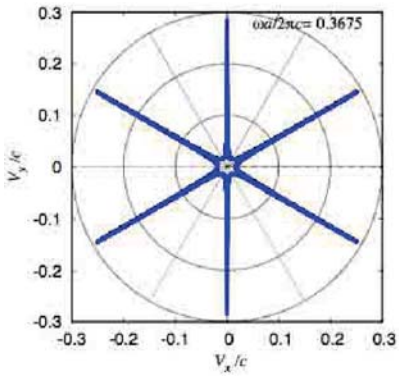

(ii) $\omega a/2\pi c = 0.3675$.

(b) Group velocity.

Figure 2.6: A dispersion relation and angular distribution of group velocity computed by tight-binding approximation.

2.1.2.3 Band calculation for two-dimensional honeycomb lattice by using tight-binding approximation

In this subsubsection, we present dispersion relation of hexagonal lattice by means of tight-binding approximation. Figure 2.7 shows A and B sites on hexagonal grid point. The position of lattice points of A and B sites can not overlap each other by parallel translation.

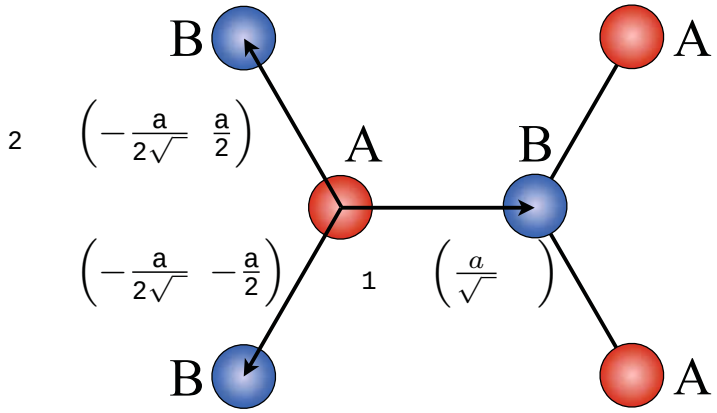

Figure 2.7: Hexagonal lattice.

The equation solved in this analysis is Helmholtz equation as follows:

$$\nabla^2 E(\mathbf{r}) + \frac{\omega^2}{c^2} E(\mathbf{r}) = 0. \tag{2.14}$$

The electric field on $\mathbf{r}$ can be expanded by the superpositions of the electric field on $\mathbf{r}_A$ and $\mathbf{r}_B$ as

$$\begin{aligned} E(\mathbf{r}) &= C_A E_A(\mathbf{r}) + C_B E_B(\mathbf{r}) \\ &= C_A \sum_{\mathbf{r}_A} E_A(\mathbf{r} - \mathbf{r}_A) \exp(\mathrm{i}\mathbf{k} \cdot \mathbf{r}_A) + C_B \sum_{\mathbf{r}_B} E_B(\mathbf{r} - \mathbf{r}_B) \exp(\mathrm{i}\mathbf{k} \cdot \mathbf{r}_B), \end{aligned} \tag{2.15}$$

where C_A and C_B are the coefficients of a linear combination. By substituting expanded form (2.15) into Eq. (2.14), the Helmholz equation becomes as follows:

$$\begin{aligned} &\nabla^2 E(\mathbf{r}) + \frac{\omega^2}{c^2} E(\mathbf{r}) \\ &= C_A \sum_{\mathbf{r}_A} \exp(\mathrm{i}\mathbf{k} \cdot \mathbf{r}_A) \nabla^2 E_A(\mathbf{r} - \mathbf{r}_A) + C_B \sum_{\mathbf{r}_B} \exp(\mathrm{i}\mathbf{k} \cdot \mathbf{r}_B) \nabla^2 E_B(\mathbf{r} - \mathbf{r}_B) \\ &+ \frac{\omega^2}{c^2} C_A \sum_{\mathbf{r}_A} \exp(\mathrm{i}\mathbf{k} \cdot \mathbf{r}_A) E_A(\mathbf{r} - \mathbf{r}_A) + \frac{\omega^2}{c^2} C_B \sum_{\mathbf{r}_B} \exp(\mathrm{i}\mathbf{k} \cdot \mathbf{r}_B) E_B(\mathbf{r} - \mathbf{r}_B). \end{aligned} \tag{2.16}$$

By multiplying $E_A^*(\mathbf{r}-\mathbf{r}_{AA})$ by both side of Eq. (2.16),

$$
\begin{aligned}
&E_A^*(\mathbf{r}-\mathbf{r}_{AA})\left[\nabla^2 E(\mathbf{r})+\frac{\omega^2}{c^2}E(\mathbf{r})\right] \\
&= C_A\sum_{\mathbf{r}_A}\exp(\mathrm{i}\mathbf{k}\cdot\mathbf{r}_A)\left[E_A^*(\mathbf{r}-\mathbf{r}_{AA})\nabla^2 E_A(\mathbf{r}-\mathbf{r}_A)\right] \\
&\quad + C_B\sum_{\mathbf{r}_B}\exp(\mathrm{i}\mathbf{k}\cdot\mathbf{r}_B)\left[E_A^*(\mathbf{r}-\mathbf{r}_{AA})\nabla^2 E_B(\mathbf{r}-\mathbf{r}_B)\right] \\
&\quad + \frac{\omega^2}{c^2}C_A\sum_{\mathbf{r}_A}\exp(\mathrm{i}\mathbf{k}\cdot\mathbf{r}_A)\left[E_A^*(\mathbf{r}-\mathbf{r}_{AA})E_A(\mathbf{r}-\mathbf{r}_A)\right] \\
&\quad + \frac{\omega^2}{c^2}C_B\sum_{\mathbf{r}_B}\exp(\mathrm{i}\mathbf{k}\cdot\mathbf{r}_B)\left[E_A^*(\mathbf{r}-\mathbf{r}_{AA})E_B(\mathbf{r}-\mathbf{r}_B)\right] \\
&= C_A\sum_{\mathbf{r}_A}\exp(\mathrm{i}\mathbf{k}\cdot\mathbf{r}_A)\alpha\delta_{AA,A} + C_B\sum_{\mathbf{r}_B}\exp(\mathrm{i}\mathbf{k}\cdot\mathbf{r}_B)\beta\delta_{AA,B} \\
&\quad + \frac{\omega^2}{c^2}C_A\sum_{\mathbf{r}_A}\exp(\mathrm{i}\mathbf{k}\cdot\mathbf{r}_A)\gamma + \frac{\omega^2}{c^2}C_B\sum_{\mathbf{r}_B}\exp(\mathrm{i}\mathbf{k}\cdot\mathbf{r}_B)\zeta \\
&= C_A\exp(\mathrm{i}\mathbf{k}\cdot\mathbf{r}_{AA})\alpha + C_B\sum_{j=1}^{3}\exp[\mathrm{i}\mathbf{k}\cdot(\mathbf{r}_{BB}+\mathbf{t}_j)]\beta \\
&\quad + \frac{\omega^2}{c^2}C_A\exp(\mathrm{i}\mathbf{k}\cdot\mathbf{r}_{AA})\zeta \\
&= C_A\left[\exp(\mathrm{i}\mathbf{k}\cdot\mathbf{r}_{AA})\alpha + \frac{\omega^2}{c^2}\exp(\mathrm{i}\mathbf{k}\cdot\mathbf{r}_{AA})\zeta\right] + C_B\sum_{j=1}^{3}\exp[\mathrm{i}\mathbf{k}\cdot(\mathbf{r}_{BB}+\mathbf{t}_j)]\beta \\
&= \exp(\mathrm{i}\mathbf{k}\cdot\mathbf{r}_{AA})\left\{C_A\left[\alpha+\frac{\omega^2}{c^2}\zeta\right] + C_B\sum_{j=1}^{3}\exp(\mathrm{i}\mathbf{k}\cdot\mathbf{t}_j)\beta\right\} \qquad (2.17)
\end{aligned}
$$

By multiplying $E_B^*(\mathbf{r}-\mathbf{r}_{BB})$ by both side of Eq. (2.16),

$$
\begin{aligned}
&E_B^*(\mathbf{r}-\mathbf{r}_{BB})\left[\nabla^2 E(\mathbf{r})+\frac{\omega^2}{c^2}E(\mathbf{r})\right] \\
&= C_A\sum_{\mathbf{r}_A}\exp(\mathrm{i}\mathbf{k}\cdot\mathbf{r}_A)\left[E_B^*(\mathbf{r}-\mathbf{r}_{BB})\nabla^2 E_A(\mathbf{r}-\mathbf{r}_A)\right] \\
&\quad + C_B\sum_{\mathbf{r}_B}\exp(\mathrm{i}\mathbf{k}\cdot\mathbf{r}_B)\left[E_B^*(\mathbf{r}-\mathbf{r}_{BB})\nabla^2 E_B(\mathbf{r}-\mathbf{r}_B)\right] \\
&\quad + \frac{\omega^2}{c^2}C_A\sum_{\mathbf{r}_A}\exp(\mathrm{i}\mathbf{k}\cdot\mathbf{r}_A)\left[E_B^*(\mathbf{r}-\mathbf{r}_{BB})E_A(\mathbf{r}-\mathbf{r}_A)\right] \\
&\quad + \frac{\omega^2}{c^2}C_B\sum_{\mathbf{r}_B}\exp(\mathrm{i}\mathbf{k}\cdot\mathbf{r}_B)\left[E_B^*(\mathbf{r}-\mathbf{r}_{BB})E_B(\mathbf{r}-\mathbf{r}_B)\right] \\
&= C_A\sum_{\mathbf{r}_A}\exp(\mathrm{i}\mathbf{k}\cdot\mathbf{r}_A)\beta'\delta_{BB,A} + C_B\sum_{\mathbf{r}_B}\exp(\mathrm{i}\mathbf{k}\cdot\mathbf{r}_B)\alpha'\delta_{BB,B} \\
&\quad + \frac{\omega^2}{c^2}C_A\sum_{\mathbf{r}_A}\exp(\mathrm{i}\mathbf{k}\cdot\mathbf{r}_A)\zeta' + \frac{\omega^2}{c^2}C_B\sum_{\mathbf{r}_B}\exp(\mathrm{i}\mathbf{k}\cdot\mathbf{r}_B)\gamma' \\
&= C_A\sum_{j=1}^{3}\exp[\mathrm{i}\mathbf{k}\cdot(\mathbf{r}_{BB}-\mathbf{t}_j)]\beta' + C_B\exp(\mathrm{i}\mathbf{k}\cdot\mathbf{r}_{BB})\alpha' \\
&\quad + 0 + \frac{\omega^2}{c^2}C_B\exp(\mathrm{i}\mathbf{k}\cdot\mathbf{r}_{BB})\zeta' \\
&= C_A\sum_{j=1}^{3}\exp[\mathrm{i}\mathbf{k}\cdot(\mathbf{r}_{BB}-\mathbf{t}_j)]\beta' + C_B\left[\exp(\mathrm{i}\mathbf{k}\cdot\mathbf{r}_{BB})\alpha' + \frac{\omega^2}{c^2}\exp(\mathrm{i}\mathbf{k}\cdot\mathbf{r}_{BB})\zeta'\right] \\
&= \exp(\mathrm{i}\mathbf{k}\cdot\mathbf{r}_{BB})\left\{C_A\sum_{j=1}^{3}\exp(-\mathrm{i}\mathbf{k}\cdot\mathbf{t}_j)\beta' + C_B\left[\alpha' + \frac{\omega^2}{c^2}\zeta'\right]\right\} \qquad (2.18)
\end{aligned}
$$

Based on Eqs. (2.17) and (2.18), the following simultaneous equation is derived as

$$
\begin{bmatrix}
\alpha+\frac{\omega^2}{c^2}\zeta & \sum_{j=1}^{3}\exp(\mathrm{i}\mathbf{k}\cdot\mathbf{t}_j)\beta \\
\left[\sum_{j=1}^{3}\exp(\mathrm{i}\mathbf{k}\cdot\mathbf{t}_j)\right]^*\beta' & \alpha'+\frac{\omega^2}{c^2}\zeta'
\end{bmatrix}
\begin{bmatrix} C_A \\ C_B \end{bmatrix} = \mathbf{0}.
$$

In order to obtain non-trivial solutions, the determinant of the above coefficient matrix becomes as follows:

$$
\begin{vmatrix}
\alpha+\frac{\omega^2}{c^2}\zeta & \sum_{j=1}^{3}\exp(\mathrm{i}\mathbf{k}\cdot\mathbf{t}_j)\beta \\
\left[\sum_{j=1}^{3}\exp(\mathrm{i}\mathbf{k}\cdot\mathbf{t}_j)\right]^*\beta' & \alpha'+\frac{\omega^2}{c^2}\zeta'
\end{vmatrix} = 0,
$$

resulting in

$$\begin{aligned}
&\left[\alpha+\frac{\omega^2}{c^2}\zeta\right]\left[\alpha'+\frac{\omega^2}{c^2}\zeta'\right]-\left[\sum_{j=1}^{3}\exp(\mathrm{i}\mathbf{k}\cdot\mathbf{t}_j)\right]\beta\left[\sum_{j=1}^{3}\exp(\mathrm{i}\mathbf{k}\cdot\mathbf{t}_j)\right]^{*}\beta'\\
&=\zeta\zeta'\left(\frac{\omega^2}{c^2}\right)^2+(\alpha+\alpha')\left(\frac{\omega^2}{c^2}\right)+\alpha\alpha'-\left|\sum_{j=1}^{3}\exp(\mathrm{i}\mathbf{k}\cdot\mathbf{t}_j)\right|^2\beta\beta'\\
&=16\pi^4\zeta\zeta'\left(\frac{\omega^2}{4\pi^2c^2}\right)^2+4\pi^2(\alpha+\alpha')\left(\frac{\omega^2}{4\pi^2c^2}\right)+\alpha\alpha'-\left|\sum_{j=1}^{3}\exp(\mathrm{i}\mathbf{k}\cdot\mathbf{t}_j)\right|^2\beta\beta'\\
&=0.
\end{aligned}$$

The above equation is solved as

$$\begin{aligned}
\left(\frac{\omega}{2\pi c}\right)^2&=\frac{2\pi^2(\alpha+\alpha')\pm\sqrt{\left[2\pi^2(\alpha+\alpha')\right]^2-16\pi^4\zeta\zeta'\left\{\alpha\alpha'-\left|\sum_{j=1}^{3}\exp(\mathrm{i}\mathbf{k}\cdot\mathbf{t}_j)\right|^2\beta\beta'\right\}}}{16\pi^4\zeta\zeta'}\\
&=\frac{(\alpha+\alpha')\pm\sqrt{\left[(\alpha+\alpha')\right]^2-4\zeta\zeta'\left[\alpha\alpha'-\left|\sum_{j=1}^{3}\exp(\mathrm{i}\mathbf{k}\cdot\mathbf{t}_j)\right|^2\beta\beta'\right]}}{8\pi^2\zeta\zeta'}.
\end{aligned}$$

Relations $\alpha=\alpha'$, $\beta=\beta'$, and $\zeta=\zeta'=1$ are assumed because of the symmetry of hexagonal lattice points on A and B sites. Then following relation is derived as

$$\begin{aligned}
\left(\frac{\omega}{2\pi c}\right)^2&=\frac{2\alpha\pm\sqrt{4\alpha^2-4\left\{\alpha^2-\left|\sum_{j=1}^{3}\exp(\mathrm{i}\mathbf{k}\cdot\mathbf{t}_j)\right|^2\beta^2\right\}}}{8\pi^2}\\
&=\frac{2\alpha\pm\beta\left|\sum_{j=1}^{3}\exp(\mathrm{i}\mathbf{k}\cdot\mathbf{t}_j)\right|}{8\pi^2}.
\end{aligned}$$

The dispersion relation of hexagonal lattice by using tight-binding approximation is finally becomes as follows:

$$\frac{\omega a}{2\pi c}=a\sqrt{\frac{2\alpha\pm\beta\left|\sum_{j=1}^{3}\exp(\mathrm{i}\mathbf{k}\cdot\mathbf{t}_j)\right|}{8\pi^2}}.$$

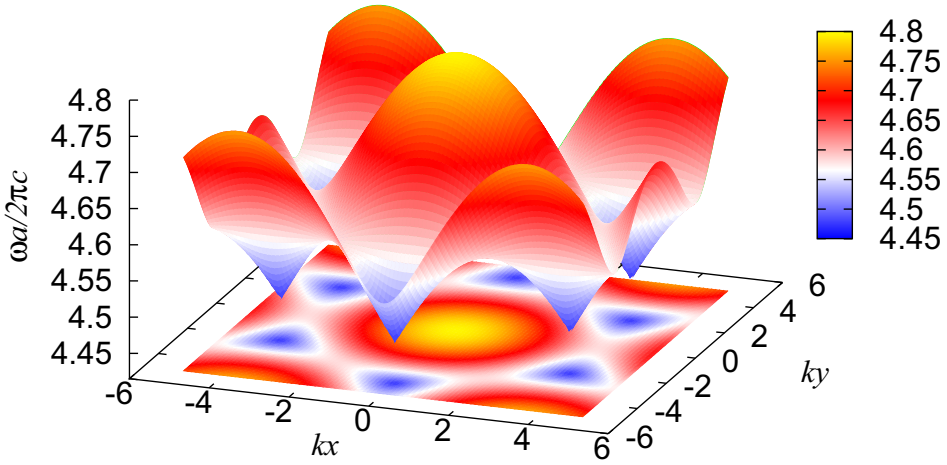

Figure 2.8: Dispersion relation $\frac{\omega a}{2\pi c} = a\sqrt{\frac{2\alpha+\beta\left|\sum_{j=1}^{3}\exp(\mathbf{i}\mathbf{k}\cdot\mathbf{t}_j)\right|}{8\pi^2}}$ ($\alpha = 10$, $\beta = 1$, $\zeta = 1$).

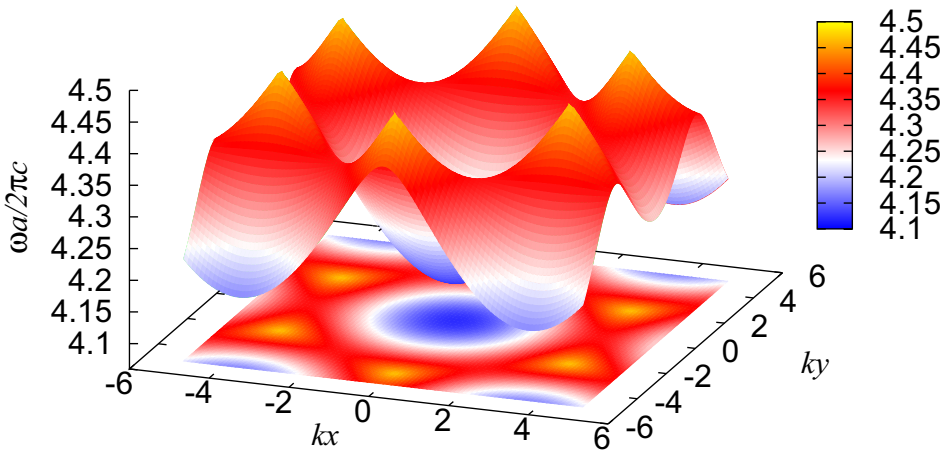

Figure 2.9: Dispersion relation $\frac{\omega a}{2\pi c} = a\sqrt{\frac{2\alpha-\beta\left|\sum_{j=1}^{3}\exp(\mathbf{i}\mathbf{k}\cdot\mathbf{t}_j)\right|}{8\pi^2}}$ ($\alpha = 10$, $\beta = 1$, $\zeta = 1$).

2.1.3 Transmission spectrum and uncoupled modes

A transmission spectrum for $\Gamma - K$ direction is shown in Fig. 2.10(a). We observe that transmittivity becomes zero within band gap frequencies.

Optical transmittance of photonic crystals have some opaque frequency ranges corresponding not only to band gaps but also to frequency ranges in which uncoupled modes exist. Uncoupled mode is not excited by incident waves that have symmetric distribution of electric field with respect to their propagation direction because uncoupled modes have anti-symmetric distributions of electric field.

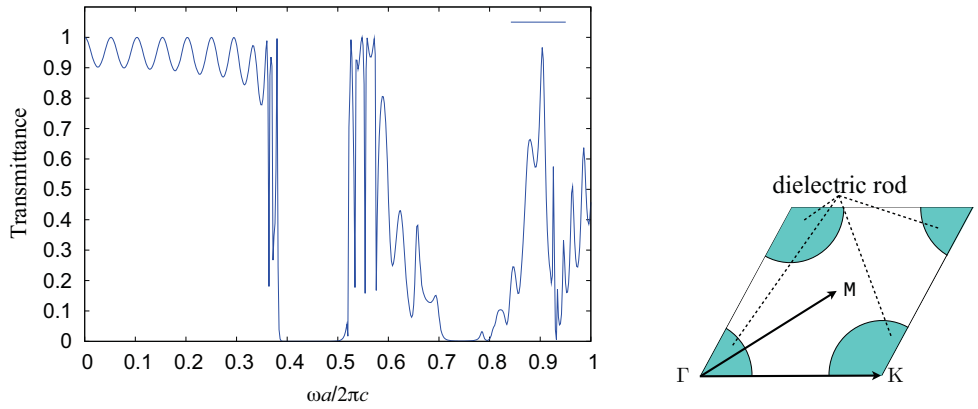

(a) Transmission spectra for $\Gamma - \mathrm{K}$ direction.

(b) Unit cell.

Figure 2.10: The transmission spectra of a 2D photonic crystal consisting of dielectric cylinders whose radius R is $R = 0.3a$ in the case of TM mode. Entire structure has 14 period and dielectric cylinders, whose permittivities are 4.0, are arranged on triangular lattices. This transmissivity is computed by plane wave expansion method.

Such uncoupled modes are related to the sign of the linear combination of eigenmodes. Reciprocal lattice vectors $\mathbf{G}_1$ and $\mathbf{G}_2$ oriented from Γ to Γ_1 and Γ to Γ_2 in Fig. 2.11, respectively, are given as follows:

$$\mathbf{G}_1 = \left(-\frac{2\pi}{a}, \frac{2\pi}{\sqrt{3}a}\right)^{\mathrm{T}}, \quad \mathbf{G}_2 = \left(-\frac{2\pi}{a}, -\frac{2\pi}{\sqrt{3}a}\right)^{\mathrm{T}}.$$

We assume that the light wave $Ae^{\mathrm{i}\mathbf{k}\cdot\mathbf{x}}$ propagating along x axis. Then, the wave vector of the assumed light waves $\mathbf{k}$ are written as

$$\mathbf{k} = (k_x, 0)^{\mathrm{T}}.$$

The wave vectors $\mathbf{k}_1$ and $\mathbf{k}_2$ shown in Fig. 2.11 are expressed with summations of the wave vector and reciprocal lattice vectors as

$$\mathbf{k}_1 = \mathbf{k} + \mathbf{G}_1 = \left(k_x - \frac{2\pi}{a}, \frac{2\pi}{\sqrt{3}a}\right)^{\mathrm{T}},$$
$$\mathbf{k}_2 = \mathbf{k} + \mathbf{G}_2 = \left(k_x - \frac{2\pi}{a}, -\frac{2\pi}{\sqrt{3}a}\right)^{\mathrm{T}}.$$

Above equilibrium state indicates $|\mathbf{k}_1| = |\mathbf{k}_2|$. The linear combination of $e^{\mathrm{i}\mathbf{k}_1\cdot\mathbf{x}}$ and $e^{\mathrm{i}\mathbf{k}_2\cdot\mathbf{x}}$ also gives the eigenmode of the light waves in periodic structures. It is written as

$$f(\mathbf{x}) = Ae^{\mathrm{i}\mathbf{k}_1\cdot\mathbf{x}} + Be^{\mathrm{i}\mathbf{k}_2\cdot\mathbf{x}}.$$

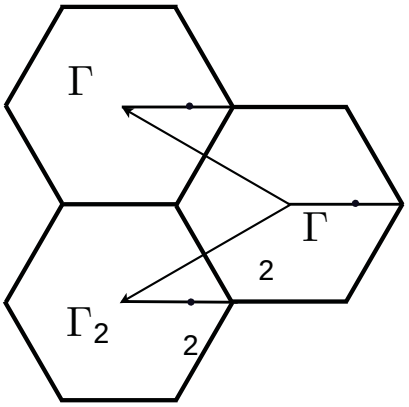

Figure 2.11: Reciprocal lattices and wave vectors.

The eigen mode $f(x, y)$ satisfies the eigen equation of E-polarization as

$$\frac{1}{\epsilon(x,y)}\left\{\frac{\partial^2}{\partial^2 x} + \frac{\partial^2}{\partial^2 y}\right\} f(x,y) = -\frac{\omega^2}{c^2} f(x,y). \tag{2.19}$$

Here, we consider the symmetry of eigenmodes with respect to x axis. We replace y with $-y$ in Eq. (2.19) as

$$\frac{1}{\epsilon(x,-y)}\left\{\frac{\partial^2}{\partial^2 x} + \frac{\partial^2}{\partial^2 (-y)}\right\} f(x,-y) = -\frac{\omega^2}{c^2} f(x,-y),$$

where $\epsilon(x,-y)$ and $\partial^2/\partial(-y)^2$ satisfy the following relations:

$$\epsilon(x,-y) = \epsilon(x,y), \quad \frac{\partial^2}{\partial(-y)^2} = \frac{\partial^2}{\partial y^2}.$$

We can rewrite Eq. (2.19) as

$$\frac{1}{\epsilon(x,y)}\left\{\frac{\partial^2}{\partial^2 x}+\frac{\partial^2}{\partial^2 y}\right\}f(x,-y)=-\frac{\omega^2}{c^2}f(x,-y). \tag{2.20}$$

Equations (2.19) and (2.20) indicate that the two eigen modes $f(x,y)$ and $f(x,-y)$ are fundamentally equal to each other. Hence, we can write the relation between those eigen modes as

$$f(x,y)=\alpha f(x,-y),$$

resulting in

$$f(x,y)=\alpha^2 f(x,y),$$

where α is a constant coefficient and bocomes

$$\alpha=\begin{cases}+1\\-1\end{cases}.$$

The eigen modes satisfying the above equations are

$$f(x,y)=\begin{cases}e^{i\mathbf{k}_1\cdot\mathbf{x}}+e^{i\mathbf{k}_2\cdot\mathbf{x}}\\e^{i\mathbf{k}_1\cdot\mathbf{x}}-e^{i\mathbf{k}_2\cdot\mathbf{x}}\end{cases}.$$

The lower eigen mode shown above becomes anti-symmetric with respect to x axis and becomes an uncoupled mode.

2.1.4 Photonic crystal laser

Photonic crystals are actively applied to laser cavities. The group velocity of light waves becomes extremely low at band edge frequencies in photonic crystals and light waves are strongly localized. Therefore, the threshold of laser action in photonic crystals becomes much lowerer than those of conventional laser devices. In addition, the polarizaions of emitted light waves are perfectly controlled by changing the geometry of the unit cell structure [20, 21].

Several advanced laser devices are developed as high Q factor cavities [6, 8, 9], large area surface emitting lasers [22], high power lasers [23], blue-violet colored lasers [24], and an inhibition and redistribution of spontaneous light emission [25], etc.

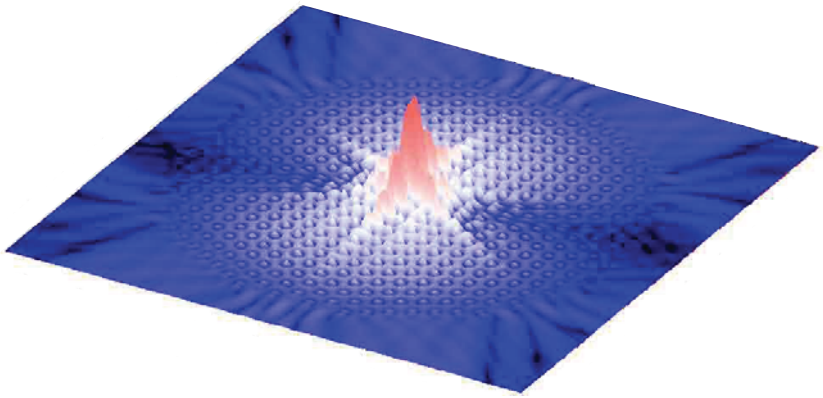

Figure 2.12: An image of a light confinement in a two-dimensional photonic crystal at a band edge frequency.

2.2 Random laser

Random lasing is laser action in disordered structures. Such lasing phenomena in disordered structures are occurring from feedback mechanisms as Anderson localization [26] and coherent backscattering caused by multiple scatterings and interference effects of light waves. The random multiple scatterings caused by disorder of periodic structures, namely, fabrication errors are undesirable phenomena in the case of photonic crystals because the scatterings worsen their ability due to the periodic structures. Such undesirable scattering becomes a bottleneck in the developments of photonic crystal devices. However, when considering random lasers, the strong multiple scatterings lead to strong localizations and lead to the oscillations of random lasing. In terms of positive utilization of random multiple scatterings, random laser receives lots of attention as new optical devices that are different from previous ones such as photonic crystals. Disordered structures are rather easy to fabricate in low cost because it requires only simple fabrication technologies. Thus, random laser has an advantage in its production cost.

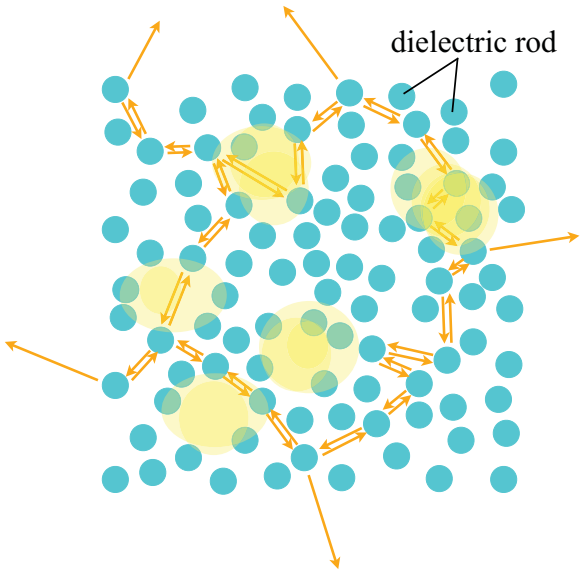

Figure 2.13: An image of random multiple scatterings and localizations in a disordered structure.

Disordered structures are also classified into three types as one-, two-, and three-dimensional ones, as shown in Fig. 2.14. It is difficult to cause random lasing in three dimensional structures [27], because the Ioffe-Regel criterion $kl < 1$

is not easily satisfied.

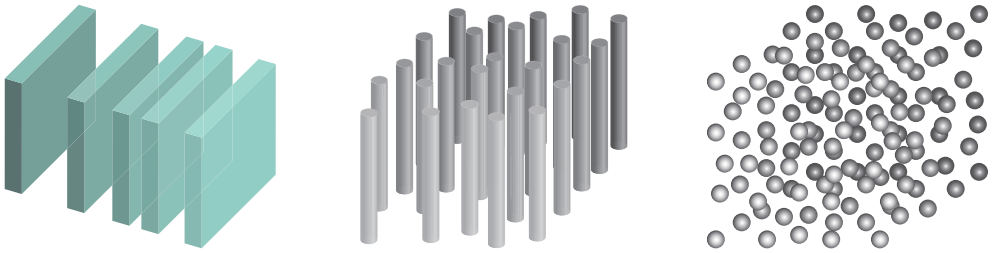

(a) One dimensional structure. (b) Two dimensional structure. (c) Three dimensional structure.

Figure 2.14: Disordered structures.

2.2.1 Lasing mechanisms

Lasing phenomena are caused by feedback mechanisms that repeat light amplifications. Random lasers are generated based on the same principles as those of normal lasers. However, the feedback mechanisms of random lasers are different from those of conventional lasers. In disordered structures, light waves are randomly scattered, and the scattered light waves interfere with each other. When random multiple scatterings become sufficiently intensive, light waves are randomly localized in disordered structures. The localization is a kind of so-called Anderson localization [26] of electromagnetic waves.

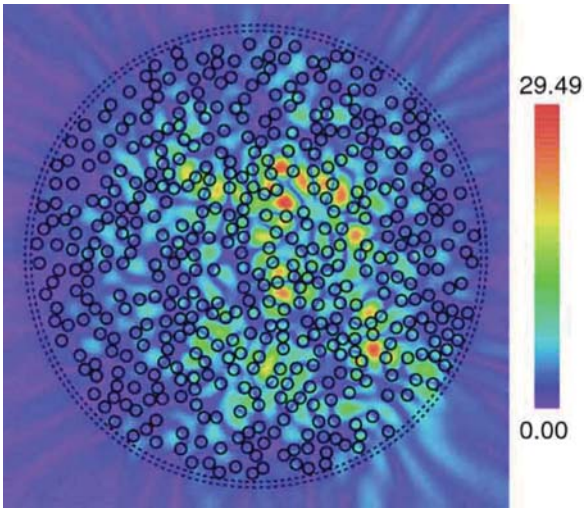

Figure 2.15: A distribution of computed electric amplitude for a lasing state in a disordered structure.

Actually, light localization occurs in various and many spaces in disordered structures as shown in Fig. 2.15. The localizations work as nano-cavities, and the speckle patterns caused by the interference of multiply scattered light waves are always observed in the distributions of their electric amplitude.

2.2.2 Anderson localization

2.2.2.1 Localization and diffusion

The migration probability of photon from grid point 0 to 1 P_1 is expressed as

$$P_1 = \begin{cases} 1 & (|t| > W) \\ |t|/W & (|t| < W) \end{cases},$$

where t is the matrix element of photon migration and W is averaged energy interval of photon. The migration probability of photon from grid point 0 to 2 P_2 becomes as

$$P_2 = \begin{cases} 1 & (|t| > W) \\ (|t|/W)^2 & (|t| < W) \end{cases},$$

and that from grid point 0 to n, P_n, can be expressed as follows:

$$P_n = \begin{cases} 1 & (|t| > W) \\ (|t|/W)^n & (|t| < W) \end{cases}.$$

When the grid point number n is infinite and random potential is sufficiently strong $|t| < W$, the migration probability of photon P_n becomes 0. Such zero-migration probability indicate that photon does not migrate and not be diffused, that is, localization.

2.2.2.2 Scaling theory and metal-insulator transition

We consider d dimensional cube whose edge length is L. The conductance of the cube is defined as $G(L)$ depending on the edge length L.

The conductance of metals is proportional to conductivity of cube σ, cross section of a cube L^{d-2}, and are inversely proportional to the length of a cube L.

Hence the conductance of metals are expressed as

$$G(L) = \sigma L^{d-1}/L = \sigma L^{d-2}. \tag{2.21}$$

When the edge length L becomes sufficiently long and the conductance of material becomes smaller than the above G, electron are considered to be localized and a metal shift to a insulator. We define normalized conductance as follows:

$$g(L) = \frac{G(L)}{e^2/\hbar}.$$

We consider $g(L_1)$ and $g(2L_1)$ which is the conductance of a cube whose edge length is $2L_1$. When the edge length of a cube L is much longer than mean free path and wavelength of light, $g(2L_1)$ depend only on $g(L_1)$. By universalizing the above consideration, $g(L_2)$ becomes the function of $g(L_1)$ where L_1 and L_2 have the following relation as

$$L_2 = \nu L_1,$$

and $g_2 = g(L_2)$ depend only on $g_1 = g(L_1)$ and ν as

$$\frac{g_2}{g_1} = f(g_1, \nu). \tag{2.22}$$

We assume the coefficient ν as a continuous function. The following relation are derived from Eq. (2.22) as

$$\lim_{\nu \to 1} \frac{\log(g_2/g_1)}{\log \nu} = \lim_{L_2 \to L_1} \frac{\log g_2 - \log g_1}{\log L_2 - \log L_1} = \left. \frac{d \log g}{d \log L} \right|_{L=L_1},$$

resulting in

$$\frac{d \log g}{d \log L} = \beta(g). \tag{2.23}$$

When we assume a system whose conductance is sufficiently large, the system is considered as metallic material. Hence, based on the assumption in Eq. (2.21), the conductance g have to satisfy the following relation as

$$g \propto L^{d-2}.. \tag{2.24}$$

By substituting Eq. (2.24) into Eq. (2.23), we can derive the following equation as

$$\beta(g) = d - 2 \quad (g \to \infty).$$

When the conductance g is small, the material is regarded as an insulator. In such case, system size L is larger than localization length ξ . Hence, the conductance g become smaller as the system size L becomes larger. Then, the the conductance g is expressed as

$$g \cong g_0 e^{-\alpha L/\xi}. \tag{2.25}$$

When the system size L is sufficiently small and the conductance is assumed to become Eq. (2.25), the function $\beta(g)$ becomes as follows:

$$\beta(g) = \log\left(\frac{g}{g_0}\right) \quad (g \to 0).$$

The above function negatively diverge when the conductance g is sufficiently small.

We know the behavior of the function $\beta(g)$ at the both limits $g \to 0$ and $g \to \infty$. The function $\beta(g)$ is assumed to change smoothly. Then we can plot the approximate graph of $\beta(g)$ in Fig. 2.16.

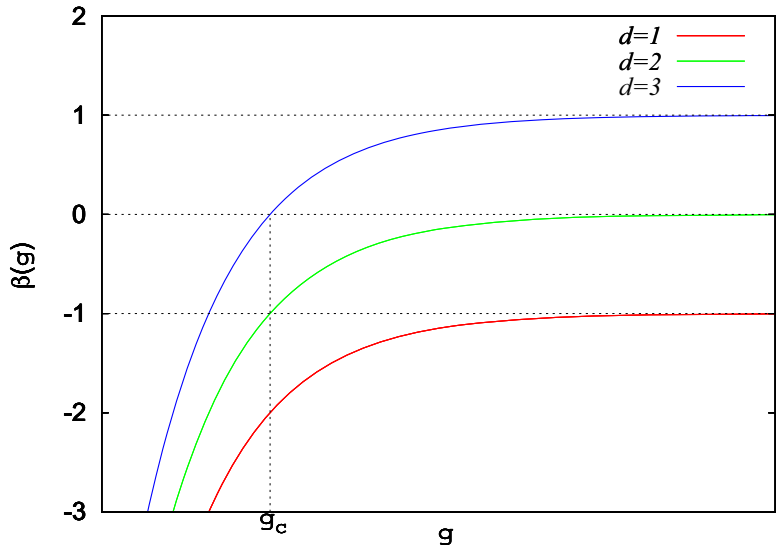

Figure 2.16: $\beta(g)$ versus g.

When the function $\beta(g)$ is smaller than 0, that is,

$$\frac{\log g}{\log L} = \beta(g) < 0,$$

$\log g$ and $\log L$ are different signs each other. Hence,

$$\log g \cdot \log L = \log(gL) < 0,$$

leading to

$$gL < 1.$$

The above inequality indicate that g decreases as L increases. Hence, when a system size becomes sufficiently large, the system becomes an insulator. In the case of low-dimensional systems as $d = 1$ and 2, $\beta(g)$ is might be smaller than 0 and the systems with a large system size becomes an insulator. Such feature do not depend on disorder potential g. On the other hand, in the case of three dimensional systems $d = 3$, the sign of $\beta(g)$ depend on g and switch at g_c. When $g < g_c$, a large system becomes an insulator as low-dimensional cases. When $g > g_c$, a large system has metallic properties because g becomes large as L increase. The metal-insulator transition occurs at $g = g_c$ in the case of three dimensional systems.

2.2.3 Optical properties

Random lasers have unique properties other laser devices cannot realize due to their unique lasing mechanisms. Random lasers can emit coherent light waves for broad angles. In the experiments of three-dimensional random lasings, the emissions for complete 4π solid angle were observed [28]. Random lasers possess large number of laser modes in broad frequency ranges. A large number of laser modes enable random lasing to emit brilliant colors. Lawandy et al. mentioned that the excitation threshold energy for random lasing is surprisingly low [10], that is, random lasers are energy-saving laser devices.

2.2.4 Previous studies and types of laser modes

From the first experimental observation of random lasers [10], light amplifying phenomena in strongly scattering media have been actively discussed whether the light amplifying phenomena are lasing phenomena or amplified spontaneous emissions [11]. Feedback mechanisms to repeat amplification of light waves are indispensable for lasing phenomena. However, it has not been thought that strongly scattering media work as cavities to confine light waves because their structures are disordered.

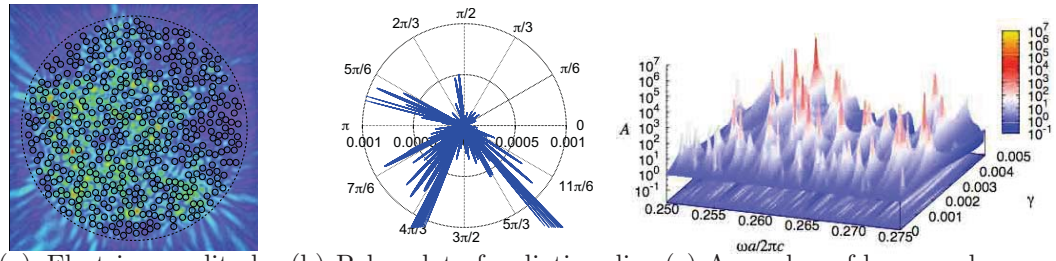

(a) Electric amplitude distribution of a lasing state.

(b) Polar plot of radiation direction of a lasing state.

(c) A number of laser modes.

Figure 2.17: Lasing properties of random lasers.

Cao et al. found "laser spikings" in the intensity spectrum of the electric field [29], namely, the electric intensity in random systems becomes extremely intensive at some frequencies. They also showed the simulations [30] of "laser spikings" and light confinements in disordered structures by means of FDTD method.

Sebbah and Vanneste [12] presented simulations of laser action including pumping of active medium expressed by four level rate equations. The effect of frequency and filling factor on the electric field intensity in random systems were investigated. The previous studies also revealed that there are two types of laser modes: one is spatially extended modes and the other is localized mode. The extended modes shown in Fig. 2.18(a) have spreading distributions of light waves in disordered structures. In such extended states, the mode covers the entire region of random systems and can lase even if the quality factor is not high. Light waves in the state of extended modes can be amplified by optically active medium in the entire region of random systems. On the other hand, lasing phenomena in the state of localized mode shown in Fig. 2.18(b) are caused by spatial confinement of light waves. Localized modes suffer from gain saturations because they cover the smaller volume of active medium and reach the saturated state of active medium immediately.

2.2.5 Applications

Random lasers are expected to be applied to laser displays because their lasing properties such as broad band and broad angular emission are ideal for displays.

Suspensions of particles, that is one of random-laser materials, is proposed to

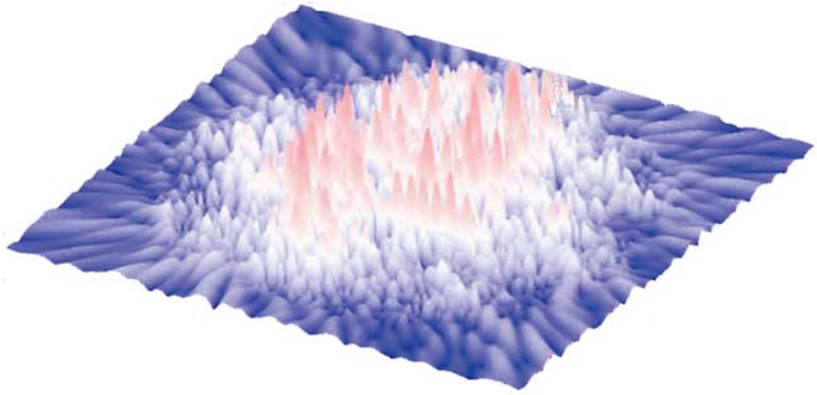

(a) Extended mode.

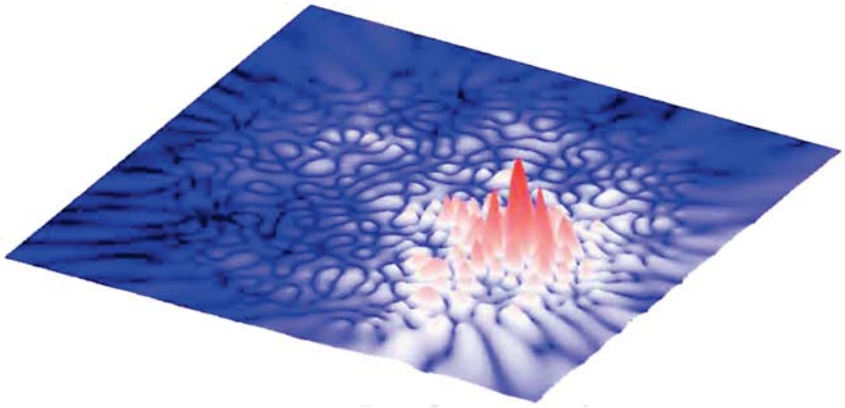

(b) Localized mode.

Figure 2.18: Laser modes.

be applied to coating on surfaces, that is, random structures are applied to color coating utilizing environment lighting [31].

The controlling of lasing frequency by tuning temperature is proposed [32, 33]. Those previous studies report that random lasings are strongly depend on environment temperature. Thus, random lasers are expected to be applied to thermal sensing.

2.2.6 Disordered structure

In this subsection, entire random systems and disordered structures are explained.

2.2.6.1 Shape and composition

We analyze lasing phenomena in two-dimensional disordered structures consisting of cylinders. Let us assume the cylinders are infinitely long in z direction and stand parallel to each other, and the positions of cylinders axes be randomly distributed. Also, light waves are assumed to propagate in xy plane.

Excitation pumping energy are given by excitation light for energizing the active medium to a state of population inversion. Incident waves are trapped by disordered structures, and optically active materials in excited state amplify light waves non-linearly.

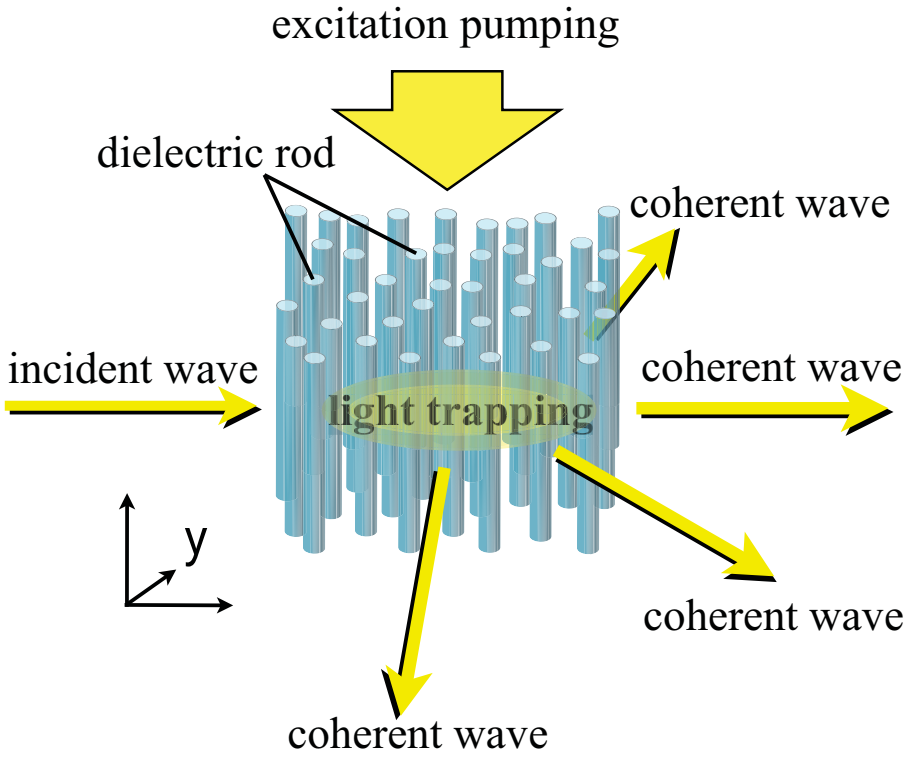

Figure 2.19: An image of a random system and a random laser.

2.2.6.2 Materials of cylinders

The cylinders are usually made of dielectric materials or metals.

Dielectric material Relative permittivity ϵ is used as the distribution of dielectric material when calculating the corresponding electromagnetic field by using Maxwell's equations [34]. In the simulations of random lasings, the dielectric materials are positioned randomly. Hence, the relative permittivity ϵ becomes position dependent function $\epsilon(\mathbf{r})$. If we consider dielectric meduim as dispersive one, the relative permittivity depend not only on the positions but also on the frequency, namely, $\epsilon = \epsilon(\mathbf{r}, \omega)$.

Metal-Drude model The relative permittivities of metals are expressed as a summation of a term for free electrons, ϵ_{f}, and a term derived from interband transition, ϵ_{ib}. The term caused by free electrons is expressed by Drude model [35] derived from the equation of motion of free electrons, as

$$m\frac{d^2\mathbf{r}}{dt^2} + m\Gamma\frac{d\mathbf{r}}{dt} = -e\mathbf{E}_0 \exp(-\mathrm{i}\omega t), \tag{2.26}$$

where $\mathbf{r}$ is a position of free electrons, m is the mass of free electrons, e is an electric charge of free electron, $\mathbf{E}_0 \exp(-i\omega t)$ is the harmonic oscillating electric field, and Γ is dumping coefficient. The solution of Eq. (2.26) becomes

$$\mathbf{r} = \frac{e\mathbf{E}_0 \exp(-\mathrm{i}\omega t)}{m(\omega^2 + \mathrm{i}\Gamma\omega)}.$$

A dipole moment is given as $\mathbf{p} = -e\mathbf{r}$. Polarization $\mathbf{P}$ is defined as dipole moment in the unit volume and is written as

$$\mathbf{P} = N\mathbf{p} = -Ne\mathbf{r},$$

where N is the number of free electrons in the unit volume. The electric displacement $\mathbf{D}$ in metals becomes

$$\mathbf{D} = \epsilon_0\epsilon\mathbf{E} = \epsilon_0\mathbf{E} + \mathbf{P}.$$

Hence relative permittivity ϵ_{f} in metal becomes

$$\epsilon_{\mathrm{f}} = \frac{\mathbf{D}}{\epsilon_0\mathbf{E}} = \frac{\epsilon_0\mathbf{E} + \mathbf{P}}{\epsilon_0\mathbf{E}} = 1 - \frac{Ne^2}{\epsilon_0 m(\omega^2 + \mathrm{i}\Gamma\omega)} = 1 - \frac{\omega_{\mathrm{p}}^2}{\omega(\omega + \mathrm{i}\Gamma)},$$

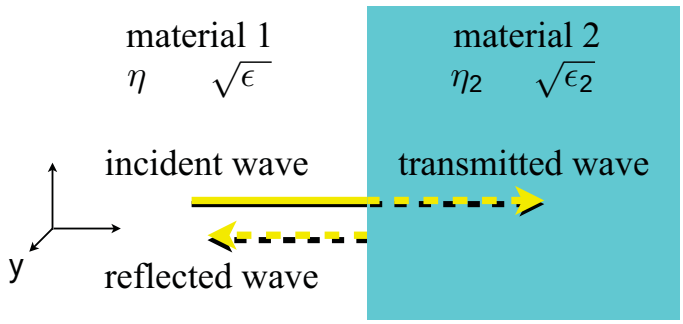

Figure 2.20: Reflectance on the surface between dissimilar materials.

where $\omega_{\rm p} = \sqrt{\dfrac{Ne^2}{\epsilon_0 m}}$ called "plasma frequency".

When the dumping coefficient Γ is sufficiently small, we can neglect Γ, thus, relative permittivity $\epsilon_{\rm f}$ in metal becomes

$$\epsilon_{\rm f} = 1 - \frac{\omega_{\rm p}^2}{\omega^2}. \tag{2.27}$$

Now, we consider reflections on the surface between dissimilar materials. Incident, reflected, and transmitted waves are written as

$$\begin{aligned} E_{\rm i}(x) &= E_{\rm i}\exp({\rm i}k_1 x), \\ E_{\rm r}(x) &= E_{\rm r}\exp(-{\rm i}k_1 x), \\ E_{\rm t}(x) &= E_{\rm t}\exp({\rm i}k_2 x), \end{aligned}$$

where $k_1 = \frac{\omega}{c}\eta_1$ and $k_2 = \frac{\omega}{c}\eta_2$ are wave numbers in the regions 1 and 2 shown in Fig. 2.20, respectively. The electric fields in the regions 1 and 2, $E_1(x)$ and $E_2(x)$, are expressed as

$$\left.\begin{aligned} E_z^1(x) &= E_{\rm i}(x) + E_{\rm r}(x) = E_{\rm i}\exp({\rm i}k_1 x) + E_{\rm r}\exp(-{\rm i}k_1 x) \\ E_z^2(x) &= E_{\rm t}(x) = E_{\rm t}\exp({\rm i}k_2 x) \end{aligned}\right\} \tag{2.28}$$

and the magnetic fields in the regions 1 and 2 are

$$\left.\begin{aligned} H_y^1(x) &= -\frac{\partial}{\partial x}E_z^1(x) \\ H_y^2(x) &= -\frac{\partial}{\partial x}E_z^2(x) \end{aligned}\right\} \tag{2.29}$$

The boundary conditions on the surface are

$$E_z^1 = E_z^2(x), \quad H_y^1(x) = H_y^2.$$

Then, from Eqs. (2.28) and (2.29), we can derive following equations:

$$E_{\mathrm{i}} \exp(\mathrm{i}k_1 x) + E_{\mathrm{r}} \exp(-\mathrm{i}k_1 x) = E_{\mathrm{t}} \exp(\mathrm{i}k_2 x),$$

$$ik_1 E_{\mathrm{i}} \exp(\mathrm{i}k_1 x) - ik_1 E_{\mathrm{r}} \exp(-\mathrm{i}k_1 x) = ik_2 E_{\mathrm{t}} \exp(\mathrm{i}k_2 x).$$

Hence, the reflectance becomes

$$R = \frac{|E_{\mathrm{r}}|}{|E_{\mathrm{i}}|} = \frac{|k_1 - k_2|}{|k_1 + k_2|} = \frac{|\eta_1 - \eta_2|}{|\eta_1 + \eta_2|}.$$

If the material 1 and 2 are air and a metal whose relative permittivity is written based on Drude model in Eq. (2.27), the above reflectance becomes 1, meaning a complete reflection.

2.2.6.3 Modeling of optically active materials

Power absorbed by polarizations The work given by the electric field $\mathbf{E}$ is written as

$$\begin{aligned}\mathbf{J} \cdot \mathbf{E} &= (\nabla \times \mathbf{H}) \cdot \mathbf{E} - \mathbf{E} \cdot \frac{\partial \mathbf{D}}{\partial t} \\ &= -\nabla \cdot (\mathbf{E} \times \mathbf{H}) - \mu_0 \mathbf{H} \cdot \frac{\partial \mathbf{H}}{\partial t} - \epsilon_0 \mathbf{E} \cdot \frac{\partial \mathbf{E}}{\partial t} - \mu_0 \mathbf{H} \cdot \frac{\partial \mathbf{M}}{\partial t} - \epsilon_0 \mathbf{E} \cdot \frac{\partial \mathbf{P}}{\partial t}. \quad (2.30)\end{aligned}$$

The final term in Eq. (2.30), $\epsilon_0 \mathbf{E} \cdot \frac{\partial \mathbf{P}}{\partial t}$, express power absorbed by polarization (dipoles) in the unit volume. When the harmonic oscillations of electric and magnetic fields are assumed as

$$\mathbf{E} = \mathbf{E}_0 e^{-\mathrm{i}\omega t},$$
$$\mathbf{H} = \mathbf{H}_0 e^{-\mathrm{i}\omega t},$$

the above absorbed power P_{D} are expressed as

$$P_{\mathrm{D}} = \frac{1}{2} \mathrm{Re} \left[\epsilon_0 \mathbf{E}^* \cdot \frac{\partial \mathbf{P}}{\partial t} \right].$$

When the polarization $\mathbf{P}$ is also assumed to becomes harmonic oscillation with the same frequency of the electric field ω, that is,

$$\mathbf{P} = \epsilon_0 \chi \mathbf{E}_0 e^{-\mathrm{i}\omega t},$$

where χ is the complex electric susceptibility of a material, the above absorbed power results in following form as

$$\begin{aligned}P_{\mathrm{D}} &= \frac{1}{2} \omega \epsilon_0 \mathbf{E} \cdot \mathbf{E}^* \chi_{\mathrm{i}}, \\ &= \frac{1}{2} \omega \epsilon_0 |E|^2 \chi_{\mathrm{i}}, \quad (2.31)\end{aligned}$$

where χ_{i} is the imaginary part of the complex electric susceptibility $\chi = \chi_{\mathrm{r}} + \mathrm{i}\chi_{\mathrm{i}}$.

Induced transition and transition probability In this paragraph, interaction between excited atoms and electromagnetic waves is considered. The energy density of the electromagnetic waves are assumed to be distributed uniformly over a frequency range near the transition frequency of atoms ν.

The induced transition probabilities of atoms from level 2 to level 1, W_{21}^{induced}, and from level 1 to level 2, W_{12}^{induced}, are assumed to be proportional to the energy density $\rho(\nu)$ as

$$\left.\begin{aligned} W_{21}^{\text{induced}} &= B_{21}\rho(\nu) \\ W_{12}^{\text{induced}} &= B_{12}\rho(\nu) \end{aligned}\right\} \tag{2.32}$$

where B_{21} and B_{12} are coefficients called *Einstein B coefficients* and the energy density $\rho(\nu)$ in the state of thermal equilibrium is given based on black body radiation and the Planck distribution low [36] as follows:

$$\rho(\nu) = \frac{8\pi n^3 h\nu^3}{c^3}\frac{1}{e^{h\nu/kT}-1}, \tag{2.33}$$

where h is Planck constant, k is Boltzmann constant, T is temperature, and n is the refractive index of active medium.

All the transition probability from level 2 to level 1 is expressed as the summation of the probabilities of induced transition and the transition of spontaneous emission, $B_{21}\rho(\nu)$ and A_{21}, as

$$W_{21} = B_{21}\rho(\nu) + A_{21}. \tag{2.34}$$

All the transition probability from level 1 to level 2 becomes as follows:

$$W_{12} = W_{12}^{\text{induced}} = B_{12}\rho(\nu). \tag{2.35}$$

In a state of thermal equilibrium, the numbers of atoms moving from level 2 to level 1 and those moving from level 1 to level 2 is equal to each other. Hence, a following relation is introduced.

$$N_2 W_{21} = N_1 W_{12}, \tag{2.36}$$

where N_1 and N_2 are the numbers of atoms on levels 1 and 2, respectively. By substituting Eqs. (2.34), (2.35) and (2.33) into Eq. (2.36), we have

$$N_2\left[B_{21}\rho(\nu) + A_{21}\right] = N_1\left[B_{12}\rho(\nu)\right],$$

resulting in

$$N_2 \left\{ B_{21} \left[\frac{8\pi n^3 h\nu^3}{c^3} \frac{1}{e^{h\nu/kT} - 1} \right] + A_{21} \right\} = N_1 \left\{ B_{12} \left[\frac{8\pi n^3 h\nu^3}{c^3} \frac{1}{e^{h\nu/kT} - 1} \right] \right\}. \tag{2.37}$$

The ratio between the numbers of atoms in levels 1 and 2 in the state of thermal equilibrium are given by Boltzmann constant [36] as

$$\frac{N_2}{N_1} = e^{-h\nu/kT}. \tag{2.38}$$

Based on comparison between Eqs. (2.37) and (2.38), we have

$$\frac{8\pi n^3 h\nu^3}{c^3(e^{h\nu/kT} - 1)} = \frac{A_{21}}{B_{12}e^{h\nu/kT} - B_{21}}.$$

In order to satisfy the above equation, the coefficients must have relations as follows:

$$\begin{aligned} B_{12} &= B_{21}, \\ \frac{A_{21}}{B_{21}} &= \frac{8\pi n^3 h\nu^3}{c^3}. \end{aligned}$$

Hence, the induced transition probabilities in Eq. (2.32) becomes

$$\begin{aligned} W_{\text{induce}} &= \frac{A_{21}c^3}{8\pi n^3 h\nu^3}\rho(\nu) \\ &= \frac{c^3}{8\pi n^3 h\nu^3 t_{\text{spont}}}\rho(\nu) \end{aligned}$$

where $t_{\text{spont}} = 1/A_{21}$ is spontaneous emission lifetime.

When the spectral distribution function of the induced transition probability, $g(\nu)$, is not uniform, the induced transition probability is written as the following integral form.

$$W_{\text{induce}} = \int \frac{c^3}{8\pi n^3 h\nu^3 t_{\text{spont}}}\rho(\nu)g(\nu)d\nu.$$

The energy of light wave of a solid color, whose frequency is ν, in unit interval of frequency is expressed as

$$\rho(\nu) = U_0\delta(\nu' - \nu),$$

where U_0 is the energy density of a solid colored light wave. Hence the induced transition probability of a solid colored light wave whose frequency is ν becomes

$$\begin{aligned} W_{\text{induce}} &= \frac{c^3 U_0}{8\pi n^3 h\nu^3 t_{\text{spont}}} g(\nu) \\ &= \frac{\lambda^2 I_0}{8\pi n^2 h\nu t_{\text{spont}}} g(\nu) \end{aligned} \tag{2.39}$$

where $I_0 = cU_0/n$ is the intensity of light waves.

Absorbed power density of light waves The power density of absorbed light waves is written in Eq. (2.31) as

$$P_{\text{D}} = \frac{1}{2}\omega\epsilon_0 |E|^2 \chi_{\text{i}},$$

and the above absorbed power density must correspond to a following equation including induced transition probability as

$$P_{\text{D}} = (N_1 - N_2) W_{\text{induce}} h\nu.$$

Based on the above relation and Eq. (2.39), the imaginary part of electric susceptibility becomes as

$$\begin{aligned} \chi_{\text{i}} &= \frac{2}{\omega\epsilon_0 |E|^2}(N_1 - N_2) W_{\text{induce}} h\nu \\ &= \frac{2(N_1 - N_2)h\nu}{\omega\epsilon_0 |E|^2} \frac{\lambda^2 I_0}{8\pi n^2 h\nu t_{\text{spont}}} g(\nu), \\ &= \frac{2(N_1 - N_2)}{\omega\epsilon_0 |E|^2} \frac{\lambda^2}{8\pi n^2 t_{\text{spont}}} \frac{c}{n} \epsilon \frac{|E|^2}{2} g(\nu), \\ &= \frac{(N_1 - N_2)}{\omega\epsilon_0/\epsilon} \frac{\lambda^2}{8\pi n^2 t_{\text{spont}}} \frac{c}{n} g(\nu), \\ &= \frac{(N_1 - N_2)\lambda^2}{16\pi^2 n^2 t_{\text{spont}}} \frac{2\pi c}{\omega} g(\nu), \\ &= \frac{(N_1 - N_2)\lambda^3}{16\pi^2 n^2 t_{\text{spont}}} g(\nu). \end{aligned} \tag{2.40}$$

In the above derivations, we use following relations as

$$\begin{aligned} I_0 &= \frac{c}{n}\epsilon\frac{|E|^2}{2} \\ n^2 &= \epsilon/\epsilon_0 \\ \lambda &= 2\pi c/\omega \end{aligned}$$

Equation (2.40) indicates that population inversion density of optically active material, $N_2 - N_1 (> 0)$, is proportional to a negative value in the imaginary part of electric susceptibility. Hence, population inversion density of optically active material can be modeled by a negative value in the imaginary part of relative permittivity, $-\gamma$ ($\gamma > 0$) [3, 4, 5]. γ is a parameter proportional to population inversion density of optically active material. Hence, γ at which a laser action occurs is interpreted as the threshold for the laser action [3, 4, 5].

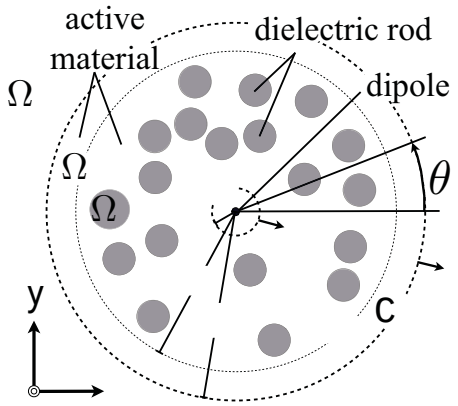

Figure 2.21: An illustration of a random system.

When we assume a system whose interspace among dielectric rods are filled with an optically active material, we set the imaginary part of relative permittivity in the interspace among the rods to $-\gamma$. The relative permittivities in the individual regions (Fig. 2.21) are given as follows:

$$\epsilon(\mathbf{x}) = \begin{cases} 1.0 + \mathrm{i}(-\gamma) & \mathbf{x} \in \Omega_{\mathrm{act}} \\ 4.0 & \mathbf{x} \in \Omega_{\mathrm{rod}} \\ 1.0 & \mathbf{x} \in \Omega_{\mathrm{out}} \end{cases} . \tag{2.41}$$

Lasing threshold of GaAs/GaAlAs double-heterostructure injection lasers We calculate lasing threshold of GaAs/GaAlAs double-heterostructure injection lasers to compare that of random lasers. All parameters used in this calculation are shown in reference [37]. The parameter γ including the imaginary part of relative permittivity is related to gain coefficient σ by

$$\gamma = \frac{\lambda n}{2\pi}\sigma, \tag{2.42}$$

where λ is the wavelength of light in vaccum and n is the refractive index of active medium by which light waves are amplified. The threshold gain coefficient

of light waves in cavity is calculated as follows:

$$\sigma = -\frac{1}{L}\ln R + \alpha_n \Gamma_n + \alpha_p \Gamma_p + \alpha_s, \tag{2.43}$$

where R is the reflectance of the cavity mirror, L is the cavity length, α_n express the coefficient of loss mainly caused by free-electron absorptions in non-excited neighboring n-type $Ga_{1-x}Al_xAs$, α_p express that in non-excited neighboring p-type $Ga_{1-x}Al_xAs$, and α_s express the coefficient of loss occurring on incomplete heterojunctions. Γ_p and Γ_n are power ratios of electric intensities within p- and n-type $Ga_{1-x}Al_xAs$, respectively, and are expressed as follows:

$$\Gamma_p = \frac{\int_{-\infty}^{-d/2} |\mathbf{E}|^2 dz}{\int_{-\infty}^{\infty} |\mathbf{E}|^2 dz},$$
$$\Gamma_n = \frac{\int_{d/2}^{\infty} |\mathbf{E}|^2 dz}{\int_{-\infty}^{\infty} |\mathbf{E}|^2 dz},$$

where d is the thickness of an active layer. The largest term expressing losses in Eq. (2.43) is generally $-\frac{1}{L}\ln R$ in the case of semiconductor lasers whose layer surface edges are not smoothed. The reflectance on the interface between GaAs ($n = 3.5$) and air is assumed to be $R = 0.31$, and the cavity length is $L = 500$ [μm]. Then, the largest term in Eq. (2.43) becomes

$$-\frac{1}{L}\ln R = 23.4 \text{ [cm}^{-1}\text{]}. \tag{2.44}$$

When assuming the summation of other losses as 10cm^{-1}, the gain coefficient in Eq. (2.43) becomes $\sigma = 33.4$ cm^{-1}. Using $\sigma = 33.4$ cm^{-1}, $n = 3.5$, and $0.75\mu\text{m} < \lambda < 0.88\mu\text{m}$ that is the range of the lasing wavelength in Eq. (2.42) yields the range of γ as

$$0.0013954 < \gamma < 0.0016373. \tag{2.45}$$

The range given in Eq. (2.45) is a little smaller than that of random lasers computed in the following parts of the presented dissertation. In other words, the threshold of semiconductor lasers is smaller than that of random lasers. Such unnatural result is caused by the huge difference between system sizes of semiconductor and random lasers. System sizes of laser devices, that is, cavity lengths have large influence on lasing thresholds because they appear in the denominator of the left hand side in Eq. (2.44). When the cavity length L is relatively large, light path in active medium becomes larger. Hence light waves are more amplified and the thresholds of the larger systems become lower. When the lasing frequency of GaAs/GaAlAs semiconductor laser for $\lambda = 0.88\mu$m is $\omega a/2\pi c = 0.225$,

which is the normalized lasing frequency of random lasers analysed in the present studies, the radius of ramdom systems becomes as $80a = 15.84\mu$m. The radius is much smaller than the cavity length of GaAs/GaAlAs semiconductor laser: $L = 500\mu$m.

2.2.6.4 Open region problem

We simulate laser action in dielectric structures caused by random scatterings in open regions. Light waves radiated for open regions are assumed to reach at infinite distance and never return.

2.3 Basic equations of electromagnetic waves

2.3.1 Maxwell's equations

The governing equations of electromagnetic waves are Maxwell's equations [34], as follows:

$$\nabla \cdot \mathbf{D}(\mathbf{x}, t) = \rho(\mathbf{x}, t),$$
$$\nabla \cdot \mathbf{B}(\mathbf{x}, t) = 0,$$
$$\nabla \times \mathbf{E}(\mathbf{x}, t) = -\frac{\partial}{\partial t}\mathbf{B}(\mathbf{x}, t), \tag{2.46}$$
$$\nabla \times \mathbf{H}(\mathbf{x}, t) = \mathbf{j}(\mathbf{x}, t) + \frac{\partial}{\partial t}\mathbf{D}(\mathbf{x}, t), \tag{2.47}$$

where $\mathbf{D}$, $\mathbf{B}$, $\mathbf{E}$, $\mathbf{H}$, and $\mathbf{j}$ satisfy

$$\mathbf{D}(\mathbf{x}, t) = \epsilon_0 \epsilon \mathbf{E}(\mathbf{x}, t), \tag{2.48}$$

$$\mathbf{B}(\mathbf{x}, t) = \mu_0 \mu \mathbf{H}(\mathbf{x}, t), \tag{2.49}$$

and

$$\mathbf{j}(\mathbf{x}, t) = 0.$$

By substituting Eqs. (2.48) and (2.49) into Eqs. (2.46) and (2.47), we can derive

$$\nabla \times \mathbf{E}(\mathbf{x}, t) = -\mu_0 \mu \frac{\partial}{\partial t}\mathbf{H}(\mathbf{x}, t), \tag{2.50}$$

and

$$\nabla \times \mathbf{H}(\mathbf{x}, t) = \epsilon_0 \epsilon \frac{\partial}{\partial t}\mathbf{E}(\mathbf{x}, t). \tag{2.51}$$

2.3.2 Basic equations of electromagnetic scattering problem

In this study, we simulate laser action in dielectric structures consisting of homogeneous rods in the case of TM mode by using the node-base FEM. We use perfectly matched layers (PMLs) [38] to simulate scatterings in open regions, and employ an optimized absorbing function [39, 40, 41] that minimizes numerical reflections.

We show a model of a dielectric system as shown in Fig. 2.22(a). We assume that dielectric rods are infinitely long in vertical direction (z-direction) and light

waves propagate within xy-plane. Figure 2.22(b) exhibits the concept of a random system from the top view. Dielectric rods are arranged randomly in the region between the circler regions $\mathrm{C_{in}}$ and $\mathrm{C_g}$, as shown in Fig. 2.22(b). An oscillating dipole is assumed to exist at the center of the circle $\mathrm{C_{in}}$ as a light source. Radii of $\mathrm{C_{in}}$ and $\mathrm{C_g}$ are denoted by $\mathrm{R_{in}}$ and $\mathrm{R_g}$, respectively. We compute the fluxes of Poynting vectors of out-flowing light waves on the circle $\mathrm{C_{out}}$ whose radius is $\mathrm{R_{out}}$. The unit outward normal vectors to $\mathrm{C_{in}}$ and $\mathrm{C_{out}}$ are denoted by $\mathbf{n}_{\mathrm{in}}$ and $\mathbf{n}_{\mathrm{out}}$, respectively. We define three regions: Ω_{act}, Ω_{rod} and Ω_{out}, where Ω_{act} is in the interspace among the rods inside the circle $\mathrm{C_{out}}$, Ω_{rod} is the union of the regions inside the rods, and Ω_{out} is the region outside the circle $\mathrm{C_{out}}$. The optically active materials are assumed to be filled in the region Ω_{act}.

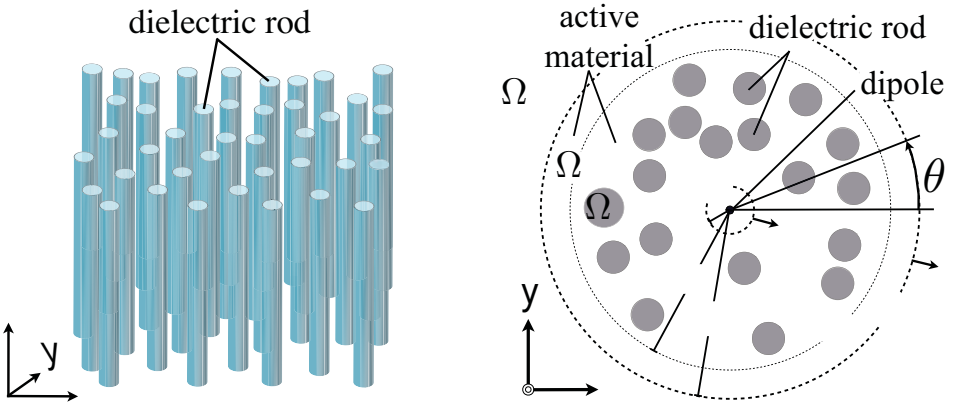

(a) A random structure model. (b) An illustration of whole random system.

Figure 2.22: Concept of random media.

We assume an electric dipole oscillating with angular frequency ω at the center of the entire region of the random system, $\mathbf{x}_0$, as a light source (Fig. 2.22). Polarization $\mathbf{P}_{\mathrm{d}}$ occurring from the oscillating electric dipole is written, as follows:

$$\mathbf{P}_{\mathrm{d}}(\mathbf{x}, t) = \mathbf{D}_{\mathrm{d}}\delta(\mathbf{x} - \mathbf{x}_0)\exp(-\mathrm{i}\omega t),$$

where $\mathbf{D}_{\mathrm{d}}$ is the polarization vector oriented from the negative charge to the positive charge, $\delta(\mathbf{x})$ is Dirac's delta function, and i is the imaginary unit. The polarization $\mathbf{P}_{\mathrm{d}}$ is included in the electric flux density $\mathbf{D}(\mathbf{x}, t)$, as

$$\mathbf{D}(\mathbf{x}, t) = \epsilon_0\epsilon(\mathbf{x})\mathbf{E}(\mathbf{x}, t) + \mathbf{P}_{\mathrm{d}}(\mathbf{x}, t), \tag{2.52}$$

where $\mathbf{E}(\mathbf{x}, t)$ is the electric field, ϵ_0 and $\epsilon(\mathbf{x})$ are the permittivity in vacuum and the position-dependent relative permittivity, respectively.

We assume that electric and magnetic fields are time-harmonic waves with the same angular frequency as that of the dipole, and can be expressed as follows:

$$\mathbf{E}(\mathbf{x}, t) = \mathbf{E}(\mathbf{x}) \exp(-\mathrm{i}\omega t), \tag{2.53}$$

$$\mathbf{H}(\mathbf{x}, t) = \mathbf{H}(\mathbf{x}) \exp(-\mathrm{i}\omega t), \tag{2.54}$$

where $\mathbf{H}(\mathbf{x}, t)$ is the magnetic field. Following two equations are derived by substituting Eqs. (2.52), (2.53), and (2.54) into Maxwell's equations.

$$\nabla \times \mathbf{E}(\mathbf{x}) = \mathrm{i}\omega\mu_0 \mathbf{H}(\mathbf{x}),$$

$$\nabla \times \mathbf{H}(\mathbf{x}) = -\mathrm{i}\omega \left[\epsilon_0 \epsilon(\mathbf{x}) \mathbf{E}(\mathbf{x}) + \mathbf{D}_\mathrm{d} \delta(\mathbf{x} - \mathbf{x}_0)\right],$$

resulting in

$$\nabla \times [\nabla \times \mathbf{E}(\mathbf{x})] - \frac{\omega^2}{c^2} \epsilon(\mathbf{x}) \mathbf{E}(\mathbf{x}) = \frac{\omega^2}{\epsilon_0 c^2} \mathbf{D}_\mathrm{d} \delta(\mathbf{x} - \mathbf{x}_0), \tag{2.55}$$

where c is the speed of light in vacuum and satisfies the relation $c = 1/\sqrt{\mu_0 \epsilon_0}$ where μ_0 is the magnetic permeability in vacuum.

We define total electric field $\mathbf{E}(\mathbf{x})$ as a sum of the scattering and incident fields as follows:

$$\mathbf{E}(\mathbf{x}) = \mathbf{E}_\mathrm{s}(\mathbf{x}) + \mathbf{E}_\mathrm{i}(\mathbf{x}), \tag{2.56}$$

where, $\mathbf{E}_\mathrm{i}(\mathbf{x})$ is the electric field in the region without scatterers, satisfying the following equation:

$$\nabla \times [\nabla \times \mathbf{E}_\mathrm{i}(\mathbf{x})] - \frac{\omega^2}{c^2} \epsilon_\mathrm{i} \mathbf{E}_\mathrm{i}(\mathbf{x}) = \frac{\omega^2}{\epsilon_0 c^2} \mathbf{D}_\mathrm{d} \delta(\mathbf{x} - \mathbf{x}_0), \tag{2.57}$$

where ϵ_i is the constant relative permittivity in Ω_out (Fig. 2.22). By substituting Eq. (2.56) into Eq. (2.55), we have

$$\begin{aligned} &\nabla \times [\nabla \times \mathbf{E}_\mathrm{s}(\mathbf{x})] - \frac{\omega^2}{c^2} \epsilon(\mathbf{x}) \mathbf{E}_\mathrm{s}(\mathbf{x}) \\ &\quad = -\left\{ \nabla \times [\nabla \times \mathbf{E}_\mathrm{i}(\mathbf{x})] - \frac{\omega^2}{c^2} \epsilon(\mathbf{x}) \mathbf{E}_\mathrm{i}(\mathbf{x}) \right\} + \frac{\omega^2}{\epsilon_0 c^2} \mathbf{D}_\mathrm{d} \delta(\mathbf{x} - \mathbf{x}_0). \end{aligned} \tag{2.58}$$

We substitute Eq. (2.57) to the right-hand side of Eq. (2.58) to have

$$\nabla \times [\nabla \times \mathbf{E}_\mathrm{s}(\mathbf{x})] - \frac{\omega^2}{c^2} \epsilon(\mathbf{x}) \mathbf{E}_\mathrm{s}(\mathbf{x}) = \frac{\omega^2}{c^2} \left[\epsilon(\mathbf{x}) - \epsilon_\mathrm{i}\right] \mathbf{E}_\mathrm{i}(\mathbf{x}). \tag{2.59}$$

When we assume TM mode, the incident field $\mathbf{E}_\mathrm{i}(\mathbf{x})$ satisfying Eq. (2.57) can be expressed by the 0th-order Hankel function of the first kind, $H_0^{(1)}$, as follows:

$$\mathbf{E}_\mathrm{i}(\mathbf{x}) = \frac{\omega^2}{\epsilon_0 c^2} \mathbf{D}_\mathrm{d} \frac{\mathrm{i}}{4} H_0^{(1)} \left(\frac{\omega}{c} \sqrt{\epsilon_\mathrm{i}} \left| \mathbf{x} - \mathbf{x}_0 \right| \right).$$

We solve Eq. (2.59) by using FEM formulated based on Galerkin's method. Finally, we are able to obtain the total electric field $\mathbf{E}(\mathbf{x})$ defined by Eq. (2.56).

2.3.2.1 Computed physical quantities

We have to compute Poynting vectors to simulate light amplification occurring in dielectric structures. Because of the assumption that electric and magnetic waves are time-harmonic, we need to compute Poynting vectors in the following time-averaged form:

$$\langle \mathbf{S} \rangle = \mathrm{Re}\left(\frac{\mathbf{E} \times \mathbf{H}^*}{2} \right),$$

where $\langle \mathbf{S} \rangle$ is the time-average of Poynting vector $\mathbf{S}$, $\mathrm{Re}(\mathbf{Z})$ means the real part of complex vector $\mathbf{Z}$, and $\mathbf{H}^*$ denotes the complex conjugate of the magnetic field.

We define the amplification factor A by the ratio of the fluxes of the Poynting vectors of light, flowing out from the dielectric system, between the excited state ($\gamma > 0$) and non-excited state ($\gamma = 0$), as follows:

$$A = \frac{\int_{\mathrm{C_{out}}} \langle \mathbf{S} \rangle \cdot \mathbf{n} \; dl|_{\gamma \geq 0}}{\int_{\mathrm{C_{out}}} \langle \mathbf{S} \rangle \cdot \mathbf{n} \; dl \; |_{\gamma=0}}. \tag{2.60}$$

The light flux is calculated by a line integral of the Poynting vector along the circle $\mathrm{C_{out}}$ in Fig. 2.22(b).

2.3.3 Conservation low of energy of light waves

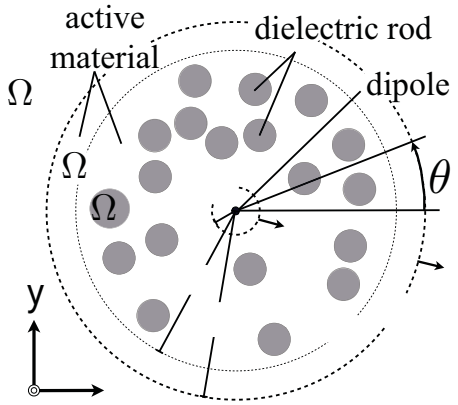

Figure 2.23: An illustration of the entire random system

When a system does not have gain, that is, $\gamma = 0$, the conservation low of the energy of light waves must hold as follows:

$$\nabla \cdot \mathbf{S} = -\frac{\partial w}{\partial t}, \tag{2.61}$$

where $\mathbf{S}$ is Poynting vector and w is energy density. The left-hand side of Eq. (2.61) indicates the energy flowing out from an arbitrary infinitesimal region, and right-hand side the reduction rate of the energy density. When the light source does not exist in a region, the energy flowing into the system and that flowing out from the system becomes equal to each other.

We consider a region between two circles $\mathrm{C_{in}}$ and $\mathrm{C_{out}}$. A light source is located in $\mathrm{C_{in}}$, and the region between $\mathrm{C_{in}}$ and $\mathrm{C_{out}}$ has no source. From the energy balance between the energy flowing into the system and that flowing out from the system, we observe

$$\int_{\mathrm{C_{in}}} \langle \mathbf{S} \rangle \cdot \mathbf{n}_{\mathrm{in}} \, dl \Big|_{\gamma=0} = \int_{\mathrm{C_{out}}} \langle \mathbf{S} \rangle \cdot \mathbf{n}_{\mathrm{out}} \, dl \Big|_{\gamma=0},$$

where $\langle \mathbf{S} \rangle$ is the time-average of $\mathbf{S}$ defined as

$$\langle \mathbf{S} \rangle = \mathrm{Re}\left[\frac{\mathbf{E} \times \mathbf{H}^*}{2}\right].$$

2.4 Boundary condition

2.4.1 Perfectly matched layer boundary condition

The basic formulation for perfectly matched layer (PML) boundary condition [38] in the case of TM mode is written in this subsection. The electric field are assumed to have only z component as

$$\mathbf{E}(\mathbf{x},t) = [0,0,E_z]^{\mathrm{T}}. \tag{2.62}$$

We substitute Eq. (2.62) into Maxwell's equation (2.50) and derive as

$$\begin{aligned}
\nabla \times \mathbf{E}(\mathbf{x},t) + \mu_0\mu\frac{\partial}{\partial t}\mathbf{H}(\mathbf{x},t) &= \begin{bmatrix} \dfrac{\partial E_z}{\partial y} - \dfrac{\partial E_y}{\partial z} \\ \dfrac{\partial E_x}{\partial z} - \dfrac{\partial E_z}{\partial x} \\ \dfrac{\partial E_y}{\partial x} - \dfrac{\partial E_x}{\partial y} \end{bmatrix} + \begin{bmatrix} \mu_0\mu\dfrac{\partial H_x}{\partial t} \\ \mu_0\mu\dfrac{\partial H_y}{\partial t} \\ \mu_0\mu\dfrac{\partial H_z}{\partial t} \end{bmatrix} \\
&= \begin{bmatrix} \dfrac{\partial E_z}{\partial y} + \mu_0\mu\dfrac{\partial H_x}{\partial t} \\ -\dfrac{\partial E_z}{\partial x} + \mu_0\mu\dfrac{\partial H_y}{\partial t} \\ \mu_0\mu\dfrac{\partial H_z}{\partial t} \end{bmatrix} \\
&= \mathbf{0},
\end{aligned}$$

from which we obtain

$$\begin{aligned}
\frac{\partial E_z}{\partial y} &= -\mu_0\mu\frac{\partial H_x}{\partial t}, \\
\frac{\partial E_z}{\partial x} &= \mu_0\mu\frac{\partial H_y}{\partial t}.
\end{aligned}$$

In the same derivation process, we derive from Eq. (2.51)

$$\nabla \times \mathbf{H}(\mathbf{x},t) - \epsilon_0\epsilon\frac{\partial}{\partial t}\mathbf{E}(\mathbf{x},t) = \begin{bmatrix} \dfrac{\partial H_z}{\partial y} - \dfrac{\partial H_y}{\partial z} \\ \dfrac{\partial H_x}{\partial z} - \dfrac{\partial H_z}{\partial x} \\ \dfrac{\partial H_y}{\partial x} - \dfrac{\partial H_x}{\partial y} - \epsilon_0\epsilon\dfrac{\partial E_z}{\partial t} \end{bmatrix} = \mathbf{0},$$

from which we obtain

$$\frac{\partial H_y}{\partial x} - \frac{\partial H_x}{\partial y} = \epsilon_0 \epsilon \frac{\partial E_z}{\partial t}.$$

We divide the z component of the electric field as

$$E_z = E_{zx} + E_{zy},$$

where E_{zx} and E_{zy} have to satisfy following relations:

$$\frac{\partial E_{zx}}{\partial x} \neq 0, \quad \frac{\partial E_{zy}}{\partial x} = 0, \quad \frac{\partial E_{zx}}{\partial y} = 0, \quad \frac{\partial E_{zy}}{\partial x} \neq 0,$$

and

$$\epsilon_0 \epsilon \frac{\partial E_{zx}}{\partial t} = \frac{\partial H_y}{\partial x},\ \epsilon_0 \epsilon \frac{\partial E_{zy}}{\partial t} = -\frac{\partial H_x}{\partial y},\ \mu_0 \mu \frac{\partial H_y}{\partial t} = \frac{\partial E_z}{\partial x},\ \mu_0 \mu \frac{\partial H_x}{\partial t} = -\frac{\partial E_z}{\partial y}.$$

Absorbing coefficients of the electric and magnetic fields in x and y directions are now denoted by $\sigma_x(x)$, $\sigma_y(y)$, $\sigma_x^*(x)$, $\sigma_y^*(y)$. They are interpreted as the electric and magnetic conductivities, σ and σ^*, for x and y directions. Above absorbing coefficients are introduced as dumping terms of electromagnetic waves as

$$\left.\begin{aligned}
\epsilon_0 \epsilon \frac{\partial E_{zx}}{\partial t} + \sigma_x(x) E_{zx} &= \frac{\partial H_y}{\partial x} \\
\epsilon_0 \epsilon \frac{\partial E_{zy}}{\partial t} + \sigma_y(y) E_{zy} &= -\frac{\partial H_x}{\partial y} \\
\mu_0 \mu \frac{\partial H_y}{\partial t} + \sigma_x^*(x) H_y &= \frac{\partial E_z}{\partial x} \\
\mu_0 \mu \frac{\partial H_x}{\partial t} + \sigma_y^*(y) H_x &= -\frac{\partial E_z}{\partial y}
\end{aligned}\right\}, \tag{2.63}$$

where the conductivities have following relations based on impedance matching condition on the boundary between scattering and PML regions as

$$\frac{\sigma_x}{\epsilon_0} = \frac{\sigma_x^*}{\mu_0}, \quad \frac{\sigma_y}{\epsilon_0} = \frac{\sigma_y^*}{\mu_0}. \tag{2.64}$$

We assume the electric and magnetic fields are in harmonic oscillation, as follows:

$$H_{zx} = \hat{H}_{zx} e^{-\mathrm{i}\omega t}, \quad H_{zy} = \hat{H}_{zy} e^{-\mathrm{i}\omega t}, \quad E_x = \hat{E}_x e^{-\mathrm{i}\omega t}, \quad E_y = \hat{E}_y e^{-\mathrm{i}\omega t}, \tag{2.65}$$

then, the time dependent terms in Eq. (2.63) become as

$$\left.\begin{aligned}
\frac{\partial E_{zx}}{\partial t} &= -\mathrm{i}\omega \hat{E}_{zx} e^{-\mathrm{i}\omega t}, & \frac{\partial E_{zy}}{\partial t} &= -\mathrm{i}\omega \hat{E}_{zy} e^{-\mathrm{i}\omega t} \\
\frac{\partial H_x}{\partial t} &= -\mathrm{i}\omega \hat{H}_x e^{-\mathrm{i}\omega t}, & \frac{\partial H_y}{\partial t} &= -\mathrm{i}\omega \hat{H}_y e^{-\mathrm{i}\omega t}
\end{aligned}\right\}. \tag{2.66}$$

By substituting Eqs. (2.65) and (2.66) into Eq. (2.63), following equations are derived.

$$\{-\mathrm{i}\omega\epsilon_0\epsilon + \sigma_x(x)\}\,\hat{E}_{zx} = \frac{\partial \hat{H}_y}{\partial x}, \quad \{-\mathrm{i}\omega\epsilon_0\epsilon + \sigma_y(y)\}\,\hat{E}_{zy} = -\frac{\partial \hat{H}_x}{\partial y},$$
$$\{-\mathrm{i}\omega\mu_0\mu + \sigma_x^*(x)\}\,\hat{H}_y = \frac{\partial \hat{E}_z}{\partial x}, \quad \left\{-\mathrm{i}\omega\mu_0\mu + \sigma_y^*(y)\right\}\hat{H}_x = -\frac{\partial \hat{E}_z}{\partial y},$$

from which we have

$$\begin{aligned}
\hat{E}_{zx} &= \frac{1}{-\mathrm{i}\omega\epsilon_0\epsilon + \sigma_x(x)}\frac{\partial \hat{H}_y}{\partial x}, \\
\hat{E}_{zy} &= -\frac{1}{-\mathrm{i}\omega\epsilon_0\epsilon + \sigma_y(y)}\frac{\partial \hat{H}_x}{\partial y}, \\
\frac{\partial \hat{H}_y}{\partial x} &= \frac{\partial}{\partial x}\left\{\frac{1}{-\mathrm{i}\omega\mu_0\mu + \sigma_x^*(x)}\frac{\partial \hat{E}_z}{\partial x}\right\}, \\
\frac{\partial \hat{H}_x}{\partial y} &= \frac{\partial}{\partial y}\left\{-\frac{1}{-\mathrm{i}\omega\mu_0\mu + \sigma_y^*(y)}\frac{\partial \hat{E}_z}{\partial y}\right\}.
\end{aligned}$$

The amplitude of the electric field $\hat{E}_z$ becomes

$$\begin{aligned}
\hat{E}_z &= \hat{E}_{zx} + \hat{E}_{zy}, \\
&= \frac{1}{-\mathrm{i}\omega\epsilon_0\epsilon + \sigma_x(x)}\frac{\partial \hat{H}_y}{\partial x} - \frac{1}{-\mathrm{i}\omega\epsilon_0\epsilon + \sigma_y(y)}\frac{\partial \hat{H}_x}{\partial y} \\
&= \frac{1}{-\mathrm{i}\omega\epsilon_0\epsilon + \sigma_x(x)}\frac{\partial}{\partial x}\left\{\frac{1}{-\mathrm{i}\omega\mu_0\mu + \sigma_x^*(x)}\frac{\partial \hat{E}_z}{\partial x}\right\} \\
&\quad - \frac{1}{-\mathrm{i}\omega\epsilon_0\epsilon + \sigma_y(y)}\frac{\partial}{\partial y}\left\{-\frac{1}{-\mathrm{i}\omega\mu_0\mu + \sigma_y^*(y)}\frac{\partial \hat{E}_z}{\partial y}\right\} \\
&= \frac{1}{\mathrm{i}\omega\epsilon_0\epsilon - \sigma_x(x)}\frac{\partial}{\partial x}\left\{\frac{1}{\mathrm{i}\omega\mu_0\mu - \sigma_x^*(x)}\frac{\partial \hat{E}_z}{\partial x}\right\} \\
&\quad + \frac{1}{\mathrm{i}\omega\epsilon_0\epsilon - \sigma_y(y)}\frac{\partial}{\partial y}\left\{\frac{1}{\mathrm{i}\omega\mu_0\mu - \sigma_y^*(y)}\frac{\partial \hat{E}_z}{\partial y}\right\},
\end{aligned}$$

then, by multipling both sides by $(\mathrm{i}\omega)^2$, the above equation becomes

$$\begin{aligned}
-\omega^2\hat{E}_z &= \frac{\mathrm{i}\omega}{\mathrm{i}\omega\epsilon_0\epsilon - \sigma_x(x)}\frac{\partial}{\partial x}\left\{\frac{\mathrm{i}\omega}{\mathrm{i}\omega\mu_0\mu - \sigma_x^*(x)}\frac{\partial\hat{E}_z}{\partial x}\right\} \\
&\quad + \frac{\mathrm{i}\omega}{\mathrm{i}\omega\epsilon_0\epsilon - \sigma_y(y)}\frac{\partial}{\partial y}\left\{\frac{\mathrm{i}\omega}{\mathrm{i}\omega\mu_0\mu - \sigma_y^*(y)}\frac{\partial\hat{E}_z}{\partial y}\right\} \\
&= \frac{1}{\epsilon_0\epsilon - \frac{1}{\mathrm{i}\omega}\sigma_x(x)}\frac{\partial}{\partial x}\left\{\frac{1}{\mu_0\mu - \frac{1}{\mathrm{i}\omega}\sigma_x^*(x)}\frac{\partial\hat{E}_z}{\partial x}\right\} \\
&\quad + \frac{1}{\epsilon_0\epsilon - \frac{1}{\mathrm{i}\omega}\sigma_y(y)}\frac{\partial}{\partial y}\left\{\frac{1}{\mu_0\mu - \frac{1}{\mathrm{i}\omega}\sigma_y^*(y)}\frac{\partial\hat{E}_z}{\partial y}\right\} \\
&= \frac{1}{\epsilon_0\epsilon + \frac{i}{\omega}\sigma_x(x)}\frac{\partial}{\partial x}\left\{\frac{1}{\mu_0\mu + \frac{i}{\omega}\sigma_x^*(x)}\frac{\partial\hat{E}_z}{\partial x}\right\} \\
&\quad + \frac{1}{\epsilon_0\epsilon + \frac{i}{\omega}\sigma_y(y)}\frac{\partial}{\partial y}\left\{\frac{1}{\mu_0\mu + \frac{i}{\omega}\sigma_y^*(y)}\frac{\partial\hat{E}_z}{\partial y}\right\}.
\end{aligned}$$

The equation solved in PML region finally becomes, as follows:

$$\begin{aligned}
&\frac{\omega^2}{c^2}\hat{E}_z + \frac{1}{\epsilon + \frac{i}{\omega\epsilon_0}\sigma_x(x)}\frac{\partial}{\partial x}\left\{\frac{1}{\mu + \frac{i}{\omega\mu_0}\sigma_x^*(x)}\frac{\partial\hat{E}_z}{\partial x}\right\} \\
&\quad + \frac{1}{\epsilon + \frac{i}{\omega\epsilon_0}\sigma_y(y)}\frac{\partial}{\partial y}\left\{\frac{1}{\mu + \frac{i}{\omega\mu_0}\sigma_y^*(y)}\frac{\partial\hat{E}_z}{\partial y}\right\} = 0. \qquad (2.67)
\end{aligned}$$

Based on Eq. (2.64), we rewrite the absorbing coefficients as

$$\hat{\sigma}_x = \frac{\sigma_x}{\epsilon_0} = \frac{\sigma_x^*}{\mu_0}, \quad \hat{\sigma}_y = \frac{\sigma_y}{\epsilon_0} = \frac{\sigma_y^*}{\mu_0}. \qquad (2.68)$$

The relative permittivity and permeability in PML region are as follows:

$$\epsilon = \mu = 1. \qquad (2.69)$$

By substituting Eqs. (2.68) and (2.69) into Eq. (2.67), we obtain the following equation:

$$\begin{aligned}
&\frac{\omega^2}{c^2}\hat{E}_z + \frac{1}{1 + \frac{i}{\omega}\hat{\sigma}_x(x)}\frac{\partial}{\partial x}\left\{\frac{1}{1 + \frac{i}{\omega}\hat{\sigma}_x(x)}\frac{\partial\hat{E}_z}{\partial x}\right\} \\
&\quad + \frac{1}{1 + \frac{i}{\omega}\hat{\sigma}_y(y)}\frac{\partial}{\partial y}\left\{\frac{1}{1 + \frac{i}{\omega}\hat{\sigma}_y(y)}\frac{\partial\hat{E}_z}{\partial y}\right\} = 0.
\end{aligned}$$

Absorbing function We use optimized absorbing functions for the Helmholtz equation [39, 40, 41]. The functions are defined as

$$\sigma_x(x) = \frac{c}{a^* - x},$$

$$\sigma_y(y) = \frac{c}{b^* - y},$$

where a^* and b^* are the distance between outer edges of PML and the origin (0,0). Above absorbing functions minimize reflected waves from outer edges of PML.

2.5 Other numerical method

In this section, we introduce several numerical methods frequently used for the analysis of optical phenomena. Basic formulations and concepts of those numerical methods are described.

2.5.1 Finite difference time domain method (FDTD method)

Finite difference time domain method (FDTD method) is one of the most popular numerical method for the analyses of electromagnetic problem. The electric and magnetic fields are discretized based on the Yee algorithm [42].

Let the electric field, magnetic field, electric displacement field, and magnetic induction field be denoted by $\mathbf{E}$, $\mathbf{H}$, $\mathbf{D}$, and $\mathbf{B}$, respectively. These quantities satisfy, under non-existence of sources, the following Maxwell's equations (in SI units):

$$\nabla \cdot \mathbf{D}(\mathbf{r}, t) = 0, \qquad \nabla \cdot \mathbf{B}(\mathbf{r}, t) = 0, \tag{2.70}$$

$$\nabla \times \mathbf{E}(\mathbf{r}, t) = -\frac{\partial}{\partial t}\mathbf{B}(\mathbf{r}, t), \qquad \nabla \times \mathbf{H}(\mathbf{r}, t) = \frac{\partial}{\partial t}\mathbf{D}(\mathbf{r}, t). \tag{2.71}$$

Also, we introduce the following relationships commonly used:

$$\mathbf{D}(\mathbf{r}, t) = \epsilon(\mathbf{r})\epsilon_0\mathbf{E}(\mathbf{r}, t), \quad \mathbf{B}(\mathbf{r}, t) = \mu_0\mathbf{H}(\mathbf{r}, t), \tag{2.72}$$

where ϵ_0 and μ_0 are the permittivity and permeability of vacuum, respectively. The speed of light in vacuum, denoted by c, then becomes as $c = (\epsilon_0\mu_0)^{-1/2}$.

By substituting Eq. (2.72) to Eq. (2.71), we can derive the following time-dependent equations

$$\epsilon(\mathbf{r})\frac{\partial \mathbf{E}(\mathbf{r}, t)}{\partial t} = \nabla \times \mathbf{H}(\mathbf{r}, t), \quad \frac{\partial \mathbf{H}(\mathbf{r}, t)}{\partial t} = -\nabla \times \mathbf{E}(\mathbf{r}, t). \tag{2.73}$$

The time derivative terms in the left hand sides of Eq. (2.73) are discretized as follows:

$$\left.\frac{\partial \mathbf{E}(\mathbf{r}, t)}{\partial t}\right|_{t=\left(n-\frac{1}{2}\Delta t\right)} = \frac{\mathbf{E}\left[\mathbf{r}, n\Delta t\right] - \mathbf{E}\left[\mathbf{r}, (n-1)\Delta t\right]}{\Delta t},$$

$$\left.\frac{\partial \mathbf{H}(\mathbf{r}, t)}{\partial t}\right|_{t=(n\Delta t)} = \frac{\mathbf{H}\left[\mathbf{r}, \left(n+\frac{1}{2}\right)\Delta t\right] - \mathbf{H}\left[\mathbf{r}, \left(n-\frac{1}{2}\right)\Delta t\right]}{\Delta t}.$$

Then, we substitute the above discretized terms into Eq. (2.73) and obtain the following equations

$$\epsilon(\mathbf{r})\frac{\mathbf{E}\left[\mathbf{r}, n\Delta t\right] - \mathbf{E}\left[\mathbf{r}, (n-1)\Delta t\right]}{\Delta t} = \nabla \times \mathbf{H}\left[\mathbf{r}, \left(n - \frac{1}{2}\right)\Delta t\right],$$

$$\frac{\mathbf{H}\left[\mathbf{r}, \left(n + \frac{1}{2}\right)\Delta t\right] - \mathbf{H}\left[\mathbf{r}, \left(n - \frac{1}{2}\right)\Delta t\right]}{\Delta t} = -\nabla \times \mathbf{E}\left[\mathbf{r}, n\Delta t\right],$$

which result in

$$\mathbf{E}\left[\mathbf{r}, n\Delta t\right] = \mathbf{E}\left[\mathbf{r}, (n-1)\Delta t\right] + \frac{\Delta t}{\epsilon(\mathbf{r})}\nabla \times \mathbf{H}\left[\mathbf{r}, \left(n - \frac{1}{2}\right)\Delta t\right] \tag{2.74}$$

and

$$\mathbf{H}\left[\mathbf{r}, \left(n + \frac{1}{2}\right)\Delta t\right] = \mathbf{H}\left[\mathbf{r}, \left(n - \frac{1}{2}\right)\Delta t\right] - \Delta t\left[\nabla \times \mathbf{E}\left[\mathbf{r}, n\Delta t\right]\right]. \tag{2.75}$$

The components of the rotations of the electric and magnetic fields in Eqs. (2.74) and (2.75) are spatially discretized based on the Yee grid shown in Fig. 2.24. The x component of Eq. (2.75) becomes

$$\begin{aligned}&\left[\frac{\partial}{\partial y}E_z\left[\mathbf{r}, n\Delta t\right] - \frac{\partial}{\partial z}E_y\left[\mathbf{r}, n\Delta t\right]\right] \\ &= -\frac{1}{\Delta t}\left\{H_x\left[\mathbf{r}, \left(n + \frac{1}{2}\right)\Delta t\right] - H_x\left[\mathbf{r}, \left(n - \frac{1}{2}\right)\Delta t\right]\right\}\end{aligned} \tag{2.76}$$

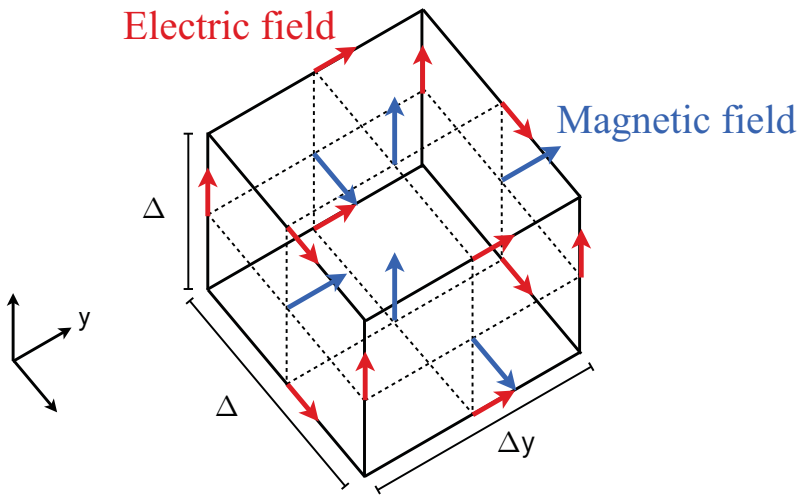

Figure 2.24: The Yee grid.

whose left and right hand sides are spatially discretized as

$$\begin{aligned}
&\left[\frac{\partial}{\partial y}E_z\left[\mathbf{r}, n\Delta t\right] - \frac{\partial}{\partial z}E_y\left[\mathbf{r}, n\Delta t\right]\right] \\
&= \frac{E_z(x, y+\Delta y/2, z, t) - E_z(x, y-\Delta y/2, z, t)}{\Delta y} \\
&\quad - \frac{E_z(x, y, z+\Delta z/2, t) - E_z(x, y, z-\Delta z/2, t)}{\Delta z}
\end{aligned}$$

and

$$\begin{aligned}
&-\frac{1}{\Delta t}\left\{H_x\left[\mathbf{r}, \left(n+\frac{1}{2}\right)\Delta t\right] - H_x\left[\mathbf{r}, \left(n-\frac{1}{2}\right)\Delta t\right]\right\} \\
&= -\frac{H_x(x, y, z, t+\Delta t/2) - H_x(x, y, z, t-\Delta t/2)}{\Delta t},
\end{aligned}$$

respectively. In the above discretizing processes, $n\Delta t$ is simply denoted by t, and (x, y, z) by $\mathbf{r}$. The x component of the magnetic field at $t + \Delta t/2$ finally results in

$$\begin{aligned}
H_x(x, y, z, t+\Delta t/2) = H_x(x, y, z, t-\Delta t/2) \\
- \frac{E_z(x, y+\Delta y/2, z, t) - E_z(x, y-\Delta y/2, z, t)}{\Delta y/\Delta t} \\
+ \frac{E_y(x, y, z+\Delta z/2, t) - E_y(x, y, z-\Delta z/2, t)}{\Delta z/\Delta t}.
\end{aligned}$$

The y and z components of the magnetic field at $t + \Delta t/2$ are also derived from Eq. (2.75), as follows:

$$\begin{aligned}
H_y(x, y, z, t+\Delta t/2) = H_y(x, y, z, t-\Delta t/2) \\
- \frac{E_x(x, y, z+\Delta z/2, t) - E_x(x, y, z-\Delta z/2, t)}{\Delta y/\Delta t} \\
+ \frac{E_z(x+\Delta x/2, y, z, t) - E_z(x-\Delta x/2, y, z, t)}{\Delta z/\Delta t}
\end{aligned}$$

and

$$\begin{aligned}
H_z(x, y, z, t+\Delta t/2) = H_y(x, y, z, t-\Delta t/2) \\
- \frac{E_y(x+\Delta x/2, y, z, t) - E_y(x-\Delta x/2, y, z, t)}{\Delta y/\Delta t} \\
+ \frac{E_x(x, y+\Delta y/2, z, t) - E_x(x, y-\Delta y/2, z, t)}{\Delta z/\Delta t}.
\end{aligned}$$

Similarly from Eq. (2.74), we can derive the x, y, and z components of the electric field at $t + \Delta t/2$ as

$$\begin{aligned} E_x(x, y, z, t + \Delta t/2) = E_x(x, y, z, t - \Delta t/2) \\ + \frac{H_z(x, y + \Delta y/2, z, t) - H_z(x, y - \Delta y/2, z, t)}{\epsilon(x, y, z)\Delta y/\Delta t} \\ - \frac{H_y(x, y, z + \Delta z/2, t) - H_y(x, y, z - \Delta z/2, t)}{\epsilon(x, y, z)\Delta z/\Delta t}, \end{aligned}$$

$$\begin{aligned} E_y(x, y, z, t + \Delta t/2) = E_y(x, y, z, t - \Delta t/2) \\ + \frac{H_x(x, y, z + \Delta z/2, t) - H_x(x, y, z - \Delta z/2, t)}{\epsilon(x, y, z)\Delta z/\Delta t} \\ - \frac{H_z(x + \Delta x/2, y, z, t) - H_z(x - \Delta x/2, y, z, t)}{\epsilon(x, y, z)\Delta x/\Delta t}, \end{aligned}$$

and

$$\begin{aligned} E_z(x, y, z, t + \Delta t/2) = E_z(x, y, z, t - \Delta t/2) \\ + \frac{H_y(x + \Delta x/2, y, z, t) - H_y(x - \Delta x/2, y, z, t)}{\epsilon(x, y, z)\Delta x/\Delta t} \\ - \frac{H_x(x, y + \Delta y/2, z, t) - H_x(x, y - \Delta y/2, z, t)}{\epsilon(x, y, z)\Delta y/\Delta t}. \end{aligned}$$

By using the above time stepping method, we are able to calculate the time domain data of electric and magnetic fields .

FDTD method is very efficient for the analysis of light waves in homogeneous medium. However, in the analyses of light waves in heterogeneous medium, staircasing error might occur. Yee grids used to discretize space in FDTD can not fit curved shapes of dielectric materials exactly. Moreover, FDTD analyses include peculiarity caused by direct-spatial discretization of Helmholtz equation derived from Maxwell's equations.

2.5.2 Plane wave expansion method (PWEM)

The plane wave expansion method is widely used to calculate band structures of photonic crystals. In this subsection, we briefly review the formulation and numerical procedure of the method [43, 44].

We consider the E-polarization (TM mode) of Maxwell's equations (2.70) and (2.71). Namely, we assume a state in which the horizontal components of the

electric field (i.e. E_x and E_y) vanish and the vertical component E_z does not depend on z. Then, Maxwell's equations can be reduced to the following scalar wave equation for E_z:

$$\frac{1}{\epsilon(\mathbf{r})}\left(\frac{\partial^2}{\partial x^2}+\frac{\partial^2}{\partial y^2}\right)E_z(\mathbf{r},t)=\frac{1}{c^2}\frac{\partial^2}{\partial t^2}E_z(\mathbf{r},t). \tag{2.77}$$

We assume the electric field is in a state of harmonic oscillation with the angular frequency ω, i.e.,

$$E_z(\mathbf{r},t)=E_0(\mathbf{r})e^{-\mathrm{i}\omega t}. \tag{2.78}$$

Substituting Eq. (2.78) into (2.77), we obtain the following two-dimensional Helmholtz equation:

$$\frac{1}{\epsilon(\mathbf{r})}\nabla^2 E_0(\mathbf{r})+\frac{\omega^2}{c^2}E_0(\mathbf{r})=0. \tag{2.79}$$

Let us find scalar values for ω, called eigenvalues, such that (2.79) holds for non-trivial values of E_0 (eigen functions).

In a photonic crystal, since $\epsilon(\mathbf{r})$ is periodic, we can expand the inverse of $\epsilon(\mathbf{r})$ into the following Fourier series:

$$\frac{1}{\epsilon(\mathbf{r})}=\sum_{\mathbf{G}}\kappa(\mathbf{G})e^{\mathrm{i}\mathbf{G}\cdot\mathbf{r}}, \tag{2.80}$$

where

$$\kappa(\mathbf{G})=\frac{1}{S_0}\int_{S_0}d\mathbf{r}\frac{1}{\epsilon(\mathbf{r})}e^{-\mathrm{i}\mathbf{G}\cdot\mathbf{r}}. \tag{2.81}$$

It is well known, correspondingly to structural periodicity, that the electric field E_0 in (2.79) can be written in the following Bloch form:

$$E_0(\mathbf{r})=u(\mathbf{r})e^{\mathrm{i}\mathbf{k}\cdot\mathbf{r}}, \tag{2.82}$$

where $u(\mathbf{r})$ is a periodic function such that

$$u(\mathbf{r}+\mathbf{a}_i)=u(\mathbf{r})$$

and $\mathbf{k}=(k_x,k_y)$ is a wave vector chosen from the Brillouin zone of the photonic crystal under consideration.

Similarly, we can expand $u(\mathbf{r})$ as follows:

$$u(\mathbf{r})=\sum_{\mathbf{G}}\psi_{\mathbf{G}}e^{\mathrm{i}\mathbf{G}\cdot\mathbf{r}}, \tag{2.83}$$

where $\mathbf{G}$ denotes the reciprocal lattice space spanned by the reciprocal lattice vectors $\mathbf{b}_1$ and $\mathbf{b}_2$ that satisfy $\mathbf{a}_i \cdot \mathbf{b}_j = \delta_{ij}$, where δ_{ij} is Kronecker's delta. The summation over $\mathbf{G}$ is actually replaced with the double summations over integers l_1 and l_2 such as $\mathbf{G} = l_1\mathbf{b}_1 + l_2\mathbf{b}_2$. Also, $\psi_{\mathbf{G}}$ denotes the Fourier coefficients of u corresponding to $\mathbf{G}$ or (l_1, l_2).

Equations (2.80) and (2.83) reduces (2.79) into the form

$$\sum_{\mathbf{G}'} \kappa(\mathbf{G} - \mathbf{G}')|\mathbf{k} + \mathbf{G}'|^2 \psi_{\mathbf{G}'} = \frac{\omega^2}{c^2}\psi_{\mathbf{G}}. \tag{2.84}$$

In order to reduce the matrix in the left-hand side to a Hermite matrix, we introduce a function defined by

$$\xi_{\mathbf{G}} = |\mathbf{k} + \mathbf{G}|\psi_{\mathbf{G}}$$

to Eq. (2.84) to yield the following eigenvalue equation:

$$\sum_{\mathbf{G}'} \kappa(\mathbf{G} - \mathbf{G}') \, |\mathbf{k} + \mathbf{G}| \, |\mathbf{k} + \mathbf{G}'| \, \xi_{\mathbf{G}'} = \frac{\omega^2}{c^2}\xi_{\mathbf{G}}. \tag{2.85}$$

PWEM is very useful for the analysis of light waves in dielectric periodic structures. However, it is difficult to analyze laser action in random systems by PWEM. Additionally, PWEM is based on the Fourier series expansion. Then, the results computed by PWEM include the effect of Gibbs phenomenon.

2.5.3 Boundary element method (BEM)

In this subsection, we present a brief derivation of the boundary integral equation of the Helmholtz equation in the case of TM mode.

2.5.3.1 Exterior problem

The boundary integral equation is derived from the following weighted residual form

$$\int_{\Omega_{\text{out}}} \psi \left[\nabla^2 E(\mathbf{r}) + \frac{\omega^2}{c^2}\epsilon_{\text{out}} E(\mathbf{r}) + f(\mathbf{r}) \right] d\Omega, \tag{2.86}$$

where Ω_{out} is the exterior domain (open region), ϵ_{out} is the relative permittivity of the exterior domain, and ψ is an arbitrary weight function but here it is chosen

as a particular solution called fundamental solution of the Helmholtz equation, as follows:

$$\nabla^2\psi + \frac{\omega^2}{c^2}\epsilon_{\text{out}}\psi = -\delta(\mathbf{r}-\mathbf{r}').$$

For a two-dimensional field, it is obtained as

$$\psi = \frac{1}{4\text{i}}H_0^{(2)}\left(\frac{\omega}{c}\sqrt{\epsilon_{\text{out}}}\,|\mathbf{r}-\mathbf{r}'|\right),$$

where i is the imaginary unit and $H_0^{(2)}$ is the Hankel function of the second kind of order 0.

The integral in Eq. (2.86) in each region is formulated as

$$\begin{aligned}
&\int_{\Omega_{\text{out}}} \psi\left[\nabla^2 E(\mathbf{r}) + \frac{\omega^2}{c^2}\epsilon_{\text{out}}E(\mathbf{r}) + f(\mathbf{r})\right] d\Omega \\
&= \int_{\Omega_{\text{out}}} \left[\psi\nabla^2 E(\mathbf{r}) + \frac{\omega^2}{c^2}\epsilon_{\text{out}}E(\mathbf{r})\psi + \psi f(\mathbf{r})\right] d\Omega \\
&= \int_{\Omega_{\text{out}}} \left\{\nabla\left[\psi\nabla E(\mathbf{r})\right] - \left[\nabla\psi\nabla E(\mathbf{r})\right] + \frac{\omega^2}{c^2}\epsilon_{\text{out}}E(\mathbf{r})\psi + \psi f(\mathbf{r})\right\} d\Omega \\
&= \int_{\Omega_{\text{out}}} \left\{\nabla\left[\psi\nabla E(\mathbf{r})\right] - \nabla\psi\nabla E(\mathbf{r}) + \frac{\omega^2}{c^2}\epsilon_{\text{out}}E(\mathbf{r})\psi + \psi f(\mathbf{r})\right\} d\Omega \\
&= \int_{\Omega_{\text{out}}} \Bigg(\nabla\left[\psi\nabla E(\mathbf{r})\right] - \left\{\nabla[E(\mathbf{r})\nabla\psi] - E(\mathbf{r})\nabla^2\psi\right\} \\
&\qquad\qquad + \frac{\omega^2}{c^2}\epsilon_{\text{out}}E(\mathbf{r})\psi + \psi f(\mathbf{r})\Bigg) d\Omega \\
&= \int_{\Omega_{\text{out}}} \nabla\left[\psi\nabla E(\mathbf{r}) - E(\mathbf{r})\nabla\psi\right] d\Omega \\
&\qquad\qquad + \int_{\Omega_{\text{out}}} E(\mathbf{r})\left[\nabla^2\psi + \frac{\omega^2}{c^2}\epsilon_{\text{out}}\psi + \psi f(\mathbf{r})\right] d\Omega \\
&= \int_{\Gamma} \mathbf{n}\cdot\left[\psi\nabla E(\mathbf{r}) - E(\mathbf{r})\nabla\psi\right] d\Gamma \\
&\qquad\qquad + \int_{\Omega_{\text{out}}} E(\mathbf{r})\left[-\delta(\mathbf{r}-\mathbf{r}')\right] d\Omega + \int_{\Omega_{\text{out}}} \psi f(\mathbf{r})\, d\Omega \\
&= \int_{\Gamma}\left[\frac{\partial E(\mathbf{r})}{\partial n}\psi - \frac{\partial\psi}{\partial n}E(\mathbf{r})\right] d\Gamma - C_i E(\mathbf{r}') + \int_{\Omega_{\text{out}}} \psi f(\mathbf{r})\, d\Omega
\end{aligned}$$

where Γ denotes the boundary and C_i is a constant depending on the location of source point $\mathbf{r}'$ as

$$C_i = \begin{cases} 1 & \mathbf{r}' \in \Omega_{\text{out}} \\ 1/2 & \mathbf{r}' \in \Gamma_i \\ 0 & \mathbf{r}' \notin \Omega_{\text{out}}, \Gamma_i \end{cases}. \tag{2.87}$$

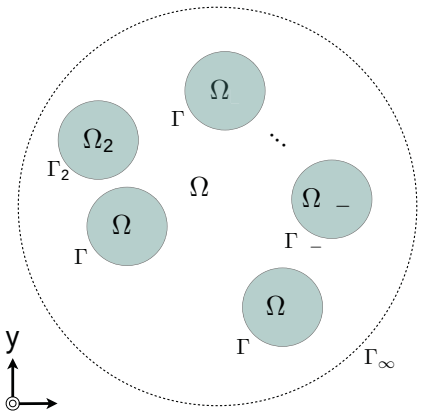

Figure 2.25: Region.

The boundary integral equation for the Helmholtz equation finally becomes as

$$C_i E(\mathbf{r}') + \int_\Gamma \left[\frac{\partial \psi}{\partial n} E(\mathbf{r}) - \frac{\partial E(\mathbf{r})}{\partial n} \psi \right] d\Gamma - \int_{\Omega_{\text{out}}} \psi f(\mathbf{r})\, d\Omega = 0.$$

Boundary element method can simulate open region problem exactly. The number of unknown quantities in boundary element analysis is much smaller than those in other numerical methods. However, we have to solve linear equations with density matrices in boundary element analysis. Some numerical approaches are proposed in order to reduce computational cost as fast multipole method and wavelet BEM. But they are difficult and complex.

2.6 Finite element method (FEM)

Finite element method is one of the most powerful numerical methods for electromagnetic analyses. Let $\psi(\mathbf{r})$ be an approximate solution of the Helmholtz equation derived from Maxwell's equations, then it satisfies

$$\nabla^2\psi(\mathbf{r}) + \frac{\omega^2}{c^2}\epsilon(\mathbf{r})\psi(\mathbf{r}) + f(\mathbf{r}) = R_\Omega,$$

where R_Ω is error originated from the approximate solution $\psi(\mathbf{r})$. A weak form is derived from the weighted residual form making an integral of the weighted error R_Ω for the whole domain Ω zero, as

$$\int_\Omega W\left[\nabla^2\psi(\mathbf{r}) + \frac{\omega^2}{c^2}\epsilon(\mathbf{r})\psi(\mathbf{r}) + f(\mathbf{r})\right] d\Omega = 0. \tag{2.88}$$

Integrating the left-hand side of Eq. (2.88) once yield the following weak form:

$$\int_\Omega \left\{\nabla W\cdot\nabla\psi(\mathbf{r}) - \frac{\omega^2}{c^2}\epsilon(\mathbf{r})\psi(\mathbf{r})W - Wf(\mathbf{r})\right\} d\Omega = \int_\Gamma W\frac{\partial\psi(\mathbf{r})}{\partial n}\, d\Gamma. \tag{2.89}$$

In order to evaluate the domain and boundary integrals of Eq. (2.89), we divide them into simple geometries, called elements, and the integrals are evaluated as sums of the integrals for these elements, as

$$\sum_e \int_{\Omega_e} \left\{\nabla W\cdot\nabla\psi(\mathbf{r}) - \frac{\omega^2}{c^2}\epsilon_e\psi(\mathbf{r})W - Wf(\mathbf{r})\right\} d\Omega = \sum_l \int_{\Gamma_l} W\frac{\partial\psi(\mathbf{r})}{\partial n}\, d\Gamma. \tag{2.90}$$

Then, the solution $\psi(\mathbf{r})$ is assumed to be approximated as a linear combination of basis functions called shape functions and ψ_i the values of ψ at discrete points defining the element shapes, as follows:

$$\psi(\mathbf{r}) = \sum_{j=1}^{n} N_j\psi_j. \tag{2.91}$$

We now choose one of the basis functions, N_i, as the weight of the weak form. Using $W = N_i$ and Eq.(2.91) in Eq.(2.90) gives

$$\sum_j\sum_e\left(\int_{\Omega_e}\nabla N_i\cdot\nabla N_j\, d\Omega\right)\psi_j - \left(\frac{\omega^2}{c^2}\right)\sum_j\sum_e\left(\int_{\Omega_e}\epsilon(\mathbf{r})N_iN_j\, d\Omega\right)\psi_j - \sum_j\sum_e\int_{\Omega_e} N_if(\mathbf{r})\, d\Omega = \sum_l\int_{\Gamma_l} N_i\frac{\partial\psi(\mathbf{r})}{\partial n}\, d\Gamma. \tag{2.92}$$

After evaluating the domain and boundary integrals in some way, analytically or numerically, we obtain a system of linear algebraic equations in the form

$$[K]\{\psi\} - \left(\frac{\omega^2}{c^2}\right)[M]\{\psi\} = \{f\}.$$

Finite element method is one of the most powerful method for the analysis of light waves in heterogeneous random systems. The matrices in linear equations solved in finite element analysis becomes sparse and such a linear equations can be solved very fast by using multi-frontal method and iterative methods. Finite element meshing can discretize analytical domains exactly and well-fit to boundaries between two different dielectric materials. Then, staircasing errors never occurs in finite element analysis. Finite element method can analyze the behavior of light waves in unperiodic structures.

We use finite element method to analyze lasing phenomena in disordered structures with the above reasons.

2.6.1 Weak form

The differential equation that should be solve for analysys region is shown as follows:

$$\frac{1}{\gamma_x}\frac{1}{\partial x}\left(\frac{1}{\gamma_x}\frac{\partial E_z}{\partial x}\right) + \frac{1}{\gamma_y}\frac{1}{\partial y}\left(\frac{1}{\gamma_y}\frac{\partial E_z}{\partial y}\right) + \frac{\omega^2}{c^2}\epsilon(\mathbf{x})E_z = 0,$$

where E_z is the electric field without time dependency, γ_x and γ_y satisfy

$$\gamma_x = \begin{cases} 1 & (|x| < a) \\ 1 + \frac{i}{\omega}\sigma_x(|x|) & (a \le |x| < a^* : \mathrm{PML}) \end{cases},$$

$$\gamma_y = \begin{cases} 1 & (|y| < b) \\ 1 + \frac{i}{\omega}\sigma_y(|y|) & (b \le |y| < b^* : \mathrm{PML}) \end{cases},$$

then, the absorbing functions $\sigma_x(x)$ and $\sigma_y(y)$ are defined as

$$\sigma_x(x) = \frac{c}{a^* - x}, \quad \sigma_y(y) = \frac{c}{b^* - y}.$$

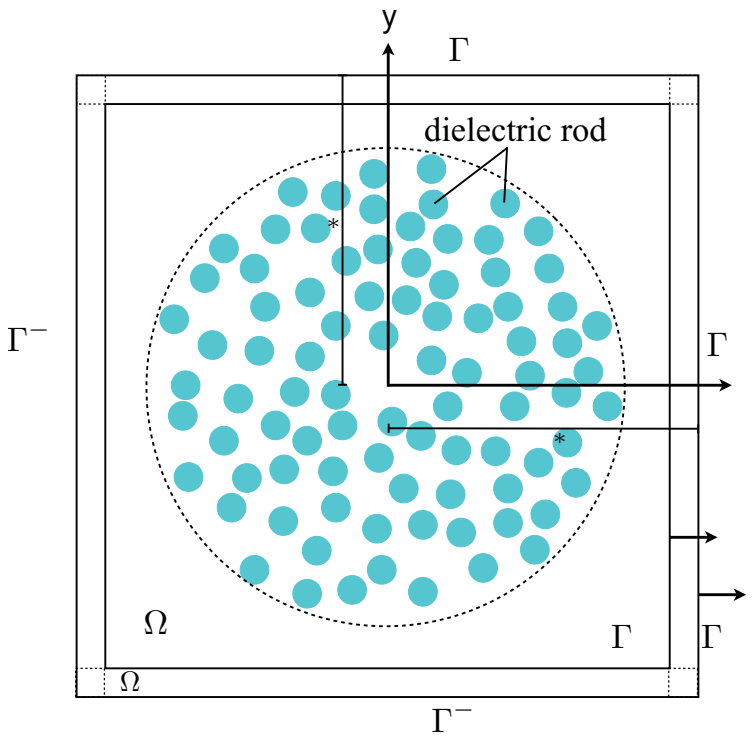

Figure 2.26: Concept of an analytical region .

The equation is rewritten by multiplying both sides of the equation by $\gamma_x\gamma_y$ as

$$\begin{aligned}
&\gamma_y \frac{1}{\partial x}\left(\frac{1}{\gamma_x}\frac{\partial E_z}{\partial x}\right) + \gamma_x \frac{1}{\partial y}\left(\frac{1}{\gamma_y}\frac{\partial E_z}{\partial y}\right) + \frac{\omega^2}{c^2}\epsilon(\mathbf{x})\gamma_x\gamma_y E_z \\
&= \frac{1}{\partial x}\left(\frac{\gamma_y}{\gamma_x}\frac{\partial E_z}{\partial x}\right) + \frac{1}{\partial y}\left(\frac{\gamma_x}{\gamma_y}\frac{\partial E_z}{\partial y}\right) + \frac{\omega^2}{c^2}\epsilon(\mathbf{x})\gamma_x\gamma_y E_z \\
&= 0.
\end{aligned}$$

Based on wighted residual method, integral equation is derived as

$$\begin{aligned}
&\int_\Omega \left\{\frac{1}{\partial x}\left(\frac{\gamma_y}{\gamma_x}\frac{\partial E_z}{\partial x}\right) + \frac{1}{\partial y}\left(\frac{\gamma_x}{\gamma_y}\frac{\partial E_z}{\partial y}\right) + \frac{\omega^2}{c^2}\epsilon(\mathbf{x})\gamma_x\gamma_y E_z\right\} W d\Omega \\
&= \int_\Omega \left\{\frac{1}{\partial x}\left(\frac{\gamma_y}{\gamma_x}\frac{\partial E_z}{\partial x}\right) W + \frac{1}{\partial y}\left(\frac{\gamma_x}{\gamma_y}\frac{\partial E_z}{\partial y}\right) W + \frac{\omega^2}{c^2}\epsilon(\mathbf{x})\gamma_x\gamma_y E_z W\right\} d\Omega \\
&= 0, \qquad (2.93)
\end{aligned}$$

where W is weight function and Ω is the analysis region including PML. The first

and second terms in the integrand of Eq. (2.93) are modified as

$$\frac{1}{\partial x}\left(\frac{\gamma_y}{\gamma_x}\frac{\partial E_z}{\partial x}\right)W = \frac{1}{\partial x}\left(\frac{\gamma_y}{\gamma_x}\frac{\partial E_z}{\partial x}W\right) - \frac{\gamma_y}{\gamma_x}\frac{\partial E_z}{\partial x}\frac{\partial W}{\partial x},$$

$$\frac{1}{\partial y}\left(\frac{\gamma_x}{\gamma_y}\frac{\partial E_z}{\partial y}\right)W = \frac{1}{\partial y}\left(\frac{\gamma_x}{\gamma_y}\frac{\partial E_z}{\partial y}W\right) - \frac{\gamma_x}{\gamma_y}\frac{\partial E_z}{\partial y}\frac{\partial W}{\partial y},$$

Then, Eq. (2.93) becomes as

$$\begin{aligned}
&\int_\Omega \left\{\frac{1}{\partial x}\left(\frac{\gamma_y}{\gamma_x}\frac{\partial E_z}{\partial x}\right)W + \frac{1}{\partial y}\left(\frac{\gamma_x}{\gamma_y}\frac{\partial E_z}{\partial y}\right)W + \frac{\omega^2}{c^2}\epsilon(\mathbf{x})\gamma_x\gamma_y E_z W\right\} d\Omega \\
&\quad = \int_\Omega \left\{\frac{1}{\partial x}\left(\frac{\gamma_y}{\gamma_x}\frac{\partial E_z}{\partial x}W\right) + \frac{1}{\partial y}\left(\frac{\gamma_x}{\gamma_y}\frac{\partial E_z}{\partial y}W\right) + \frac{\omega^2}{c^2}\epsilon(\mathbf{x})\gamma_x\gamma_y E_z W\right\} d\Omega \\
&\qquad + \int_\Omega \left\{-\frac{\gamma_y}{\gamma_x}\frac{\partial E_z}{\partial x}\frac{\partial W}{\partial x} - \frac{\gamma_x}{\gamma_y}\frac{\partial E_z}{\partial y}\frac{\partial W}{\partial y}\right\} d\Omega \\
&\quad = 0.
\end{aligned} \tag{2.94}$$

We classify the analysis region into two parts: a region in which light waves scatter, and PML region. Then, Eq.(2.94) is modified as

$$\begin{aligned}
&\int_\Omega \left\{\frac{1}{\partial x}\left(\frac{\gamma_y}{\gamma_x}\frac{\partial E_z}{\partial x}W\right) + \frac{1}{\partial y}\left(\frac{\gamma_x}{\gamma_y}\frac{\partial E_z}{\partial y}W\right) + \frac{\omega^2}{c^2}\epsilon(\mathbf{x})\gamma_x\gamma_y E_z W\right\} d\Omega \\
&\qquad + \int_\Omega \left\{-\frac{\gamma_y}{\gamma_x}\frac{\partial E_z}{\partial x}\frac{\partial W}{\partial x} - \frac{\gamma_x}{\gamma_y}\frac{\partial E_z}{\partial y}\frac{\partial W}{\partial y}\right\} d\Omega \\
&\quad = \int_{\Omega_{\text{scattering}}+\Omega_{\text{PML}}} \left\{\frac{1}{\partial x}\left(\frac{\gamma_y}{\gamma_x}\frac{\partial E_z}{\partial x}W\right) + \frac{1}{\partial y}\left(\frac{\gamma_x}{\gamma_y}\frac{\partial E_z}{\partial y}W\right)\right. \\
&\qquad\qquad \left. + \frac{\omega^2}{c^2}\epsilon(\mathbf{x})\gamma_x\gamma_y E_z W\right\} d\Omega \\
&\qquad + \int_{\Omega_{\text{scattering}}+\Omega_{\text{PML}}} \left\{-\frac{\gamma_y}{\gamma_x}\frac{\partial E_z}{\partial x}\frac{\partial W}{\partial x} - \frac{\gamma_x}{\gamma_y}\frac{\partial E_z}{\partial y}\frac{\partial W}{\partial y}\right\} d\Omega \\
&\quad = \int_{\Omega_{\text{scattering}}} \left\{\frac{1}{\partial x}\left(\frac{\gamma_y}{\gamma_x}\frac{\partial E_z}{\partial x}W\right) + \frac{1}{\partial y}\left(\frac{\gamma_x}{\gamma_y}\frac{\partial E_z}{\partial y}W\right) + \frac{\omega^2}{c^2}\epsilon(\mathbf{x})\gamma_x\gamma_y E_z W\right\} d\Omega \\
&\qquad + \int_{\Omega_{\text{scattering}}} \left\{-\frac{\gamma_y}{\gamma_x}\frac{\partial E_z}{\partial x}\frac{\partial W}{\partial x} - \frac{\gamma_x}{\gamma_y}\frac{\partial E_z}{\partial y}\frac{\partial W}{\partial y}\right\} d\Omega \\
&\qquad + \int_{\Omega_{\text{PML}}} \left\{\frac{1}{\partial x}\left(\frac{\gamma_y}{\gamma_x}\frac{\partial E_z}{\partial x}W\right) + \frac{1}{\partial y}\left(\frac{\gamma_x}{\gamma_y}\frac{\partial E_z}{\partial y}W\right) + \frac{\omega^2}{c^2}\epsilon(\mathbf{x})\gamma_x\gamma_y E_z W\right\} d\Omega \\
&\qquad + \int_{\Omega_{\text{PML}}} \left\{-\frac{\gamma_y}{\gamma_x}\frac{\partial E_z}{\partial x}\frac{\partial W}{\partial x} - \frac{\gamma_x}{\gamma_y}\frac{\partial E_z}{\partial y}\frac{\partial W}{\partial y}\right\} d\Omega
\end{aligned}$$

$$
\begin{aligned}
&= \int_{\Omega_{\text{scattering}}} \left\{ \nabla \cdot (\nabla E_z W) - \nabla E_z \cdot \nabla W + \frac{\omega^2}{c^2} \epsilon(\mathbf{x}) E_z W \right\} d\Omega \\
&\quad + \int_{\Omega_{\text{PML}}} \left\{ \frac{1}{\partial x} \left(\frac{\gamma_y}{\gamma_x} \frac{\partial E_z}{\partial x} W \right) + \frac{1}{\partial y} \left(\frac{\gamma_x}{\gamma_y} \frac{\partial E_z}{\partial y} W \right) + \frac{\omega^2}{c^2} \epsilon(\mathbf{x}) \gamma_x \gamma_y E_z W \right\} d\Omega \\
&\quad + \int_{\Omega_{\text{PML}}} \left\{ -\frac{\gamma_y}{\gamma_x} \frac{\partial E_z}{\partial x} \frac{\partial W}{\partial x} - \frac{\gamma_x}{\gamma_y} \frac{\partial E_z}{\partial y} \frac{\partial W}{\partial y} \right\} d\Omega \\
&= \int_{\Gamma_{\text{in}}} (\nabla E_z \cdot \mathbf{n}_{\Gamma\text{in}}) \, W d\Gamma + \int_{\Omega_{\text{scattering}}} \left\{ -\nabla E_z \cdot \nabla W + \frac{\omega^2}{c^2} \epsilon(\mathbf{x}) E_z W \right\} d\Omega \\
&\quad + \int_{\Gamma_{\text{out}}} \left\{ \left(\frac{\gamma_y}{\gamma_x} \frac{\partial E_z}{\partial x} W \right) n_x^{\Gamma\text{out}} + \left(\frac{\gamma_x}{\gamma_y} \frac{\partial E_z}{\partial y} W \right) n_y^{\Gamma\text{out}} \right\} d\Gamma \\
&\quad + \int_{\Gamma_{\text{in}}} \left\{ \left(\frac{\gamma_y}{\gamma_x} \frac{\partial E_z}{\partial x} W \right) (-n_x^{\Gamma\text{in}}) + \left(\frac{\gamma_x}{\gamma_y} \frac{\partial E_z}{\partial y} W \right) (-n_y^{\Gamma\text{in}}) \right\} d\Gamma \\
&\quad + \int_{\Omega_{\text{PML}}} \left\{ -\frac{\gamma_y}{\gamma_x} \frac{\partial E_z}{\partial x} \frac{\partial W}{\partial x} - \frac{\gamma_x}{\gamma_y} \frac{\partial E_z}{\partial y} \frac{\partial W}{\partial y} + \frac{\omega^2}{c^2} \epsilon(\mathbf{x}) \gamma_x \gamma_y E_z W \right\} d\Omega, \\
&= 0,
\end{aligned} \tag{2.95}
$$

where Γ_{in} is the boundary between $\Omega_{\text{scattering}}$ and Ω_{PML}, Γ_{out} is the outer boundary of Ω_{PML}, $\mathbf{n}_{\Gamma\text{in}} = (n_x^{\Gamma\text{in}}, n_y^{\Gamma\text{in}})$ and $\mathbf{n}_{\Gamma\text{out}} = (n_x^{\Gamma\text{out}}, n_y^{\Gamma\text{out}})$ are unit outward normal vectors to the boundaries Γ_{in} and Γ_{out}, respectively.

Because the absorbing coefficients γ_x and γ_y are continuous across the boundary between the scattering region and PML region and $\gamma_x = \gamma_y = 1$ in the scattering region, $\gamma_x/\gamma_y = \gamma_y/\gamma_x = 1$ on Γ_{in}. Therefore, we find the boundary integrals for Γ_{in} in Eq. (2.95) vanish, as

$$
\begin{aligned}
&\int_{\Gamma_{\text{in}}} (\nabla E_z \cdot \mathbf{n}_{\Gamma\text{in}}) \, W d\Gamma + \int_{\Gamma_{\text{in}}} \left\{ \left(\frac{\gamma_y}{\gamma_x} \frac{\partial E_z}{\partial x} W \right) (-n_x^{\Gamma\text{in}}) + \left(\frac{\gamma_x}{\gamma_y} \frac{\partial E_z}{\partial y} W \right) (-n_y^{\Gamma\text{in}}) \right\} d\Gamma \\
&\quad = \int_{\Gamma_{\text{in}}} (\nabla E_z \cdot \mathbf{n}_{\Gamma\text{in}}) \, W d\Gamma - \int_{\Gamma_{\text{in}}} \left\{ \left(\frac{\partial E_z}{\partial x} W \right) n_x^{\Gamma\text{in}} + \left(\frac{\partial E_z}{\partial y} W \right) n_y^{\Gamma\text{in}} \right\} d\Gamma \\
&\quad = 0
\end{aligned} \tag{2.96}
$$

Using Eq. (2.96), we have the following weak form:

$$
\begin{aligned}
&\int_{\Gamma_{\text{out}}} \left\{ \left(\frac{\gamma_y}{\gamma_x} \frac{\partial E_z}{\partial x} W \right) n_x^{\Gamma\text{out}} + \left(\frac{\gamma_x}{\gamma_y} \frac{\partial E_z}{\partial y} W \right) n_y^{\Gamma\text{out}} \right\} d\Gamma \\
&\qquad + \int_{\Omega_{\text{scattering}}} \left\{ -\nabla E_z \cdot \nabla W + \frac{\omega^2}{c^2} \epsilon(\mathbf{x}) E_z W \right\} d\Omega \\
&\qquad + \int_{\Omega_{\text{PML}}} \left\{ -\frac{\gamma_y}{\gamma_x} \frac{\partial E_z}{\partial x} \frac{\partial W}{\partial x} - \frac{\gamma_x}{\gamma_y} \frac{\partial E_z}{\partial y} \frac{\partial W}{\partial y} + \frac{\omega^2}{c^2} \epsilon(\mathbf{x}) \gamma_x \gamma_y E_z W \right\} d\Omega \\
&\quad = 0
\end{aligned} \tag{2.97}
$$

The boundary $\Gamma_{\rm out}$ is divided into four parts, $\Gamma^x_{\rm out}$, $\Gamma^y_{\rm out}$, $\Gamma^{-x}_{\rm out}$, and $\Gamma^{-y}_{\rm out}$ as shown in Fig. 2.26. On these boundaries, x and y becomes as follows:

$$\begin{aligned} x &= a^* \quad \text{on } \Gamma^x_{\rm out}, \\ y &= b^* \quad \text{on } \Gamma^x_{\rm out}, \\ x &= -a^* \quad \text{on } \Gamma^{-x}_{\rm out}, \\ y &= -b^* \quad \text{on } \Gamma^{-y}_{\rm out}. \end{aligned}$$

Also, the outward normal vector $\mathbf{n}_{\mathbf{\Gamma}_{\rm out}}$ and the absorbing coefficients $\frac{\gamma_y}{\gamma_x}$ and $\frac{\gamma_y}{\gamma_x}$ become as

$$\mathbf{n}_{\mathbf{\Gamma}_{\rm out}} = (n_x^{\Gamma{\rm out}}, n_y^{\Gamma{\rm out}}) = \begin{cases} (1,0) & \text{on } \Gamma^x_{\rm out} \\ (0,1) & \text{on } \Gamma^y_{\rm out} \\ (-1,0) & \text{on } \Gamma^{-x}_{\rm out} \\ (0,-1) & \text{on } \Gamma^{-y}_{\rm out} \end{cases},$$

and

$$\begin{aligned} \frac{\gamma_y}{\gamma_x} &= \left.\frac{\omega(a^*-x)\left[\omega(b^*-y)+{\rm i}c\right]}{\omega(b^*-y)\left[\omega(a^*-x)+{\rm i}c\right]}\right|_{x=a^*} = 0 \qquad \text{on } \Gamma^x_{\rm out} \text{ and } \Gamma^{-x}_{\rm out}, \\ \frac{\gamma_x}{\gamma_y} &= \left.\frac{\omega(b^*-y)\left[\omega(a^*-x)+{\rm i}c\right]}{\omega(a^*-x)\left[\omega(b^*-y)+{\rm i}c\right]}\right|_{y=b^*} = 0 \qquad \text{on } \Gamma^y_{\rm out} \text{ and } \Gamma^{-y}_{\rm out}. \end{aligned}$$

Using these relationships, the first term of Eq. (2.97) becomes as follows:

$$\begin{aligned} &\int_{\Gamma_{\rm out}} \left\{ \left(\frac{\gamma_y}{\gamma_x} \frac{\partial E_z}{\partial x} W \right) n_x^{\Gamma{\rm out}} + \left(\frac{\gamma_x}{\gamma_y} \frac{\partial E_z}{\partial y} W \right) n_y^{\Gamma{\rm out}} \right\} d\Gamma \\ &\quad = \int_{\Gamma^x_{\rm out}} \left\{ \left(0 \frac{\partial E_z}{\partial x} W \right) 1 + \left(\frac{\gamma_x}{\gamma_y} \frac{\partial E_z}{\partial y} W \right) 0 \right\} d\Gamma \\ &\qquad + \int_{\Gamma^y_{\rm out}} \left\{ \left(\frac{\gamma_y}{\gamma_x} \frac{\partial E_z}{\partial x} W \right) 0 + \left(0 \frac{\partial E_z}{\partial y} W \right) 1 \right\} d\Gamma \\ &\qquad + \int_{\Gamma^{-x}_{\rm out}} \left\{ \left(0 \frac{\partial E_z}{\partial x} W \right) (-1) + \left(\frac{\gamma_x}{\gamma_y} \frac{\partial E_z}{\partial y} W \right) 0 \right\} d\Gamma \\ &\qquad + \int_{\Gamma^{-y}_{\rm out}} \left\{ \left(\frac{\gamma_y}{\gamma_x} \frac{\partial E_z}{\partial x} W \right) 0 + \left(0 \frac{\partial E_z}{\partial y} W \right) (-1) \right\} d\Gamma \\ &\quad = 0. \end{aligned} \tag{2.98}$$

Therefore, the weak form including PML boundary condition finally becomes

as follows:

$$\begin{aligned}\int_{\Omega_{\text{scattering}}} &\left\{\nabla E_z \cdot \nabla W - \frac{\omega^2}{c^2}\epsilon(\mathbf{x}) E_z W\right\} d\Omega \\ &+ \int_{\Omega_{\text{PML}}} \left\{\frac{\gamma_y}{\gamma_x}\frac{\partial E_z}{\partial x}\frac{\partial W}{\partial x} + \frac{\gamma_x}{\gamma_y}\frac{\partial E_z}{\partial y}\frac{\partial W}{\partial y} - \frac{\omega^2}{c^2}\epsilon(\mathbf{x})\gamma_x\gamma_y E_z W\right\} d\Omega \\ &= 0.\end{aligned}$$

CHAPTER 3

Random lasing in disordered structures consisting of optically active cylinders

3.1 Introduction

Random lasers can be caused by light localizations in disordered structures, caused by multiple scattering and interferences of scattered light waves. Light localizations are expected to work as feedback mechanisms. When light waves localized in optically active materials, light waves are amplified repeatedly, and such repeated amplification of light waves lead to laser actions. Hence, it is important to localize light waves in optically active materials to oscillate laser actions. The properties of laser actions are strongly depend on the location of light localization and optically active materials.

In this section, we present simulations of laser actions in two-dimensional random systems by using FEM. We compare laser actions in two different random systems: optically active materials among nonactive rods, and optically active rods in nonactive media. Electric amplitude distributions and radiative directions are also investigated to comprehend the properties of random laser actions. Thresholds of laser actions in two different random systems are also investigated.

3.2 Analysis models

Fig.3.1(a) shows a top view of two-dimensional disordered structure analyzed in this chapter. The disordered structure consist of dielectric rods assumed to be infinitely long in z-direction (longitudinal direction). We arrange the rods of homogeneous dielectric material randomly, whose radii of cross sections are a, in a circular domain whose radius is $40a$. The number of the rods is 480 and the filling factor of the rods in the circular domain is 30%, and the width of the domain surrounded by PML is $88a$.

Analysis models are created by the following procedure. First, the cross section radius of the rod is chosen as the characteristic length. The normalized radii of the rods then become 1, and the origin of the coordinates are assumed to be at the center of the square domain.

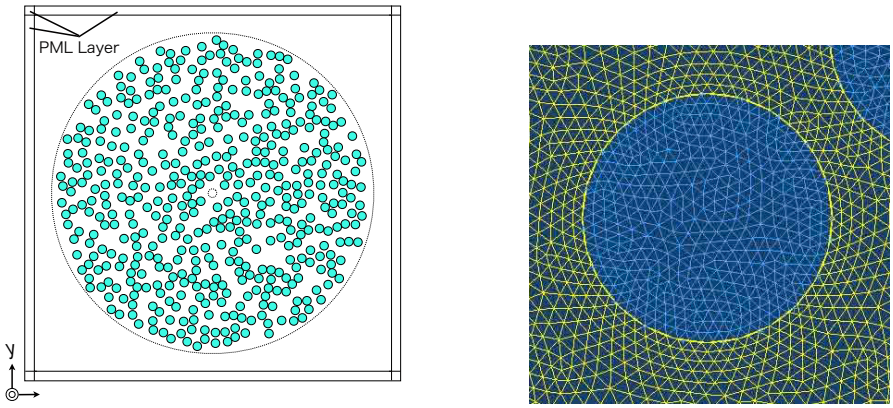

(a) 2D disordered dielectric system. (b) Dielectric rod divided by meshes.

Figure 3.1: Analysis model.

The positions of ith rods, (x_i, y_i), are determined as, $(x_i, y_i) = (80R_1 - 40, 80R_2 - 40)$, where R_1 and R_2 are random numbers in the range [0,1] produced by using drand function implemented in Fortran90. If ith rod overlaps with other rods numbered from 1 to $i-1$, or if the ith rod is not included at all within the circler region whose radius is $40a$, we try to generate the position of ith rod again with another random number.

We show an obtained finite element model in the neighborhood of a rod in 3.1(b). The average element size is approximately $a/10$, and in the smallest case, $\lambda/18$ where λ denotes the wavelength. We discretize the regions close to the circles

C_{in} and C_{out} with finer mesh whose element size is approximately $a/30$, and $\lambda/54$ in the smallest case to improve the computational accuracy of the amplification factor defined in Eq. (2.60). The amplification factor requires the conjugate magnetic field $\mathbf{H}^*$ calculated with $\nabla \times \mathbf{E}^*$ based on Maxwell's equations. The rotation of the electric field $\nabla \times \mathbf{E}$ are computed by partial differentiations of the basis functions in elements which are close to the circles C_{in} and C_{out}. The partial differentiations reduce the computational accuracy of the amplification factor. The analysis model analyzed in this chapter has 833130 nodal points and 1661658 elements.

3.2.1 Optically active materials

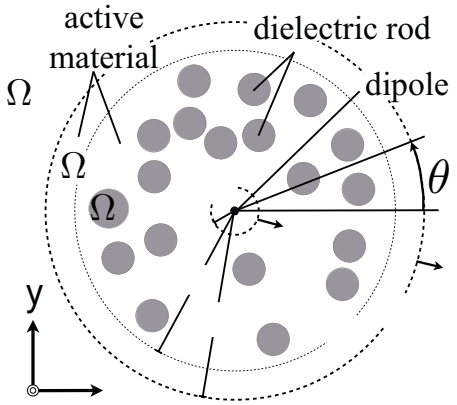

Figure 3.2: An concept of entire random system.

For a random system consisting of optically active rods in nonactive media, $-\gamma$ are given to dielectric constants of rods as,

$$\epsilon(\mathbf{x}) = \begin{cases} 1.0 & \mathbf{x} \in \Omega_{\text{act}} \\ 4.0 + \mathrm{i}(-\gamma) & \mathbf{x} \in \Omega_{\text{rod}} \\ 1.0 & \mathbf{x} \in \Omega_{\text{out}} \end{cases} . \tag{3.1}$$

3.3 Results

Simulated results are shown in this subsection. We assume a oscillating dipole as a light source located at the center of the random system $(x_0, y_0) = (0, 0)$. We compute the amplification factor for the ranges of $0.21 \leq \omega a/2\pi c \leq 0.27$ and $0 \leq \gamma \leq 0.03$. Above range of normalized frequency $\omega a/2\pi c$ corresponds to the

wavelength range 481 [nm] $\leq \lambda \leq$ 619 [nm], and the radius of the whole random system is $40a = 5.2$ [μm] when the radii of cross-subsection of dielectric rods are $a = 130$ [nm].

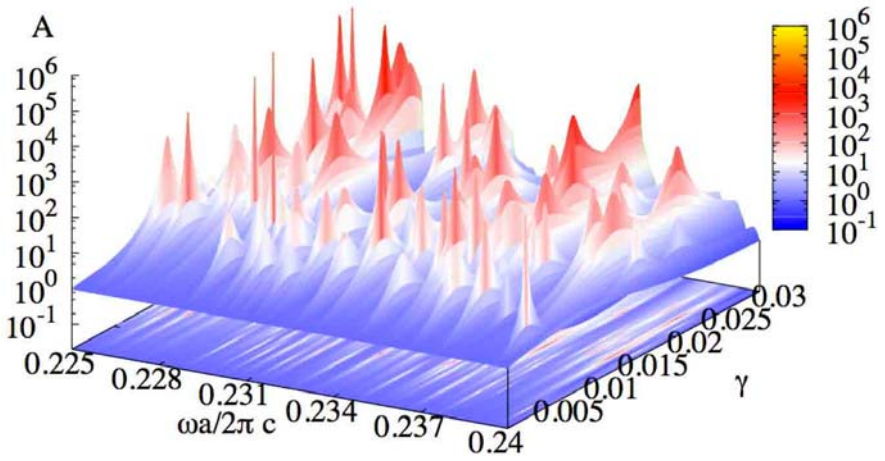

Figure 3.3: Amplification factor in the case of giving γ in rods.

We classify the types of laser mode by using the distribution of the number of nodes on the electric amplitude. First, we count the numbers of nodes whose electric amplitudes are included in each range determined by dividing the difference between maximum and minimum absolute values of nodal values to 50 parts. Next, we plot the number of nodes as a function of the electric amplitude. We classify a laser mode as a localized one when the number of node reduce decrease monotonically as the electric amplitude increases, and classify it as a extended one when the change of the number of node has a peak.

We simulate laser actions in a disordered structure consisting of optically active rods in non-active media. In these numerical simulations, we give a negative value $-\gamma$ to the imaginary part to the relative permittivity in the rod region $\Omega_{\rm rod}$ in Fig. 3.2. We assume homogeneous excitations of optically active rods, namely constant γ, also in this analysis.

Figure 3.3 shows the result of laser actions in a disordered structure assumed to comprise optically active rods. The amplification factors are plotted with a log-scale. The numbers of computation points are 501 and 201 for $0.225 \leq \omega a/2\pi c \leq 0.240$ and $0.0 \leq \gamma \leq 0.03$. There are some round peaks. The number of round peaks increase for $0.24 < \omega a/2\pi c$.

Figure 3.4 shows the electric amplitudes and radiative angular distributions

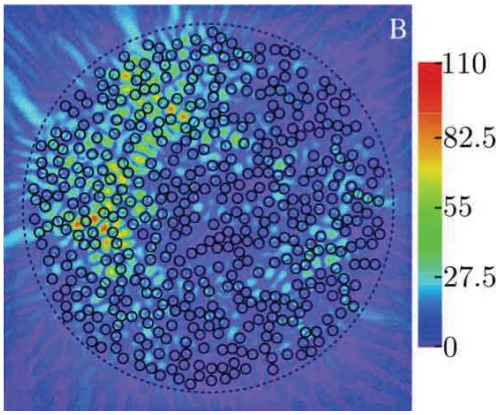

(a) Electric intensity distribution ($\omega a/2\pi c = 0.22689, \gamma = 0.02685$).

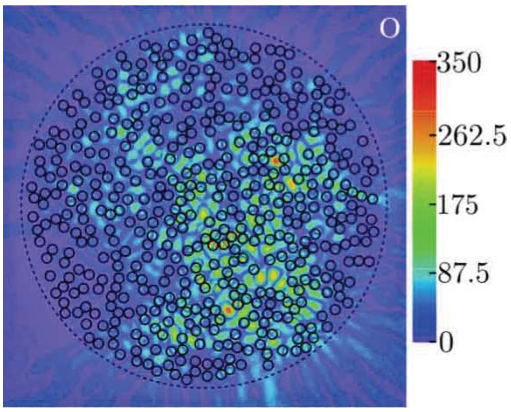

(b) Electric intensity distribution ($\omega a/2\pi c = 0.22872, \gamma = 0.01110$).

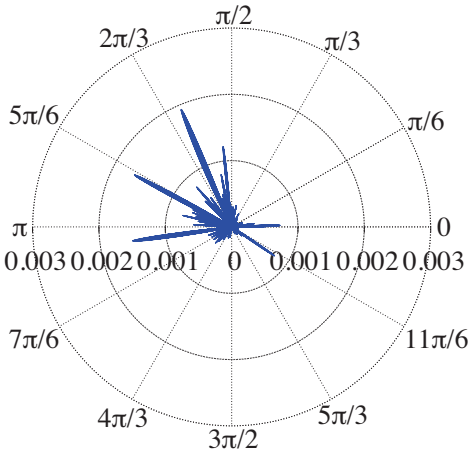

(c) Radiation direction ($\omega a/2\pi c = 0.22689, \gamma = 0.02685$).

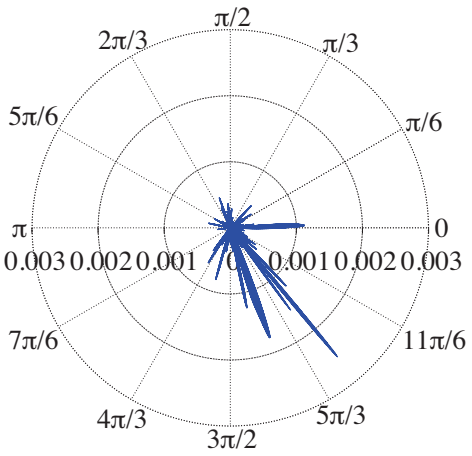

(d) Radiation direction ($\omega a/2\pi c = 0.22872, \gamma = 0.01110$).

Figure 3.4: Electric intensity distributions and radiative directions of extended modes.

of extended laser modes, and Fig. 3.5 shows those of localized ones.

We show two results for electric amplitude distributions and radiative angular distribution of extended modes in Fig. 3.5. The results for electric amplitude normalized by the maximum amplitude of the dipole radiation are plotted in color maps in 3.5(a). The result for the angular distribution of radiations shown in 3.5(b) is plotted in polar coordinates. The angular coordinate corresponds to the radiative angle θ defined in Fig. 3.2, and the radial coordinate to $\delta\langle\mathbf{S}\rangle$, defined as follows:

$$\delta\langle\mathbf{S}\rangle = \frac{\int_{C_\theta}\langle\mathbf{S}\rangle\cdot\mathbf{n}\ dl|_{\gamma>0}}{\int_{\mathrm{C_{out}}}\langle\mathbf{S}\rangle\cdot\mathbf{n}\ dl\ |_{\gamma>0}}. \tag{3.2}$$

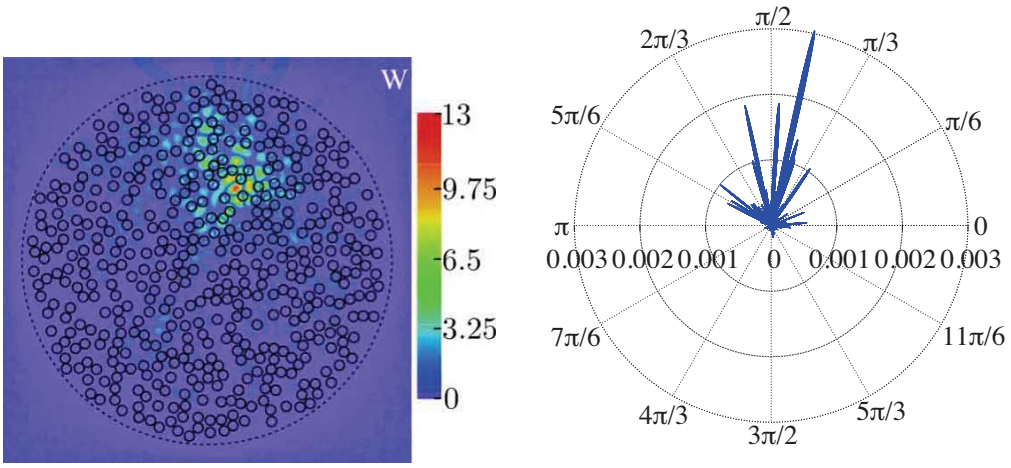

(a) Electric intensity distribution ($\omega a/2\pi c = 0.22968, \gamma = 0.006150$).

(b) Radiation direction ($\omega a/2\pi c = 0.22968, \gamma = 0.006150$).

Figure 3.5: Electric intensity distribution and radiative direction of a localized mode.

The denominator of $\delta\langle \mathbf{S} \rangle$ is a line integral of the normal component of Poynting vector along the circle C_{out} and the numerator is one along C_θ that is one of the edges of the elements in θ direction coinciding with C_{out}. In this example, C_{out} is uniformly divided into segments and C_θ equals $80\pi a/8667$.

Although electric amplitudes may be expected to become high within rods because the rods are optically active, light waves are localized actually in the interspaces among the active rods as shown in Figs. 3.4(a), 3.4(b). In view of the electric amplitude distributions, light waves may leak into active rods and be amplified by excited active rods. Such a characteristic of light localizations is commonly observed in the results of lasing phenomena in five random systems with different rod arrangements.

3.3.1 Lasing threshold

We investigate lasing threshold, namely, minimum γ at which sharp peaks of amplification factors are observed. The average, minimum, maximum of minimum γ in five samples are shown in Table 3.1.

Table 3.1: Average, minimum, and maximum values of minimum γ.

Average	Minimum	Maximum
0.004560	0.003300	0.005700

3.4 Conclusion

In this chapter, laser actions in a disordered structure consisting of active rods in non-active media, are simulated numerically. The amplification factors are computed by using FEM with changing frequency and the parameter γ expressing the degree of excitation of optically active materials. Random systems consisting of active rods are not appropriate for lower threshold laser action because light waves are localized in interspaces among active rods.

CHAPTER 4

Random lasing in disordered structures with optically active materials in interspace among dielectric cylinders

4.1 Introduction

This chapter shows laser action and the threshold of random laser in random systems with optically active materials in interspace among dielectric cylinders. The objective of this chapter is showing the threshold of laser action in random systems with active gain in interspaces among dielectric cylinders by investigating the properties of random lasing.

In section 4.2, we simulate random lasing in the random systems and investigate lasing threshold to compare lasing threshold in the random systems consisting of optically active cylinders in chapter 3. We compare lasing threshold of random lasers in random systems with active gain in interspaces among dielectric cylinders with that of random lasers consisting of optically active cylinders shown in chapter 3.

In section 4.3, we investigate the effect of lasing frequency on lasing properties of random lasers. The above effects are investigated by analyzing the laser action in two-dimensional random systems whose interspace among dielectric rods are filled with active medium by means of finite element method. Electric amplitude distributions of lasing states, which emerge as sharp peaks of the above amplification factor, are investigated to figure out the types of laser modes. In order to investigate lasing frequency, we calculate the amplification factor for a certain range of the frequency. We compute amplification factors with changing frequency and population inversion density of active medium to investigate the dependence of laser action on the population inversion. We classify laser modes into three types and investigate the relation between laser modes, frequency and excitation of active medium.

In section 4.4, both the amplification factor and intensity of electric field in random systems are computed by using a finite element method in order to compare our study in section 4.2 with the previous studies in which only the intensities of electric field are computed by using FDTD. The relation between the amplification of light waves flowing out from random structures and intensity of electric field in the random structures are investigated. Moreover, the distributions of electric field amplitudes of lasing states and unexcited states at lasing frequencies are compared. We evaluate similarities between those distributions objectively by using normalized mean square error (NMSE). The above similarity of those distributions indicate the role of disordered structures. The dependence of the similarity on population inversion density of active medium are newly revealed.

Next, we propose appropriate random systems with optically active materials in interspaces among dielectric cylinders for low-threshold random lasing. As the factors composing random systems, filling factor of dielectric cylinders and the amount of positional disorder of dielectric cylinders are considered.

In section 4.5, the effect of the filling factor of dielectric cylinders on lasing threshold is investigated and appropriate filling factor for low-threshold random lasing is presented. Lasing phenomena in disordered structures with filling factors of dielectric cylinders 10%, 20%, 30%, 40%, and 50% are analyzed. Light amplifications in disordered structures, namely, the amplification of Poynting vectors of the light emitted from two-dimensional random media , are computed in wide frequency range. Amplification of light is computed by changing both frequency and excitation parameter in each frequency range in which random laser occurs. The spacial distributions of the electric field amplitude of lasing state are investigated. Light waves tend to be confined in smaller volume as the filling factor of dielectric cylinders increases. The threshold of laser action occurring in a disordered structure with each filling factor is investigated.

In section 4.6, appropriate amount of positional disorder for low-threshold random lasing is presented. The dependence of the lasing threshold on the amount of positional disorder in photonic crystal structures is newly studied. A two-dimensional model of a photonic crystal consisting of dielectric cylinders arranged on a triangular lattice within a circular region is considered. The cylinders are assumed to be homogeneous and infinitely long. Positional disorder of the cylinders is introduced to the photonic crystals. The population inversion

density of the optically active medium is modeled by the negative imaginary part of dielectric constant. The ratio between radiative power of electromagnetic field without amplification and that with amplification is computed as a function of the frequency and the imaginary part of the dielectric constant, and the threshold of the imaginary part, namely population inversion density for laser action is obtained. These analyses are carried out for various amounts of disorder. The variation of the lasing threshold from photonic-crystal laser to random laser is revealed by systematic computations with numerical method of reliable accuracy for the first time. Moreover, a novel phenomenon, that the lasing threshold have a minimum against the amount of disorder, is found. In order to investigate the properties of the lasing states within the circular system, the distributions of the electric field amplitudes of the states are also calculated.

4.2 Random lasing

4.2.1 Introduction

This section present simulated lasing phenomena in random systems with optically active medium in interspaces among dielectric cylinders. Random lasers are lasing phenomena caused by multiple scattering and interference effects in disordered structures. Light waves are localized various and complex regimes in disordered structures because of such lasing mechanisms. It is necessary for low threshold laser action to localized light waves in optically active medium because light localizations work as feedback mechanisms in order to amplify light waves repeatedly. Hence, it is important to investigate the tendency of light localizations in disordered structures. Amplification of radiation power is computed as the function of frequency and the negative imaginary part of relative permittivity by using FEM. Lasing states emerging as the sharp peaks of the surface of amplification factor are observed in lower excited state of active medium than observed lasing states in chapter 3 because light waves tend to be localized in interspaces among dielectric cylinders. It is revealed that random systems with active medium within the interspaces is more appropriate for lower threshold laser action than random systems consisting of optically active cylinders.

4.2.2 Analysis model

The analysis model computed in this section is the same as the one explained in subsection 3.2.

4.2.2.1 Optically active materials

We compare the properties of random laser action of two different types of random systems. For a random system in which optically active materials are filled in the interspaces among nonactive rods, we give a negative value $-\gamma(\gamma > 0)$ of the imaginary part of the dielectric constant of that region, as follows:

$$\epsilon(\mathbf{x}) = \begin{cases} 1.0 + \mathrm{i}(-\gamma) & \mathbf{x} \in \Omega_{\mathrm{act}} \\ 4.0 & \mathbf{x} \in \Omega_{\mathrm{rod}} \\ 1.0 & \mathbf{x} \in \Omega_{\mathrm{out}} \end{cases} . \tag{4.1}$$

4.2.3 Results

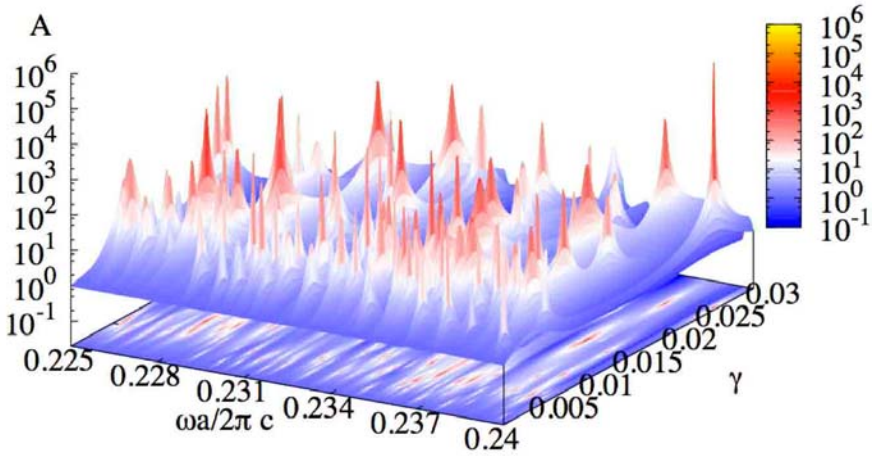

Figure 4.1: Amplification factor in the case of giving γ in interspace among rods.

We analyze the laser action in a disordered structure whose interspaces among non-active rods are filled with optically active materials. In this analysis, we give the parameter γ, which is proportional to the population inversion density, to the dielectric constants in the interspaces among the rods, namely in the region $\Omega_{\rm act}$ in Fig. 3.2. We assume that the optically active materials are excited homogeneously and the parameter γ in all interspaces between the rods is constant.

Figure 4.1 shows the simulated laser action. We plot the amplification factor A as a function of normalized frequency $\omega a/2\pi c$ and γ, where z-axis values are plotted on the logarithmic scale. The numbers of computation points are 501 for $0.225 \leq \frac{\omega a}{2\pi c} \leq 0.240$ and 201 for $0.0 \leq \gamma \leq 0.03$. The bottom plane in Fig. 4.1 shows the position $(\omega a/2\pi c, \gamma)$ of each laser action. We observe a large number of laser action over a broad frequency range, especially in the small γ range. This result can be interpreted so that a lot of low-threshold laser action occur in the disordered structure. In the highly excited state of optically active materials, namely, in large γ range, the number of laser action relatively decrease.

We observe the high electric amplitudes in interspaces among dielectric rods in Figs. 4.2(a) and 4.2(b) which show the electric amplitude distributions of steep peaks marked M and T in Fig. 4.1. How to see Figs. 4.2(c) and 4.2(d) is the same as how to see Figs. 3.4(c), 3.4(d) and 3.5(b). Such distributions of the electric amplitude of lasing states with localizations in the interspaces are natural because the interspaces filled with optically active materials. Figures. 4.2(c) and 4.2(d)

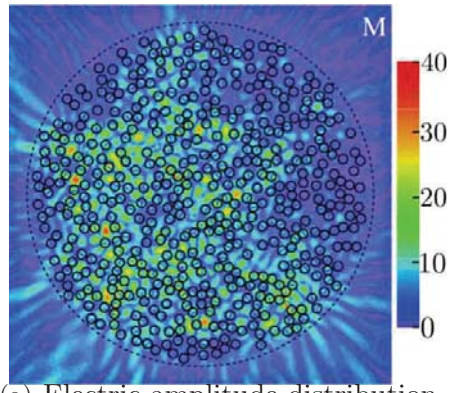

(a) Electric amplitude distribution ($\omega a/2\pi c = 0.22734, \gamma = 0.008250$).

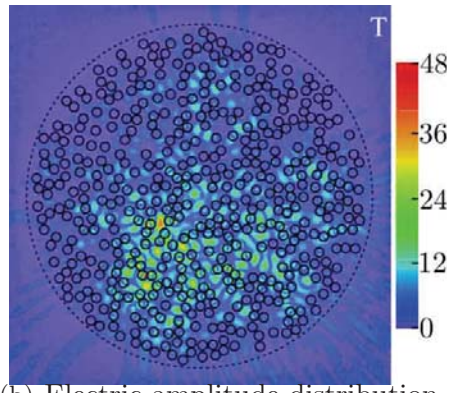

(b) Electric amplitude distribution ($\omega a/2\pi c = 0.23058, \gamma = 0.003600$).

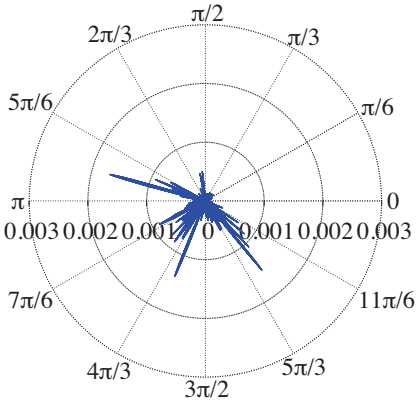

(c) Radiation direction ($\omega a/2\pi c = 0.22734, \gamma = 0.008250$).

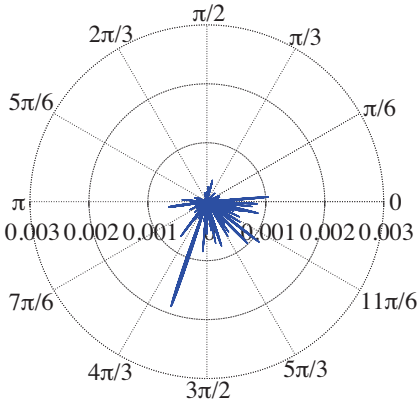

(d) Radiation direction ($\omega a/2\pi c = 0.23058, \gamma = 0.003600$).

Figure 4.2: Electric amplitude distributions and radiation directions of extended modes.

show the broad angular emissions of extended laser modes. Radiation directions are strongly depend on the locations of localizations. We find it difficult to control radiation directions of random laser action.

We also show the distribution of the amplitude of electric field and the variation of the radiation power of localized modes defined by Eq. (3.2) in Fig. 4.3. Light waves become intensive in the interspaces also in the localized case. By comparing the radiation power distributions of localized modes with those of extended modes, we find that the localized laser modes tend to emit the light waves into the space within a narrow angle.

Characteristics of light localizations and radiation directions are common in five samples with different rod arrangements.

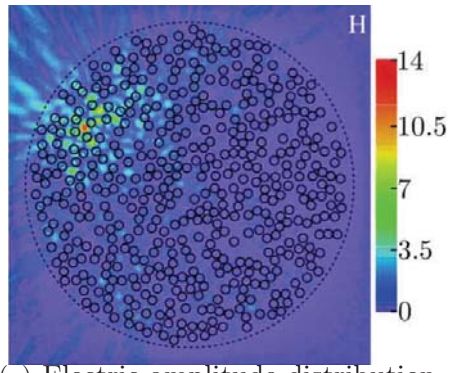

(a) Electric amplitude distribution ($\omega a/2\pi c = 0.22515, \gamma = 0.01710$).

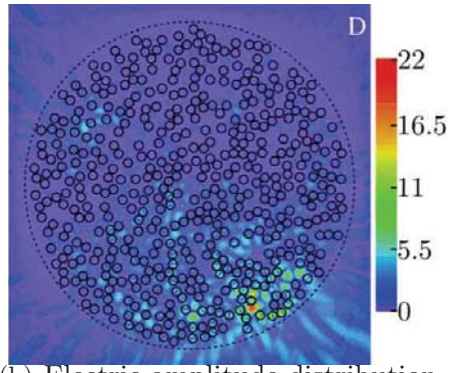

(b) Electric amplitude distribution ($\omega a/2\pi c = 0.22503, \gamma = 0.01860$).

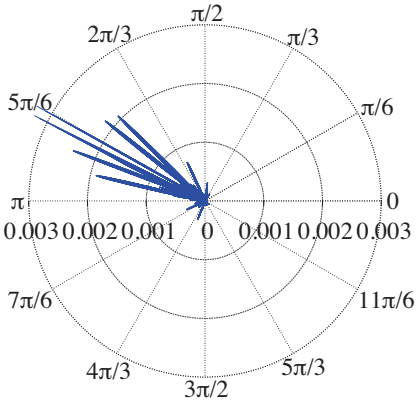

(c) Radiation direction ($\omega a/2\pi c = 0.22515, \gamma = 0.01710$).

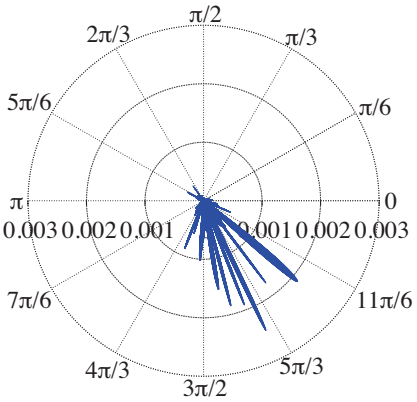

(d) Radiation direction ($\omega a/2\pi c = 0.22503, \gamma = 0.01860$).

Figure 4.3: Electric amplitude distributions and radiation directions of localized modes.

4.2.3.1 Lasing threshold

We investigate lasing threshold, namely, minimum γ at which sharp peaks of amplification factors are observed. The average, minimum, maximum of minimum γ in five samples are shown in Table 4.1.

Table 4.1: Average, minimum, and maximum values of minimum γ.

Average	Minimum	Maximum
0.001663	0.00120	0.00255

Based on the comparison between results shown in Tables 3.1 and 4.1, the lasing threshold of laser action in random systems with active medium in interspaces among dielectric rods tend to becomes lower than that in random systems

consisting of optically active rods.

4.2.4 Conclusion

In this section, laser action in a disordered structure whose interspaces among dielectric rods are filled with active medium are simulated. The amplification factors are computed with changing the frequency and the parameter γ expressing the degree of excitation of optically active materials. The properties of laser action in two different disordered structures, shown in this section and chapter 3, have been compared, and we obtained the following lasing properties:

- Both of extended and localized modes provoke laser action.
- Most of the lasing phenomena are caused by extended modes.
- Lasing phenomena caused by extended modes emit light waves into the spaces in broader angles than those caused by localized modes do.
- Thresholds of laser action in disordered structures with optically active materials in interspaces among non-active rods become lower than those consisting of active rods in non-active media.

4.3 Frequency dependence of the properties of random laser action

4.3.1 Introduction

Random lasers can emit coherent light within broad frequency ranges for broad angle. This random lasers' ability is not realized by conventional laser devices. Random lasers are expected to be applied to display applications, thermal sensing, etc. [28]. Random lasers are triggered by random multiple scattering and interference effect. The laser modes of random lasers are classified into localized and extended modes [28]. The intermediate condition between localized and extended modes are called transition mode [45]. Since the lasing properties of random lasers are influenced by such laser modes, investigating the relation between laser modes, frequency and excitation of active medium are important. However, no discussion on the relations of such laser modes against frequency and excitation of active medium is found in the previous studies.

In chapter 3 and section 4.2, we presented simulations of lasing phenomena in two-dimensional random systems by using FEM. We compared lasing phenomena in two different random systems: optically active materials among nonactive rods, and optically active rods in nonactive media. Based on the results obtained there, the first system was found to be more advantageous in reducing the threshold of laser action because the light waves become localized in the interspace among the rods.

In this section, we present an investigation on laser action for a wide frequency range in the case of TM mode and seek lasing frequencies. We also present a study on spatial maps of the electric amplitude and laser mode distributions in each lasing frequency.

4.3.2 Analysis model

We assume a system whose interspace among dielectric rods are filled with an optically active material, and set the imaginary part of relative permittivity in interspace among rods to $-\gamma$. The relative permittivities in individual regions are given as follows:

$$\epsilon(\mathbf{x}) = \begin{cases} 1.0 + \mathrm{i}(-\gamma) & \mathbf{x} \in \Omega_{\mathrm{act}} \\ 4.0 & \mathbf{x} \in \Omega_{\mathrm{rod}} \\ 1.0 & \mathbf{x} \in \Omega_{\mathrm{out}} \end{cases}, \tag{4.2}$$

where Ω_{act} is the region of interspaces among dielectric cylinders, Ω_{rod} is the region in cylinders, and Ω_{out} is the open region.

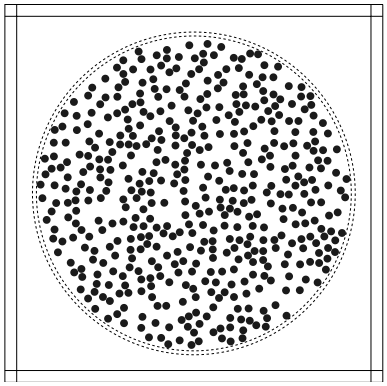

Figure 4.4: An analysis model.

Parameter	Value
Number of rod	480
Radius of rods, a	1
Filling factor, f	0.3 (30%)
$\mathrm{R_{in}}$	$1.5a$
$\mathrm{R_g}$	$40a$
$\mathrm{R_{out}}$	$41a$
Width of PML	3a
Width of physical domain	90a
Mean free path, l	$a\left(\sqrt{\frac{2\pi}{\sqrt{3}f}} - 2\right)$
Position of center, (x_0, y_0)	$(0, 0)$

Table 4.2: Parameters in geometry

Figure 4.4 shows the present analysis model. The number of dielectric rods illustrated by the solid circles in Fig. 4.4 is 480 and the filling factor of the dielectric rods is 30%. The radii of the cross sections of the rods are assumed to be the same, and the radius a is used as the characteristic length. The size of the analysis models is normalized by the characteristic length. The circles $\mathrm{C_g}$ and $\mathrm{C_{out}}$ surrounding the dielectric structure are illustrated by broken lines. The radius of $\mathrm{C_g}$ is $40a$, while that of $\mathrm{C_{out}}$ is $41a$. The center positions of the dielectric rods are determined based on pseudo random numbers generated by `drand` Fortran function.

4.3.3 Results

We calculate amplification factor defined in Eq. (2.60) for frequency range $0.1 \leq \omega a/2\pi c \leq 0.4$ with fixed population inversion densities, $\gamma = 0.001$, 0.002, and 0.005.

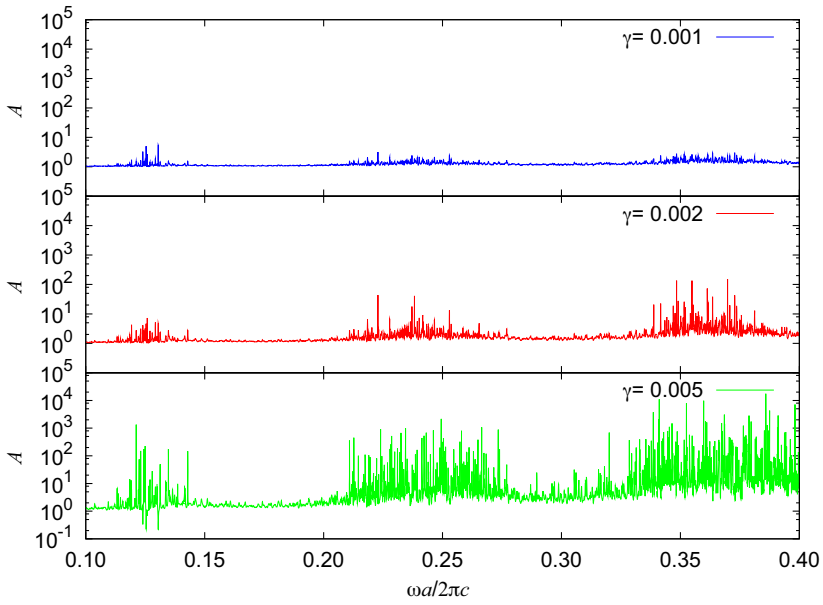

Figure 4.5: Laser action for $0.1 \leq \omega a/2\pi c \leq 0.4$ (fine mesh).

Figure 4.5 shows the results of lasing phenomena in the disordered structure. For the state corresponding to $\gamma = 0.001$, the amplification factor values are smaller than 10^1 and large divergent peaks of the amplification factor are not observed. For higher excited states of optically active material, $\gamma = 0.002$ and 0.005, the amplification factor values exceed 10^2 and diverge. We observe three lasing frequencies within the ranges $0.121 \leq \omega a/2\pi c \leq 0.136$, $0.225 \leq \omega a/2\pi c \leq 0.255$, and $0.345 \leq \omega a/2\pi c \leq 0.375$, especially, for the results with $\gamma = 0.002$.

4.3.3.1 Laser action

We simulate laser action by changing both the frequency $\omega a/2\pi c$ and the population inversion density γ. The amplification factor values are plotted as the function of $(\omega a/2\pi c, \gamma)$. We seek divergent peaks of amplification factor, which are interpreted as lasing phenomena, by sweeping the surface of the amplification

factor.

Random lasing phenomena in the lower frequency range Figure 4.6 shows the results of the lasing phenomena obtained for the lower frequency range $0.121 \leq \omega a/2\pi c \leq 0.136$ that corresponds to $0.179 \leq kl/2\pi \leq 0.201$ where k and l are wave number and transfer mean free path (TMFP). TMFP is the length of the one step of random walk, that is, the average distance between neighboring dielectric cylinders. In general, random laser action occurs when a half of the wavelength is close to the length of TMFP, namely $kl/2\pi \approx 0.5$. However, TMFP is much smaller than a half of the wavelength of light waves in the frequency range. The number of random lasing phenomena oscillating in the frequency range is 47.

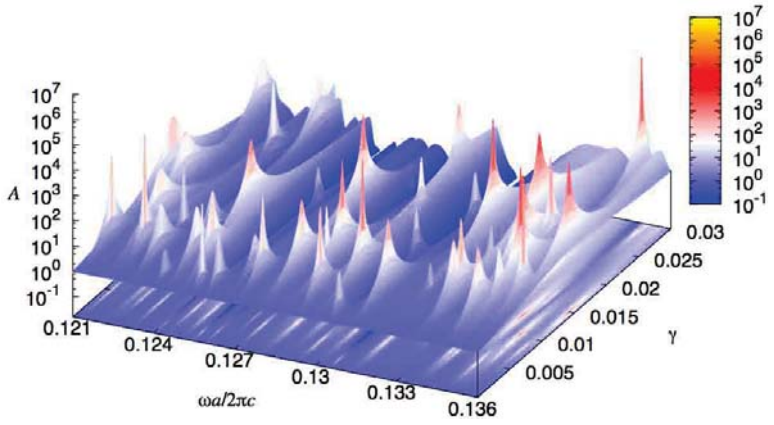

Figure 4.6: Laser action in the range of $0.121 \leq \omega a/2\pi c \leq 0.136$ (coarse mesh).

To understand the mechanisms causing the laser action in the low frequency range, $0.121 \leq \omega a/2\pi c \leq 0.136$, we investigate electric amplitude distributions (EADs) of some lasing phenomena. Figures 4.7 and 4.8 show EADs of the extended and localized modes, respectively. In dielectric structures, light waves are intensively localized in large vacant spaces created by disordered distribution of the dielectric rods, especially in extended modes. Moreover, for EADs of different lasing modes shown in Fig. 4.7, we observe that the light waves become intense within some common vacant spaces between rods. Such a characteristic of light localization may lead to a smaller number of lasing phenomena. Namely, light waves cannot be localized in interspaces between rods except for large vacant spaces because the wave length of the light wave is longer than TMFP.

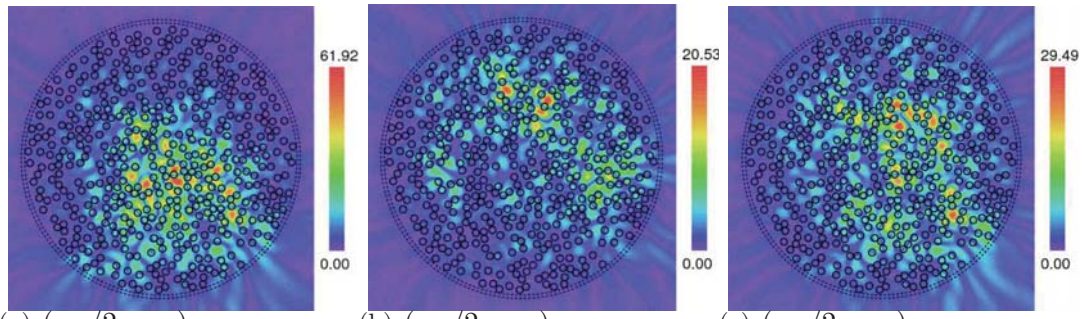

(a) $(\omega a/2\pi c, \gamma) = (0.13480, 0.00510)$. (b) $(\omega a/2\pi c, \gamma) = (0.13360, 0.00630)$. (c) $(\omega a/2\pi c, \gamma) = (0.13518, 0.00675)$.

Figure 4.7: Electric amplitude distributions of extended modes in frequency range $0.121 \leq \omega a/2\pi c \leq 0.136$.

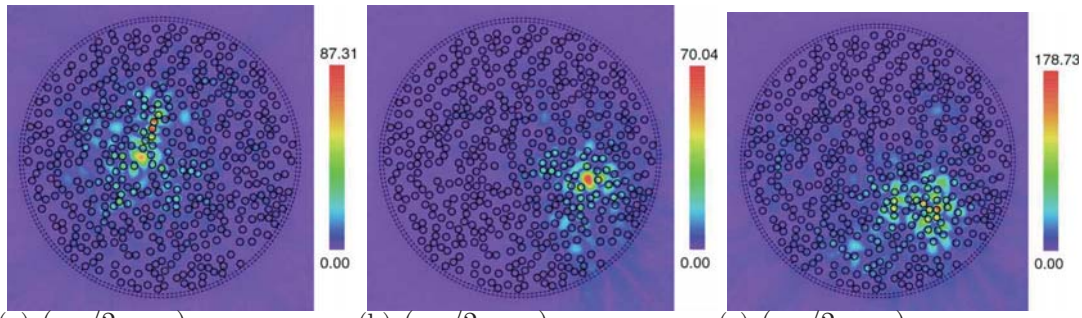

(a) $(\omega a/2\pi c, \gamma) = (0.12404, 0.00165)$. (b) $(\omega a/2\pi c, \gamma) = (0.12704, 0.00420)$. (c) $(\omega a/2\pi c, \gamma) = (0.12126, 0.00495)$.

Figure 4.8: Electric amplitude distributions of localized modes in frequency range $0.121 \leq \omega a/2\pi c \leq 0.136$.

Random lasing phenomena in range $0.225 \leq \omega a/2\pi c \leq 0.255$ Figure 4.9 shows the result of lasing phenomena for frequency range $0.225 \leq \omega a/2\pi c \leq 0.255$ which corresponds to $0.332 \leq kl/2\pi \leq 0.376$. The numbers of the divergent peaks of the amplification factor A are 120 and 138 in Figs. 4.9(a) and 4.9(b), respectively. In comparison with Fig. 4.6, it remarkably increases in the frequency range $0.225 \leq \omega a/2\pi c \leq 0.255$ that is equal to $0.332 \leq kl/2\pi \leq 0.377$. A half of the wavelength in the above frequency range is a little longer than TMFP, say, for $kl/2\pi = 0.500$, the half-wavelength is equal to TMFP.

Figures 4.10 and 4.11 show the results of EADs for the extended and localized modes in frequency range $0.225 \leq \omega a/2\pi c \leq 0.255$, respectively. The light waves are localized not only in the large vacant spaces but also in the narrow

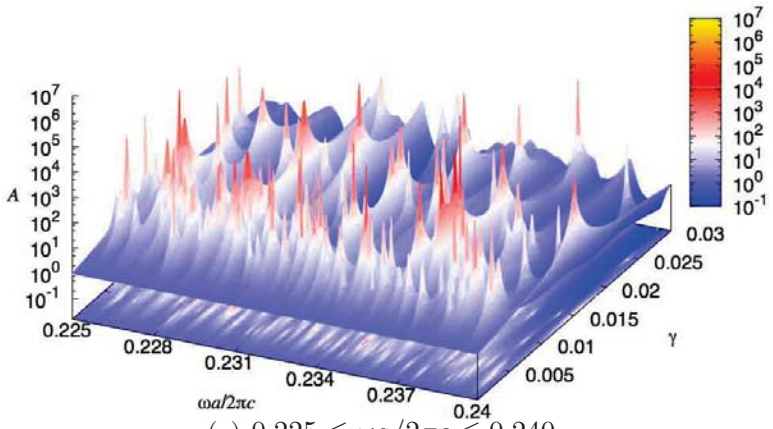

(a) $0.225 \leq \omega a/2\pi c \leq 0.240$.

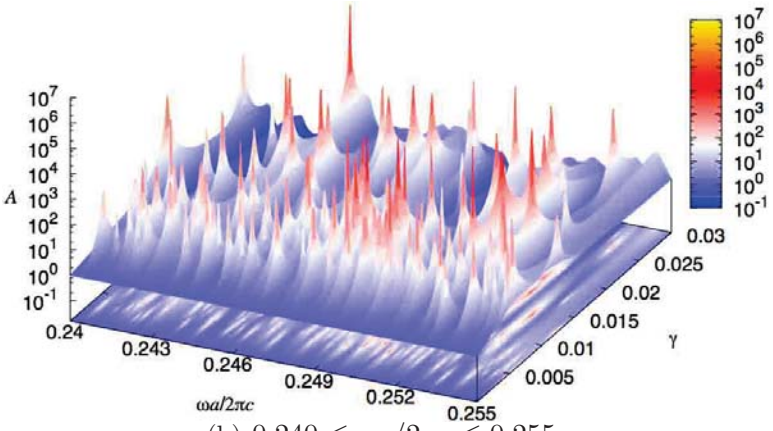

(b) $0.240 \leq \omega a/2\pi c \leq 0.255$.

Figure 4.9: Laser action for $0.225 \leq \omega a/2\pi c \leq 0.255$ (coarse mesh).

interspaces between the rods. Some light waves permeate through the surfaces of the dielectric rods and are localized in them. We can naturally consider that the light waves, whose half-wavelength is a little longer than TMFP, oscillate in the disordered structure.

Random lasing phenomena in the higher frequency range Figure 4.12 shows the result of the lasing phenomena for frequency range $0.345 \leq \omega a/2\pi c \leq 0.375$. A fine meshed model are used to analyze light waves of high frequencies. The result is computed only for the range $0.00 \leq \gamma \leq 0.01$ due to the large computation cost.

Figure 4.13 shows the electric amplitude distributions in the state of extended modes for frequency range $0.345 \leq \omega a/2\pi c \leq 0.375$. A half-wavelength of light is approximately equal to TMFP in this frequency range, and hence, we observe

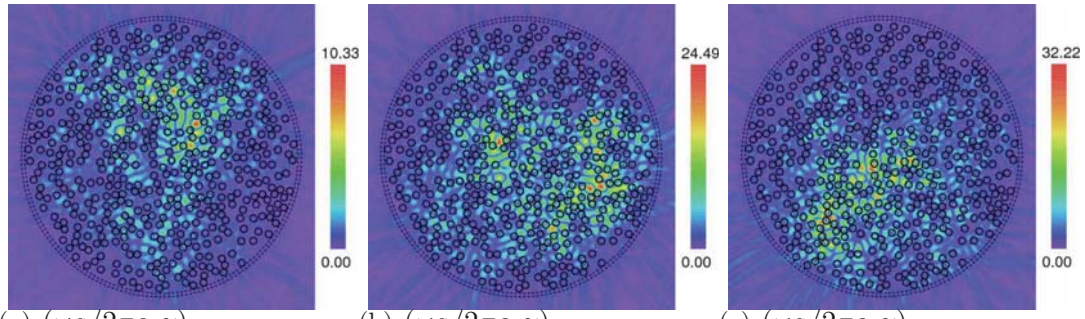

(a) $(\omega a/2\pi c, \gamma) = (0.23076, 0.0033000)$. (b) $(\omega a/2\pi c, \gamma) = (0.24188, 0.0025500)$. (c) $(\omega a/2\pi c, \gamma) = (0.25316, 0.0027000)$.

Figure 4.10: Electric amplitude distributions of extended modes in frequency range $0.225 \leq \omega a/2\pi c \leq 0.255$ (coarse mesh).

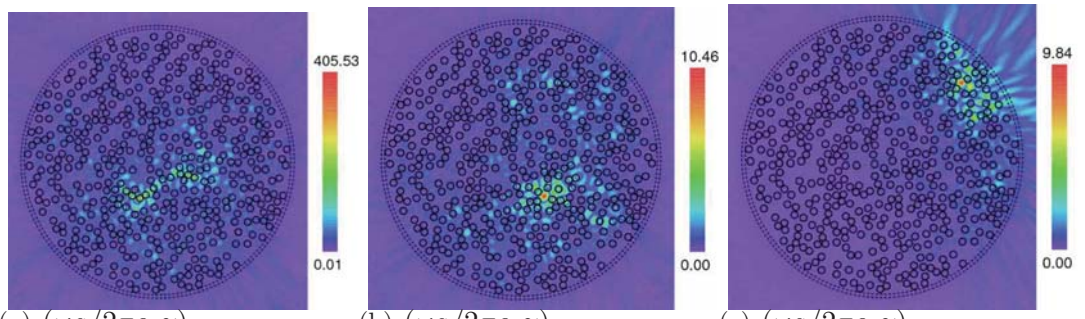

(a) $(\omega a/2\pi c, \gamma) = (0.22798, 0.0033000)$. (b) $(\omega a/2\pi c, \gamma) = (0.23434, 0.028500)$. (c) $(\omega a/2\pi c, \gamma) = (0.24224, 0.028500)$.

Figure 4.11: Electric amplitude distributions of localized modes in frequency range $0.225 \leq \omega a/2\pi c \leq 0.255$ (coarse mesh).

fine interference patterns caused by random light scatterings. Light waves spread spatially in the dielectric structure.

4.3.3.2 Distribution of laser modes

In this subsubsection, we show the results of the distribution of laser modes classified into localized, extended and transition modes.

Classification of laser mode types Each nodal value E_{I} can be normalized by the maximum and minimum nodal values, $\max\{E_{\mathrm{I}}\}$ and $\min\{E_{\mathrm{I}}\}$, as

$$E_{\mathrm{I}}^{\mathrm{n}} = \frac{E_{\mathrm{I}} - \min\{E_{\mathrm{I}}\}}{\max\{E_{\mathrm{I}}\} - \min\{E_{\mathrm{I}}\}}. \tag{4.3}$$

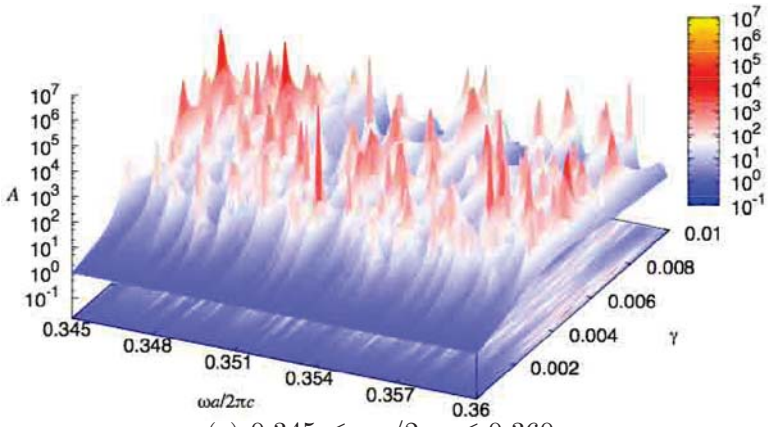

(a) $0.345 \leq \omega a/2\pi c \leq 0.360$.

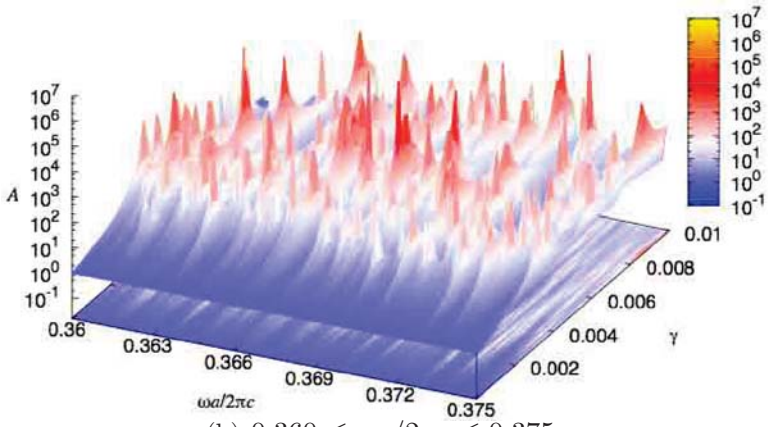

(b) $0.360 \leq \omega a/2\pi c \leq 0.375$.

Figure 4.12: Laser action in the range of $0.345 \leq \omega a/2\pi c \leq 0.375$ (fine mesh).

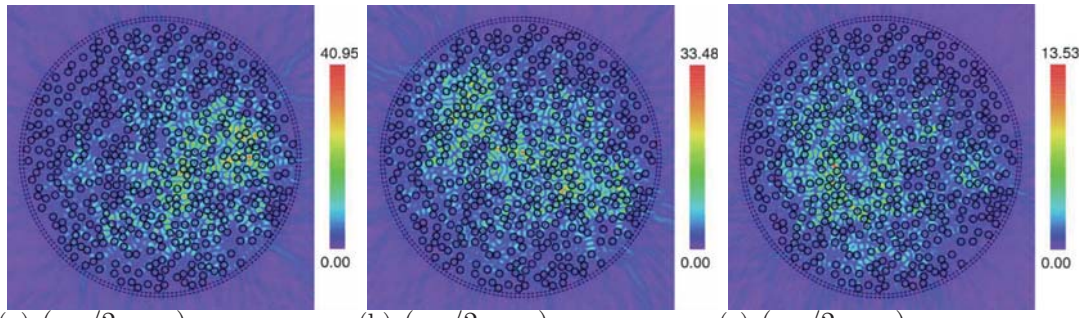

(a) $(\omega a/2\pi c, \gamma) = (0.34838, 0.0019500)$.

(b) $(\omega a/2\pi c, \gamma) = (0.35486, 0.0019500)$.

(c) $(\omega a/2\pi c, \gamma) = (0.36162, 0.0019500)$.

Figure 4.13: Electric amplitude distributions of extended modes in frequency range $0.345 \leq \omega a/2\pi c \leq 0.375$ (fine mesh).

Then, the data of normalized nodal values $E_{\mathrm{I}}^{\mathrm{n}}$ are binarized with the threshold $E_{\mathrm{I}}^{\mathrm{n}} = 0.1$. Binarized images are shown in Fig. 4.15. The electric amplitudes are

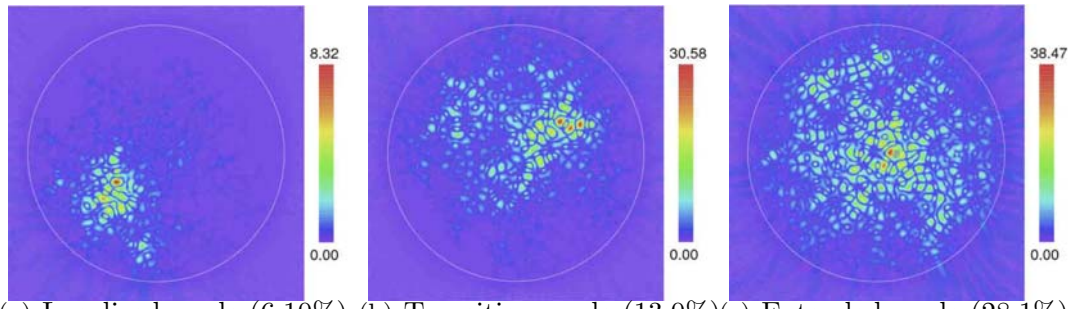

(a) Localized mode (6.10%). (b) Transition mode (13.0%). (c) Extended mode (28.1%).

Figure 4.14: Original images of electric amplitude distributions.

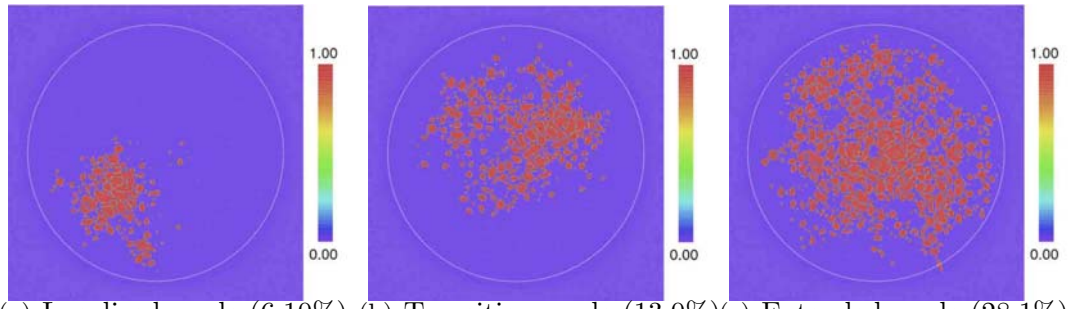

(a) Localized mode (6.10%). (b) Transition mode (13.0%). (c) Extended mode (28.1%).

Figure 4.15: Binarized images of electric amplitude distributions.

interpolated linearly within each element, and the points at which the interpolated electric amplitude corresponds to the threshold are found.

In the circle C_{out}, we calculate the total area of the regions in which normalized nodal values are higher than the threshold. The laser modes are determined as localized ones when this total area is smaller than 10% of the area of C_{out}, while they are determined as extended ones when the total area is larger than 25% of the area of C_{out}. When the total area is larger than 10% and smaller than 25% of the are of C_{out}, the laser modes are determined as transition modes.

Results We investigate the distribution of laser mode, i.e., localized and extended modes, for population inversion density γ and amplification factor. We classify the types of laser modes using the ratio between the area in which light waves exist in C_{out}, and the area of C_{out}. An intermediate state between a localized and an extended modes is classified as a transition mode. To find the common tendency of distributions, we analyze five different models, with the same 30% filling factor but with different random arrangements, for frequency

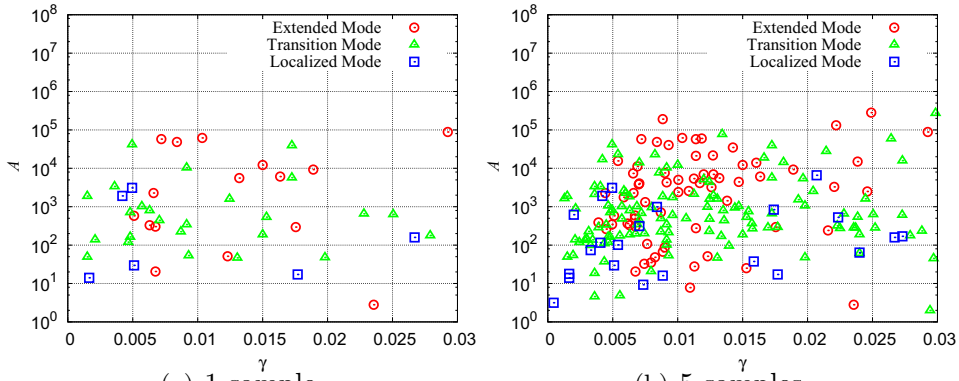

(a) 1 sample. (b) 5 samples.

Figure 4.16: Laser mode types in frequency range $0.121 \leq \omega a/2\pi c \leq 0.136$.

ranges $0.121 \leq \omega a/2\pi c \leq 0.136$ and $0.225 \leq \omega a/2\pi c \leq 0.255$, and three models for frequency range $0.345 \leq \omega a/2\pi c \leq 0.375$.

Figure 4.16(a) shows the distribution of the laser modes detected in the result shown in Fig. 4.6 for frequency range $0.121 \leq \omega a/2\pi c \leq 0.136$. Figure 4.16($b$) shows that of the models with five different rod arrangements. Laser modes of the lower threshold lasing phenomena occurring in the range $\gamma < 0.003$ are localized and correspond to transition modes. The lasing phenomena having larger amplification factors $A > 10^4$ tend to be of extended and transition modes.

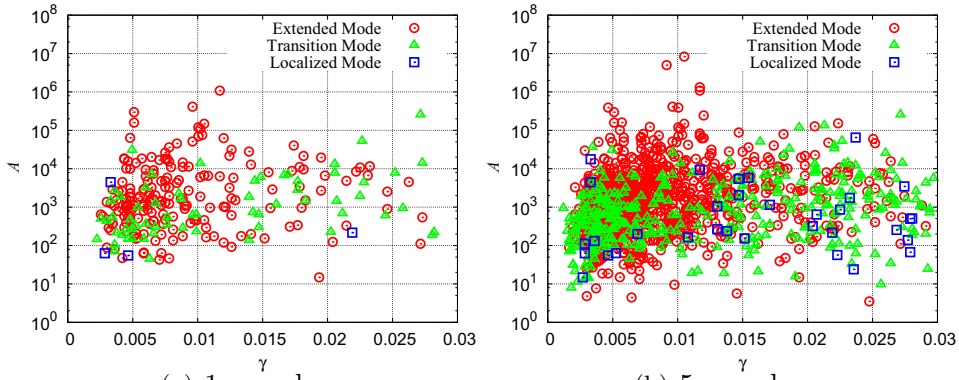

(a) 1 sample. (b) 5 samples.

Figure 4.17: Laser mode types for frequency range $0.225 \leq \omega a/2\pi c \leq 0.255$.

Figure 4.17(a) shows the distribution of the laser mode for frequency range $0.225 \leq \omega a/2\pi c \leq 0.255$, obtained from the result shown in Fig. 4.9. Also, Fig. 4.17(b) shows a distribution obtained from the five different random arrangement models. We observe a common tendency in the results shown in Figs. 4.17(a)

and 4.17(b). The lowest threshold laser action is in transition mode that is intermediate state between localized and extended modes. The laser modes having higher amplification factor values belong to extended modes. In extended modes, the light waves spread spatially in the random systems and are amplified by the large amount of the optically active material. Hence, the amplification factors of extended mode become large, and the number of localized modes is obviously few.

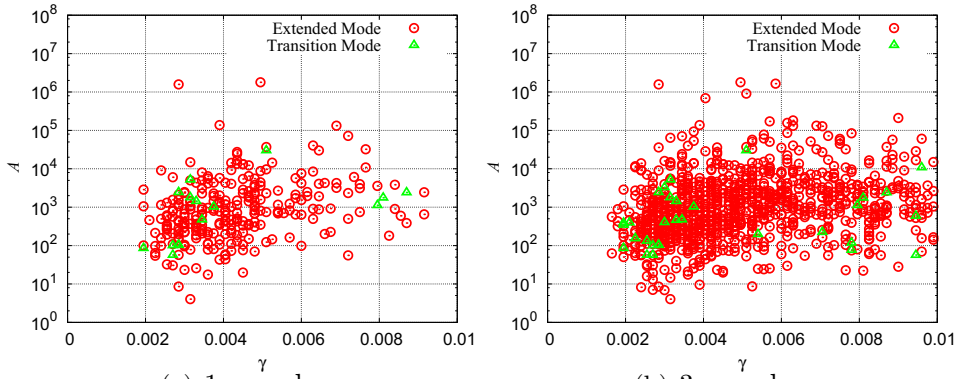

(a) 1 sample. (b) 3 samples.

Figure 4.18: Laser mode types for frequency range $0.345 \leq \omega a/2\pi c \leq 0.375$.

Figure 4.18(a) shows the distribution of the laser mode of the dielectric structure shown in Fig. 4.4 for frequency range $0.345 \leq \omega a/2\pi c \leq 0.375$ corresponding to $0.510 \leq kl/2\pi \leq 0.554$. Most of the laser modes are extended ones, and localized modes disappear in the ranges of this frequency and γ. In this frequency range, TMFP approximately equals a half-wavelength of light: $kl/2\pi \approx 0.5$. In such cases, light waves are localized as standing waves in the interspaces between neighboring rods. Such standing waves exist broadly in random systems.

4.3.3.3 Lasing threshold

We investigate lasing threshold, namely, minimum γ at which sharp peaks of amplification factors are observed. The average, minimum, maximum of minimum γ in five samples are shown in Table 4.3. In the lower frequency ranges $0.121 \leq \omega a/2\pi c \leq 0.136$, average of lasing frequency is highest. Lasing threshold in $0.225 \leq \omega a/2\pi c \leq 0.255$ tends to become lowest.

Table 4.3: Average, minimum, and maximum values of minimum γ in each lasing frequency ranges.

Lasing frequency range	Average	Minimum	Maximum
$0.121 \leq \omega a/2\pi c \leq 0.136$ (5 samples)	0.002747	0.00045	0.00330
$0.225 \leq \omega a/2\pi c \leq 0.255$ (5 samples)	0.001663	0.00120	0.00255
$0.345 \leq \omega a/2\pi c \leq 0.375$ (3 samples)	0.001680	0.00150	0.00210

4.3.4 Conclusion

In this section, we investigated the dependence of lasing properties on frequencies. We simulated laser action for frequency range $0.1 \leq \omega a/2\pi c \leq 0.4$. Three lasing frequency ranges have been observed and laser action in each lasing frequency have been simulated by using FEM. The following results have been obtained.

- The number of lasing phenomena in the higher frequency range is much more than that of the lower frequency range.
- Light waves are localized in large vacant interspaces among rods in the lower frequency range. In the case of the higher frequency, light waves exist as standing waves not only in the large interspace but also in the small interspace among neighboring rods, and spread spatially in the disordered structures.
- In the case of the lower frequency, both localized and extended modes are observed, however, as the frequency increases, the localized one disappear and most laser modes become the extended ones.
- Lasing threshold tends to become lowest in $0.225 \leq \omega a/2\pi c \leq 0.255$.

4.4 Dependency of laser action on electric field intensity in randomly distributed dielectric cylinders

4.4.1 Introduction

After the first experimental observation of a random lasing phenomenon by Lawandy in 1994 [10], many researchers have discussed whether the light amplifying phenomena are lasing phenomena or amplified spontaneous emissions (ASEs) [11] because disordered structures do not seem to work based on any feedback mechanisms. Wiersma and Cao et al. observed extreme enhancements of the electric intensity in disordered structures, called laser spikings, in their experimental studies [46, 30]. Sebbah and Vanneste et al. simulated laser spikings by using FDTD [12, 47]. Above experimental and numerical studies concluded that the light amplifying phenomena are lasing ones. In addition, Sebbah et al. compared the distributions of electric field amplitude in the non-excited and excited states of active medium and concluded that dielectric random structures work as cavities to confine light waves [12]. Most previous studies of random laser by using numerical simulations show the results of spectrum of electric intensity, computed by FDTD, in dielectric random structures.

In our previous study, we simulate lasing phenomena in disordered structures by computing the amplification of light waves emitted from random systems by using a finite element method [48]. The dependences of lasing properties are revealed by modeling population inversion density of active medium as negative imaginary part of relative permittivity [3, 4, 5].

In this section, both the amplification factor and intensity of electric field in random systems are computed by using a finite element method in order to compare our previous study with the previous studies in which only the intensities of electric field are computed by using FDTD. The relation between the amplification of light waves flowing out from random structures and intensity of electric field in the random structures are investigated.

4.4.1.1 Definitions of amplification factor and intensity of electric field

We compute Poynting vector of light waves flowing out from dielectric structures in time-averaged form because of the assumption of time-harmonic waves of electric and magnetic fields.

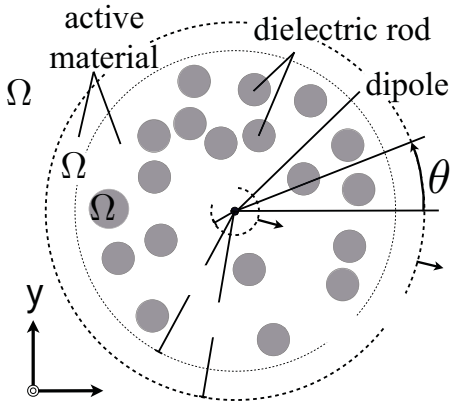

Figure 4.19: An concept of entire random system.

The time-averaged form of Poynting vector $\mathbf{S}$ is as follows:

$$\langle \mathbf{S} \rangle = \mathrm{Re}\left(\frac{\mathbf{E} \times \mathbf{H}^*}{2} \right), \tag{4.4}$$

where $\mathbf{H}^*$ is the conjugate of the magnetic field. The amplification factor computed in this simulations is defined as

$$A = \frac{\int_{\mathrm{C_{out}}} \langle \mathbf{S} \rangle \cdot \mathbf{n}_{\mathrm{out}} \; dl|_{\gamma>0}}{\int_{\mathrm{C_{out}}} \langle \mathbf{S} \rangle \cdot \mathbf{n}_{\mathrm{out}} \; dl \; |_{\gamma=0}}, \tag{4.5}$$

where $\mathbf{n}_{\mathrm{out}}$ is a normal-unit-outward vector against the circle $\mathrm{C_{out}}$ surrounding dielectric structures. The amplification factor defined as the ratio of radiative powers between non-excited and excited states of active medium in Eq. (4.5) shows the light amplification occurring from the excitation of active medium and light confinement in dielectric disordered structures.

The intensity of electric field in dielectric disordered structures is defined as

$$EI = \frac{\sum\limits_{e} \int_{\Omega_{\mathrm{act}}+\Omega_{\mathrm{rod}}} |\mathbf{E}(\mathbf{x})|^2 dS}{\sum\limits_{e} \int_{\Omega_{\mathrm{act}}+\Omega_{\mathrm{rod}}} |\mathbf{E}_{\mathrm{i}}(\mathbf{x})|^2 dS}. \tag{4.6}$$

The value EI gives the ratio of electric field intensities in the case of no-scatter within non-excited medium and in the case of scatters within excited active medium. The intensity of electric field interpolated by linear basis function is integrated in each element, and summation of the integrated intensity in each element in two regions, Ω_{act} and Ω_{rod}, is computed.

4.4.2 Analysis models

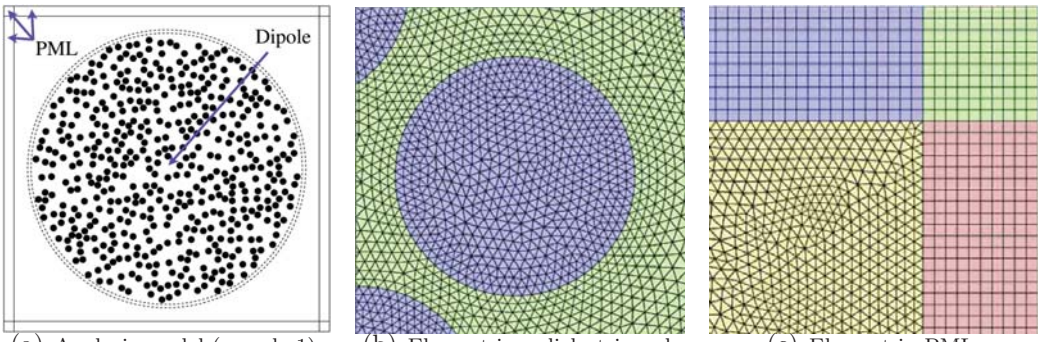

(a) Analysis model (sample 1). (b) Element in a dielectric rod. (c) Element in PML.

Figure 4.20: Analysis model and finite element mesh.

Parameter	Value
Number of rod	480
Radius of rods, a	1 : characteristic length
Filling factor, f	0.3 (30%)
Radius of C_{in}, R_{in}	$1.5a$
Radius of C_g, R_g	$40a$
Radius of C_{out}, R_{out}	$41a$
Width of PML	3a
Width of physical domain	90a
Mean free path, l	$a\left(\sqrt{2\pi/\sqrt{3}f} - 2\right)$
Position of center, (x_0, y_0)	$(0, 0)$

Table 4.4: Parameters in geometry

We analyze lasing phenomena occurring in two-dimensional disordered systems consisting of dielectric cylinders. Interspace among the cylinders in the systems is assumed to be filled with active medium. Fig. 4.20(a) shows one of the two-dimensional disordered systems. The number of dielectric cylinders expressed as black circles in Fig. 4.20(a) is 480 and filling factor of the dielectric cylinders is 30%.

We list parameters to create analysis models in Table 4.4. Figures 4.20(b) and 4.20(c) show finite element meshing in a cylinder and PML, respectively. The numbers of nodes and elements are 985092 and 1956502. The edge lengths of the elements in the cylinders are approximately $a/13$ and $\lambda/27$ in the worst case, where λ is the shortest wavelength investigated in the present analysis. Regions on the circle C_{out} are discretized by smaller elements whose edge lengths are approximately 1/8 times of those of elements mentioned above because the reduction of computational accuracy is caused by the rotation of the electric field, $\nabla \times \mathbf{E}$, needed for the calculation of $\mathbf{H}^*$ including the time-averaged Poynting vector in Eq. (4.4).

4.4.3 Results

We consider an oscillating dipole as a light source located at $\mathbf{x}_0 = (0, 0)$, and compute the amplification factor for the ranges $0.225 \leq \omega a/2\pi c \leq 0.240$ and $0.00 \leq \gamma \leq 0.02$. The frequency range is $0.332 \leq kl/2\pi \leq 0.355$ where k and l are the wavenumber and mean free path, respectively. When the radii of the cross section of the cylinders are $a = 130$[nm], the above frequency range correspond to visible wavelength range, 481[nm]$\sim$619[nm], and the radius of the whole disordered structure is $40a = 5.2[\mu\text{m}]$. The numbers of computation points are taken 751 and 141 for $\omega a/2\pi c$ and γ axes, respectively. It took approximately 30 seconds for a computation for each set of the values of $\omega a/2\pi c$ and γ.

4.4.3.1 Amplification factor and electric field intensity

Figures 4.21 and 4.22 show the amplification factor defined by Eq. (4.5) and the intensity of electric field defined by Eq. (4.6). The amplification factor and the intensity have peaks on $\omega a/2\pi c$-γ plane. We observe that low-threshold lasings occur at the frequencies at which the intensity becomes high in non-excited state of active material ($\gamma = 0$).

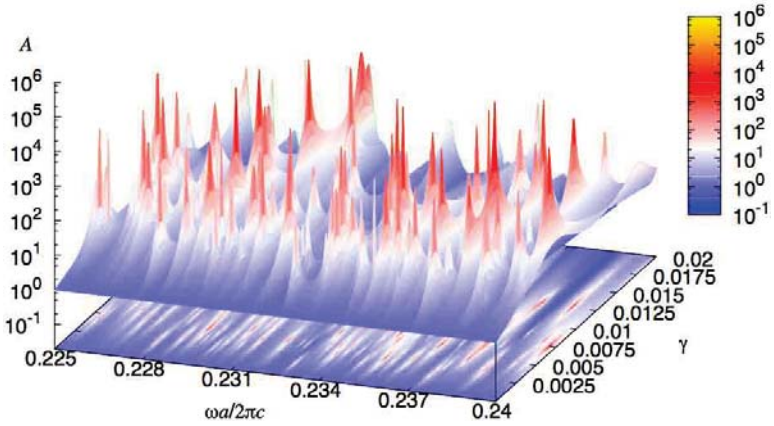

Figure 4.21: Laser oscillation in a disordered system (sample 1).

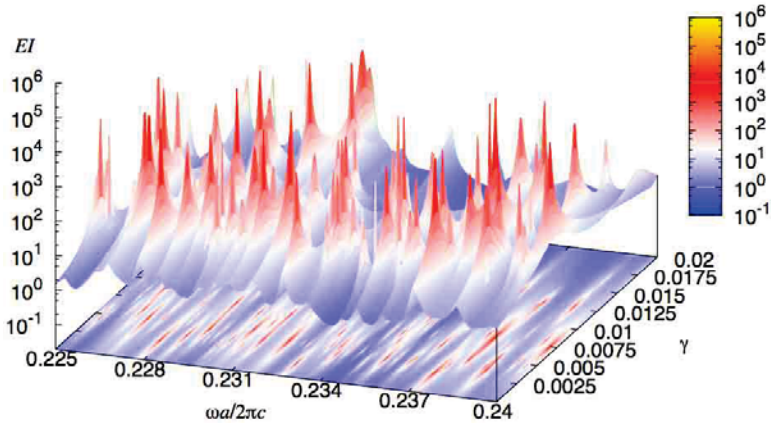

Figure 4.22: Electric intensity in a disordered system (sample 1).

4.4.3.2 Cavity modes and non-cavity modes

Based on the obtained results of the amplification factor and the electric field intensity, we pay attention to the frequencies at which the electric field intensities become high in non-excited state of the active material, that is, $\gamma = 0$. We investigate electric amplitude distributions in the state of the highest three intensities of the electric field without excitation of active material and those of lasing states at the same frequencies in the lowest excited state. Figure 4.23 shows the results of the distributions. Figures 4.23(a), 4.23(b) and 4.23(c) show the electric amplitude distributions without the excitation of active material, while Figs. 4.23(d), 4.23(e) and 4.23(f) show those of lasing states, that is, excited states. The values plotted in Fig. 4.23 are the electric field amplitudes normalized by the

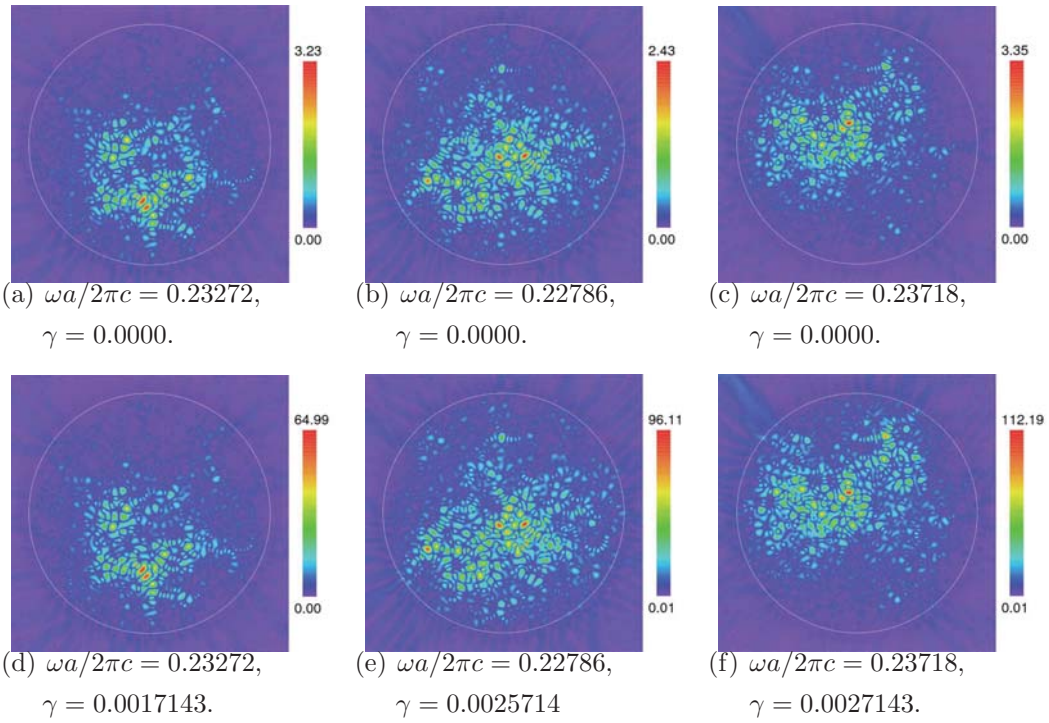

(a) $\omega a/2\pi c = 0.23272$, $\gamma = 0.0000$. (b) $\omega a/2\pi c = 0.22786$, $\gamma = 0.0000$. (c) $\omega a/2\pi c = 0.23718$, $\gamma = 0.0000$.

(d) $\omega a/2\pi c = 0.23272$, $\gamma = 0.0017143$. (e) $\omega a/2\pi c = 0.22786$, $\gamma = 0.0025714$ (f) $\omega a/2\pi c = 0.23718$, $\gamma = 0.0027143$.

Figure 4.23: Electric amplitude distribution of cavity-modes (sample 1).

maximum value of the incident field. In Fig. 4.23, the values of $\omega a/2\pi c$ and γ are written in five significant figures. Comparing the electric amplitude distributions between the non-excited and lasing states, we observe the localization patterns of the two states at the same frequencies are similar to each other. Such similarities have already been mentioned in the previous study [12] and are interpreted that dielectric disordered structures work as cavities. The lasing modes shown in Figs. 4.23(d), 4.23(e), and 4.23(f) are called "cavity modes".

On the other hand, we find the existence of "non-cavity modes" that have different patterns of light localizations in lasing states from that of non-excited states of active medium. In non-cavity modes, the disordered structures do not work as cavities. Although we find no similarity between two distributions of electric field amplitude in Figs. 4.24(a) and 4.24(d), we find some common patterns of the distributions in the right sides of Figs. 4.24(b) and 4.24(e), and in the regions around the center of Figs. 4.24(c) and 4.24(f).

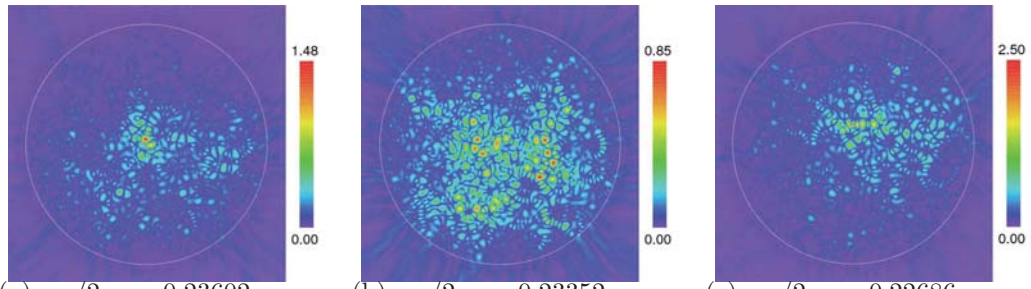

(a) $\omega a/2\pi c = 0.23602$, $\gamma = 0.0000$. (b) $\omega a/2\pi c = 0.23352$, $\gamma = 0.0000$. (c) $\omega a/2\pi c = 0.22686$, $\gamma = 0.0000$.

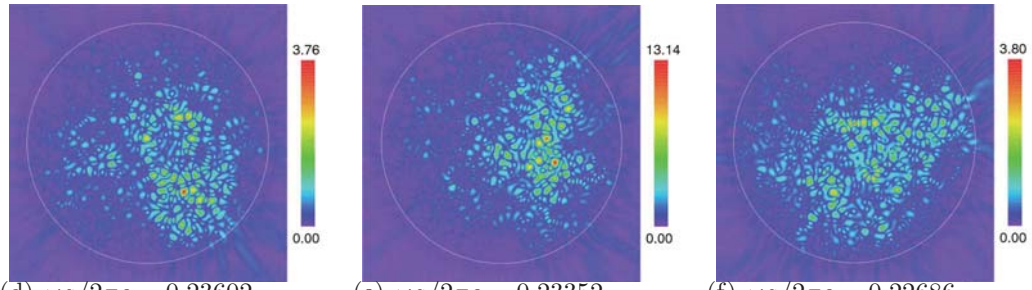

(d) $\omega a/2\pi c = 0.23602$, $\gamma = 0.0022857$. (e) $\omega a/2\pi c = 0.23352$, $\gamma = 0.0025714$. (f) $\omega a/2\pi c = 0.22686$, $\gamma = 0.0030000$.

Figure 4.24: Electric amplitude distribution of non-cavity-modes (sample 1).

4.4.3.3 Evaluation of the similarities between distribution regimes

We have to evaluate the similarities of the distribution patterns between non-excited ($\gamma = 0$) and lasing states ($\gamma > 0$) in order to decide whether random structures work as cavities or not. We use normalized mean square error (NMSE) for this purpose. NMSE is a numerical method to evaluate similarities between images. NMSE is defines as the square sum of the differences of pixel values of two images. The summation is normalized by the square sum of the pixel values of the original image. A smaller value of NMSE indicates a high similarity between the two images. We use NMSE defined by treating the nodal values as the pixel values, as follows:

$$\mathrm{NMSE} = \frac{\sum_{\mathrm{j}=1}^{\mathrm{N}} \left(\left|\mathbf{E}_{\mathrm{n}}^{\mathrm{j}}\right|_{\gamma>0} - \left|\mathbf{E}_{\mathrm{n}}^{\mathrm{j}}\right|_{\gamma=0} \right)^2}{\sum_{\mathrm{j}=1}^{\mathrm{N}} \left|\mathbf{E}_{\mathrm{n}}^{\mathrm{j}}\right|_{\gamma=0}^2}, \tag{4.7}$$

where j denotes a node number, N is the total number of nodes, and $\mathbf{E}_{\mathrm{n}}^{j}$ is the nodal values of the electric amplitudes normalized to be in the range $0 \leq |\mathbf{E}_{\mathrm{n}}^{j}| \leq 1$. In Table 4.5, we give the values of NMSE of the distributions shown in Figs. 4.23

and 4.24. The NMSE values for cavity modes are much smaller than those of non-cavity modes and reflect the similarity between the distributions well.

Table 4.5: NMSE of laser mode in Figs. 4.23 and 4.24 (sample 1).

Figure No.	Normalized Frequency	NMSE
4.23(a), 4.23(d)	0.23272	0.025714
4.23(b), 4.23(e)	0.22786	0.036990
4.23(c), 4.23(f)	0.23718	0.056546
4.24(a), 4.24(d)	0.23602	0.59442
4.24(b), 4.24(e)	0.23352	0.39460
4.24(c), 4.24(f)	0.22686	0.34264

4.4.3.4 Distribution of cavity and non-cavity modes against population inversion density γ

In this subsubsection, we investigate the distribution of laser modes evaluated by NMSE against frequency and population inversion density γ. We classify the values of NMSEs of laser modes at the interval of 0.1 except for the range NMSE > 0.4 because we consider that laser modes whose NMSEs exceed 0.4 do not work as cavities. We additionally investigate the distributions of four models whose rod arrangements are different from each other to confirm the general tendency of the distributions. The distributions of classified laser modes of one and five samples are shown in Figs. 4.25(a) and 4.25(b), respectively.

The laser modes whose NMSEs are relatively small are cavity modes. We observe a tendency that laser modes corresponding to cavity modes are distributed in smaller range of population inversion density γ. The same tendency is also observed in the result of five models shown in Fig. 4.25(b). However, in the higher range of population inversion density γ, only the non-cavity modes occur. These results of the laser mode distributions indicate that lasing phenomena caused by cavity modes, namely, lasing phenomena caused by Anderson localizations [26], can occur in the state of lower pumping of active material. The reason why the existence of non-cavity modes has not been mentioned in the previous study [12] can be considered that only the state of lower pumping of active material has been investigated and non-cavity modes did not appear. The existence of non-

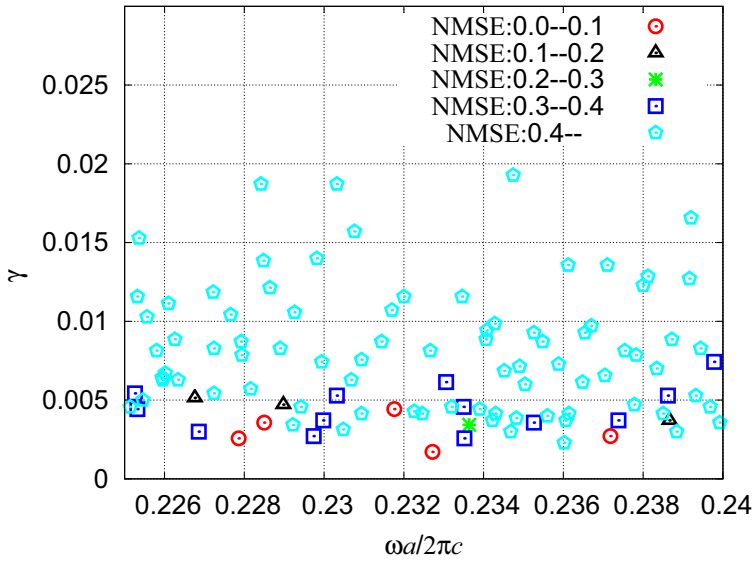

(a) 1 sample.

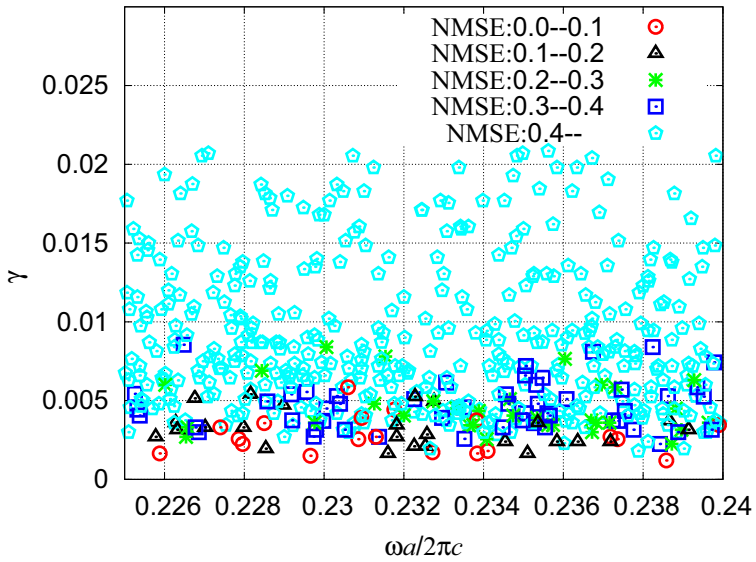

(b) 5 samples.

Figure 4.25: Distribution of laser mode with five ranges of NMSE.

cavity modes are discovered by our present study in which the dependences of lasing phenomena on both the frequency and population inversion density γ are investigated.

4.4.4 Conclusion

In the present study, the dependence of amplification of light waves flowing out from random systems on the electric field intensity in the systems is investigated by using FEM.

Lasing frequencies and population inversion densities of peaks observed in the results of amplification factor correspond to those of the electric field intensities in the random systems. Low-threshold lasing phenomena occur at the frequencies at which the intensities become to be in the state of no pumping of active material. Two types of laser modes, cavity and non-cavity modes, are observed. The cavity modes appear only in the low excited states of the active material, but the non-cavity modes are observed also in the higher excited states. Above tendency concerning the distribution of laser modes are also observed in the results for the five random structures whose rod arrangements are different from each other, and can be considered as a general tendency.

4.5 The effect of filling factor for lasing phenomena in dielectric random media

4.5.1 Introduction

In the random lasers, dielectric random media work as cavities in which light waves are confined [12, 49], thus, lasing phenomena are triggered also when the optically active material is in a low excited state [10]. Hence, lasing properties strongly depend on the structures of random media. Random scatterings are expected to become intensive as the filling factor of dielectric materials increases, and the strong scatterings lead to random lasing. Therefore, the filling factor of dielectric materials in random media is one of the important factors for laser action.

In the mean time, the amount of optically active materials in random systems is also an important factor for laser oscillations. In chapter 3 and section 4.2, we presented the analyses of lasing phenomena occurring in two different two-dimensional random media (2D-RM): one with optically active materials among nonactive dielectric rods and the other with optically active rods in nonactive media. We found that the first one can lase under a lower pumping than that of the second one, because light waves are localized in the interspace among dielectric rods. In the first random system, rate of the amount of optically active materials obviously reduces as the filling factor of dielectric rods increases. Therefore, the strength of scatterings in random media has a trade-off relationship with the amount of optically active materials.

We focus on the effect of filling factor of dielectric materials on random laser action and lasing threshold. Sebbah et al. investigated the relation between the filling factors and electric field intensity in random systems by means of the finite difference time domain method [12]. Chang et al. studied the influence of filling factor for localization length and decay length in one-dimensional systems [17]. Ramiro et al. investigated experimentally the transmittance and reflectance of optical crystals of various filling factors [50]. However, the dependence of lasing threshold on filling factor of dielectric materials has not been investigated so far.

In this study, we simulate numerically the laser action in two dimensional dielectric random media whose filling factor of dielectric rods is in the range between 10% and 50% to investigate appropriate filling factors for laser oscillation.

Positional disorder of dielectric rods is considered in this study. The case of light propagation for perpendicular direction against the cylinders, and one of the two polarizations, that is TM mode, are considered. Similar situations assumed here can be realized experimentally. Although the lasing along the cylinders and that in TE mode would also be interests of analysis, they are intractable due to its large computational cost and are material subjects in the future. We compute the flux of Poynting vector of light waves emitted from a random system with changing population inversion density, of optically active materials, modeled by negative imaginary part of relative permittivity. We employ perfectly matched layer (PML) [38] to treat scatterings of open regions with finite domains.

4.5.2 Analysis models

We analyze laser action in 2D-RM consisting of homogeneous dielectric rods by using finite element method (FEM). Dielectric rods are assumed to be infinitely long in z-direction and light waves are assumed to propagate within xy-plane. Also, we assume TM mode, i.e., the electric field has only z component. Figure 4.26(a) illustrates, from top view, the concept of random media. An oscillating electric polarization along the z axis is located at the center of whole random structure as a light source. We define three different circles: $\mathrm{C_{in}}$, $\mathrm{C_g}$, and $\mathrm{C_{out}}$, as shown in the figure. The light source is placed in $\mathrm{C_{in}}$, all of dielectric rods are placed in $\mathrm{C_g}$, and the flux of Poynting vector is computed on $\mathrm{C_{out}}$. $\mathbf{n}_{\mathrm{in}}$ and $\mathbf{n}_{\mathrm{out}}$ are unit outward normal vectors to the circles $\mathrm{C_{in}}$ and $\mathrm{C_{out}}$. Interspace between dielectric rods inside the circle $\mathrm{C_{out}}$ is denoted by Ω_{act}. Active materials are filled in the region Ω_{act}. Regions in dielectric rods and outside the circle $\mathrm{C_{out}}$ are denoted by Ω_{rod} and Ω_{out}. R_{in}, R_{g} and R_{out} are the radii of the circles $\mathrm{C_{in}}$, $\mathrm{C_g}$ and $\mathrm{C_{out}}$, respectively.

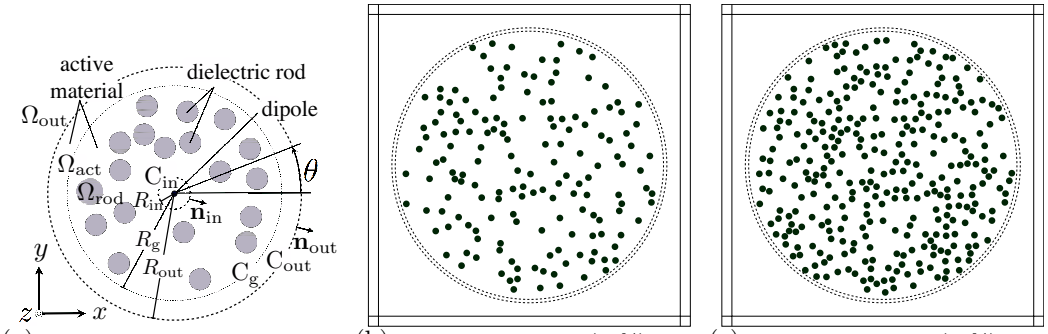

(a) Concept of two-dimensional random system.

(b) Filling Factor=0.1 (10%), The number of rods is 160.

(c) Filling Factor=0.2 (20%), The number of rods is 320.

(d) Filling Factor=0.3 (30%), The number of rods is 480.

(e) Filling Factor=0.4 (40%), The number of rods is 640.

(f) Filling Factor=0.5 (50%), The number of rods is 800.

Figure 4.26: Analysis models of each filling factor.

Table 4.6: Parameter of geometry

Parameter	Figure	value
Radius of rods	a	1
Radius of C_{in}	R_{in}	$1.5a$
Radius of C_{g}	R_{g}	$40a$
Radius of C_{out}	R_{out}	$41a$
Filling factor	f	0.1, 0.2, 0.3, 0.4, 0.5
Mean free path	l	$a\left(\sqrt{2\pi/\sqrt{3}f}-2\right)$
Position of center	(x_0, y_0)	$(0, 0)$
Width of PML		3a
Width of physical domain		90a

Dielectric rods are assumed to be homogeneous and randomly distributed within the circle C_g. The center positions of rods, (x_r, y_r), are given as follows:

$$\begin{bmatrix} x_r \\ y_r \end{bmatrix} = \begin{bmatrix} 2R_g \times \rho_x - R_g \\ 2R_g \times \rho_y - R_g \end{bmatrix}, \tag{4.8}$$

where R_g is the radius of the circle C_g, ρ_x and ρ_y are the pseudo random numbers generated by `drand` Fortran function with standard uniform distribution on the open interval (0, 1). If the rod area overlaps above the areas of other rods whose center positions had already been determined, or, if the whole region of a rod is not included within the circle C_g, we have to generate the center position again.

Filling factors of dielectric rods in each models are 10%, 20%, 30%, 40%, and 50%. Make analysis models with filling factor greater than 60% is difficult, because disordered distribution of dielectric rods needs some amount of space. Figure 4.26 shows analysis models created for the above filling factors. Solid circles represent dielectric rods, and two large outermost circles of dotted lines correspond to C_g and C_{out}. The physical domain is surrounded by PML [38] to prevent numerical reflections on the internal square-shaped boundary. We use an optimized absorbing function that minimizes the numerical reflection [41].

In our computations, the radius of the rods, a, is treated as the characteristic length. All the lengths are normalized by a. The light source is located at the center of the dielectric media, $\mathbf{x}_0 = (0, 0)$. All parameters used to make analysis models are shown in Table 1.

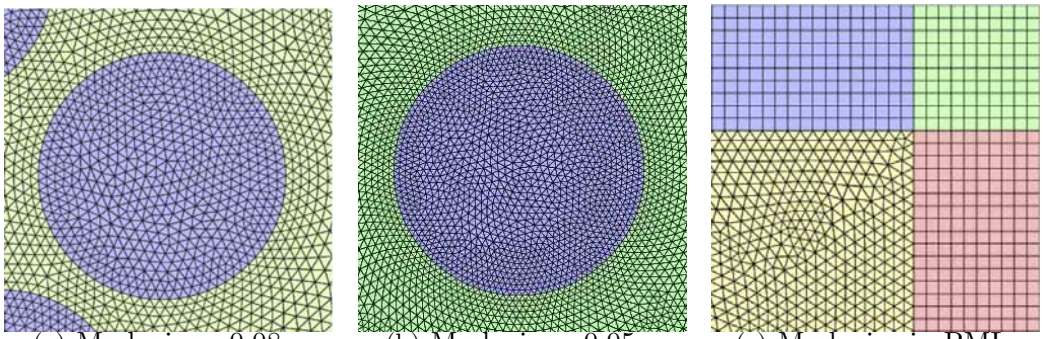

(a) Mesh size : $0.08a$. (b) Mesh size : $0.05a$. (c) Mesh size in PML.

Figure 4.27: Finite element meshing in physical and PML regions.

Figure 4.27 shows the finite element meshes of the analysis models. We use two types of mesh consisting of different sizes as shown in Figs. 4.27(a) and 4.27(b). Blue circles in Figs. 4.27(a) and 4.27(b) are the dielectric rods. Element

sizes are approximately $0.08a$ ($\simeq a/13$) for the mesh shown in Fig. 4.27(a) and $0.05a$ ($\simeq a/20$) for that in Fig. 4.27(b). Figure 4.27(c) shows the elements of PML area. By employing the square elements for PML area, the integrals including the absorbing function can be evaluated easily by using Gauss-Legendre quadrature formula.

In Table 4.7, we show the numbers of nodes and elements of each analysis model shown in Fig. 4.26.

Table 4.7: The number of nodes (NN) and elements (NE) of the models shown in Fig. 4.26.

Filling Factor	NN	NE
10% (Element Size:0.08a)	986525	1959368
10% (Element Size:0.05a)	1848712	3683742
20% (Element Size:0.08a)	972203	1930724
20% (Element Size:0.05a)	1908413	3803144
30% (Element Size:0.08a)	985092	1956502
30% (Element Size:0.05a)	1976566	3939450
40% (Element Size:0.08a)	1008494	2003306
40% (Element Size:0.05a)	2069769	4125856
50% (Element Size:0.08a)	1042334	2070986
50% (Element Size:0.05a)	2157910	4302138

4.5.3 Result

4.5.3.1 Lasing frequency

To investigate lasing frequency, we compute the amplification factors of light waves emitted from dielectric structures of the filling factors 10%, 20%, 30%, 40%, and 50%, with the fixed population inversion densities $\gamma = 0.001$, 0.002, and 0.005.

Figure 4.28 shows the computational results for amplification factor in the frequency range $0.1 \leq \omega a/2\pi c \leq 0.4$ with $\gamma = 0.001$, $\gamma = 0.002$ and 0.005. We observe divergent peaks of amplification factor in the results for the filling factors of 20%, 30%, 40%, and 50%.

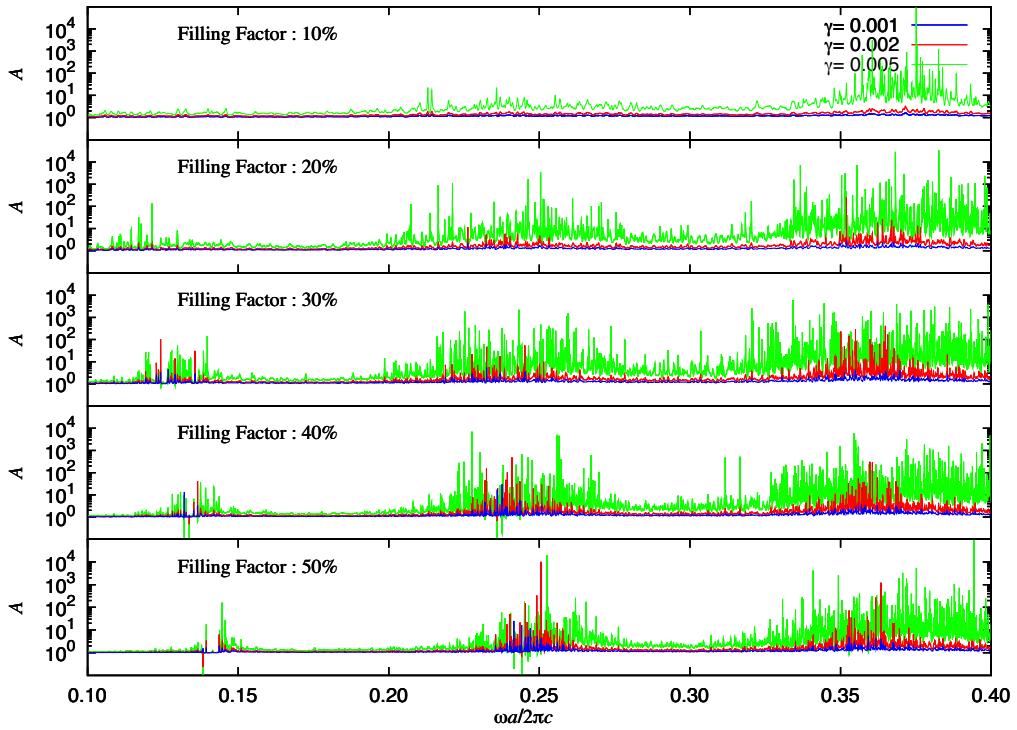

Figure 4.28: Laser action in the range of $0.1 \leq \omega a/2\pi c \leq 0.4$, (finite elements: $0.05a$).

Lasing phenomena observed in the results for the filling factors of 40% and 50% are remarkable in the ranges of $0.230 \leq \omega a/2\pi c \leq 0.245$ and $0.235 \leq \omega a/2\pi c \leq 0.250$, respectively. Lasing frequency becomes wider as the population inversion density γ increases. In the frequency range $0.225 \leq \omega a/2\pi c \leq 0.255$, laser action does not occur, even in the higher excited state $\gamma = 0.005$, in the dielectric structure with the filling factor of 10%.

Table 4.8: Filling factor and lasing frequency.

Filling Factor	Frequency Range
20%	$0.225 \leq \omega a/2\pi c \leq 0.255$
30%	$0.225 \leq \omega a/2\pi c \leq 0.255$
40%	$0.230 \leq \omega a/2\pi c \leq 0.245$
50%	$0.235 \leq \omega a/2\pi c \leq 0.250$

4.5.3.2 Lasing threshold

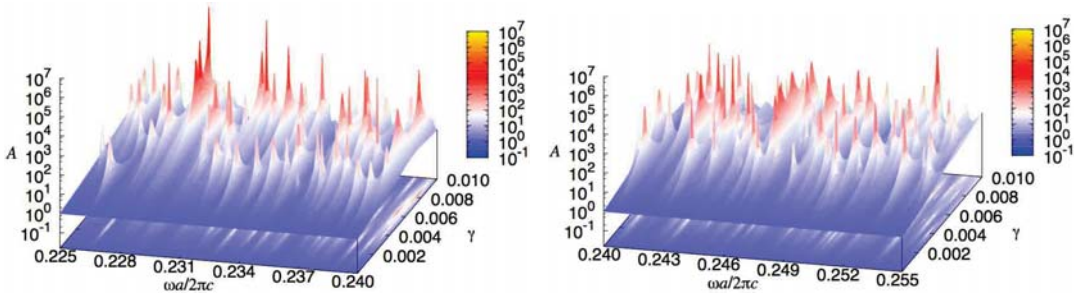

(a) $0.225 \leq \omega a/2\pi c \leq 0.240$. (b) $0.240 \leq \omega a/2\pi c \leq 0.255$.

Figure 4.29: Laser action in disordered structure of filling factor: 20% (finite elements : $0.08a$).

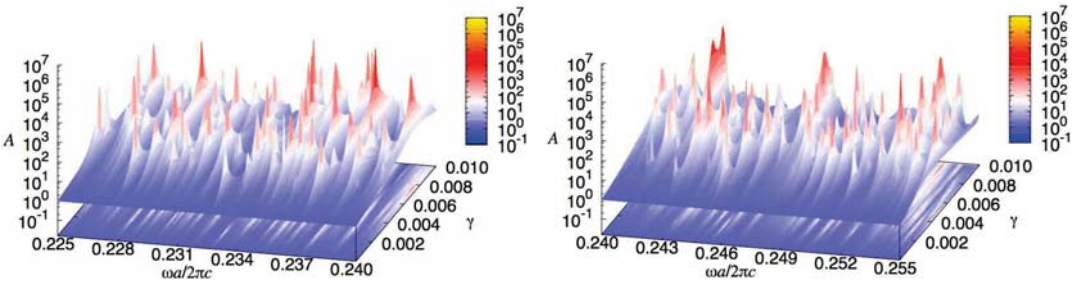

(a) $0.225 \leq \omega a/2\pi c \leq 0.240$. (b) $0.240 \leq \omega a/2\pi c \leq 0.255$.

Figure 4.30: Laser action in disordered structure of filling factor: 30% (finite elements : $0.08a$).

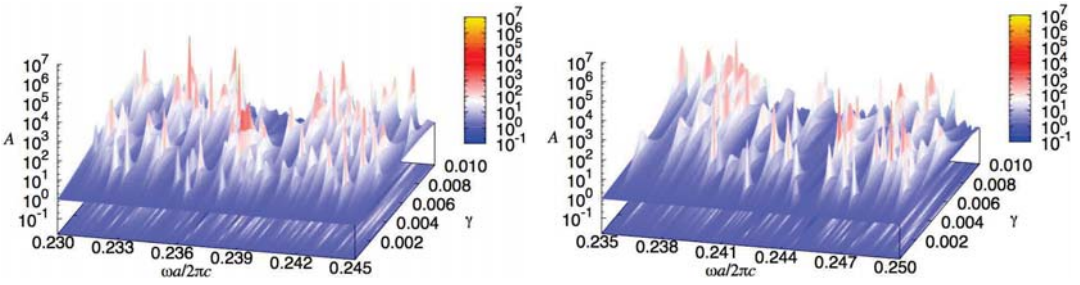

(a) Filling factor 40%. (b) Filling factor 50%.

Figure 4.31: Laser action in disordered structure of filling factors : 40% and 50% (finite elements : $0.08a$).

In this section, we pay attention to the effect of filling factor for lasing threshold. As stated in the previous sections, the population inversion density of optically active materials is proportional to the parameter γ defined in Eq. (2.41). Therefore, the parameter γ represents the lasing threshold of each lasing phe-

nomenon. Based on the results in Fig. 4.28, the lasing frequency ranges of each dielectric structures are determined. We show them in Table 4.8.

We compute the amplification factor, defined by Eq. (2.60), by changing not only the frequency but also the population inversion density γ. We found that laser action did not occur in dielectric structures with filling factor 10% from the results shown in Fig. 4.28.

Figures 4.29, 4.30, 4.31(a), and 4.31(b) are the results of laser action in dielectric structures whose filling factors are 20%, 30%, 40%, and 50%, respectively. These results show the relation between frequency, lasing threshold γ, and amplification factor whose divergent peaks are interpreted as lasing phenomena.

We investigate the lasing threshold represented by γ and the electric amplitude distribution (EAD) of lasing states. The thresholds of laser action, $\gamma = 8.7500 \times 10^{-4}$, in the dielectric structures with filling factors 40% and 50% are lower than the threshold $\gamma = 1.7500 \times 10^{-3}$ in the structure with the filling factor 30%. We plot EADs of lasing states with the lowest four thresholds, occurring in the dielectric structures, normalized by the incident electric field amplitude on the circle $\mathrm{C_{out}}$, that is, $\frac{|\mathbf{E}^{\mathrm{n}}|}{\left|\mathbf{E}_{\mathrm{i}}^{\mathrm{n}}\right|_{\mathrm{C_{out}}}}$. The positions of each lasing phenomenon, $(\omega a/2\pi c, \gamma)$, are shown in five significant figures.

Figure 4.32 illustrates the EADs of lasing states in a structure with filling factor 20%. The electric fields are spatially extended and cover the entire system. Figure 4.33 illustrates the EADs of lasing states occurring in a dielectric structure with filling factor 30%. The electric fields are found to become intensive in the interspace among the dielectric rods, namely, the electric field amplitude becomes large in the optically active material. Figures 4.34 and 4.35 illustrate the EADs of lasing states occurring in the dielectric structures with filling factors 40% and 50%, respectively. The electric fields also become intensive in the interspace among dielectric rods in the results for the filling factors of 40% and 50%. From the results shown in Figs. 4.32, 4.33, 4.34, and 4.35, we find that light waves are diffused for the filling factors of 20% and 30%, while they are localized for those of 40% and 50%. Such localizations in dielectric structures with higher filling factors might be generated by strong multiple scatterings, and cause the lower-threshold laser action.

We analyze five samples for each filling factor to confirm the tendency in the lasing thresholds. The square symbols in Fig. 4.36 represent the average of the

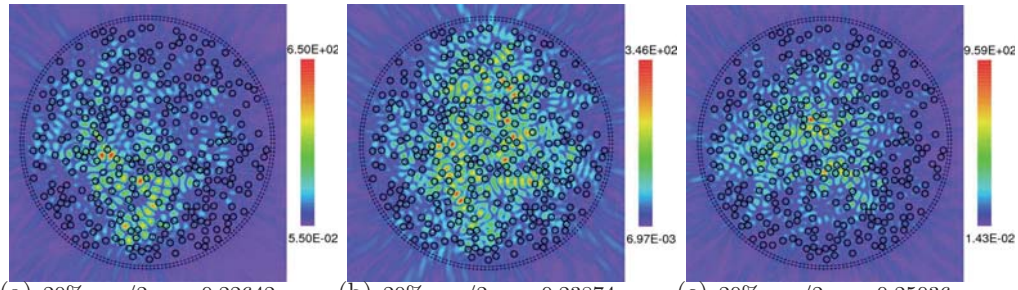

(a) 20%, $\omega a/2\pi c = 0.22642$, $\gamma = 2.7500 \times 10^{-3}$. (b) 20%, $\omega a/2\pi c = 0.23874$, $\gamma = 3.1250 \times 10^{-3}$. (c) 20%, $\omega a/2\pi c = 0.25036$, $\gamma = 3.1250 \times 10^{-3}$.

Figure 4.32: EADs of lasing states in a structure with filling factors 20%.

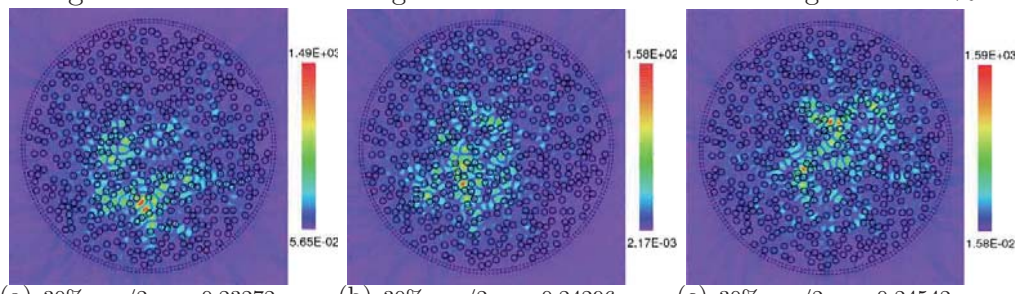

(a) 30%, $\omega a/2\pi c = 0.23272$, $\gamma = 1.7500 \times 10^{-3}$. (b) 30%, $\omega a/2\pi c = 0.24296$, $\gamma = 1.8750 \times 10^{-3}$. (c) 30%, $\omega a/2\pi c = 0.24542$, $\gamma = 2.0000 \times 10^{-3}$.

Figure 4.33: EADs of lasing states in a structure with filling factors 30%.

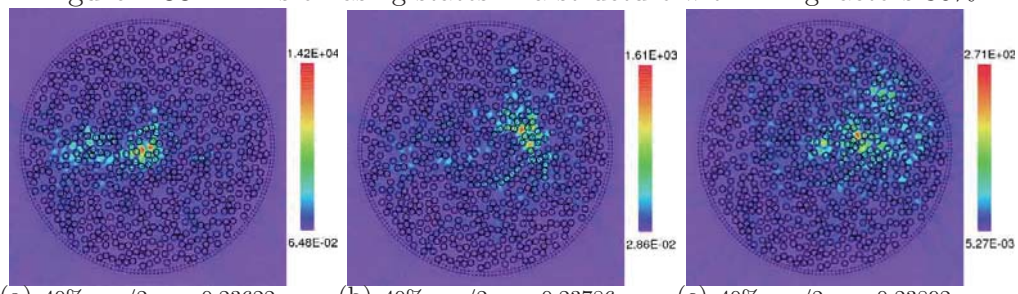

(a) 40%, $\omega a/2\pi c = 0.23622$, $\gamma = 8.7500 \times 10^{-4}$. (b) 40%, $\omega a/2\pi c = 0.23786$, $\gamma = 1.1250 \times 10^{-3}$. (c) 40%, $\omega a/2\pi c = 0.23892$, $\gamma = 1.7500 \times 10^{-3}$.

Figure 4.34: EADs of lasing states in a structure with filling factors 40%.

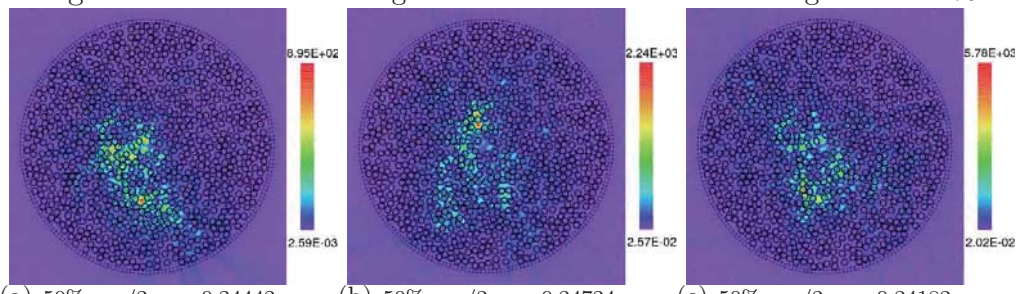

(a) 50%, $\omega a/2\pi c = 0.24442$, $\gamma = 8.7500 \times 10^{-4}$. (b) 50%, $\omega a/2\pi c = 0.24724$, $\gamma = 1.1250 \times 10^{-3}$. (c) 50%, $\omega a/2\pi c = 0.24182$, $\gamma = 1.2500 \times 10^{-3}$.

Figure 4.35: EADs of lasing states in a structure with filling factors 50%.

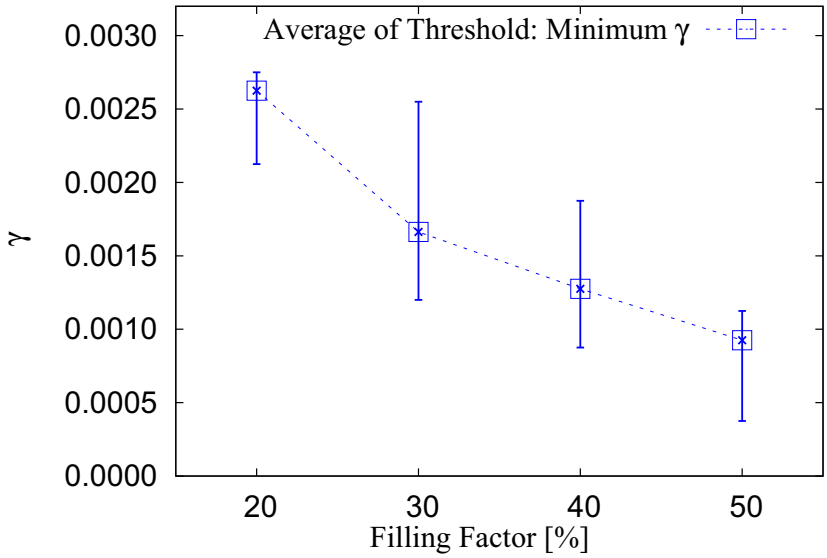

Figure 4.36: Lasing threshold versus filling factor.

smallest values of γ at which the lasing phenomena occurr for five models with the different filling factors, and the vertical bars on the square symbols show the ranges of γ of five models. We observe a reduction in the lasing threshold against the increase in the filling factor. A higher filling factor is found to be appropriate for lower-threshold laser generation. We do not found any big difference in the results of five different rod arrangements for each filling factor with respect to lasing frequency and EAD.

4.5.4 Conclusions

In this section, we investigated the appropriate filling factor for lower-threshold laser action by modeling the population inversion density of optically active material with a negative imaginary part of relative permittivity. Lasing threshold becomes lower as filling factor increases. We confirmed this tendency by analyzing five different models. The strength of scattering has been found to be more important than the amount of optically active materials to make the lasing threshold lower.

4.6 Transition from photonic-crystal laser to random laser

4.6.1 Introduction

Both the lasing phenomena in random systems [10, 11, 28, 51, 12, 14, 18, 13, 47, 15, 29, 30, 52, 53] and those in photonic crystals [1, 2, 54, 55, 56], have hopeful properties that the conventional laser devices cannot give. Photonic crystals are widely used in various optical devices for controlling light waves because of their noticeable abilities caused by their periodic structures. It is known that low-threshold laser action can be realiezed in photonic crystals [3, 4, 5] due to the extremely low group velocities at band edge frequencies. Random lasers occur from multiple scatterings and interference effects, causing Anderson localizations[26], in disordered structures, thus their laser modes take various and complex forms. Lawandy et al. mentioned that the lasing threshold of random lasers was extremely low [10].

In sections 4.2, 4.3, 4.5, and chapter 3, we discussed lasing threshold of random lasers. The effects of positions of active medium [48] and filling factor of dielectric cylinders [57] on the lasing threshold were investigated and appropriate dielectric structures for lower threshold laser action were proposed.

Photonic crystals including small amounts of disorders have been investigated actively. There are many numerical and experimental studies on the effects of disorders on the optical properties of photonic crystals, such as band structures [58, 59, 60], light localizations [58, 61, 62], transmissions [60, 63, 64, 65, 66, 67, 68, 69, 70, 71, 72], and reflectance[73]. These previous studies treated various types of disorders, for example, in size [64, 70, 72, 74, 75, 76], positions [18, 12, 13, 47, 65, 68, 71, 74, 77, 78, 79], shapes of dielectric material [58, 80, 81], refractive indices [66, 70, 75], surface roughness [82, 83, 84, 79, 68, 65, 78], and fabrication errors[85, 86]. Additionally, we can also find a paper showing the effects of disorder on lasing phenomena in dielectric structures. Kwan et al. [87] studied the effect of position and size-disorder on the emission spectra, and the lasing frequency at the highest intensity emission with a fixed pumping rate. However, no studies are found on the influence of disorder on lasing threshold.

In this section, we present an investigation on the transition from photonic-crystal laser to random laser as a new research topic to realize lower threshold laser action. We simulate lasing phenomena numerically to investigate the

changes of lasing thresholds under the influence of disorders in two-dimensional dielectric structures. Disorder of dielectric structures is treated by giving positional disorders of dielectric cylinders. The amount of disorder is parameterized with the length between the grid points corresponding to the centers of fictitious rods distributed periodically and the centers of randomly distributed rods. We reveal the change of lasing threshold against the amount of disorder and find an appropriate one for lower-threshold laser action.

4.6.2 Analysis model

We show a model of a dielectric system in Fig. 4.37(a). Dielectric rods are assumed to be infinitely long in vertical direction (z-direction) and light waves propagate within xy-plane. Figure 4.37(b) shows the concept of a random system from the top view. Dielectric rods are arranged randomly in the region between circles $\mathrm{C_{in}}$ and $\mathrm{C_g}$, as shown in Fig. 4.37(b). An oscillating dipole is assumed to exist at the center of the circle $\mathrm{C_{in}}$ as a light source. Radii of $\mathrm{C_{in}}$ and $\mathrm{C_g}$ are denoted by R_{in} and R_{g}, respectively. We compute the fluxes of Poynting vectors of out-flowing light waves on the circle $\mathrm{C_{out}}$ whose radius is R_{out}. The unit outward normal vectors to $\mathrm{C_{in}}$ and $\mathrm{C_{out}}$ are denoted by $\mathbf{n}_{\mathrm{in}}$ and $\mathbf{n}_{\mathrm{out}}$, respectively. We define three regions: Ω_{act}, Ω_{rod} and Ω_{out}, where Ω_{act} is in the iterspace between the rods inside the circle $\mathrm{C_{out}}$, Ω_{rod} is the union of the regions inside the rods, and Ω_{out} is the region outside the circle $\mathrm{C_{out}}$. The optically active materials are assumed to be filled in the region Ω_{act}.

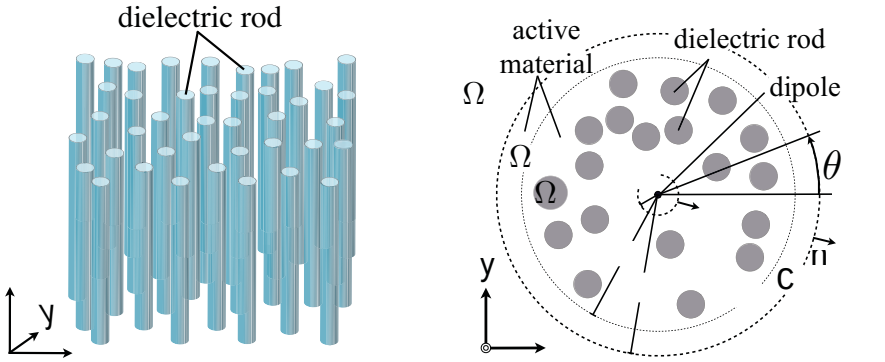

(a) A random structure model. (b) An illustration of whole random system.

Figure 4.37: Concept of random media.

4.6.2.1 Model parameters

Table 4.9: Model parameters.

Parameter	Denotation	Value
Radius of rods	a	1 : characteristic length
Filling factor	f	0.3 (30%)
Radius of C_{in}	R_{in}	$1.5a$
Radius of C_g	R_g	$39a$
Radius of C_{out}	R_{out}	$40a$
TMFP	l	$a\left(\sqrt{2\pi/\sqrt{3}f} - 2\right)$
Periodic length		$l + 2a$
Position of center	(x_0, y_0)	$(0, 0)$
Width of PML		$3a$
Width of whole model		$93a$
The number of rod		432

In Table 4.9 is shown the parameters used to create the analysis models. The radii of the cross sections of the rods are assumed to be the same, and the radius, a, is treated as the characteristic length. The size of the analysis models is normalized by a. We create the analysis model of the periodic structure, corresponding to $|\Delta \mathbf{x}_r|_{max} = 0$, of triangular lattice, by giving the TMFP, denoted by l, and the periodic length of the periodic structure. The values of the TMFP and the periodic length are given as $l = 1.47735a$ and $3.47735a$, respectively. The coordinate values of the rod's center are specified in single precision numbers.

4.6.2.2 Disordered systems

A parameter used to control disorder of the rod arrangement is defined in Fig. 4.38. The circles drawn by broken lines illustrate fictitious rods of a periodic structure. The centers of these circles are used as the datum points to control the rods arranged in disorder. Centers of the circles are denoted by $\mathbf{x}_p$. A circle drawn by a solid line illustrates a rod arranged in disorder, whose center is denoted by $\mathbf{x}_r$.

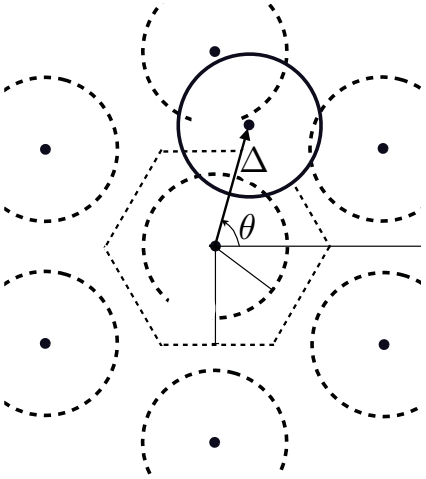

Figure 4.38: Parameterization of disorder by $\Delta\mathbf{x}_{\mathrm{r}}$.

The disordered position $\mathbf{x}_{\mathrm{r}}$ is determined by a sum of $\mathbf{x}_{\mathrm{p}}$ and a random vector $\Delta\mathbf{x}_{\mathrm{r}}$, as follows:

$$\mathbf{x}_{\mathrm{r}}(n,m) = \mathbf{x}_{\mathrm{p}}(n,m) + \Delta\mathbf{x}_{\mathrm{r}}, \tag{4.9}$$

where n and m are latiice-point numbers and $(n,m) \neq (0,0)$. $\mathbf{x}_{\mathrm{p}}$ are defined as

$$\mathbf{x}_{\mathrm{p}}(n,m) = n\mathbf{r}_1 + m\mathbf{r}_2, \tag{4.10}$$

where $\mathbf{r}_1$ and $\mathbf{r}_2$ are lattice vectors defined as

$$\mathbf{r}_1 = [\ 3.47735a \times \sqrt{3}/2,\ 3.47735a \times 1/2\ ]^{\mathrm{T}}, \tag{4.11}$$

$$\mathbf{r}_2 = [\ 0.0,\ 3.47735a\ ]^{\mathrm{T}}, \tag{4.12}$$

where $3.47735a$ is the periodic length.

We restrict the length of the random vector $\Delta\mathbf{x}_{\mathrm{r}}$ as

$$0 \leq |\Delta\mathbf{x}_{\mathrm{r}}| \leq |\Delta\mathbf{x}_{\mathrm{r}}|_{\max}, \tag{4.13}$$

where $|\Delta\mathbf{x}_{\mathrm{r}}|_{\max}$ is the maximum length of the random vector. The amounts of disorders in dielectric structures are evaluated with $|\Delta\mathbf{x}_{\mathrm{r}}|_{\max}$. In the case $|\Delta\mathbf{x}_{\mathrm{r}}|_{\max} = 0$, a dielectric structure becomes periodic. In Fig. 4.38, L_{H}, the distance between the edge of the hexagonal lattice and the center of the rod

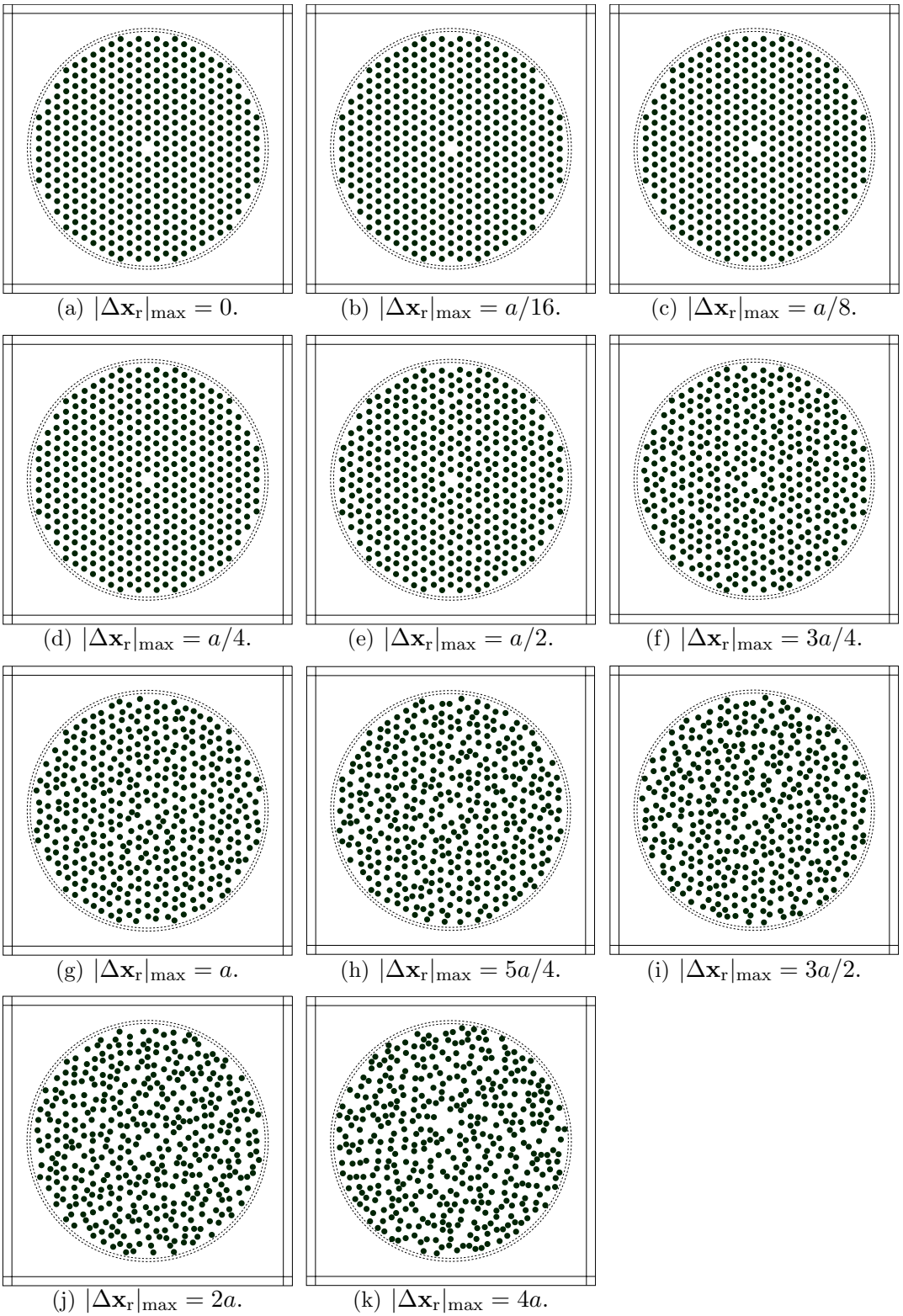

(a) $|\Delta \mathbf{x}_\mathrm{r}|_\mathrm{max} = 0$. (b) $|\Delta \mathbf{x}_\mathrm{r}|_\mathrm{max} = a/16$. (c) $|\Delta \mathbf{x}_\mathrm{r}|_\mathrm{max} = a/8$.

(d) $|\Delta \mathbf{x}_\mathrm{r}|_\mathrm{max} = a/4$. (e) $|\Delta \mathbf{x}_\mathrm{r}|_\mathrm{max} = a/2$. (f) $|\Delta \mathbf{x}_\mathrm{r}|_\mathrm{max} = 3a/4$.

(g) $|\Delta \mathbf{x}_\mathrm{r}|_\mathrm{max} = a$. (h) $|\Delta \mathbf{x}_\mathrm{r}|_\mathrm{max} = 5a/4$. (i) $|\Delta \mathbf{x}_\mathrm{r}|_\mathrm{max} = 3a/2$.

(j) $|\Delta \mathbf{x}_\mathrm{r}|_\mathrm{max} = 2a$. (k) $|\Delta \mathbf{x}_\mathrm{r}|_\mathrm{max} = 4a$.

Figure 4.39: Analysis models.

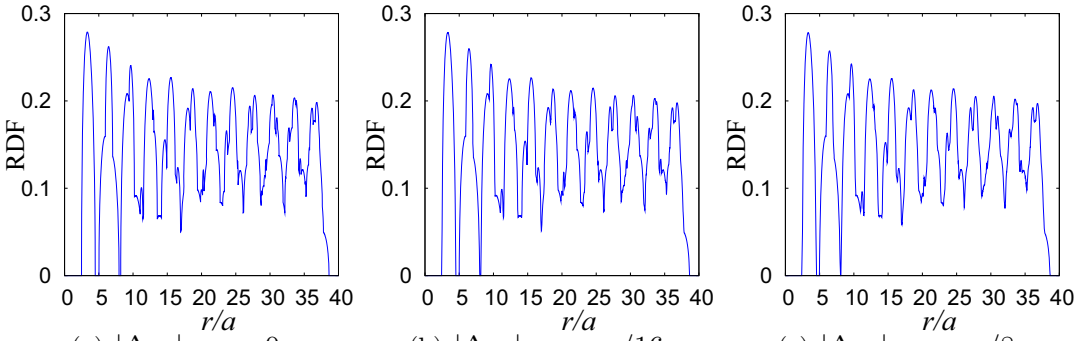

(a) $|\Delta \mathbf{x}_\mathrm{r}|_\mathrm{max} = 0$. (b) $|\Delta \mathbf{x}_\mathrm{r}|_\mathrm{max} = a/16$. (c) $|\Delta \mathbf{x}_\mathrm{r}|_\mathrm{max} = a/8$.

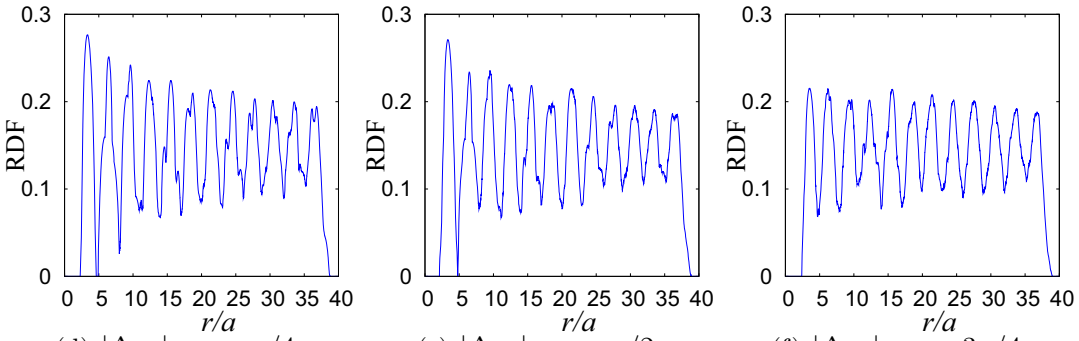

(d) $|\Delta \mathbf{x}_\mathrm{r}|_\mathrm{max} = a/4$. (e) $|\Delta \mathbf{x}_\mathrm{r}|_\mathrm{max} = a/2$. (f) $|\Delta \mathbf{x}_\mathrm{r}|_\mathrm{max} = 3a/4$.

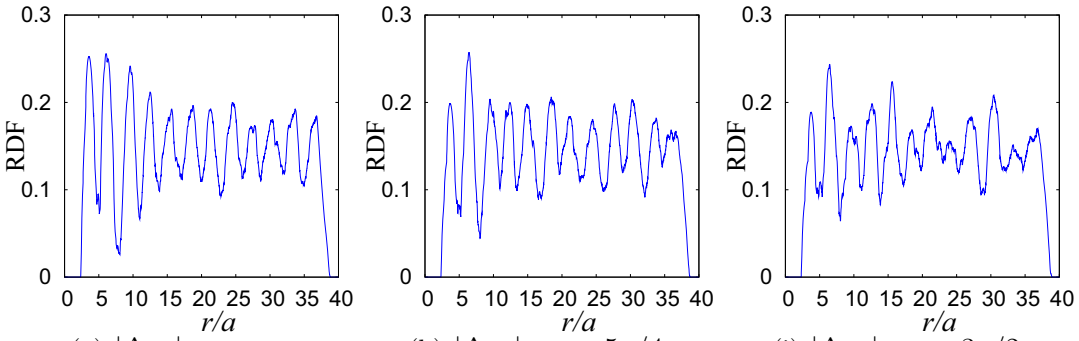

(g) $|\Delta \mathbf{x}_\mathrm{r}|_\mathrm{max} = a$. (h) $|\Delta \mathbf{x}_\mathrm{r}|_\mathrm{max} = 5a/4$. (i) $|\Delta \mathbf{x}_\mathrm{r}|_\mathrm{max} = 3a/2$.

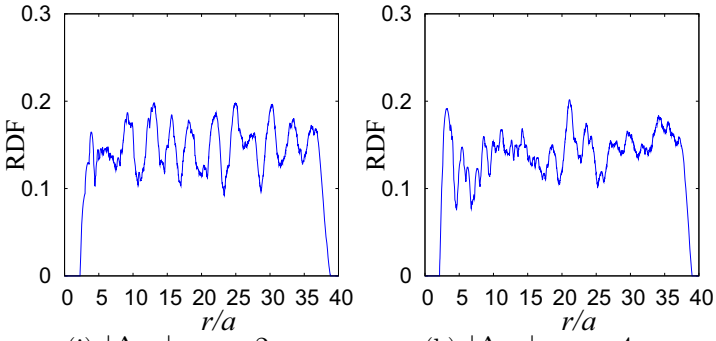

(j) $|\Delta \mathbf{x}_\mathrm{r}|_\mathrm{max} = 2a$. (k) $|\Delta \mathbf{x}_\mathrm{r}|_\mathrm{max} = 4a$.

Figure 4.40: Analysis models and radial distribution functions (RDFs).

periodically distributed and included in the lattice, is equal to $1.73867a$, a half of the periodic length. Therefore, when $L_\mathrm{H} < |\Delta \mathbf{x}_\mathrm{r}|_\mathrm{max}$, the center of the rod

distributed randomly is located within the adjacent hexagonal lattice. When $|\Delta \mathbf{x}_{\mathrm{r}}|_{\max}$ is smaller than $L_{\mathrm{H}} - a = 0.73867a$, the entire region of the rod is included in each lattices.

We analyze lasing phenomena in dielectric structures for various $|\Delta \mathbf{x}_{\mathrm{r}}|_{\max}$. The analysis models for these values are shown in Fig. 4.40 with radial distribution functions. Radial distribution functions describe the change of the density of dielectric cylinders as the function of the distance from the center of dielectric structures. The functions express how dielectric structures are disordered.

4.6.3 Results

4.6.3.1 Lasing frequency

Figure 4.41 shows the result of laser action in the periodic structure.

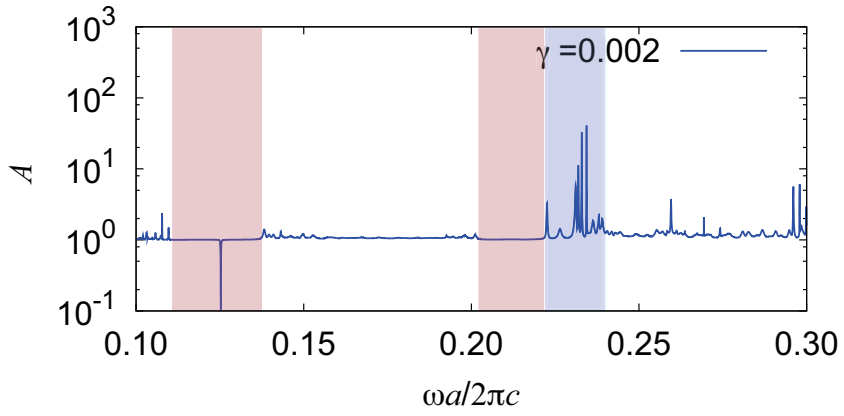

Figure 4.41: Amplification factor versus normalized frequency $\omega a/2\pi c$ for $\gamma = 0.002$.

We compute the amplification factor for the frequency range $0.1 \leq \omega a/2\pi c \leq 0.3$ with fixed population inversion density $\gamma = 0.002$ to investigate lasing frequencies of the periodic structure corresponding to $|\Delta \mathbf{x}_{\mathrm{r}}|_{\max} = 0$. We also show the band structure of the periodic structure, computed by the plane wave expansion method, in Fig. 4.42. In the result shown in Fig. 4.41, we cannot achieve sufficient computational accuracy in red-colored frequency ranges corresponding to band gaps in Fig. 4.42.

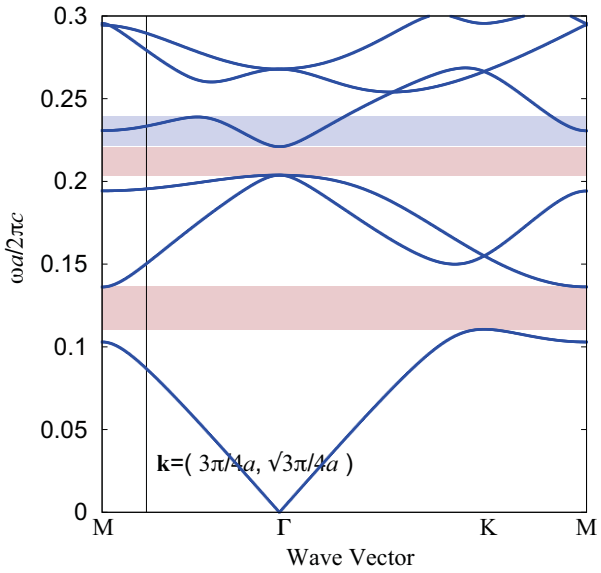

Figure 4.42: Dispersion relation of light waves in the periodic structure.

We observe laser action in the frequency range colored blue in Fig. 4.41, $0.222 \leq \omega a/2\pi c \leq 0.240$. We observe this frequency range, in which laser action occurs, corresponds to that of fourth-lowest band in Fig. 4.42. We show in Fig. 4.43 the electric field intensity distributions corresponding to the wave vector, $\mathbf{k} = (3\pi/4a, \sqrt{3}\pi/4a)$, of each band in Fig. 4.42. Figure 4.43(a) shows the unit cell of the periodic structure. We find in the distribution of the fourth-lowest band shown in Fig. 4.43(e), the electric field intensity in interspace among dielectric rods becomes high, i.e., the electric field becomes intensive within an optically active material. The laser action in Fig. 4.41 is thought to be caused by such light localization in an optically active material.

4.6.3.2 Laser action

We compute the amplification factors A defined by Eq. (2.60) for the ranges of $0.222 \leq \omega a/2\pi c \leq 0.240$ and $0.000 \leq \gamma \leq 0.021$, corresponding to the fourth lowest band. Figure 4.45 shows the laser action in the dielectric structures for each value of the disorder index $|\Delta \mathbf{x}_{\mathrm{r}}|_{\max}$. We calculate the amplification factors for 127,041 grid points for $\omega a/2\pi$c and γ, by dividing $\omega a/2\pi$c and γ directions uniformly into 900 an 140 intervals, respectively, and seek the steep peaks of the surface of amplification factor A.

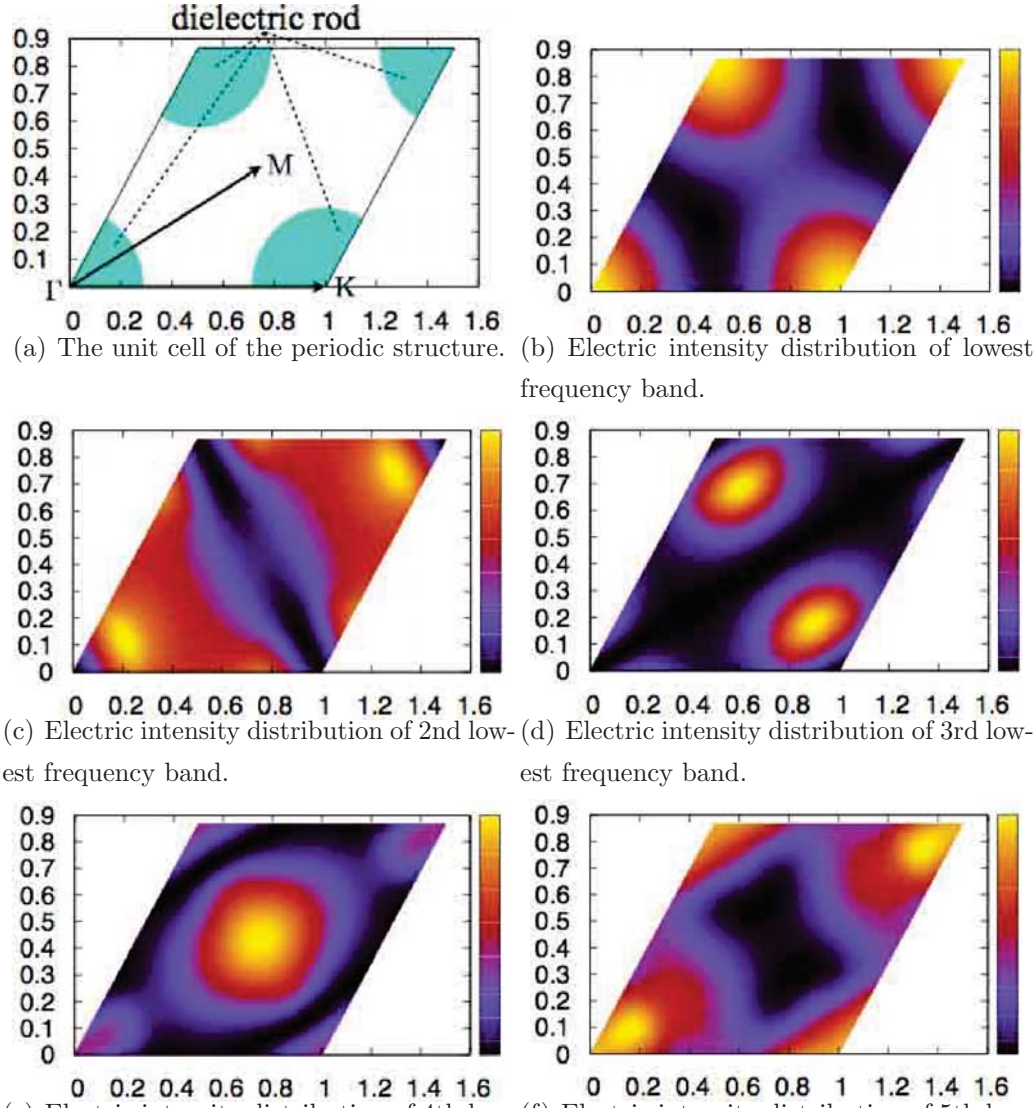

(a) The unit cell of the periodic structure.

(b) Electric intensity distribution of lowest frequency band.

(c) Electric intensity distribution of 2nd lowest frequency band.

(d) Electric intensity distribution of 3rd lowest frequency band.

(e) Electric intensity distribution of 4th lowest frequency band.

(f) Electric intensity distribution of 5th lowest frequency band.

Figure 4.43: Electric intensity distributions in the unit cell of the periodic structure.

Figure 4.44(a) shows the distribution of the amplification factor corresponding to the combinations of $\omega a/2\pi c$ and γ. From this result, we find specific combinations of the values of $\omega a/2\pi c$ and γ at which lasing phenomena occur in the periodic structure. Excitation within the fourth lowest band in the dispersion relation occurs as the surface of the amplification factor A and the lasing phenomena occur at their peaks. Figure 4.44(b) shows a laser action occurring at band-edge frequency. This laser action occurs at the smallest value of γ among the results of the periodic structure. Therefore, this laser action is considered to

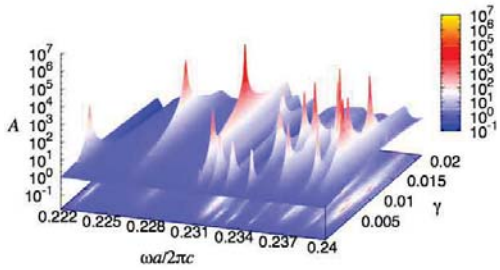

(a) $|\Delta \mathbf{x}_{\mathrm{r}}|_{\max}/a = 0$(periodic structure).

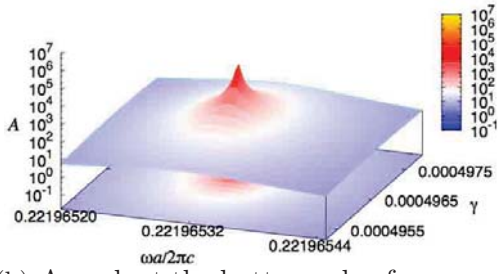

(b) A peak at the bottom edge frequency $\omega a/2\pi c = 0.22196531$ of the 4th band for $|\Delta \mathbf{x}_{\mathrm{r}}|_{\max}/a = 0$ (periodic structure).

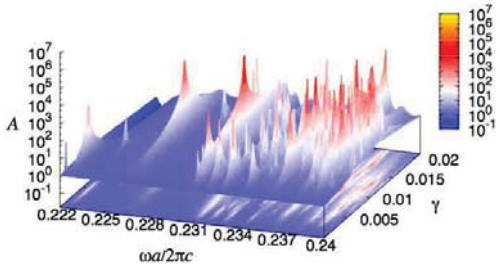

(c) $|\Delta \mathbf{x}_{\mathrm{r}}|_{\max}/a = 1/16$.

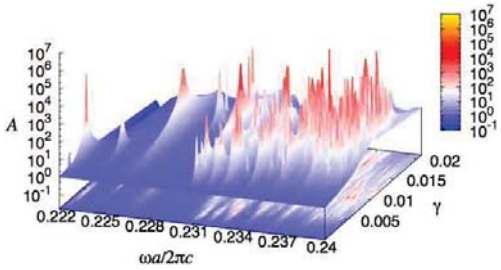

(d) $|\Delta \mathbf{x}_{\mathrm{r}}|_{\max}/a = 1/8$.

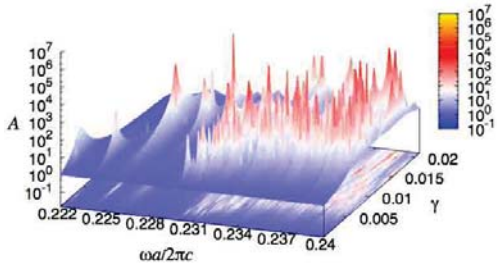

(e) $|\Delta \mathbf{x}_{\mathrm{r}}|_{\max}/a = 1/4$.

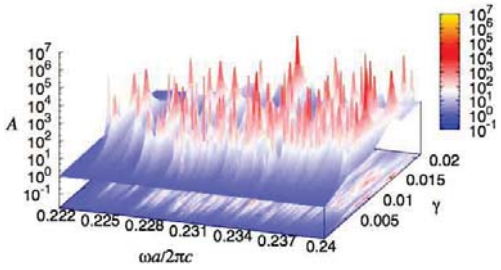

(f) $|\Delta \mathbf{x}_{\mathrm{r}}|_{\max}/a = 1/2$.

Figure 4.44: Amplification factor A versus normalized frequency $\omega a/2\pi c$ and γ for each $|\Delta \mathbf{x}_{\mathrm{r}}|_{\max}$.

be the lowest threshold one. The value of the amplification factor of this laser action is greater than 10^4.

In Figs. 4.44(c) to 4.45(f), we observe that surface of amplification factor reflects the effect of disorder on laser action. The lasing phenomena caused by random light scatterings noticeably emerge as the disorder of the structure increases. Such lasing phenomena are found more in higher frequency range $0.23 \leq \omega a/2\pi c \leq 0.24$, in the results for small amounts of disorder, $|\Delta \mathbf{x}_{\mathrm{r}}|_{\max} = a/16$, $a/8$, and $a/4$, shown in Figs. 4.44(c), 4.44(d), and 4.44(e), respectively. Lasing phenomena occurring in the periodic structure are also found even in the results of small amounts of disorder. However, in the case of higher disorder, i.e. $a/2 \leq |\Delta \mathbf{x}_{\mathrm{r}}|_{\max}$, lasing phenomena caused by random light scatterings become

noticeable also in the lower frequency range, and lasing phenomena found in the periodic structure disappear.

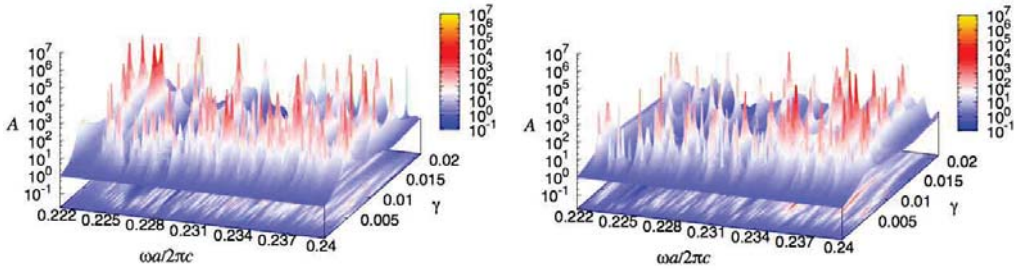

(a) $|\Delta \mathbf{x}_\mathrm{r}|_\mathrm{max}/a = 3/4$. (b) $|\Delta \mathbf{x}_\mathrm{r}|_\mathrm{max}/a = 1$.

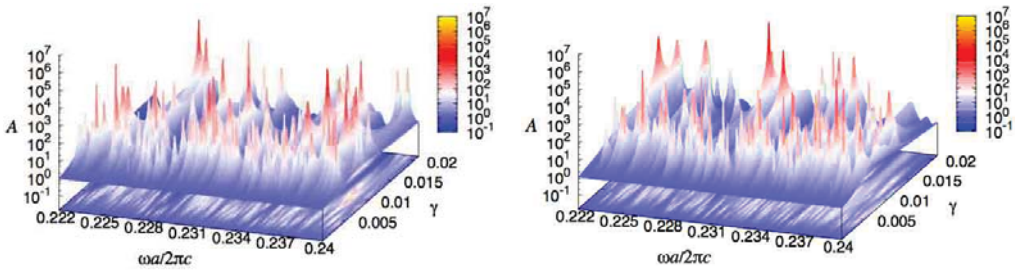

(c) $|\Delta \mathbf{x}_\mathrm{r}|_\mathrm{max}/a = 5/4$. (d) $|\Delta \mathbf{x}_\mathrm{r}|_\mathrm{max}/a = 3/2$.

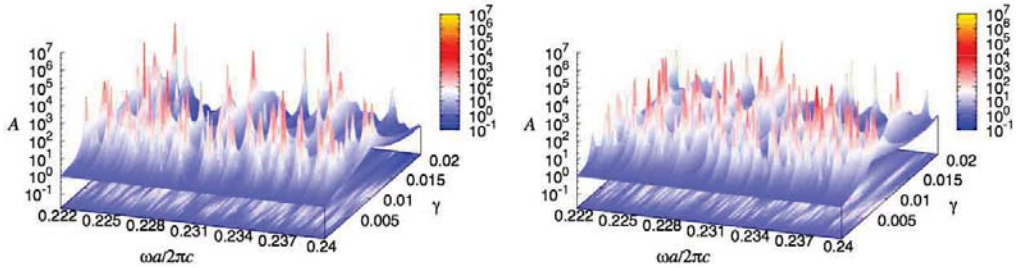

(e) $|\Delta \mathbf{x}_\mathrm{r}|_\mathrm{max}/a = 2$. (f) $|\Delta \mathbf{x}_\mathrm{r}|_\mathrm{max}/a = 4$.

Figure 4.45: Amplification factor A versus normalized frequency $\omega a/2\pi c$ and γ for each $|\Delta \mathbf{x}_\mathrm{r}|_\mathrm{max}$.

4.6.3.3 Lasing threshold

Parameter γ, interpreted as the imaginary part of relative permittivity, is proportional to population inversion density of optically active material. Hence, steep peaks of the amplification factors in the region with small γ are interpreted as occurrences of low-threshold laser generation. To find how lasing threshold changes in accordance with the increase of the disorder index $|\Delta \mathbf{x}_\mathrm{r}|_\mathrm{max}$, we investigate the smallest value of γ at which laser action occurs. To seek the more precise values of $\omega a/2\pi c$ and γ at which the lowest-threshold laser action occurs, we scan the

neighborhood of the amplification peak using finer numerical steps.

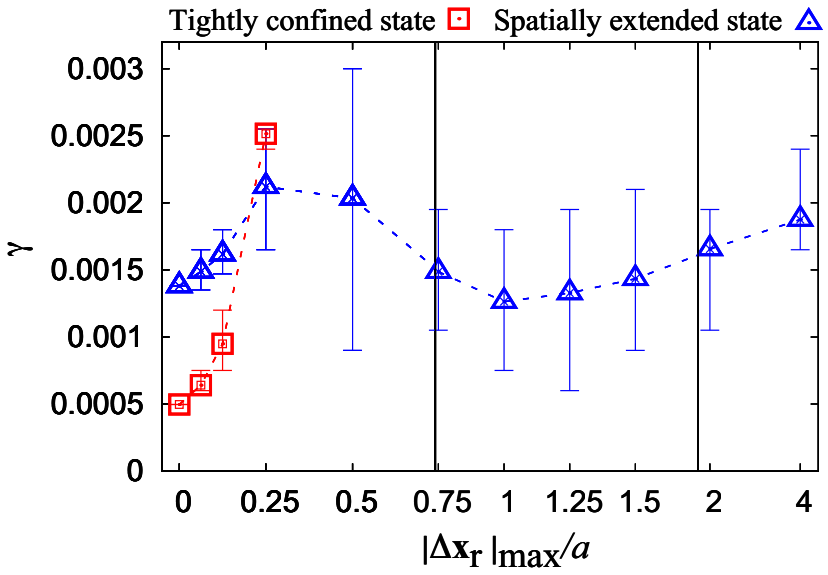

Figure 4.46: Relation between disorder index $|\Delta \mathbf{x}_{\mathrm{r}}|_{\max}$ and the average value of lowest lasing thresholds γ with error bar.

Average values of the lowest thresholds for different disorder index values are plotted in Fig. 4.46 with error bars showing the ranges of γ. We analyze 10 different types of rod arrangement for each disorder index other than $|\Delta \mathbf{x}_{\mathrm{r}}|_{\max} = 0$ to check the lasing threshold tendency. We find two types of lowest-threshold laser modes: those with tight confinement and spacial extension of light wave.

The threshold of the tightly confined mode, plotted by red squares and line in Fig. 4.46, rises as the disorder index increases. Such laser modes finally disappear when $a/2 \leq |\Delta \mathbf{x}_{\mathrm{r}}|_{\max}$.

We show next the electric amplitude distributions (EADs) of tightly confined laser mode in Fig. 4.47. The angular distributions of group velocities of light waves in a periodic array are computed with tight-binding approximation and are shown in Fig. 4.48. From the comparison between the results shown in Figs. 4.47 and 4.48, we confirm that such tightly confined modes occur from the periodic array structure of dielectric rods. We observe that light wave confinement becomes weak as the disorder index increases, particularly in Fig. 4.47(d). Such leakage of light is considered to lead to the rise in the lasing threshold of the laser action with the tight confinement of light wave.

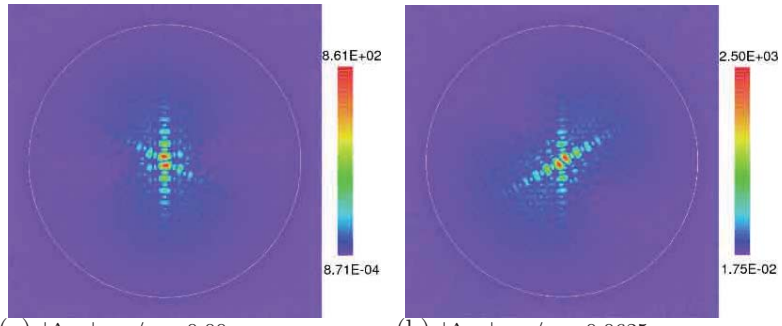

(a) $|\Delta \mathbf{x}_{\mathrm{r}}|_{\max}/a = 0.00$, $(\frac{\omega a}{2\pi c}, \gamma) = (0.22196531, 0.0004965)$.

(b) $|\Delta \mathbf{x}_{\mathrm{r}}|_{\max}/a = 0.0625$, $(\frac{\omega a}{2\pi c}, \gamma) = (0.2221812, 0.0007350)$.

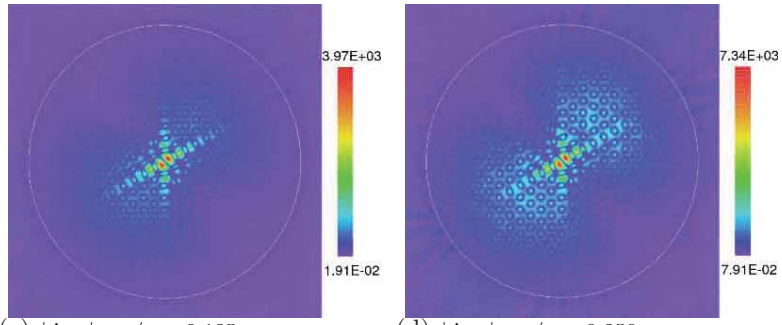

(c) $|\Delta \mathbf{x}_{\mathrm{r}}|_{\max}/a = 0.125$, $(\frac{\omega a}{2\pi c}, \gamma) = (0.2223220, 0.001140)$.

(d) $|\Delta \mathbf{x}_{\mathrm{r}}|_{\max}/a = 0.250$, $(\frac{\omega a}{2\pi c}, \gamma) = (0.2222716, 0.002490)$.

Figure 4.47: Electric amplitude distributions of lasing states with tight confinement (sample 1).

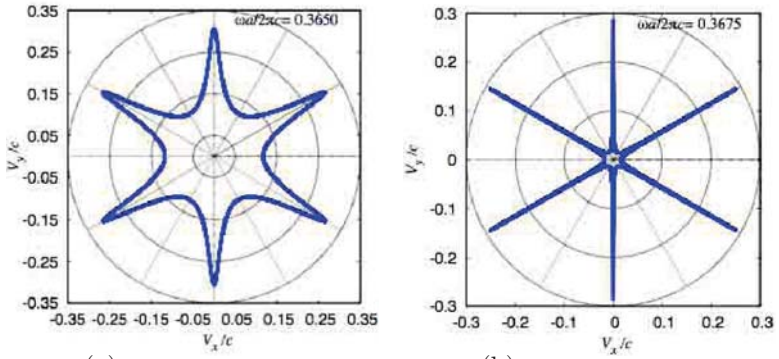

(a) $\omega a/2\pi c = 0.3650$.

(b) $\omega a/2\pi c = 0.3675$.

Figure 4.48: Polar plots of the group velocity of tight-binding model.

We also show the lowest threshold lasing phenomena with spacial extension of light wave in Fig. 4.46. Blue triangles and line in the Figures show the dependence of the threshold of the lasing phenomena with spatial extension on the disorder index. As this index increases, the threshold rises in $|\Delta \mathbf{x}_{\mathrm{r}}|_{\max}/a < 0.250$, then decreases in $0.250 < |\Delta \mathbf{x}_{\mathrm{r}}|_{\max}/a < 1.00$. In Fig. 4.46, the average threshold of

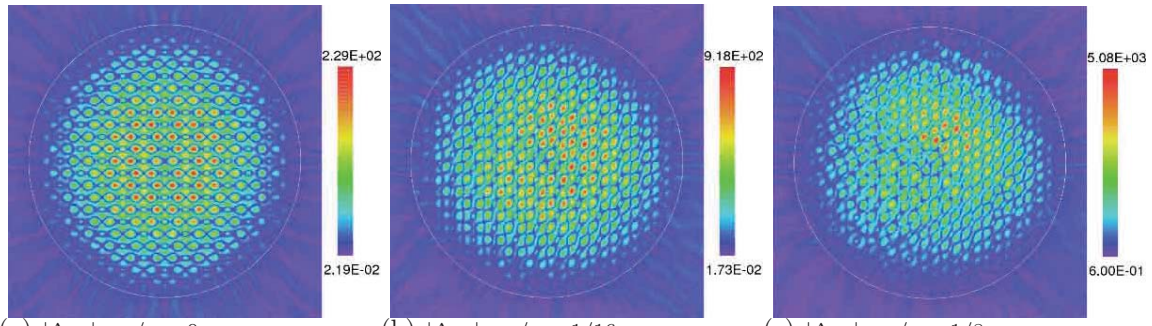

(a) $|\Delta\mathbf{x}_\mathrm{r}|_\mathrm{max}/a = 0$, $(\frac{\omega a}{2\pi c}, \gamma) = (0.2310212, 0.001380)$.
(b) $|\Delta\mathbf{x}_\mathrm{r}|_\mathrm{max}/a = 1/16$, $(\frac{\omega a}{2\pi c}, \gamma) = (0.2309824, 0.001380)$.
(c) $|\Delta\mathbf{x}_\mathrm{r}|_\mathrm{max}/a = 1/8$, $(\frac{\omega a}{2\pi c}, \gamma) = (0.2308372, 0.001470)$.

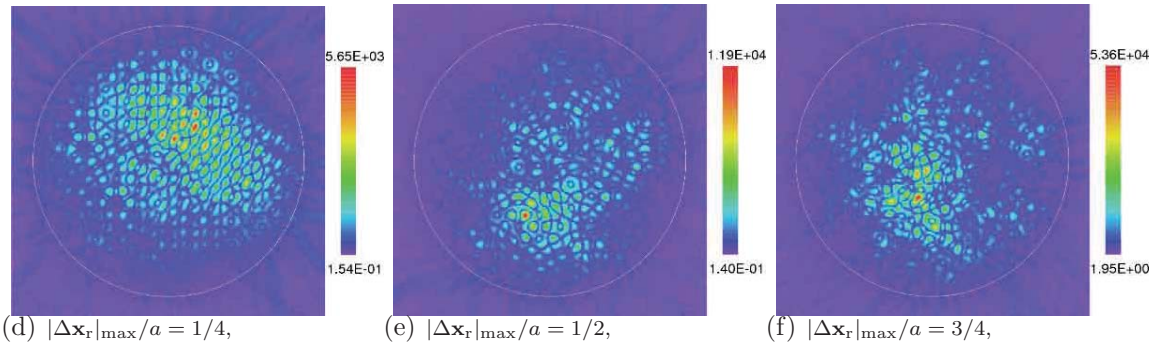

(d) $|\Delta\mathbf{x}_\mathrm{r}|_\mathrm{max}/a = 1/4$, $(\frac{\omega a}{2\pi c}, \gamma) = (0.2300848, 0.001995)$.
(e) $|\Delta\mathbf{x}_\mathrm{r}|_\mathrm{max}/a = 1/2$, $(\frac{\omega a}{2\pi c}, \gamma) = (0.2297800, 0.001785)$.
(f) $|\Delta\mathbf{x}_\mathrm{r}|_\mathrm{max}/a = 3/4$, $(\frac{\omega a}{2\pi c}, \gamma) = (0.2280060, 0.001515)$.

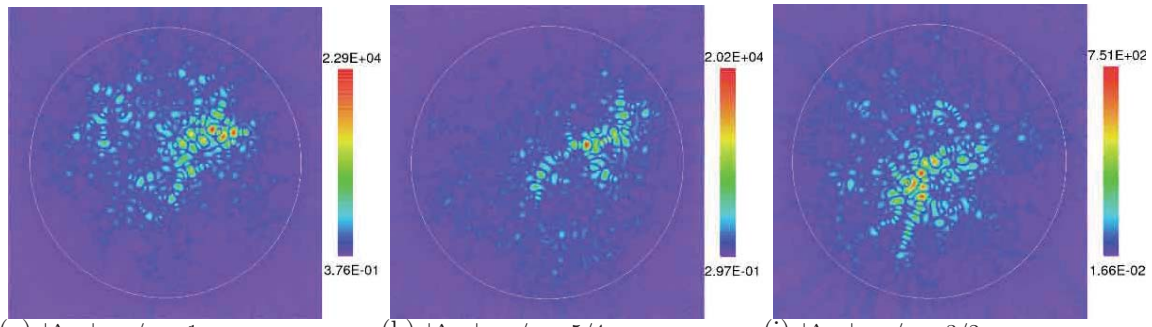

(g) $|\Delta\mathbf{x}_\mathrm{r}|_\mathrm{max}/a = 1$, $(\frac{\omega a}{2\pi c}, \gamma) = (0.2238840, 0.001080)$.
(h) $|\Delta\mathbf{x}_\mathrm{r}|_\mathrm{max}/a = 5/4$, $(\frac{\omega a}{2\pi c}, \gamma) = (0.2276240, 0.001575)$.
(i) $|\Delta\mathbf{x}_\mathrm{r}|_\mathrm{max}/a = 3/2$, $(\frac{\omega a}{2\pi c}, \gamma) = (0.2226504, 0.001740)$.

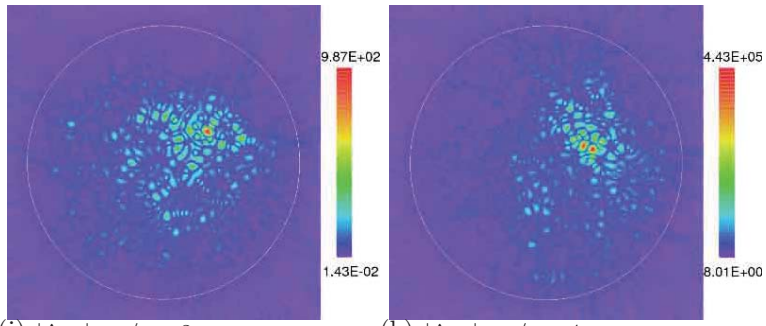

(j) $|\Delta\mathbf{x}_\mathrm{r}|_\mathrm{max}/a = 2$, $(\frac{\omega a}{2\pi c}, \gamma) = (0.2299456, 0.001515)$.
(k) $|\Delta\mathbf{x}_\mathrm{r}|_\mathrm{max}/a = 4$, $(\frac{\omega a}{2\pi c}, \gamma) = (0.2321304, 0.002430)$.

Figure 4.49: Electric amplitude distributions for laser modes with spatial extension (sample 1).

10 different rods arrangements rises again in $1.00 < |\Delta \mathbf{x}_\mathrm{r}|_\mathrm{max}/a$. The average threshold becomes minimum at $|\Delta \mathbf{x}_\mathrm{r}|_\mathrm{max}/a = 1.00$.

We show in Fig. 4.49 the EADs of the spatially extended modes. We observe in Figs. 4.49(a), 4.49(b), 4.49(c), and 4.49(d) the collapse of the localization forms from that of the periodic structure as the disorder index increases. Lasing threshold of the laser action with spatial extension is found to decrease in $0.250 < |\Delta \mathbf{x}_\mathrm{r}|_\mathrm{max}/a < 1.00$. In view of the EADs shown in Figs. 4.49(e) and 4.49(g), such decrease of lasing threshold is caused by increase in multiple scatterings.

We observe the average of lasing threshold becomes locally minimum at $|\Delta \mathbf{x}_\mathrm{r}|_\mathrm{max}/a = 1.00$, and another increase of the lasing threshold for $1.00 < |\Delta \mathbf{x}_\mathrm{r}|_\mathrm{max}/a$ in Fig. 4.46. When shifting the positions of the rods using the random numbers, there is a possibility that the shifted rod may overlaps for $0.73867 \leq |\Delta \mathbf{x}_\mathrm{r}|_\mathrm{max}/a$. In such a case, the random number value is discarded and a regenerated random number is used to determine the shifted position of the rod. Therefore, the average of the random numbers employed to generate the random arrangement of the rods may differ from 0.5 of the admissible shift range.

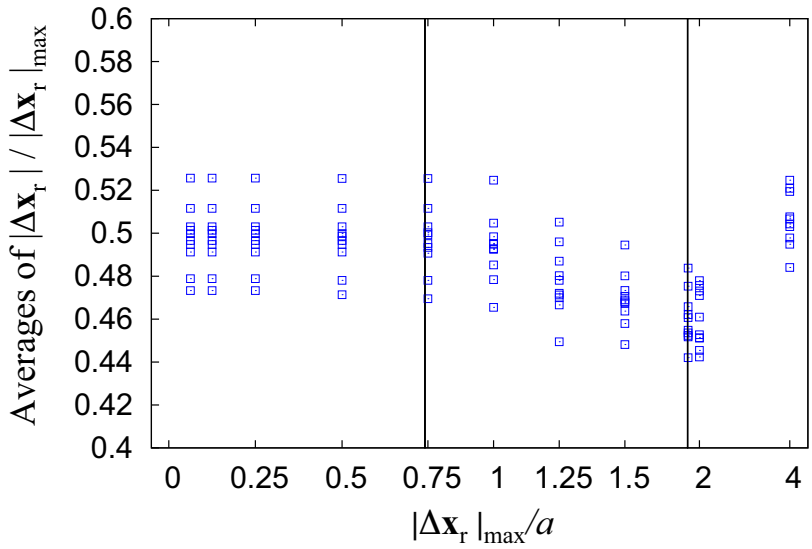

Figure 4.50: Average values of $\frac{|\Delta \mathbf{x}_\mathrm{r}|}{|\Delta \mathbf{x}_\mathrm{r}|_\mathrm{max}}$ for each $|\Delta \mathbf{x}_\mathrm{r}|_\mathrm{max}$.

Figure 4.50 shows the averages of $\frac{|\Delta \mathbf{x}_\mathrm{r}|}{|\Delta \mathbf{x}_\mathrm{r}|_\mathrm{max}}$ of all samples analyzed in the present study. The average becomes 0.5 theoretically if all the generated random num-

bers are used to rearrange the rods because the distributions of $|\Delta \mathbf{x}_\mathrm{r}|$ are given by random numbers of a uniform distribution between 0 and 1. In the range $0.73867 \leq |\Delta \mathbf{x}_\mathrm{r}|_\mathrm{max}/a \leq 2.00$, the effect of discard of some random numbers are observed clearly. The average values tend to decrease as $|\Delta \mathbf{x}_\mathrm{r}|_\mathrm{max}$ increases.

The serious influence occurs when the average of $|\Delta \mathbf{x}_\mathrm{r}|$ corresponds to $0.73867a$. Considering the average of the random number $m = 0.5$, its dispersion $\rho = 1/12$, and the standard deviation $\sigma = \sqrt{1/12}$, we find that the influence of discarding some of the random numbers occurs for

$$(m - \sigma)|\Delta \mathbf{x}_\mathrm{r}|_\mathrm{max} < 0.73867a < (m + \sigma)|\Delta \mathbf{x}_\mathrm{r}|_\mathrm{max}, \tag{4.14}$$

resulting in

$$0.93660 < |\Delta \mathbf{x}_\mathrm{r}|_\mathrm{max}/a < 3.49544. \tag{4.15}$$

This range agrees well with the results shown in Fig. 4.50. Hence, the local minimum of the lasing threshold observed in Fig. 4.46 may be the result of the employment of non-uniform random numbers to avoid the overlapping to the rods when shifting them from the hexagonal grids.

4.6.4 Conclusion

Investigations of lasing phenomena and lasing thresholds of disordered structures are presented based on FE analyses by changing the disorder index. The threshold of the laser action in the periodic structure is extremely low because of the zero-group velocity at the band edge frequency. However, the lasing phenomena are sensitive to the degrees of disorder, and the threshold of the photonic crystal laser rises by the effect of a small amount of disorder. As the disorder increases, lasing phenomena shift from photonic crystal lasers to random ones, and the threshold of laser action once rises, then it decreases. However, a further increase in the disorder causes the rise of the lasing threshold again.

4.7 Conclusions

In this chapter, we present the simulated results of lasing phenomena in random systems with optically active materials in interspaces among dielectric cylinders. We list knowledges revealed in our studies shown in this chapter on low-threshold random lasing.

- Light waves in disordered structures tend to be localized in interspaces among dielectric cylinders. Hence, random systems with optically active medium in the interspaces are appropriate for low-threshold laser action.
- In lower lasing frequency range, $0.121 \leq \omega a/2\pi c \leq 0.136$, averaged lasing threshold of five samples tend to become larger than other two lasing frequency ranges.
- In lasing frequency range $0.225 \leq \omega a/2\pi c \leq 0.255$, averaged lasing threshold of random lasing in five samples becomes minimum.
- The peaks of rising of electric intensity in disordered structures well-correspond to the peaks of amplification factor.
- It is generally referred that random lasers occur even the cavity-quality factor of dielectric structures is low. However, light confinement by disordered structures is quite important for low threshold laser action. In section 4.4, we reveal that cavity modes tend to oscillate laser action in lower excited states.
- The lasing threshold of random lasers becomes lower as filling factor increases. In section 4.5, the results of electric amplitude distributions show that light confinement becomes strong as filling factor increases. The above two results indicate that strong light confinement is important for low-threshold random lasing.
- Lasing threshold becomes lowest in the case of periodic structures, namely, photonic crystal lasers. In the case of random lasers, averaged lasing threshold of ten samples becomes minimum at intermediate structures between periodic and sufficiently disordered structures.

CHAPTER 5

Laser action in disordered structures consisting of metallic cylinders

5.1 Introduction

Random lasers [10, 88, 12, 28] are lasing phenomena in disordered structures usually composed of dielectric materials. Such lasing phenomena occur from random multiple scatterings and interference effect of scattered light in disordered structures. Hence, the quality factor of disordered structures are not important for random lasing but multiple scatterings are most important. It is well known that metals highly reflect light waves whose frequencies are lower than plasma frequency on their surfaces because of existence of "surface plasmon".

Surface plasmon is coherent oscillations of electrons and can be excited by light waves near the surface of metals. The coherent oscillations of electrons cause polarizations and the relative permittivity of metals are written as Drude model [35]. Because of the existence of electrons, metals have high reflectance explained in paragraph 2.2.6.2. The excited states of surface plasmon are called "surface plasmon polariton".

In our previous studies, we investigate threshold of random lasers by means of finite element analysis. We now consider that metal is an ideal material for lower threshold random lasing because of their high reflectance on their surfaces. We find several previous studies about metallic random lasers. Kang observed random lasing enhanced by resonant surface plasmon in gold nanoshell/water solution [89]. He showed the relation between pump power and signal intensity. Lawandy reported the increase of surface enhanced scattering [90]. However, no discussions are found on the threshold of metallic random lasers.

In this chapter, we investigate lasing phenomena in disordered structures consisting of metallic cylinders. The population inversion density of optically active medium is modeled by negative imaginary part of relative permittivity. We newly

investigate the properties of metallic random laser by using finite element method accelerated by multi-frontal method. The thresholds of metallic random lasers are compared with those of dielectric ones computed in previous section 4.6. The thresholds of metallic random lasers become much lower than those of dielectric ones.

5.2 Analysis model

We show one of the samples analyzed in this study in Fig. 5.1(a). The geometry is the same one analyzed in our previous study in section 4.6 and is created by disordered index $|\Delta \mathbf{x_r}|_{\max}/a = 1$ that means the maximum distance between the center of each cylinder and each fictitious grid point of triangular lattice is equal to a that is radii of cylinders. Such disordered structures created by $|\Delta \mathbf{x_r}|_{\max}/a = 1$ tend to lase in lowest pumping in the case of dielectric disordered structures. Finite element meshing is shown in Fig. 5.1(b). The distance between nodes are approximately $a/33$ deserving $\lambda/60$ in the worst case.

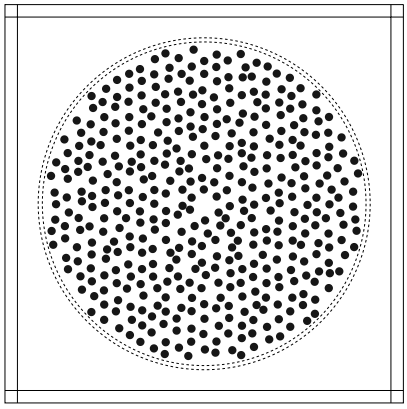

(a) An analysis model (sample 1).

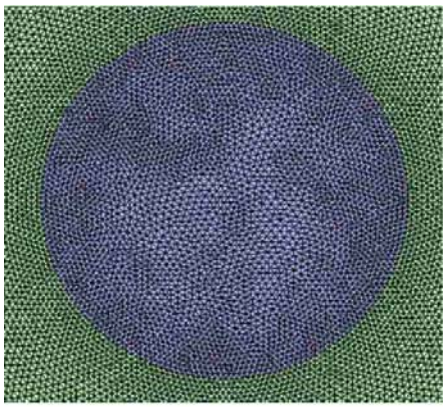

(b) Finite element meshing in a cylinder.

Figure 5.1: An analysis model and finite element meshing.

Optically active material are modeled by negative imaginary part of relative permittivity $-\gamma$. Metallic cylinders are expressed by Drude model. Relative permittivities in each region are given as follows:

$$\epsilon(\mathbf{x}) = \begin{cases} 1.0 + \mathrm{i}(-\gamma) & \mathbf{x} \in \Omega_{\mathrm{act}} \\ 1 - \frac{\omega_{\mathrm{p}}^2}{\omega^2} & \mathbf{x} \in \Omega_{\mathrm{cylinder}} \\ 1.0 & \mathbf{x} \in \Omega_{\mathrm{out}} \end{cases}, \tag{5.1}$$

where $\Omega_{\rm act}$ is the interspace among metallic cylinders, $\Omega_{\rm cylinder}$ is the region in metallic cylinders, and $\Omega_{\rm out}$ is open region which is outside of random systems. We assume silver as a material of cylinders and a plasma frequency used in this analysis is $\omega_{\rm p} = 1.37 \times 10^{16}$ [s^{-1}]. The radii of cylinders are assumed to be 100 [nm]. Then, normalized plasma frequency becomes 0.72731.

We analyze 10 samples to confirm the average threshold of random lasers. The numbers of nodes and elements in each sample are listed in Table 5.1.

Table 5.1: The number of nodes (NN) and elements (NE)of each models.

Sample No.	NN	NE
1	4454591	8895500
2	4443507	8873332
3	4449018	8884354
4	4456037	8898392
5	4435885	8858088
6	4440466	8867250
7	4431171	8848660
8	4445639	8877596
9	4437645	8861608
10	4437439	8861196

5.3 Result

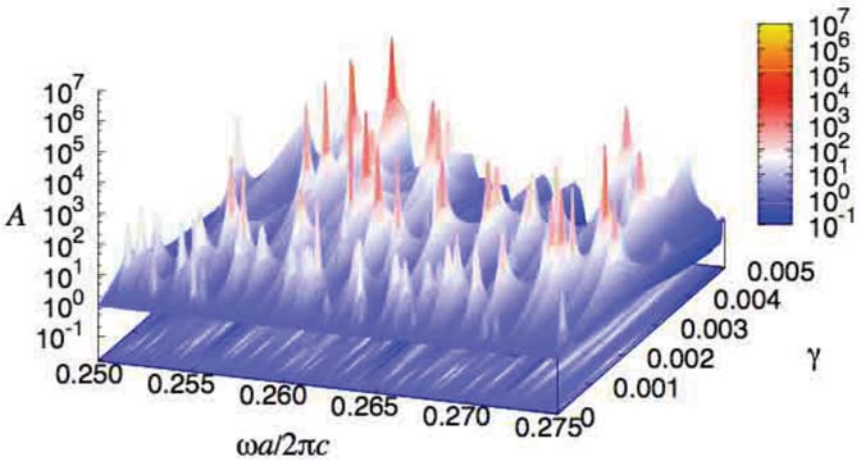

Figure 5.2: Metallic disordered structure (sample 1).

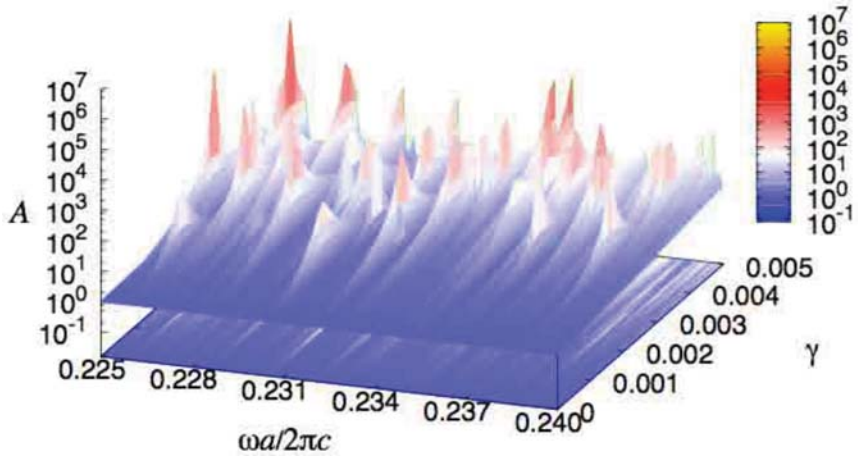

Figure 5.3: Dielectric disordered structure (sample 1).

We compute amplification factor defined in Eq. (2.60) by changing frequency and population inversion density for the ranges $0.250 \leq \omega a/2\pi c \leq 0.275$ and $0.00 \leq \gamma \leq 0.005$. The results of computed amplification factor of light waves emitted from a disordered structure consisting of metallic cylinders are shown in

Fig. 5.2. Figure 5.3 shows computed amplification factors in the case of dielectric cylinders.

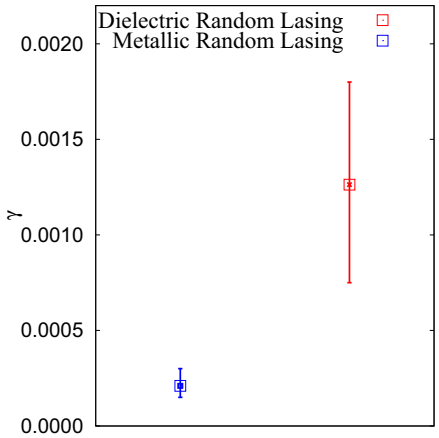

	Metal	Dielectric
Average	0.000210	0.001263
Minimum	0.000150	0.000750
Maximum	0.000300	0.001800

Table 5.2: Average, minimum and maximum values of γ.

Figure 5.4: Lasing thresholds of random lasing in metallic and dielectric disordered structures.

We can clearly observe that lasing phenomena in a metallic disordered structure start to occur at smaller values of γ than those in a dielectric one. The threshold of random lasing in a metallic disordered structure becomes extremely low. The average, minimum and maximum values of γ are shown in Fig. 5.4 and Table 5.2.

Figure 5.5 shows electric amplitude distributions of lasing states occurring at lowest four γ. It seems that light waves strongly confined in interspaces among metallic cylinders but do not penetrate into cylinders.

Figures 5.6(a) and 5.6(b) show the dependence of lasing threshold on lasing frequency and relative permittivity. The values of γ, normalized frequency, relative permittivity of metallic cylinders at which laser action occurs in Fig 5.2 are plotted. It is difficult to characterize the dependence of lasing threshold on lasing frequency and relative permittivity.

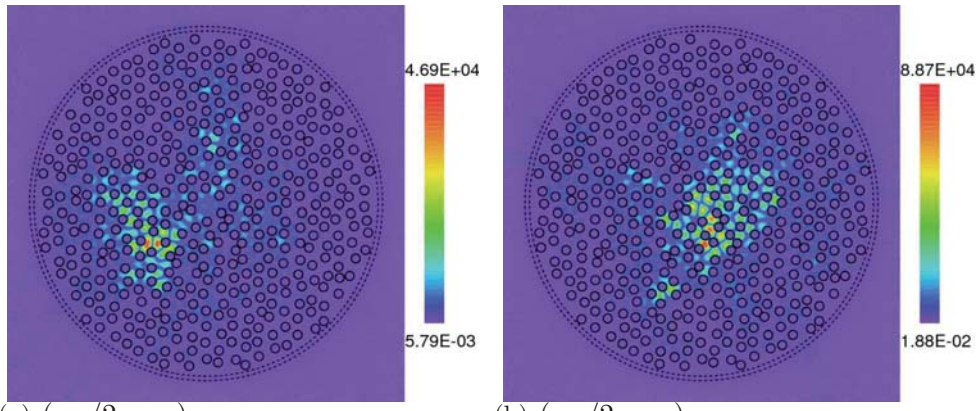

(a) $(\omega a/2\pi c, \gamma) = (0.2659292, 0.000150)$.

(b) $(\omega a/2\pi c, \gamma) = (0.2713668, 0.000160)$.

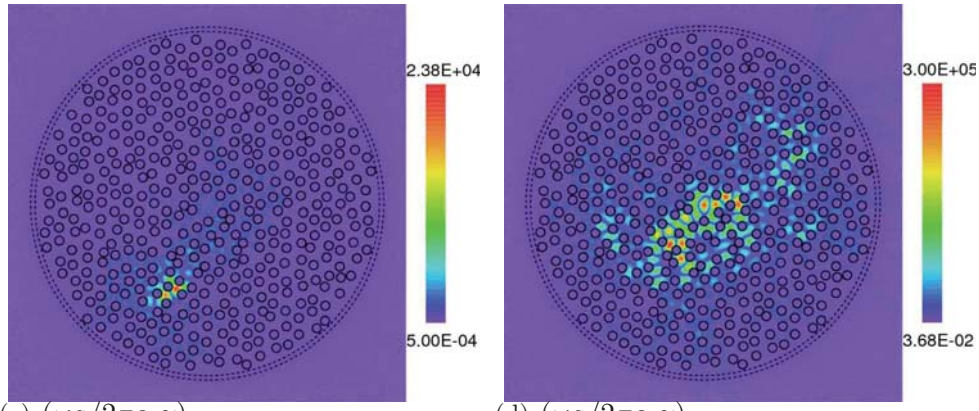

(c) $(\omega a/2\pi c, \gamma) = (0.2707160, 0.000175)$.

(d) $(\omega a/2\pi c, \gamma) = (0.2548204, 0.000205)$.

Figure 5.5: Electric amplitude distributions of lasing states in a metallic disordered structure (sample 1).

5.4 Conclusion

Random lasing phenomea in disordered structures consisting of metallic cylinders are precisely simulated by using finite element method. The lasing threshold of metallic random lasers are newly revealed by the comparison with the threshold of random lasers in dielectric disordered structures. The lasing threshold of metallic random lasers becomes much smaller than that of dielectric random lasers.

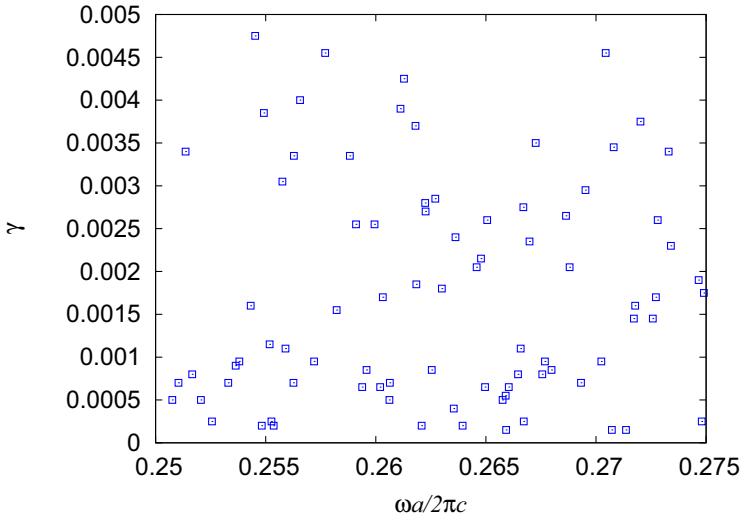

(a) The dependence of lasing threshold on lasing frequency.

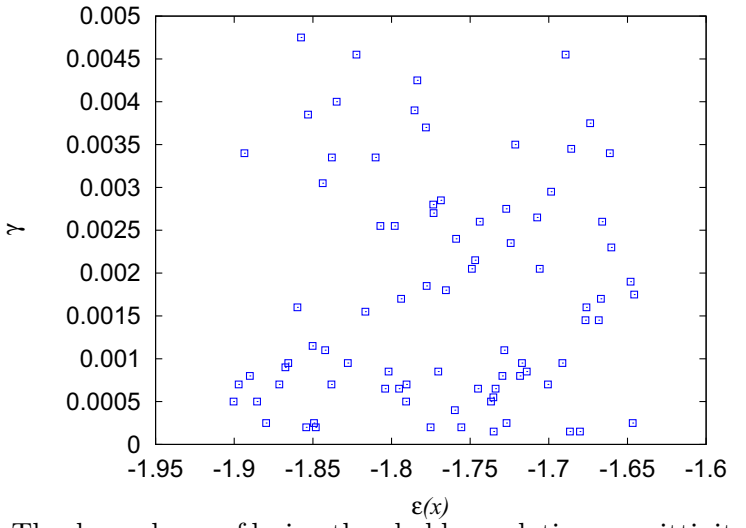

(b) The dependence of lasing threshold on relative permittivity.

Figure 5.6: The dependence of lasing threshold on lasing frequency and relative permittivity (sample 1).

CHAPTER 6

Laser action in honeycomb photonic crystals with random dangling bonds

6.1 Introduction

Laser devices in which photonic crystals [1, 2] are used as cavities, namely, photonic crystal lasers can lase even in the state of low excitation pumping of active materials because of extremely low group velocity at band edge frequency. On the other hand, lasing phenomena in disordered structures, called "random lasers" [12, 28], can lase in broad band frequencies and emit coherent light waves for broad angle. Such unique lasing phenomena in disordered structures can be realized by using feedback mechanisms as Anderson localization and coherent backscatterings caused by random multiple scattering and interference effect of light waves. Most of random lasing investigated in previous studies occur in disordered structures composed of dielectric rods in the case of two-dimensions, or dielectric particles in the case of three-dimensions. Light-trapping disordered structures contain various types of disorder as positional disorder, size disorder, disorder of relative permittivity, shape disorder and so on. Florescu et al. investigated the effect of random rink removal in honeycomb structures on band structures [19]. Such honeycomb structures including random link removals is a new type of disordered structures and are different from structures investigated in previous studies. Random lasing phenomena might occur in such honeycomb structures, however, no studies about the random lasing are found. Hence, we analyse random lasing phenomena in honeycomb structures including random link removals in the case of TM mode by using finite element method. We also analyze lasing phenomena in ordinary honeycomb structures and those with no dielectric rinks.

6.2 Analysis models

An ordinary honeycomb structure analyzed in this study is shown in Fig. 6.1. The honeycomb structure posses 10 periods ($10a$) from the center of entire structure to outside of the structures. The number of hexagonal hollows and dielectric link possibly removed are 331 and 930. The shape of removed dielectric link is rectangle shown in Fig. 6.1 as a colored rectangle. We determine the distance between the center of hexagonal hollows and dielectric rinks as $L_{\mathrm{H}} = 0.36228a$, that is, the filling factor of dielectric materials in a colored triangle in Fig. 6.1 equals to 30%. The angle between x axis and a vector oriented from the center of the entire stiructure to outside of the structure is defined as θ. Parameters needed in order to create analysis models are listed in Table 4.2. We define hexagonal hollow regions, regions in dielectric links, and outside of honeycomb structures as Ω_{act}, Ω_{d}, and Ω_{out}, respectively. PML boundary condition [38] is implemented for the analyses of light scattering in open region. We use optimized absorbing function for Helmholtz equation [41] to minimize spurious reflections.

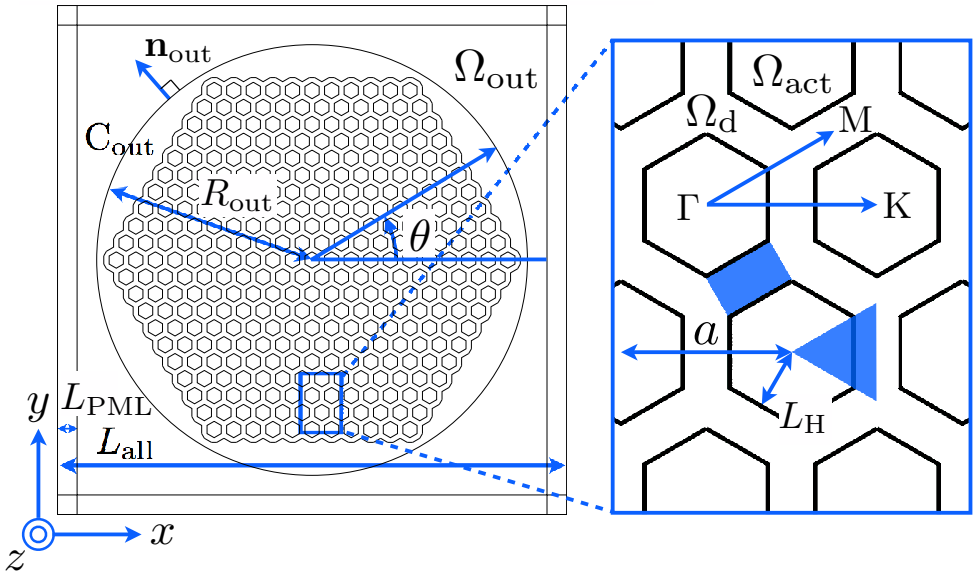

Figure 6.1: A honeycomb structure.

An analysis model including random link removals is shown in Fig. 6.2(a). We analyze 5 analysis modes with different arrangements of removed links to confirm common properties and phenomena. The number of removed links is 100 tentatively.

Table 6.1: Parameter of geometry

Parameter	Meaning	Value
a	Periodic length (characteristic length)	1
f	Filling factor of dielectric material	0.3
R_{out}	Radius of the circlr $\mathrm{C}_{\mathrm{out}}$	$11a$
L_{H}	Distance between the center of hexagonal hollow and a dielectric link	$a\sqrt{\frac{3}{16}(1-f)}$ $= 0.36228a$
L_{all}	Width of entire analytical region	$26a$
L_{PML}	Width of PML	a

Removed links are determined by two integers (I_{H} and I_{L}) satisfying $1 \leq I_{\mathrm{H}} \leq 331$ and $1 \leq I_{\mathrm{L}} \leq 6$. First, the integer $I_{\mathrm{H}} = 1$ is given to a hexagonal hollow on far left in top stair in Fig. 6.1. Next, we give integers from far left hexagonal hollow to far right one with increasing the integers. Then, the integer 11 is given to far right hexagonal hollow. After that, the integer 12 is given to far left hexagonal hollow in second top stair and integers is given to each hexagonal hollow in second top stair by the same rules. We repeat the above procedure for each stair, and finally, the integer $I_{\mathrm{H}} = 331$ is given to a hexagonal hollow on far right in bottom stair.

The other integer I_{L} is given to links surrounding each hexagonal hollow in a clockwise fashion, starting with the upper right hand link.

We can determine randomly removed dielectric links by two-integers $(I_{\mathrm{H}}, I_{\mathrm{L}})$ as shown above. However, we have to determine the integers again if the determined links have been already removed. Additionally, we do not remove outermost links because all hexagonal hollows are assumed to be filled with active materials. In the above cases, we determine I_{H} and I_{L} again and do not count the above outermost links as removed links. If there are independent dielectric structures which do not link an entire honeycomb structure, we remove the independent ones. The integers I_{H} and I_{L} are determined as follows:

$$[I_{\mathrm{H}}, I_{\mathrm{L}}] = [\ \mathrm{Int}\,(331 * R_{\mathrm{H}} + 1)\,,\ \mathrm{Int}\,(6 * R_{\mathrm{L}} + 1)\ ] \tag{6.1}$$

where R_{H} and R_{L} are real numbers generated by the intrinsic function "drand" in Fortran language with standard uniform distribution on the open interval $(0, 1)$. We have to generate those real numbers again if $I_{\mathrm{H}} = 332$ or $I_{\mathrm{L}} = 7$.

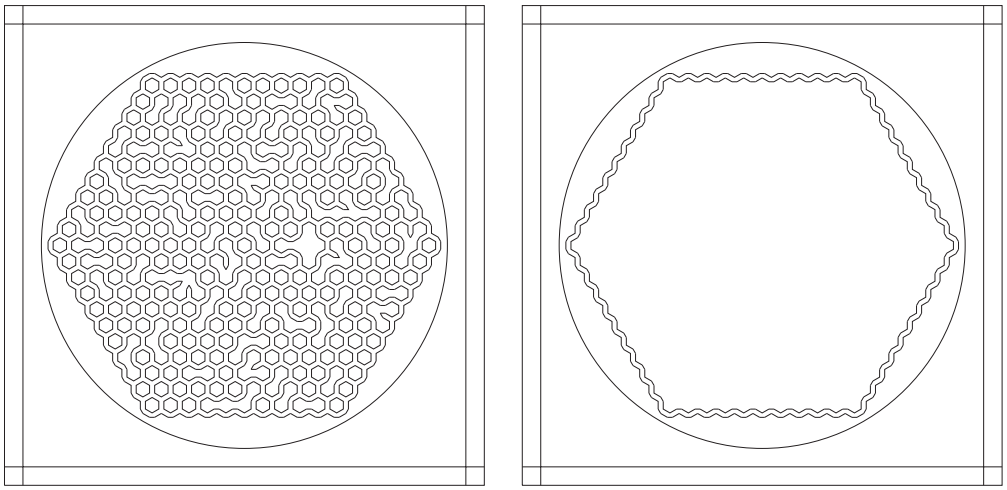

(a) A honeycomb structure with 100 removed dielectric links (sample 1).

(b) A honeycomb structure with no dielectric link.

Figure 6.2: A honeycomb structure with removed dielectric links

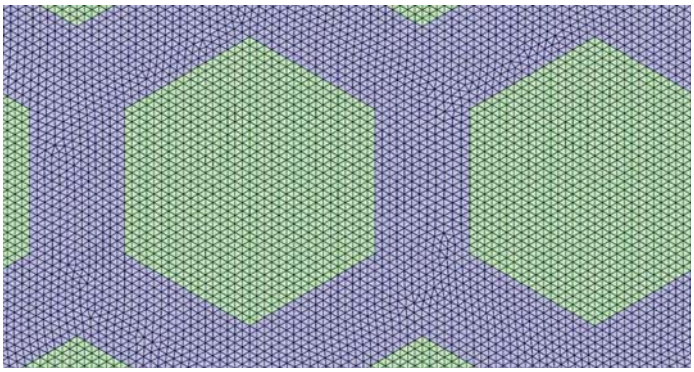

Figure 6.3: Finite elements.

We need to analyze lasing phenomena in more than one structure because we need to investigate common phenomena in disordered structures. Different sequences of numbers, R_{H} and R_{L}, can be generated by changing seed given to rand function, that is, different arrangements of removed links. In this analyses, we analyze five samples having different arrangements of removed links with each other.

Finite element meshing of an analysis model is shown in Fig. 6.3. The distance between two nodes are approximately $a/40$ where a is the periodic length of ordinary honeycomb model. The numbers of nodes and elements in each analysis model shown in Table 6.2.

Table 6.2: The numbers of nodes and elements.

Model	Figure No.	Node	Element
ordinary honeycomb structure	6.1	1042498	2073954
honeycomb structures with random link removals	6.2(a)	1050868	2090694
honeycomb structures with no dielectric link	6.2(b)	884917	1758792

6.3 Results

6.3.1 Lasing frequencies

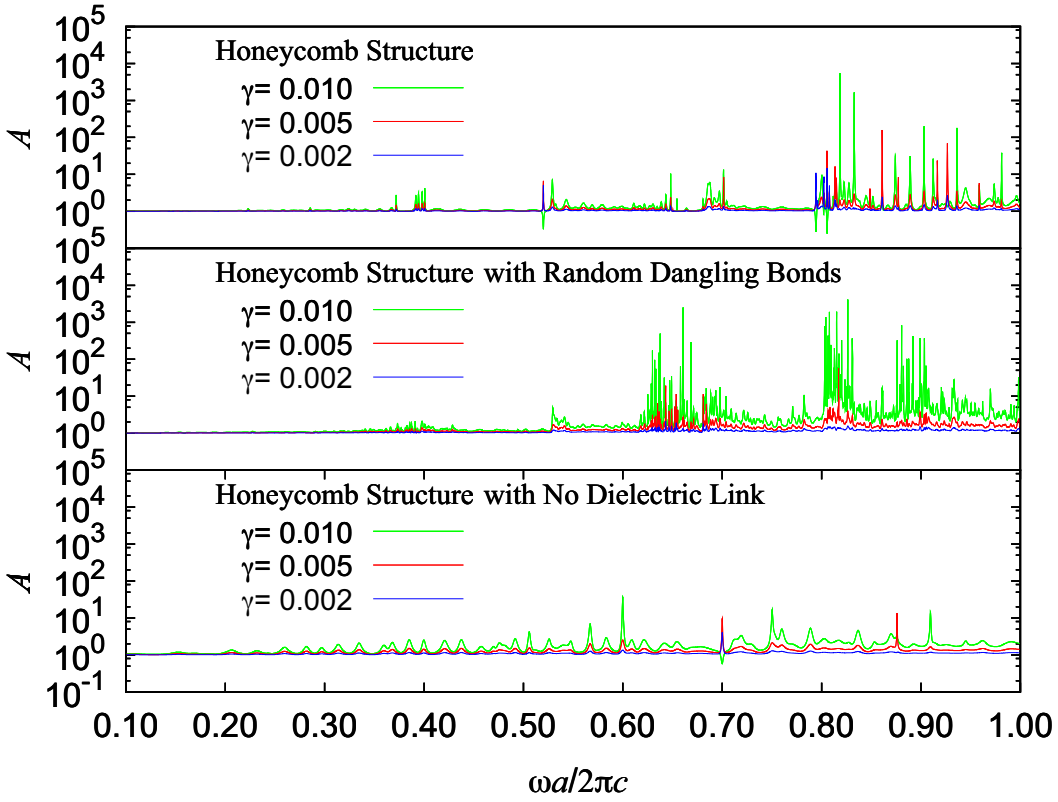

Figure 6.4: Spectrum of the amplification factor in the range $0.1 \leq \omega a/2\pi c \leq 1.0$ for $\gamma = 0.002, 0.005$, and 0.010. The number of computation points are 10001 for $\omega a/2\pi c$ axis.

We investigate lasing frequencies in the ordinary honeycomb structure, honeycomb structures with random link removals, and honeycomb structures with no dielectric link. The amplification factors are computed for the frequency range

$0.1 \leq \omega a/2\pi c \leq 1.0$, with fixed population inversion density $\gamma = 0.002$, 0.005 and 0.010. Those results are shown in Fig. 6.4.

In the result of the ordinary honeycomb structure, we observe that the amplification factor becomes relatively large in the range $0.790 \leq \omega a/2\pi c \leq 0.820$ with $\gamma = 0.002$. The band structure of the ordinary honeycomb structure computed by plane wave expansion method are shown in Fig. 6.5 with electric intensity distributions of 3rd, 4th and 5th lowest frequency bands at wave vector $\mathbf{k} = (\pi/3a, 0)$.

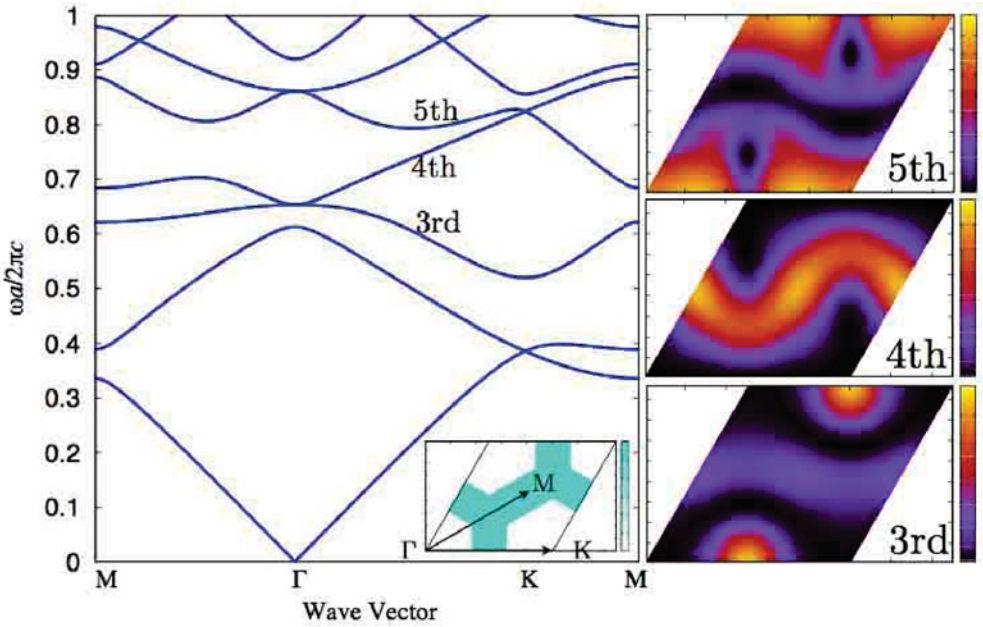

Figure 6.5: The band structure of the honeycomb structure and the distributions of electric field intensity, in a unit cell, of 3rd, 4th, and 5th lowest bands on wave vector $\mathbf{k} = (\pi/3a, 0)$.

Based on the comparison between lasing frequency and the band structure of the ordinary honeycomb structure, shown in Fig. 6.4 and Fig. 6.5, 5th lowest frequency band becomes band edges near the frequency $\omega a/2\pi c = 0.80$ for the directions $\mathrm{M} - \Gamma$ and $\Gamma - \mathrm{K}$. In this simulation, honeycomb structures whose hexagonal hollows are filled with active materials are assumed and the intensity of electric field in the hexagonal hollows becomes high in 5th lowest frequency band. Hence the 5th lowest frequency band are considered to be excited near the frequency $\omega a/2\pi c = 0.80$ and oscillate laser action.

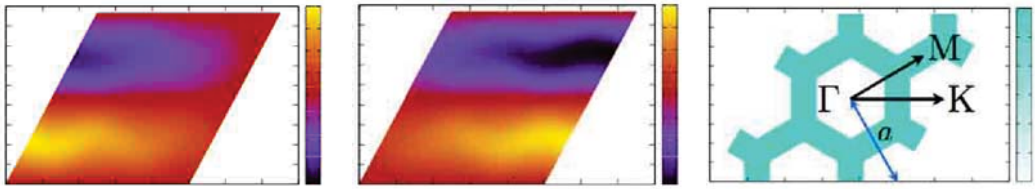

(a) Real part. (b) Imaginary part. (c) Structure.

Figure 6.6: Anti-symmetrical electric field distributions of 4th band on wave vector $\mathbf{k} = (\pi/3a, 0)$ with respect to the Γ-K direction. The number of expanded plane waves is 10201.

In the state of no light amplification $\gamma = 0$, the energy of light transferring is conserved as explained in section 2.3.3. However, in the frequency range $0.648 \leq \omega a/2\pi c \leq 0.680$, the energy is not conserved. Such collapse of our simulation is caused by an uncoupled mode of 4th lowest frequency band. Such an uncoupled mode has anti-symmetric distribution shown in Fig. 6.6 with respect to the propagating direction $\Gamma - \mathrm{K}$ and cannot be excited in periodic structures having symmetric distribution of dielectric materials. For propagation for $\Gamma - \mathrm{L}$ where L is a point between K and M, the distribution of electric fields becomes un-symmetric with respect to the propagating direction and light propagations for $\Gamma - \mathrm{L}$ cannot not excited in periodic structures as well. The reason why light propagations for $\Gamma - \mathrm{M}$ direction are not observed in the computations are considered that nodes are not well-ordered for $\Gamma - \mathrm{M}$ and cannot express $\Gamma - \mathrm{M}$ direction strictly in finite element meshing.

In the result of a honeycomb structure with random link removals, noticeable amplifications of light are not observed in the state of $\gamma = 0.002$. However, in the state of $\gamma = 0.005$, light waves are strogny amplified in the ranges $0.625 \leq \omega a/2\pi c \leq 0.695$ and $0.800 \leq \omega a/2\pi c \leq 0.835$.

Amplification factors in the result of honeycomb structure with no dielectric links have several peaks but they are relatively small.

Based on the above results of the amplification factor for large frequency range, we investigate lasing phenomena in the ordinary honeycomb structure for the range $0.790 \leq \omega a/2\pi c \leq 0.820$ and those in honeycomb structures with random link removals for the range $0.625 \leq \omega a/2\pi c \leq 0.695$ and $0.800 \leq \omega a/2\pi c \leq 0.835$ in detail.

6.3.2 The analysis for laser action in the ordinary honeycomb structure

Firstly, we analyze lasing phenomena in the ordinary honeycomb structure. Optically active materials are assumed to be excited homogeneously and the parameter γ is constant in the region $\Omega_{\rm act}$.

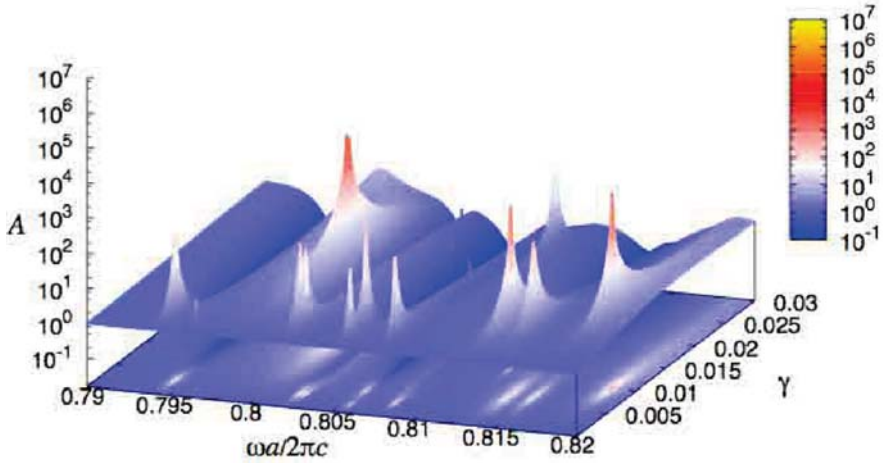

Figure 6.7: Amplification factor computed in the honeycomb model for the range $0.790 \leq \omega a/2\pi c \leq 0.820$ and $0.00 \leq \gamma \leq 0.03$. The numbers of computation points are 501 and 201 for $\omega a/2\pi c$ and γ axes, respectively.

We plot the result of computed amplification factors as a functions of $\omega a/2\pi c$ and γ in Fig. 6.7. The number of peaks of amplification factor is 43 and the peaks are interpreted as oscillation of lasing phenomena. The minimum value of γ at which laser action occurs is $\gamma = 0.00150$.

In Figs. 6.8 and 6.9, we show the distributions of the electric field amplitude and radiation directions of lasing states occurring in the state of lowest two excitation pumping, that is, smallest two γ at which laser action occurs. In Fig. 6.8, the amplitude of the electric field on each node normalized by the amplitude of incident field on the circle $\mathrm{C_{out}}$, $|\mathbf{E}| \,/\, |\mathbf{E}_{\rm i}|_{\mathrm{C_{out}}}$, are plotted. In Fig. 6.9, radiation angle θ is plotted in angle and following value A_θ is plotted in radius as

$$A_\theta = \frac{\int_{\mathrm{C}^\theta_{\rm out}} \langle \mathbf{S} \rangle \cdot \mathbf{n}^\theta_{\rm out} \, dl \Big/ L^\theta_{\rm out}}{\int_{\mathrm{C_{out}}} \langle \mathbf{S} \rangle \cdot \mathbf{n}_{\rm out} \, dl \Big/ 2\pi R_{\rm out}}, \tag{6.2}$$

where $\mathrm{C}^\theta_{\rm out}$ is a edge located on the circle $\mathrm{C_{out}}$ for θ direction from the center of the entire structure, $L^\theta_{\rm out}$ is the length of the edge, $\mathbf{n}^\theta_{\rm out}$ is the outward unit

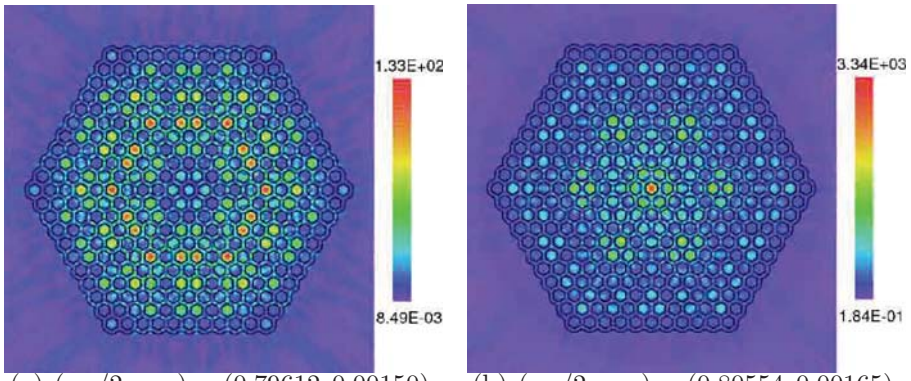

(a) $(\omega a/2\pi c, \gamma) = (0.79612, 0.00150)$. (b) $(\omega a/2\pi c, \gamma) = (0.80554, 0.00165)$.

Figure 6.8: Electric amplitude distributions of lasing states of lowest two thresholds in honeycomb structures in the range $0.790 \leq \omega a/2\pi c \leq 0.820$.

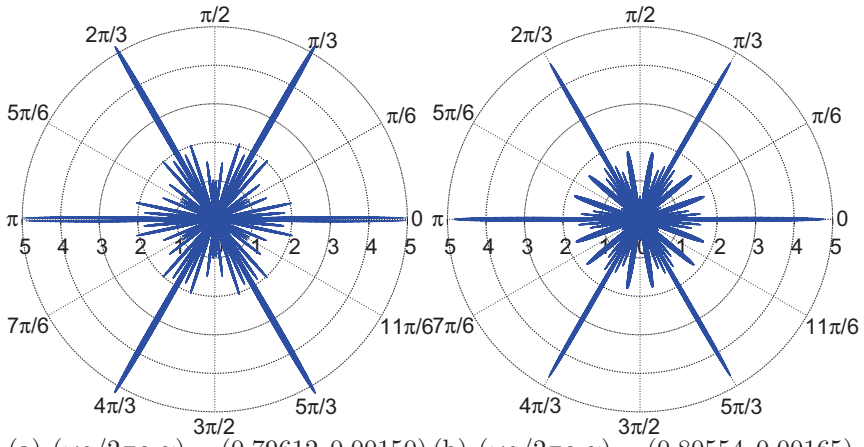

(a) $(\omega a/2\pi c, \gamma) = (0.79612, 0.00150)$.(b) $(\omega a/2\pi c, \gamma) = (0.80554, 0.00165)$.

Figure 6.9: Polar plots of radiation directions of lasing states of lowest two thresholds in honeycomb structures in the range $0.790 \leq \omega a/2\pi c \leq 0.820$.

normal vector on the edge, and $2\pi R_{\text{out}}$ is the length of the circumference of C_{out}. In short, A_θ is the ratio between radiation power of light waves through the edge $\text{C}^{\theta}_{\text{out}}$ and that through the entire circle C_{out}.

We can observe that the electric field becomes intensive in hexagonal hollows in both electric amplitude distributions. Above distributions well correspond to the distribution of electric intensity in the 5th lowest frequency band. In the results of radiation directions, we confirm intensive radiations for specific directions.

6.3.3 The analysis for laser action in the honeycomb structure with random link removals

Next, we analyze laser action in the honeycomb structure with random link removals. The way to understand results is same as those in previous subsection.

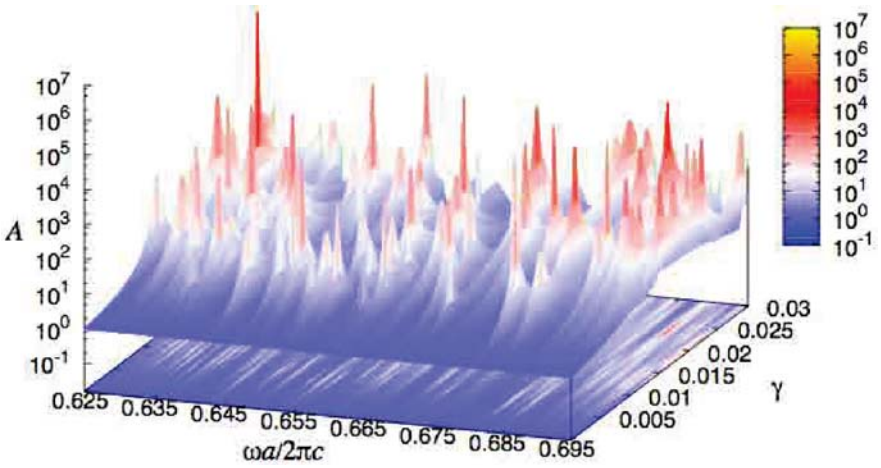

Figure 6.10: Amplification factor, for the range $0.625 \leq \omega a/2\pi c \leq 0.695$, computed in the honeycomb structure with random dangling bonds. The numbers of computation points are 1001 and 201 for $\omega a/2\pi c$ and γ axes, respectively.

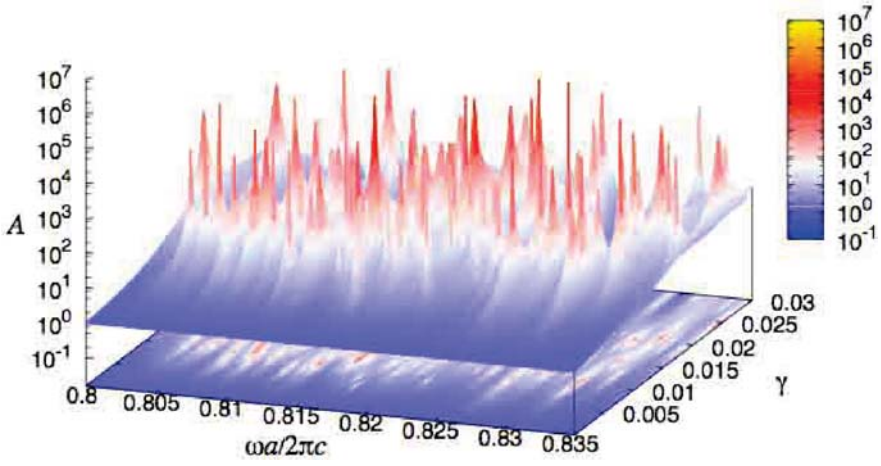

Figure 6.11: Amplification factor, for the range $0.800 \leq \omega a/2\pi c \leq 0.835$, computed in the honeycomb structure with random dangling bonds. The numbers of computation points are 501 and 201 for $\omega a/2\pi c$ and γ axes, respectively.

Figures 6.10 and 6.11 show the results of computed amplification factors of light waves emitting from the honeycomb structure with random link removals.

We observe random lasing even if the number of removed links is only 100 in 930. The value of the parameter γ.

The minimum value of γ at which lasing peak occurs indicate population inversion density of lasing state, namely, lasing threshold. The values are $\gamma = 0.00645$ in the frequency range $0.625 \leq \omega a/2\pi c \leq 0.695$ and $\gamma = 0.00510$ in the frequency range $0.800 \leq \omega a/2\pi c \leq 0.835$. We analyze five models with different arrangement of removed links. Average, minimum, and maximum of lasing thresholds in five models are shown in Table 6.3. These values shown in Table 6.3 are relatively higher than those of lasing phenomena in disordered structures consisting of dielectric cylinders ($0.001 \leq \gamma \leq 0.003$)[49].

Table 6.3: Average, minimum, and maximum values of minimum γ in five models.

Lasing frequency range	Average	Minimum	Maximum
$0.625 \leq \omega a/2\pi c \leq 0.695$	0.00585	0.00450	0.00735
$0.800 \leq \omega a/2\pi c \leq 0.835$	0.00534	0.00510	0.00555

We show the electric amplitude distributions and the radiation directions of lasing states of lowest two γ in the range of $0.625 \leq \omega a/2\pi c \leq 0.695$ in Figs. 6.12 and 6.13, respectively. In this frequency range, electric amplitude becomes high in hexagonal hollows. This distribution of the electric amplitude is similar to the distribution of electric intensity of 5th lowest frequency band. We also plot the the electric amplitude distributions and the radiation directions of lasing states of lowest two γ in the range $0.800 \leq \omega a/2\pi c \leq 0.835$ in Figs. 6.14 and 6.15. The distributions of electric amplitude is unique. Light waves localized in dielectric links and such distribution correspond to the distribution of electric intensity of 4th lowest frequency ranges shown in Fig. 6.5. Those common regimes of light localizations indicate that the effect of optical properties in the ordinary honeycomb structure appear in the results of structures with random link removals. Such regimes are commonly observed in other four structures with different arrangements of removed dielectric links.

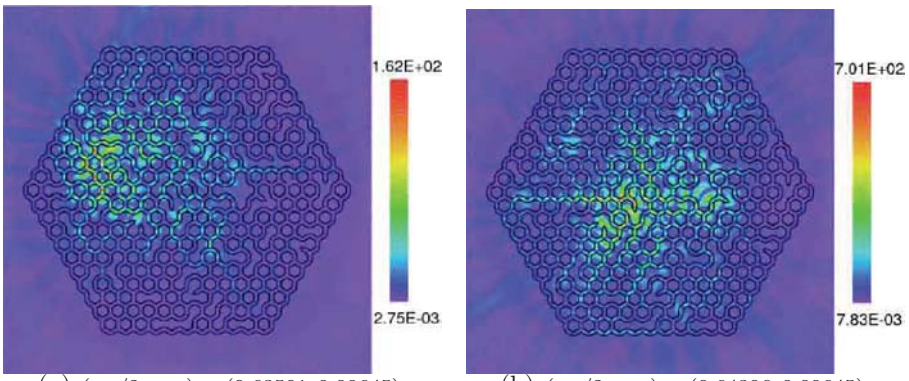

(a) $(\omega a/2\pi c, \gamma) = (0.63501, 0.00645)$. (b) $(\omega a/2\pi c, \gamma) = (0.64306, 0.00645)$.

Figure 6.12: Electric amplitude distributions of lasing states of lowest two thresholds in the honeycomb structure with random dangling bonds in the range $0.625 \leq \omega a/2\pi c \leq 0.695$.

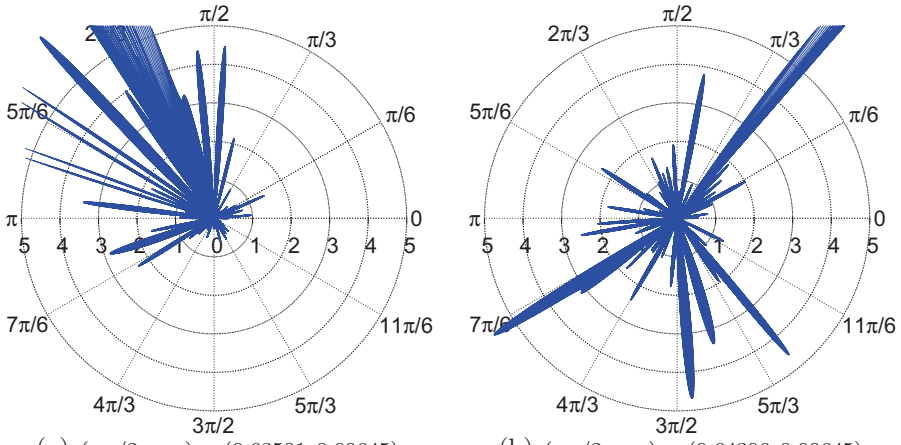

(a) $(\omega a/2\pi c, \gamma) = (0.63501, 0.00645)$. (b) $(\omega a/2\pi c, \gamma) = (0.64306, 0.00645)$.

Figure 6.13: Polar plots of radiation directions of lasing states of lowest two thresholds in the honeycomb structure with random dangling bonds in the range $0.625 \leq \omega a/2\pi c \leq 0.695$.

6.4 Considerations for lasing threshold and three-dimensional analysis

The lasing thresholds of random lasing occurring in honeycomb structure with random link removals tend to becomes higher than those in disordered structures consisting of dielectric cylinders, mentioned above. One of the reason why we consider is that the disorder occurring from removals of dielectric links is not sufficient. In other word, the number of removed links is not sufficient. In previous

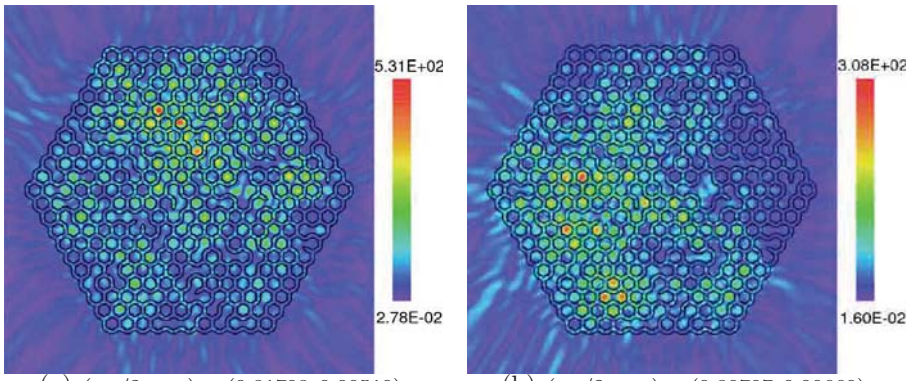

(a) $(\omega a/2\pi c, \gamma) = (0.81708, 0.00510)$. (b) $(\omega a/2\pi c, \gamma) = (0.80707, 0.00660)$.

Figure 6.14: Electric amplitude distributions of lasing states of lowest two thresholds in the honeycomb structure with random dangling bonds in the range $0.800 \leq \omega a/2\pi c \leq 0.835$.

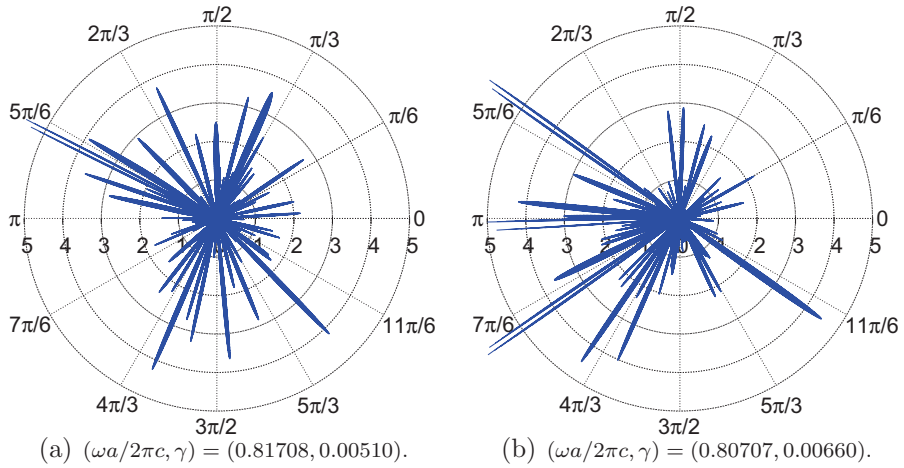

(a) $(\omega a/2\pi c, \gamma) = (0.81708, 0.00510)$. (b) $(\omega a/2\pi c, \gamma) = (0.80707, 0.00660)$.

Figure 6.15: Polar plots of radiation directions of lasing states of lowest two thresholds in the honeycomb structure with random dangling bonds in the range $0.800 \leq \omega a/2\pi c \leq 0.835$.

section 4.6, we revealed that lasing threshold once rise as the amount of disorder increases. The results of the simulations of lasing phenomena in honeycomb structures with random link removals show that the effect of optical properties in the ordinary honeycomb structure remain in the results of disordered structures.

Another reason is that continuous random scatterings in active materials are interrupted by dielectric links because hexagonal hollows in which active materials are filled do not connect with each other. in contrast, in the case of random systems, consisting of dielectric cylinders, whose interspace among cylinders are

filled with active materials, continuous scatterings in active materials are easy to occurs.

However, the higher lasing threshold cased by the issues mentioned above possibly bring to lower one by increasing the number of removed links.

In the present study, we simulate lasing phenomena in two-dimensional systems assumed infinitely long for z direction. However, in practical devices, the systems are finite for z direction. When we include the finiteness for z direction in our simulation, namely, three-dimensional simulations, lasing threshold might rise because of radiation modes for z direction. The three-dimensional analyses are our future works.

6.5 Conclusions

In the present study, we analyze lasing phenomena in honeycomb structures with random link removals by using finite element method. The amplification of light waves emitted from the honeycomb structures is computed. Based on the results of distributions of the electric amplitude and radiation directions, random lasing occurs in the honeycomb structures. However lasing threshold of random lasing in the honeycomb structures is higher than that in disordered structures consisting of cylinders.

CHAPTER 7

Conclusions

In the present study, appropriate disordered structures for lower threshold laser action are presented by means of finite element method. Lasing properties of random lasers in two-dimensional random systems consisting of homogeneous cylinders are investigated. The population inversion density of optically active medium is modeled by giving a negative value to the imaginary part of the relative permittivity. By using this modeling, the dependence of the properties of random lasers on the excitation of active medium and the threshold of random lasers are investigated. In order to achieve lower threshold random lasing, the following results are obtained.

1. Light waves in two-dimensional disordered structures tend to be localized in interspaces among cylinders. For this reason, it is desirable that optically active medium fill the interspaces among cylinders in order to realize lower threshold random lasing.

2. The distribution of localized, extended, and transition modes are strongly influenced by lasing frequency. In the lower frequency $0.121 \leq \omega a/2\pi c \leq 0.136$, the average of lasing threshold are higher than other two higher frequency ranges investigated in this study. Averaged lasing threshold of some random systems becomes lowest in the range $0.225 \leq \omega a/2\pi c \leq 0.255$.

3. The relation between light amplification and the intensity of electric field in random systems are investigated and found that their peaks correspond well to each other. The similarities between the distributions of electric field amplitudes of non-excited and lasing states are evaluated by NMSE. Lasing phenomena in lower excited states of active medium tend to occur from laser modes with low value of NMSE. It is found that cavity modes tend to oscillate low-threshold lasing phenomena.

4. Appropriate filling factor for low-threshold laser action are investigated and

found that light confinement becomes strong as the filling factor of dielectric cylinders increases. Disordered structures with higher filling factor are more appropriate for lower threshold laser action.

5. The relation between the amount of positional disorder of cylinders and lasing threshold of random lasing are newly unveled. Lasing threshold of laser action in periodic dielectric structures becomes lowest because of extremely low-group velocity. In the case of random lasing, lasing threshold tends to have a minimum in the transition from photonic-crystal lasers to random lasers.

6. Metals are ideal materials for lower-threshold random lasing because metals enable disordered structures to occur extremely intensive multiple scatterings, which activate lasing phenomena even in extremely low excitation state of active medium.

7. Lasing phenomena in honeycomb structures with random link removals are simulated and found that the threshold of laser action in the honeycomb structures is higher than that of the random systems consisting of dielectric rods within active medium. The simulated result has shown that continuous scatterings in active medium are necessary for lower threshold laser action.

Appendix

A.1 Band structure of photonic crystals

A.1.1 Photonic crystal models

We consider four types of two-dimensional PC model which includes infinitely long rods in the vertical direction, say, z-direction. In each model, the shapes of rods across a horizontal plane (xy-plane) are round, hexagonal, or square. Triangular lattice photonic crystals are expected to make wider bandgaps than those of square lattice [91]. Hence, we arrange the rods to form triangular lattices as illustrated in Fig. A.1. In this figure, ϵ_1, ϵ_2, and ϵ_3 denote the dielectric constants of the cavity, rod, and matrix, respectively; $\mathbf{a}_1$ and $\mathbf{a}_2$ represent the lattice vectors and S_0 is the area of the unit lattice (cell). For simplicity, we assume $\mathbf{a}_1$ and $\mathbf{a}_2$ have the same length a. The dielectric constant $\epsilon(\mathbf{r})$ has the periodicity such as

$$\epsilon(\mathbf{r} + \mathbf{a}_i) = \epsilon(\mathbf{r}) \tag{A.1}$$

for $i = 1$ and 2. Also, α and β are parameters to determine the size of rods; in the case of the round type, for example, α and β express the interior and exterior radii of each rod, respectively. Note that the ratio $\alpha/\beta(< 1)$ denotes the *thinness* of rods.

From the symmetry of each structure, the first Brillouin zone is determined as the triangular wedge ΓKM as shown in Fig. A.1.

In contrast to the dual periodic model, we call the round, hexagonal, and square models as the single periodic models.

A.1.1.1 Numerical procedure

For a given wave vector $\mathbf{k}$ in Brillouin zone, we solve the eigenvalue equation (2.85) numerically to obtain a set of eigen frequencies $\omega(\mathbf{k})$. To this end, we need to evaluate the coefficients $\kappa(\mathbf{G})$ and truncate the infinite summation over $\kappa(\mathbf{G})$ to a finite one.

In order to evaluate $\kappa(\mathbf{G})$, we divide smallest width of the part of high dielectric constant into more than 35 parts in band calculations of single periodic

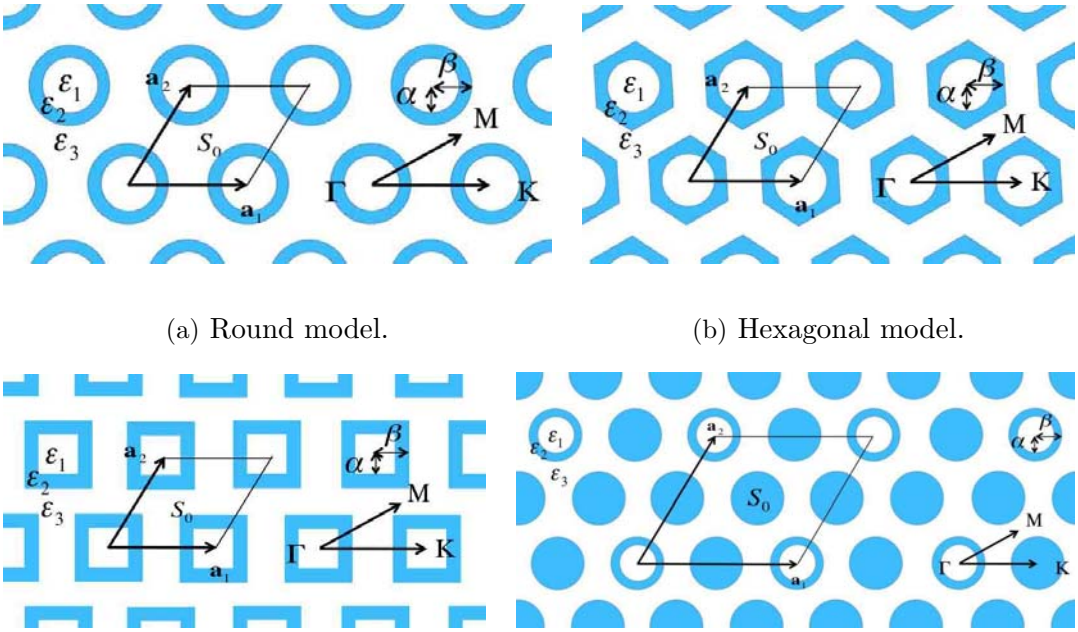

(a) Round model.

(b) Hexagonal model.

(c) Square model.

(d) Dual periodic model comprises solid and hollow round rods.

Figure A.1: Photonic crystal models with hollow rods.

structures, and 30 parts in the calculations of dual periodic structures. Specifically, we divide x and y directions of the unit lattice into 1200 for single periodic structure, and 1800 for dual periodic structure, respectively. When we plot all the eigen frequencies thus computed against the wave vector $\mathbf{k}$, we can observe some frequency regions (bands) where none of eigen frequencies exist for any $\mathbf{k}$ in Brillouin zone. This indicates that any light waves that belong to the regions are not allowed to propagate through the PC in any directions. Such frequency regions are called photonic bandgaps.

A.1.2 Numerical results

We investigate how the cross-sectional geometries of rods influence the position of bandgaps in frequency. To see the result clearly, we used *bandgap map* [91], in which we plot all the computed eigen frequencies for all the wave vectors against a certain geometrical parameter (e.g. normalized size of rod).

First, we show the results of round, hexagonal, and square models in subsections $A.1.2.1$ and $A.1.2.2$. Then we mention the results of the dual periodic model in subsection $A.1.3$.

In the following calculations, we use $a = 140$ [nm], $\epsilon_1 = \epsilon_3 = 1.0$ (air), and $\epsilon_2 = 5.76$ (diamond) unless otherwise stated. Also, the number of vectors $\mathbf{G}$ in Eq. (2.85) is set to 7569 and 10201 (i.e. $-43 \leq l_1, l_2 \leq 43$ and $-50 \leq l_1, l_2 \leq 50$) in band calculation of single and dual periodic structures, respectively.

A.1.2.1 Solid rods — Influence of rod's size on bandgap

We computed the dispersion relations for *solid* rods (i.e. $\alpha = 0$) in order to compare bandgaps with those for the following *hollow* rods ($\alpha \neq 0$).

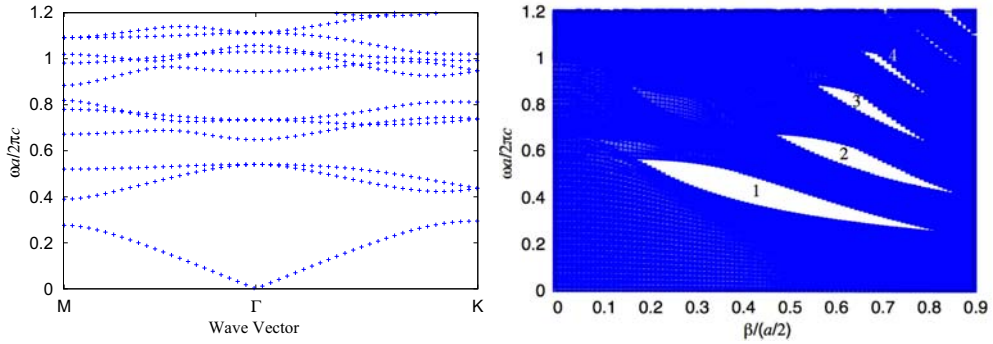

(a) Dispersion relation of solid round model : $\frac{\beta}{a/2} = 0.60$.

(b) Round model.

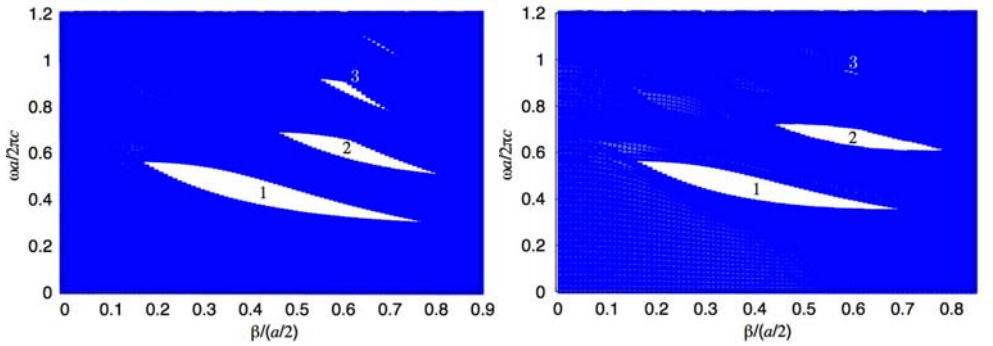

(c) Hexagonal model.

(d) Square model.

Figure A.2: Bandgap maps of three models with *solid* rods.

In order to find the dependency of bandgaps on β, we repeated calculation by changing the values of β from 0 to $a/2$ for the round and hexagonal models and from 0 to $\sqrt{3}a/4$ for the square model. In Fig. A.2(a), the dispersion relation of solid round model for a typical case: $\beta/(a/2) = 0.6$. We observe bandgaps for normalized frequency range $0.276 \leq \omega a/(2\pi c) \leq 0.389$, $0.540 \leq \omega a/(2\pi c) \leq 0.648$ and $0.818 \leq \omega a/(2\pi c) \leq 0.884$. By plotting the side views

of dispersion relation diagram in K $\rightarrow$ Γ $\rightarrow$ M direction for various values of $\beta/(a/2)$ simultaneously to a single diagram, we obtain a diagram as shown in Fig. A.2(b). Obviously we can see the parameter ranges corresponding to bandgaps as the regions numbered as 1, 2, 3, and 4, at a glance, in the figure.

The bandgap maps of the three models with solid rods are shown in Fig. A.2, in which white areas correspond to two dimensional photonic bandgaps. In any models (or shapes of rods), the position of each bandgap becomes lower in frequency as the rod's size increases. However, only in the square model, the bandgap in high frequency regime is quite small. We guess that the differences between the case of square and other shaped rods are caused by the symmetry of the rod's shape for the direction $\Gamma - \mathrm{M}$ and $\Gamma - \mathrm{K}$. Round and hexagonal shaped rods can make reflective surfaces to the incident light for each direction. Moreover, round shaped rods can make it for all directions in x-y plane. Square shape rods can make it only for $\Gamma - \mathrm{K}$ direction, however, can not make for $\Gamma - \mathrm{M}$ direction.

In Table $A.1$, we tabulate the ranges of the lowest three bandgaps observed in Fig. A.2 and also the parameters $\beta/(a/2)$ that correspond to the widest bandgaps.

Table A.1: Normalized frequency ranges (column 'range') of the lowest three bandgaps and the normalized rod's sizes (column 'max') that give the widest bandgaps in the case of *solid* rods.

Bandgap No.	Round		Hexagonal		Square	
	range	max	range	max	range	max
1	0.23 – 0.57	0.38	0.28 – 0.57	0.36	0.34 – 0.58	0.34
2	0.39 – 0.68	0.65	0.49 – 0.69	0.60	0.59 – 0.74	0.58
3	0.60 – 0.89	0.65	0.74 – 0.92	0.61	0.90 – 0.97	0.59

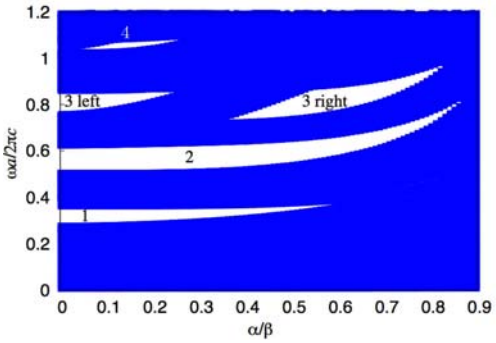

(a) Round rod ($\beta/(a/2) = 0.65$).

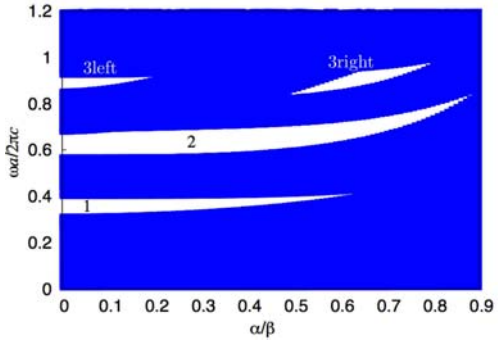

(b) Hexagonal rod ($\beta/(a/2) = 0.60$).

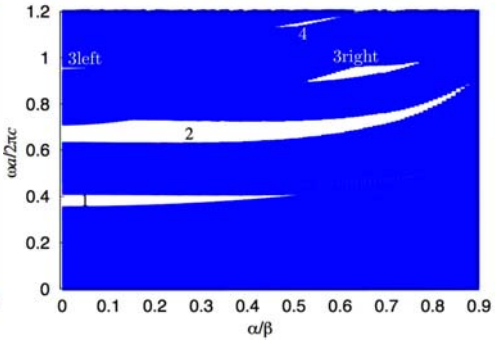

(c) Square rod ($\beta/(a/2) = 0.58$).

Figure A.3: Bandgap maps of hollow rods.

Table A.2: Normalized frequency ranges ('range') of the lowest three bandgaps of the *hollow* rods and the normalized rod thinness ('max') that correspond to the widest bandgaps.

Bandgap No.	Round		Hexagonal		Square	
	range	max	range	max	range	max
1	0.28 – 0.39	0.0	0.31 – 0.43	0.0	0.35 – 0.41	0.0
2	0.50 – 0.84	0.24	0.57 – 0.87	0.12	0.62 – 0.88	0.16
3 left	0.75 – 0.85	0.0	0.86 – 0.92	0.0	0.94 – 0.96	0.0
3 right	0.72 – 0.99	0.55	0.82 – 0.99	0.64	0.88 – 1.00	0.64
4	0.72 – 0.99	0.12	N/A	N/A	1.12 –	—

A.1.2.2 Hollow rods — Influence of rod's thinness on bandgap

We computed the bandgaps for *hollow* rods (i.e. $\alpha \neq 0$). In this case, we investigated the influence of thinness α/β to the bandgap.

The total width of bandgaps becomes largest in each crystal structures if $\beta = 0.65$, 0.60, and 0.58, respectively.

Hence, we varied α for a fixed value of β, where $\beta = 0.65$, 0.60, and 0.58 were used for the round, hexagonal, and square shape, respectively.

Figure A.3 plots the bandgap maps versus α/β. In contrast to Fig. A.2 for solid rods, the fourth bandgap is newly obtained in the round model. In addition, we observe that the third bandgaps are split into two parts, though it is not clear in the square model. We consider that this *reappearance* of the bandgap on the way of thinning the rod is caused by weakening of the reflection on the rod's surface and its enhancement effect on the inner surface of the hollow portions. Table $A.2$ summarizes the observed bandgaps for the hollow rods.

A.1.3 Dual periodic model

We investigated the bandgaps of the dual periodic model [92, 93] shown in Fig. A.1(d). In the following calculations, the radii of the solid rods was fixed to $0.65 \times a/4$ and we set $a = 280$ [nm]. The rod size $0.65 \times a/4$ gives largest width bandgaps of round shape model in Table $A.1$.

A.1.3.1 Solid rods only

First, we considered all the rods were solid (i.e. $\alpha = 0$) and calculated by varying only β. Figure. A.4 shows the result, from which we observe that the bandgap which lies around $(\omega a/2\pi c, \beta/(a/4) = (1.0, 0.3)$ remarkably increases as $\beta/(a/4)$ increases from 0.0 to 0.22. Moreover, at $\beta/(a/4) = 0.65$, which is the same case as the single periodic structure, we observe the largest total bandgap width for areas labeled as No.4, 5, and 7.

A.1.3.2 Solid and hollow rods

We calculated the bandgaps for solid and hollow rods by changing α while fixing $\beta/(a/4)$ to 0.22 and 0.65. No.2 bandgap which is the largest one in Fig. A.4, having the largest width for $\beta = 0.22 \times a/4$.

In Fig. A.5(a) is shown the bandgap map for the smaller rod: $\beta/(a/4) = 0.22$. Most of the bandgaps were smaller than the previous ones in Fig. A.4, and the positions of bandgaps are not sensitive to β. Note that we could not obtain the results for $\beta/(a/4) \gtrsim 0.70$ because it took too much computation time to solve (2.85) for the parameters.

The result for the larger rod ($\beta/(a/4) = 0.65$) is shown in Fig. A.5(b). Similarly to other PC models with hollow rods, we observe the reappearance of bandgaps. The bandgap reappearance is also observed in lower frequency regime in Fig. A.5(b). This phenomenon is considered to be natural because hollow rods are arranged to make a longer period and the longer period tends to give a lower frequency.

From comparison of the results between smaller and larger rods, we find the size of hollow portion does not have a significant effect for the reappearance of bandgaps in the case of small rod.

Let us also compare the results shown in Fig. A.3(a) and Fig. A.5(b). If $\alpha = 0$, the round model shown in Fig. A.1(a) and the dual periodic round model shown in Fig. A.1(d) become the same. The position of bandgaps shown in Fig. A.3(a) rises gradually in accordance with the increase in β, while it is steady in Fig. A.5(b). We can conjecture that these different behaviors of bandgap appearance are caused by the difference of the filling fraction of higher dielectric material; the decrease of the filling fraction causes the rise of the bandgap position. In the dual periodic structure, the effect of the increase in the hollow portions of the rods is small against the entire filling fraction. This consideration does not conflict with the result of the solid rods in which we observe the drops of the position of bandgaps as the size of rods increases.

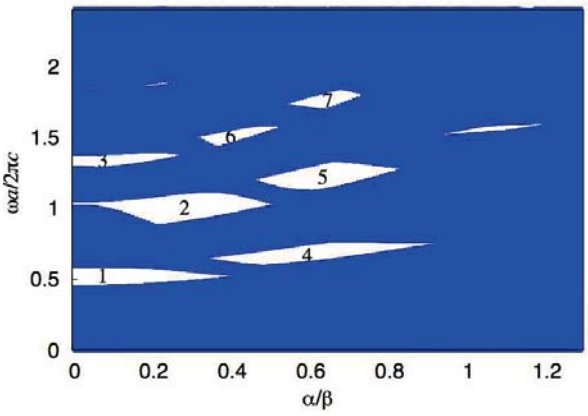

Figure A.4: Solid rods only : $\alpha = 0$.

Table A.3: Normalized frequency ranges ('range') of the labeled seven bandgaps of the dual periodic structures and the normalized rod thinness ('max') that correspond to the widest bandgaps.

Bandgap No.	range	max
1	0.44 – 0.59	0.00
2	0.87 – 1.11	0.22
3	1.27 – 1.40	0.08
4	0.58 – 0.77	0.65
5	1.10 – 1.33	0.65
6	1.43 – 1.59	0.37
7	1.69 – 1.85	0.65

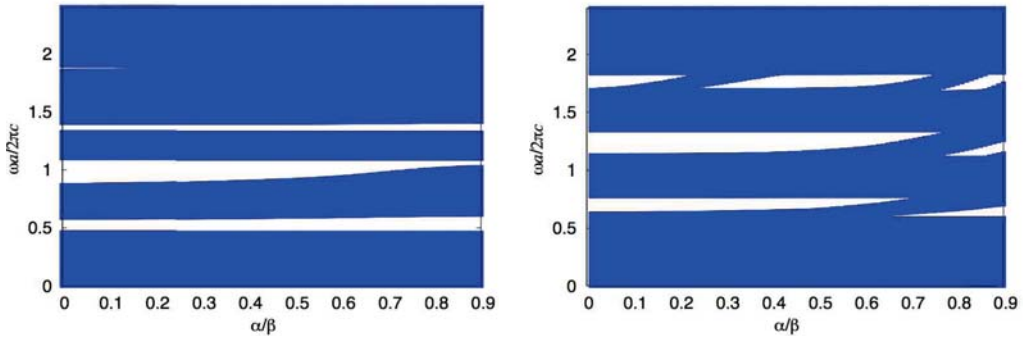

(a) Solid and hollow rods : $\beta/(a/4) = 0.22$.

(b) Solid and hollow rods : $\beta/(a/4) = 0.65$.

Figure A.5: Bandgap maps for the dual periodic model.

A.1.4 Concluding remarks

In this study, we have investigated the bandgaps of two-dimensional photonic crystals consisting of solid and hollow rods through numerical calculations based on the plane-wave expansion method. We considered four models of photonic crystals : round, hexagonal, square, and double periodic models as shown in Fig.

A.1, and calculated the bandgaps for given parameters (α and β) that define the geometryf of each models. From the results, we obtained the following remarks:

- Rod shapes and sizes affect the width of bandgaps. The symmetry of the rod shape is important to make the bandgap width wider.
- Hollowing the rods causes the reappearance of bandgaps in the bandgap map. This phenomenon can also be found in the result of dual periodic structures.
- The bandgap behaviors depend on the filling fraction of crystal structure. The smaller filling fraction raises the bandgap position. However, in the dual periodic structure, the effect of hollowing the rods against the filling fraction of the unit cell is small, and we observed steady bandgap positions.

References

[1] K. Ohtaka. Energy band of photons and low-energy photon diffraction. *Phys. Rev. B*, 19:5057, 1979.

[2] E. Yablonovitch. Inhibited spontaneous emission in solid-state physics and electronics. *Phys. Rev. Lett.*, 58:2059, 1987.

[3] K. Ohtaka. Density of states of slab photonic crystals and the laser oscillation in photonic crystals. *J. Lightwave Technol.*, 17:2161, 1999.

[4] K. Sakoda. Enhanced light amplification due to group-velocity anomaly peculiar to two- and three-dimensional photonic crystals. *Opt. Express*, 4:167, 1999.

[5] K. Sakoda, K. Ohtaka, and T. Ueta. Low-threshold laser oscillation due to group-velocity anomaly peculiar to two- and three-dimensional photonic crystals. *Opt. Express*, 4:481, 1999.

[6] Bong-Shik Song, Susumu Noda, Takashi Asano, and Yoshihiro Akahane. Ultra-high-q photonic double- heterostructure nanocavity. *nature materials*, 4:pp. 207–210, 2005.

[7] S. Noda, M. Fujita, and T. Asano. Spontaneous-emission control by photonic crystals and nanocavities. *Nature Photonics*, 1:pp. 449–458, 2007.

[8] M. Notomi, T. Tanabe, A. Shinya, E. Kuramochi, H. Taniyama, S. Mitsugi, and M. Morita. Nonlinear and adiabatic control of high-q photonic crystal nanocavities. *Opt. Express*, 15:pp. 17458–17481, 2007.

[9] Yoshinori Tanaka, Jeremy Upham, Takushi Nagashima, Tomoaki Sugiya, Takashi Asano, and Susumu Noda. Dynamic control of the q factor in a photonic crystal nanocavity. *Nature Materials*, 6:pp. 862–865, 2007.

[10] N. M. Lawandy, R. M. Balachandra, A. S. L. Gomez, and E. Sauvain. Laser action in strongly scattering media. *Nature (London)*, 368:436, 1994.

[11] D. S. Wiersma, M. P. van Albada, and A. Lagendijk. Random laser ? *Nature (London)*, 373:203, 1995.

[12] P. Sebbah and C. Vanneste. Random laser in the localized regime. *Phys. Rev. B*, 66:144202, 2002.

[13] C. Vanneste and P. Sebbah. Localized modes in random arrays of cylinders. *Phys. Rev. E*, 71:026612, 2005.

[14] P. Sebbah, B. Hu, J. K. Klosner, and A. Z. Genack. Extended quasimodes within nominally localized random waveguides. *Phys. Rev. Lett.*, 96:183902, 2006.

[15] C. Vanneste and P. Sebbah. Complexity of two-dimensional quasimodes at the transition from weak scattering to anderson localization. *Phys. Rev. A*, 79:041802, 2009.

[16] A. L. Burin, M. A. Ratner, H. Cao, and R. P. H. Chang. Model for a random laser. *Phys. Rev. Lett.*, 87:215503, 2001.

[17] S. H. Chang, H. Cao, and S. T. Ho. Cavity formation and light propagation in partially ordered and completely random one-dimensional systems. *IEEE J. Quan. Electronics*, 39:p. 364, 2003.

[18] C. Vanneste and P. Sebbah. Selective excitation of localized modes in active random media. *Phys. Rev. Lett.*, 87:183903, 2001.

[19] M. Florescu, S. Torquato, and P. J. Steinhardt. Effects of random link removal on the photonic band gaps of honeycomb networks. *Appl. Phys. Lett.*, 97:201103, 2010.

[20] Susumu Noda, Mitsuru Yokoyama, Masahiro Imada, Alongkarn Chutinan, and Masamitsu Mochizuki. Polarization mode control of two-dimensional photonic crystal laser by unit cell structure design. *Science*, 293:pp. 1123–1125, 2001.

[21] Mitsuru Yokoyama and Susumu Noda. Polarization mode control of two-dimensional photonic crystal laser having a square lattice structure. *IEEE JOURNAL OF QUANTUM ELECTRONICS*, 39:pp. 1074–1080, 2003.

[22] M. Schulz-Ruhtenberg, I.V. Babushkin, N.A. Loiko, T. Ackemann, and K.F. Huang. Transverse patterns and length-scale selection in vertical-cavity surface-emitting lasers with a large square aperture. *Appl. Phys. B*, 81:pp. 945–953, 2005.

[23] J. Limpert, N. Deguil-Robin, I. Manek-H?nninger, F. Salin, F. R?ser, A. Liem, T. Schreiber, S. Nolte, H. Zellmer, A. T?nnermann, J. Broeng, A. Petersson, and C. Jakobsen. High-power rod-type photonic crystal fiber laser. *Opt. Exp.*, 13:pp. 1055–1058, 2005.

[24] Hideki Matsubara, Susumu Yoshimoto, Hirohisa Saito, Yue Jianglin, Yoshinori Tanaka, and Susumu Noda. Gan photonic-crystal surface-emitting laser at blue-violet wavelengths. *Science*, 319:pp. 445–447, 2008.

[25] Masayuki Fujita, Shigeki Takahashi, Yoshinori Tanaka, Takashi Asano, and Susumu Noda. Simultaneous inhibition and redistribution of spontaneous light emission in photonic crystals. *Science*, 308:pp. 1296–1298, 2005.

[26] P. W. Anderson. Absence of diffusion in certain random lattices. *Phys. Rev.*, 109:1492, 1958.

[27] E. Abrahams, P. W. Anderson, D. C. Licciardello, and T. V. Ramakrishnan. Scaling theory of localization: Absence of quantum diffusion in two dimensions. *Phys. Rev. Lett.*, 42:pp. 673–676, 1979.

[28] D. S. Wiersma. The physics and applications of random lasers. *Nature Physics*, 4:359, 2008.

[29] H. Cao, Y. G. Zhao, S. T. Ho, E. W. Seelig, Q. H. Wang, and R. P. H. Chang. Random laser action in semiconductor powder. *Phys. Rev. Lett.*, 82:2276, 1999.

[30] H. Cao, J. Y. Xu, D. Z. Zhang, S. H. Chang, S. T. Ho, E. W. Seeling, X. Liu, and R. P. H. Chang. Spatial confinement of laser light in active random media. *Phys. Rev. Lett.*, 84:5584, 2000.

[31] R. M. Laine, S. C. Rand, T. Hinklin, and G. R. Williams. Ultra powders and their use as lasing media. *US Patent*, 6:656,588, 2003.

[32] Diederik S. Wiersma and Stefano Cavalieri. Light emission: A temperature-tunable random laser. *Nature*, 414:pp. 708–709, 2001.

[33] Sushil Mujumdar, Stefano Cavalieri, and Diederik S. Wiersma. Temperature-tunable random lasing: numerical calculations and experiments. *J. Opt. Soc. Am. B*, 21:pp. 201–207, 2004.

[34] J. Clerk Maxwell. A dynamical theory of the electromagnetic field. *Phil. Trans. R. Soc. Lond.*, 155:pp. 459–512, 1865.

[35] P. Drude. Zur elektronentheorie der metalle. *Annalen der Physik*, 308:pp. 370–402, 1900.

[36] C. Kittel. *Elementary Statistical Physics*. Wiley, New York, 1958.

[37] A. Yariv. *Quantum Electronics 6th edition (in Japanese)*. Maruzen, 2010.

[38] J. P. Berenger. A perfectly matched layer for the absorption of electromagnetic waves. *J. Comput. Phys.*, 114:185, 1994.

[39] A. Bermúdez, L. Hervella-Nieto, A. Prieto, and R. Rodríguez. An exact bounded pml for the helmholtz equation. *C. R. Acad, Sci. Paris, Ser. I*, 339:803, 2004.

[40] A. Bermúdez, L. Hervella-Nieto, A. Prieto, and R. Rodríguez. Numerical simulation of time-harmonic scattering problems with an optimal pml. *Variational Formulations in Mechanics:Theory and Applications*, 13:58, 2006.

[41] A. Bermúdez, L. Hervella-Nieto, A. Prieto, and R. Rodríguez. An optimal perfectly matched layer with unbounded absorbing function for time-harmonic acoustic scattering problems. *J. Comput. Phys.*, 223:469, 2007.

[42] K. Yee. Numerical solution of initial boundary value problems involving maxwell's equations in isotropic media. *IEEE Trans. Antennas Propagat.*, 14:pp. 302–307, 1966.

[43] K. Sakoda. Optical transmittance of a two-dimensional triangular photonic lattice. *Phys. Rev. B*, 51:pp. 4672–4675, 1995.

[44] K. Sakoda. Transmittance and bragg reflectivity of two-dimensional photonic lattices. *Phys. Rev. B*, 52:pp. 8992–9002, 1995.

[45] J. Andreasen, A. A. Asatryan, L. C. Botten, M. A. Byrne, H. Cao, L. Ge, L. Labont?, P. Sebbah, A. D. Stone, H. E. T?reci, , and C. Vanneste. Modes of random lasers. *Advances in Optics and Photonics*, 3:pp. 88–127, 2011.

[46] D. S. Wiersma, M. P. van Albada, and Ad Lagendijk. Coherent backscattering of light from amplifying random media. *Phys. Rev. Lett.*, 75:pp.1739–1742, 1995.

[47] C. Vanneste, P. Sebbah, and H. Cao. Lasing with resonant feedback in weakly scattering random systems. *Phys. Rev. Lett.*, 98:143902, 2007.

[48] G. Fujii, T. Matsumoto, T. Takahashi, and T. Ueta. Finite element analysis for laser oscillation in random system consisting of heterogeneous dielectric materials. *Trans. Jpn. Soc. Comput. Methods Eng.*, 10:117, 2010.

[49] G. Fujii, T. Matsumoto, T. Takahashi, and T. Ueta. Study on electric intensity dependency of laser action in randomly distributed dielectric rod. *IEEJ Trans. EIS*, 132:pp. 1–7, 2012.

[50] B. G. Ramiro, M. A. Illarramendi, I. Aramburu, J. Fernández, R. Balda, and M. Al-Saleh. Light propagation in optical crystal powders: effects of particle size and volume filling factor. *J. Phys.: Condens. Matter*, 19:456213, 2007.

[51] P. Sebbah, R. Pnini, and A. Z. Genack. Field and intensity correlation in random media. *Phys. Rev. E*, 62:7348, 2000.

[52] H. Cao, J. Y. Xu, S. H. Chang, and S. T. Ho. Transition from amplified spontaneous emission to laser action in strongly scattering media. *Phys. Rev. E*, 61:1985, 2000.

[53] S. Mujumdar, M. Ricci, R. Torre, and D. S. Wiersma. Amplified extended modes in random lasers. *Phys. Rev. Lett.*, 93:053903, 2004.

[54] E. Yablonovitch and T. J. Gmitter. Photonic band structure: The face-centered-cubic case. *Phys. Rev. Lett.*, 63:1950, 1989.

[55] E. Yablonovitch. Photonic band-gap structures. *J. Opt. Soc. Am. B*, 10:283, 1993.

[56] G. Fujii, T. Matsumoto, T. Takahashi, and T. Ueta. A study on optical properties of photonic crystals consisting of hollow rods. *IOP Conf. Ser.: Mater. Sci. Eng.*, 10:012072, 2010.

[57] G. Fujii, T. Matsumoto, T. Takahashi, and T. Ueta. A study on the effect of filling factor for laser action in dielectric random media. *Appl. Phys. A*, 2011.

[58] A. Rodriguez, M. Ibanescu, J. D. Joannopoulos, and S. G. Johnson. Disorder-immune confinement of light in photonic-crystal cavities. *Opt. Lett.*, 30:3192, 2005.

[59] Z.-Y. Li and Z.-Q. Zhang. Fragility of photonic band gaps in inverse-opal photonic crystals. *Phys. Rev. B*, 62:1516, 2000.

[60] E. Lidorikis, M. M. Sigalas, E. N. Economou, and C. M. Soukoulis. Gap deformation and classical wave localization in disordered two-dimensional photonic-band-gap materials. *Phys. Rev. B*, 61:13458, 2000.

[61] T. Schwartz, G. Bartal, S. Fishman, and M. Segev. Transport and anderson localization in disordered two-dimensional photonic lattices. *Nature*, 446:52, 2007.

[62] Y. Lahini, A. Avidan, F. Pozzi, M. Sorel, R. Morandotti, D. N. Christodoulides, and Y. Silberberg. Anderson localization and nonlinearity in one-dimensional disordered photonic lattices. *Phys. Rev. Lett.*, 100:013906, 2008.

[63] H. Li, B. Cheng, and D. Zhang. Two-dimensional disordered photonic crystals with an average periodic lattice. *Phys. Rev. B*, 56:10734, 1997.

[64] M. A. Kaliteevski, J. M. Martinez, D. Cassagne, and J. P. Albert. Disorder-induced modification of the transmission of light in a two-dimensional photonic crystal. *Phys. Rev. B*, 66:113101, 2002.

[65] T. Prasad, V. L. Colvin, and D. M. Mittleman. The effect of structural disorder on guided resonances in photonic crystal slabs studied with terahertz time-domain spectroscopy. *Opt. Express*, 15:16954, 2007.

[66] Yu. A. Vlasov, M. A. Kaliteevski, and V. V. Nikolaev. Different regimes of light localization in disordered photonic crystal. *Phys. Rev. B*, 60:1555, 1999.

[67] M. Patterson, S. Hughes, S. Combrié, N.-V.-Q. Tran, A. De Rossi, R. Gabet, and Y. Jaouën. Disorder-induced coherent scattering in slow-light photonic crystal waveguides. *Phys. Rev. Lett.*, 102:253903, 2009.

[68] R. Ferrini, D. Leuenberger, R. Houdré, H. Benisty, M. Kamp, and A. Forchel. Disorder-induced losses in planar photonic crystals. *Opt. Lett.*, 31:1426, 2006.

[69] M. M. Sigalas, C. M. Soukoulis, C. T. Chan, R. Biswas, and K. M. Ho. Effect of disorder on photonic band gaps. *Phys. Rev. B*, 59:12767, 1999.

[70] A. A. Asatryan, P. A. Robinson, L. C. Botten, R. C. McPhedran, N. A. Nicorovici, and C. M. de Sterke. Effects of geometric and refractive index disorder on wave propagation in two-dimensional photonic crystals. *Phys. Rev. E*, 62:5711, 2000.

[71] W. R. Frei and H. T. Johnson. Finite-element analysis of disorder effects in photonic crystals. *Phys. Rev. B*, 70:165116, 2004.

[72] A. A. Asatryan, P. A. Robinson, L. C. Botten, R. C. McPhedran, N. A. Nicorovici, and C. M. de Sterke. Effects of disorder on wave propagation in two-dimensional photonic crystals. *Phys. Rev. E*, 60:6118, 1999.

[73] H. Li, H. Chen, and X. Qiu. Band-gap extension of disordered 1d binary photonic crystals. *Physica B*, 279:164, 2000.

[74] X. Wang and K. Kempa. Effects of disorder on subwavelength lensing in two-dimensional photonic crystal slabs. *Phys. Rev. B*, 71:085101, 2005.

[75] T. N. Langtry, A. A. Asatryan, and L. C. Botten. Effects of disorder in two-dimensional photonic crystal waveguides. *Phys. Rev. E*, 68:026611, 2003.

[76] V. N. Astratov, J. P. Franchak, and S. P. Ashili. Optical coupling and transport phenomena in chains of spherical dielectric microresonators with size disorder. *Appl. Phys. Lett.*, 85:5508, 2004.

[77] K. C. Kwan, X. Zhang, Z. Q. Zhang, and C. T. Chan. Effects due to disorder on photonic crystal-based waveguides. *Appl. Phys. Lett.*, 82:4414, 2003.

[78] D. P. Fuell, S. Hughes, and M. M. Dignam. Effect of disorder strength on the fracture pattern in heterogeneous networks. *Phys. Rev. B*, 76:144201, 2008.

[79] D. Gerace and L. C. Andreani. Effects of disorder on propagation losses and cavity q-factors in photonic crystal slabs. *Photonics and Nanostructures - Fundamentals and Applications*, 3:120, 2005.

[80] A. Golshani, H. Pier, E. Kapon, and M. Moser. Photon mode localization in disordered arrays of vertical cavity surface emitting lasers. *Appl. Phys. Lett.*, 85:2454, 1999.

[81] J. Topolancik and F. Vollmer. Random high-q cavities in disordered photonic crystal waveguides. *Appl. Phys. Lett.*, 91:201102, 2007.

[82] T. A. Leskova, A. A. Maradudin, I. V. Novikov, A. V. Schegrov, and E. R. Méndez. Design of one-dimensional band-limited uniform diffusers of light. *Appl. Phys. Lett.*, 73:1943, 1998.

[83] E. R. Méndez, E. E. García, T. A. Leskova, A. A. Maradudin, J. Muñoz-Lopez, and I. Simonsen. Design of one-dimensional random surfaces with specified scattering properties. *Appl. Phys. Lett.*, 81:798, 2002.

[84] E. R. Méndez, T. A. Leskova, A. A. Maradudin, and J. Muñoz-Lopez. Design of one-dimensional random surfaces with specified scattering properties. *Opt. Lett.*, 29:2917, 2004.

[85] S. Fan, P. R. Villeneuve, and J. D. Joannopoulos. Theoretical investigation of fabrication-related disorder on the properties of photonic crystals. *J. Appl. Phys.*, 78:1415, 1995.

[86] L. O. Faolain, T. P. White, D. O. Brien, X. Yuan, M. D. Settle, and T. F. Krauss. Dependence of extrinsic loss on group velocity in photonic crystal waveguides. *Opt. Express*, 15:13129, 2007.

[87] K. C. Kwan, X. M. Tao, and G. D. Peng. Transition of lasing modes in disordered active photonic crystals. *Opt. Lett.*, 32:2720, 2007.

[88] Diederik S. Wiersma and Ad Lagendijk. Light diffusion with gain and random lasers. *Phys. Rev. E*, 54:4256, 1996.

[89] Jin U. Kang. Observation of random lasing in gold-silica nanoshell/water solution. *Appl. Phys. Lett.*, 89:221112, 2006.

[90] N. M. Lawandy. Observation of random lasing in gold-silica nanoshell/water solution. *Appl. Phys. Lett.*, 89:221112, 2006.

[91] J. D. Joannopoulos, S. G. Johnson, J. N. Winn, and R. D. Meade. *Photonic Crystals: Molding the Flow of Light 2nd ed.* Princeton: Princeton University Press, 2008.

[92] R. Shimada, T. Koda, T. Ueta, and K. Ohtaka. Energy spectra in dual-periodic multilayer structures. *J. Phys. Soc. Jpn.*, 67:pp. 3414–3419, 1998.

[93] R. Shimada, T. Koda, T. Ueta, and K. Ohtaka. Strong localization of bloch photons in dual-periodic dielectric multilayer structures. *J. Appl. Phys.*, 90:pp. 3905–3909, 2001.